ABSTRACT

THE IMPACT OF ABIOTIC AND BIOGENIC MN OXIDE COATINGS ON CONTAMINANT MOBILITY, BIOAVAILABILITY, AND ATTENUATION

by
Thipnakarin Boonfueng

Abiotic and biogenic manganese oxide coatings significantly impact the mobility and bioavailability of metals in soils and sediments. While sorption to discrete Mn oxides has been investigated in a number of studies, coatings have not received as much attention. Abiotic nanocrystalline (hydrous manganese oxide (HMO)) and crystalline Mn oxides (birnessite and pyrolusite) coated on montmorillonite were studied for formation, structure, stability, and surface properties. Coatings dominated the clay surface characteristics where the surface charge behaved similar to that of the discrete oxide and the local structure was consistent with the pure oxide phase. Furthermore, in sorption studies, Zn and Pb ions formed inner-sphere complexes as tridentate and bidentate corner-sharing structures, respectively. On the other hand, vacancy sites along the oxide surface were occupied by Ni. In biomineralization, a nano-particulate Mn oxide coated the sheathed *Leptothrix discophora* SP-6 forming a dendritic biofilm structure. The surface charge and the local structure were consistent with that of abiotic HMO where the oxide potentially forms a polymer-like precursor to birnessite consistent with the phyllomanganate family. Surface properties of the coated bacteria are dominated by the oxide as Zn formed inner-sphere complexes resulting in octahedral structures. On the other hand, sorption to the sheathed *L. discophora* SP-6 involved complexation with phosphoryl (84%) and carboxyl (16%) groups. The slow sorption process, intraparticle surface diffusion, was observed in abiotic and biogenic oxide systems, indicating that Mn oxide present as coatings or discrete particles acts as a sink for metal contaminants.

THE IMPACT OF ABIOTIC AND BIOGENIC MN OXIDE COATINGS ON CONTAMINANT MOBILITY, BIOAVAILABILITY, AND ATTENUATION

by
Thipnakarin Boonfueng

A Dissertation
Submitted to the Faculty of
New Jersey Institute of Technology
In Partial Fulfillment of the Requirements for the Degree of
Doctor of Philosophy in Environmental Engineering

Department of Civil and Environmental Engineering

August 2006

APPROVAL PAGE

THE IMPACT OF ABIOTIC AND BIOGENIC MN OXIDE COATINGS ON CONTAMINANT MOBILITY, BIOAVAILABILITY, AND ATTENUATION

Thipnakarin Boonfueng

Dr. Lisa Axe, Dissertation Advisor — Date
Associate Professor of Civil and Environmental Engineering, NJIT

Dr. Methi Wecharatana, Committee Member — Date
Professor of Civil and Environmental Engineering, NJIT

Dr. Trevor A. Tyson, Committee Member — Date
Professor of Physics, NJIT

Dr. Dittmar Hahn, Committee Member — Date
Associate Professor of Biology, Texas State University

Dr. Nathan Yee, Committee Member — Date
Assistant Professor of Earth and Environmental Sciences, Rutgers,
The State University of New Jersey (Joint Program Faculty with Civil and Environmental Engineering Department, NJIT)

Dr. James A. Dyer, Committee Member — Date
Senior Consultant for DuPont Engineering Research and Technology, DE

BIOGRAPHICAL SKETCH

Author: Thipnakarin Boonfueng

Degree: Doctor of Philosophy

Date: August 2006

Undergraduate and Graduate Education:

- Doctor of Philosophy in Environmental Engineering
  New Jersey Institute of Technology, Newark, NJ, 2006

- Bachelor of Engineering in Chemical Engineering
  Kasetsart University, Bangkok, Thailand, 1999

Major: Environmental Engineering

Presentations and Publications:

Boonfueng, T., Axe, L., Yee, N., and Tyson, T.A. Zn sorption mechanisms onto sheathed *Leptothrix Discophora* SP-6 and the impact of nanoparticulate, biogenic Mn oxide coating (*submitted*)

Boonfueng, T., Axe, L., Yee, N., and Dittmar, H. Biogenic Mn Oxide – Nano-Particle Formation, Characterization, and Encrustation into the Sheathed *Leptothrix Discophora* SP-6 Biofilm (*submitted*)

Boonfueng, T., Axe, L., Xu, Y., and Tyson, T.A. Nickel and Lead Sequestration in Manganese Oxide-Coated Montmorillonite. *Journal of Colloid and Interface Science*, in press.

Boonfueng, T., Axe, L., Xu, Y., and Tyson, T.A. (2006) Impact of Mn oxide coatings on Zn distribution. *Journal of Colloid and Interface Science*, 298(2), 615-623.

Xu, Y., Boonfueng, T., Axe, L., Maeng, S., and Tyson, T.A. (2006) Surface complexation of Pb(II) on amorphous iron and manganese oxide: spectroscopic and time studies. *Journal of Colloid and Interface Science,* 299(1), 28-40.

Boonfueng, T., Axe, L., and Xu, Y. (2005) Properties and structure of manganese oxide-coated clay. *Journal of Colloid and Interface Science,* 281(1), 80-92.

Fan, M., Boonfueng, T., Xu, Y., Axe, L., and Tyson, T.A. (2005) Modeling Pb Sorption to Microporous Amorphous Oxides as Discrete Particles and Coatings. *Journal of Colloid and Interface Science*, 281(1), 39-48.

Boonfueng, T., and Axe, L. 2004 Adsorption of Heavy Metals on Manganese Oxide Coated Clay, *Proceedings of the Eleventh International Symposium on Water-Rock Interactions,* (Ed. Wanty, R.B. and Seal, R.R.II), Taylor & Francis Group plc, London, UK, 1259-1263.

Boonfueng, T., Axe, L.,and Yee, N. Zn(II) Sorption Mechanisms on biogenic Mn oxide Sheathed *Leptothrix discophora* SP-6 Surface, Division of Geochemistry, 231st American Chemical Society National Meeting - Atlanta, GA, March 26-30, 2006.

Boonfueng, T, Axe, L., and Xu, Y., Sequestration of Pb by Hydrous Mananese Oxid-Coated Clay, SS-67: Speciation of metals and metalloids in the environment: Control by mineral structures and surface processes, 15th Annual Goldschmidt Conference, University of Idaho, May 19, 2005.

Boonfueng, T. and Axe, L. Macro and Microscopic Studies on Zn Sorbed onto Manganese Oxide-coated clay, American Chemical Society 78th Colloid and Surface Science Symposium, Chemical Reactivity and Sorption Phenomena, Yale University, CT, June 20-23, 2004.

Boonfueng, T., Axe, L., Fan, M., Xu, Y. Long-term studies on zinc sorption onto hydrous manganese oxide coated montmorillonite, Advances in Environmental Reaction Kinetics and Thermodynamics: Long-term Fate of Anthropogenic Contaminants, Division of Environmental Chemistry program, 228th American Chemical Society National Meeting - Philadelphia, PA, August 23-26, 2004.

Fun, M., Xu, Y., Boonfueng, T., Yuan, W., Axe, L., Tyson, T.A., Intraparticle surface diffusion of Pb in amorphous Fe and Mn oxides, Physicochemical Processes in Environmental Systems: A Symposium in Honor of Professor Walter J. Weber, Jr, 226th American Chemical Society National Meeting - New York, NY, September 7-11, 2003.

Boonfueng, T. and Axe, L., Lead adsorption studies on hydrous manganese oxide (HMO), montmorillonite, and HMO coated montmorillonite, Physicochemical Processes in Environmental Systems: A Symposium in Honor of Professor Walter J. Weber, Jr, Division of Environmental Chemistry program, 226th American Chemical Society National Meeting - New York, NY, September 7-11, 2003.

Boonfueng, T. and Axe, L., Surface properties of manganese oxide coated montmorillonite, Poster Session, Division of Geochemistry, 226th American Chemical Society National Meeting - New York, NY, September 7-11, 2003.

Xu, Y., Axe, L., Maeng, S., Trivedi, P., Boonfueng, T., Tyson, T.A., Pandya, K., Adsorption of heavy metals on iron oxide coated silica, Poster Session, Division of Geochemistry, 226th American Chemical Society National Meeting - New York, NY, September 7-11, 2003.

Chareonpanich, M., Boonfueng, T., and Limtrakul, J. (2002) Production of aromatic hydrocarbons from Mae-Moh lignite. *Fuel Processing Technology*, 79(2), 171-179.

To my family for their patience, understanding, support, and love.

ACKNOWLEDGEMENT

I would like to thank the many people who have contributed to this works. Special thanks are due to my research advisor, Dr. Lisa Axe who provided me her valuable time, energy, and the encouragement and reassurance. I would like to thank Dr. Dittmar Hahn, Dr. Trevor A. Tyson, Dr. Nathan Yee, Dr. James A. Dyer, and Dr. Methi Wecharatana for actively participating in my committee and providing valuable support and guidance from their own areas of expertise.

I am very thankful for the National Science Foundation Grant No BES 0089903 and the DuPont Young Professor Grant for providing financial support for this research. I also would like to thank all my professors, the laboratory staff, and the staff of the Department of Civil and Environmental Engineering for their help. I would like extend my gratitude to Dr. Kaumidi Pandya for her assistance and technical support at beamline X11, National Synchrotron Light source, Brookhaven National Laboratory.

My special gratitude goes to Dr. Ying Xu, Dr. Sungmin Maeng and Dr. Paras Trivedi, for being such a wonderful colleague and more than that, a good friend. Many of my fellow graduate students, Sun Punurai and Krit Punburananon are deserving of recognition for their warm friendship and great support. I also wish to thank Samantha Butisigh for her assistance over the summer 2005. To my parent, who has given me tremendous love and support, I feel fortunate to be their children. I also would like to thanks my sisters, Krithpaka and Fifa for being a great and important cheerleader during my study. It is only because of the support from my family and friends that I was able to make it.

TABLE OF CONTENTS

TABLE OF CONTENTS
(Continued)

TABLE OF CONTENTS
(Continued)

Chapter **Page**

LIST OF TABLES

LIST OF FIGURES

LIST OF FIGURES
(Continued)

Figure **Page**

LIST OF FIGURES
(Continued)

Figure **Page**

LIST OF FIGURES
(Continued)

Figure **Page**

LIST OF FIGURES
(Continued)

Figure **Page**

LIST OF FIGURES
(Continued)

Figure **Page**

LIST OF FIGURES
(Continued)

Figure **Page**

CHAPTER 1

INTRODUCTION

In the environment, Manganese oxides are ubiquitous in soils and sediments, occur as discrete particles and coatings and originate via abiotic and biogenic processes. This oxide is present in various forms, ranging from amorphous to crystalline in structure. In this research, several types of Mn oxides are investigated including hydrous Mn oxide (HMO), birnessite, pyrolusite, as well as biogenic Mn oxide, produced from Mn oxidizing bacteria, *Leptothrix discophora* SP-6. HMO, exhibiting no long-range structure, is prevalent in nature and has a very large surface area, microporous structure, and a high affinity for metal ions. Crystalline oxides, birnessite and pyrolusite, are common in soils and sediments too playing a role in metal distribution and mobility. Although abiotic Mn oxides often serve as a model system in studies, biogenic processes dominate. Therefore, the surface properties and structure of biogenic Mn oxide is compared to the abiotic oxide.

Mn oxides form via a number of different mechanisms in the transition from reducing to oxidizing conditions. They have been observed to associate with clay minerals, sand, and organic matter, occurring in, for example, sediments from marine environments, streams, lakes, and hot springs (Manceau et al. 2003; Dong et al. 2000; Manderneck et al. 1995; Tani et al. 2003; Nelson et al. 1995). Clay is a common substrate that plays a vital role in sorption of metal ions in aqueous environments. Understanding the occurrence and forms of Mn oxides associated with clay minerals is important for assessing heavy metal interactions with these surfaces. The effect of Mn oxide coatings

on heavy metal distribution is evaluated to better understand mobility, bioavailability, and attenuation.

This dissertation includes a literature review on Mn oxide occurrence and behavior. Hypotheses and objectives are presented and experimental procedures to test hypotheses are described. Results are presented on surface properties of abiotic Mn oxides, both amorphous and crystalline, as well as clay minerals kaolinite and montmorillonite. These two clays were selected as potential substrates for the Mn oxide coatings because they are prevalent in soil and sediment environments, possess large specific surface areas, and exhibit structural charge. Studies on abiotic and biogenic Mn oxides coatings are also discussed with respect to their impact on metal distribution for zinc, nickel, and lead. The dissertation concludes with a summary of the findings and potential work for future studies.

CHAPTER 2

ABIOTIC AND BIOGENIC MANGANESE OXIDE COATINGS AND THEIR IMPACT ON METAL DISTRIBUTION

Manganese oxides have been exploited since the ancient times; today they are among the most important minerals in the environment. Mn oxides are found in a wide variety of geological environments and are nearly ubiquitous in soils and sediments, existing as discrete particles and coatings, originating via chemical and biological processes. Mn oxide coatings are often associated with clay minerals which occur widely in such sedimentary rocks as mudstones and shales, in marine sediments, and in soils. Although clays and Mn oxides have been studied extensively as discrete systems, their behavior in heterogeneous systems has not been investigated to the same extent. Furthermore, Mn oxides produced from biologically mediated reactions are observed with organic matter or extracellular polymeric substances excreted by organisms. In this chapter, the following is reviewed from the perspective of their occurrence and significance in the environment: abiotic Mn oxides, biogenic Mn oxide, Mn oxide coatings, and the impact of oxide coatings on metal contaminant distribution.

2.1 Abiotic Mn Oxides

Hydrous manganese oxide (HMO), vernadite (δ-MnO_2), and birnessite minerals are poorly crystalline oxides that are commonly found in soils and sediments (Jenne, 1977, Lion et al. 1982, Balistrieri and Murray, 1982, Wenfeng et al. 2000; Exon et al. 2002, Hochella et al. 2005, Manceau et al. 2005). HMO, the most amorphous structure, has a very large surface area, microporous structure, and high affinity for metal ions, providing

an efficient scavenging pathway for heavy metals in oxic systems (Balistrieri and Murray, 1982). In this study, the term amorphous is used in referring to a poorly crystalline mineral that does not exhibit long-range order. Although a number of researchers (Axe et al. 2000; Manceau et al. 1987; Manceau and Combes, 1988; Pasten, 2002) have studied HMO morphology and mineralogy as well as its impact on metal mobility, the actual long-range structure still remains unclear as diffraction data fail to provide a unique solution (Manceau et al. 1987; Pasten, 2002). However, based on vernadite and asbolane ($(Co, Ni)_{1-y}(MnO_2)_{2-x}(OH)_{2-2y-2x}\cdot nH_2O$), Manceau and coworkers (e.g., Manceau et al. 1987, Manceau et al. 1988) proposed that the structure appears to have a random framework of edge- and corner-sharing MnO_6 octahedra, not strictly related to well-crystallized Mn minerals; this observation is consistent with other studies (Axe et al. 2000; Pasten, 2002; Friedl et al. 1997). Vernadite is a hydrous slightly crystalline mineral which shows only two lines at 1.4 and 2.1 Å and may represent a disordered birnessite (Silvester et al. 1997). The more crystalline forms of Mn oxide, birnessite and pyrolusite, exist in soils and sediments also playing a role in the distribution of metal contaminants.

Generally, the building block for most Mn oxides is octahedral MnO_6, which exhibits either a tunneled or layered structure (McKenzie, 1989; Morgan and Stumm, 1964) (Figure 2.1). Layered (7.2 Å apart) octahedral birnessite is the most common crystalline, Mn mineral identified in soils (McKenzie, 1989; Chukhrov and Gorshkov, 1981; Giovanoli, 1980) belonging to the phyllomanganate family. One out of six octahedral sites is unoccupied, and vacancies are balanced by counter ions such as Na^+, K^+, or Mg^{2+}. Birnessite has been used as a model manganese oxide in environmental

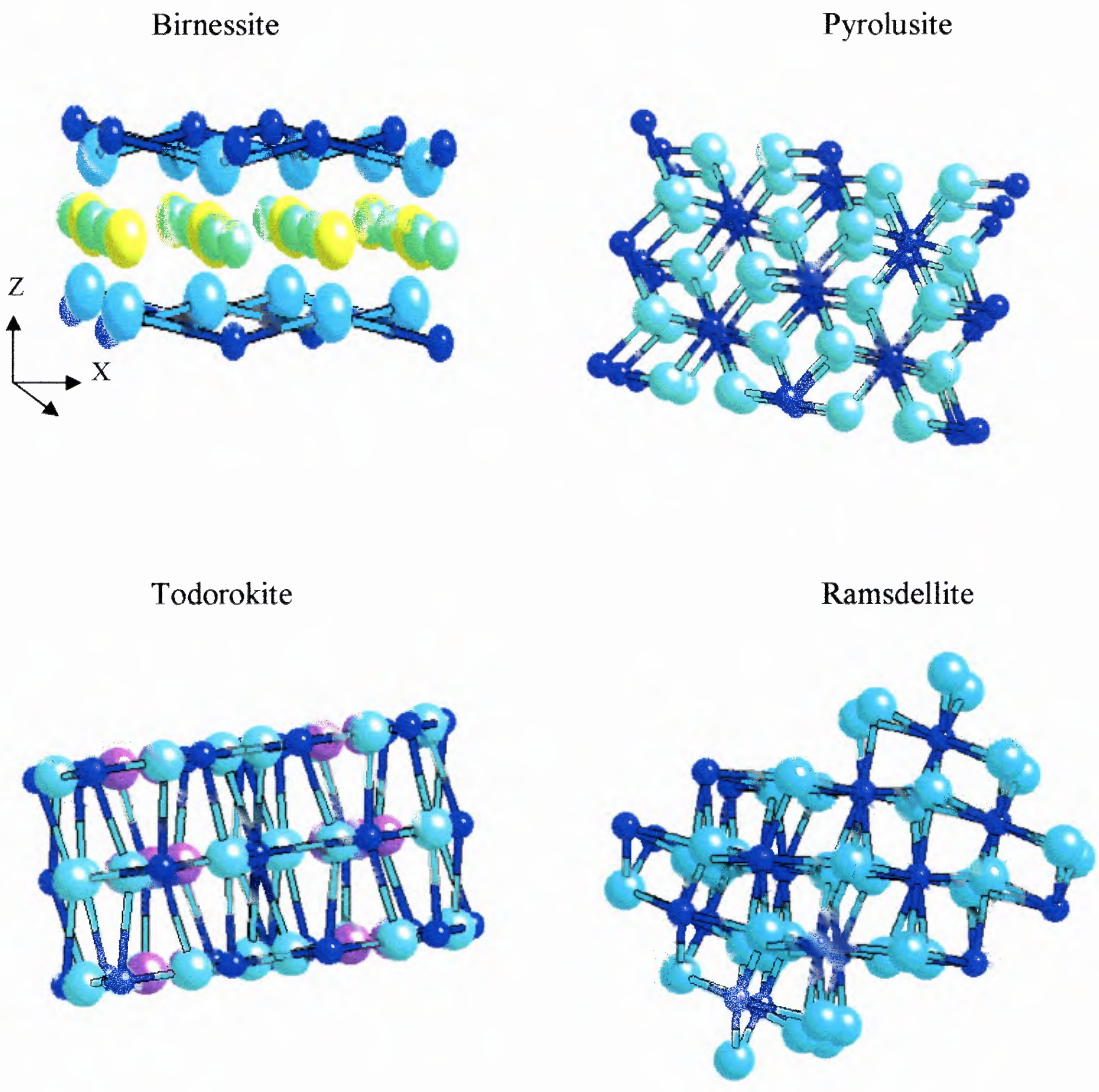

Figure 2.1 The structure of Mn oxides: layered structure (e.g., birnessite) and tunneled structure (e.g., pyrolusite, todorokite and ramsdellite). The dark and light blue balls illustrate Mn and O atoms respectively, and the green, yellow, and purple balls are symbols of H_2O, Na^+, and OH^-, respectively.

studies (Manceau and Charlet, 1992; Manceau et al. 2003) as it has unique surface charge properties, a high affinity for cations, and a redox active surface (Chukhrov et al. 1987; Healey and Herring, 1966; Scott and Morgan, 1995). However, because it is metastable, birnessite may transform to pyrolusite (β-MnO_2), which exhibits a tunneled structure and commonly occurs in low temperature hydrothermal deposits (McKeown and Post, 2001). The single chains of edge-sharing MnO_6 octahedra apportion corners with neighboring chains to form a framework structure, creating tunnels with square cross sections (McKeown and Post, 2001). Mn oxides play an important role in adsorption as well as oxidation; for example, birnessite and pyrolusite have been observed to oxidize Cr(III) to Cr(VI) (Banerjee and Nesbit, 1999; Kim et al. 2002; Chung and Zasoski, 2002), As(III) to As(V) (Manning et al. 2002; Tournassat et al. 2002), and Se(IV) to Se(VI) (Scott and Morgan, 1996).

Studies simulating natural coatings include Al and Fe oxyhydroxide-coated montmorillonite (Celis et al. 1997; Green-Pederson and Pind, 2000; Helmy et al. 1994); Mn, Fe, and Al-coated silica (Stahl and James, 1991, b; Tsadilas et al. 1998; Zachara et al. 1995); and biogenic Mn and Fe oxide films or coatings (Nelson et al. 2003, Tani et al. 2003, Dong et al. 2003, Vilalobos et al. 2005). In simulating abiotic coatings, oxides have been coated or deposited by various methods that include for example precipitation, adsorption, wet or dry oxidation, and calcinations (Stahl and James, 1991; Al-Degs et al. 2001; Fan, 1996; Zaki et al. 1995). The effect of pH, temperature, and oxide loading has been studied to some extent, for example, Green-Pederson and Pind (2000) found ferrihydrite- and lepidocrocite-coated montmorillonite resulted in a significant amount of Fe on the surface that increased surface area and dominated the particle size distribution.

The pH_{iep} of the coatings was close to that of the pure oxide. Sorption of Ni was greatest on the ferrihydrite-coated surface although lepidocrocite also improved the sorption characteristics as compared to montmorillonite. Stahl and James (1991) produced Mn oxide-coated sand as a function of temperature and obtained a birnessite coating at room temperature and a pyrolusite one at 105 °C. Both coatings increased Zn affinity for the surface as compared to the uncoated sand.

While Al and Fe oxides deposited on minerals such as clay have been studied to some degree, the formation and properties of Mn oxide-coated clay have not been investigated. The enrichment of clay minerals may be an important factor in controlling manganese oxide mineralogy. Understanding the occurrence and forms of Mn oxide in the presence of montmorillonite is important for assessing heavy metal interactions with these surfaces and therefore metal mobility and bioavailability. Furthermore, although abiotic oxides are used as model systems in studying contaminant distribution, biomineralization is the dominant pathway for Mn oxide occurrence in the environment and therefore, it formation and properties are discussed in the next section.

2.2 Biogenic Mn Oxides

For microorganisms, plants, and animals, manganese is an essential trace element. Mn serves as an activator by enzymes, as a terminal electron acceptor in respiration, and as an energy source or electron donor to some autotrophic and mixotrophic bacteria, resulting in oxidation and reduction reactions of Mn(II) and Mn(IV). In general, Mn(II) oxidation is mediated by microorganisms found in aquatic, soil-sediment, and marine environments (Bromfield, 1979; Villalobos et al. 2003; Barger et al. 2000); its oxidation

is characterized as an enzymatic reaction of aquatic bacteria involving multicopper oxidase (Brouwers et al. 1999, 2000). *Leptothrix discophora* SP-6 is one such organism that is sheath forming, gram negative, and is found in freshwater habitats including lakes, ponds, swamps, or springs (Ghiorse, 1984). Although the oxidation kinetics for *L. discophora* SS1 and SP-6 strains were studied in the well-defined minimum salt-vitamins-pyruvate medium (MSVP) (Zhang et al. 2002, Pasten, 2002), oxidation in a system more representative of substrate available in the subsurface environment has not be studied. For example, a complex medium of peptone and yeast extract (PY) is comprised of protein from milk and autolyzed yeast which is rich in carbon, nitrogen, vitamins, and amino acids that serve as a growth factor stimulating the synthesis of proteins (Madigan et al. 2000). On the other hand, in MSVP, bacteria convert pyruvate to amino acids during respiration. Interestingly, Emerson and Ghiorse (1993) observed a significant amount of uronic acid and amino sugar in the extracellular polysaccharide sheath produced in the MSVP medium, while Romano and Peloquin (1963) found neutral sugar (glucose) in the extracellular polysaccharide sheath using peptone, yeast extract, and glucose (PYG). This sheath can buffer the microenvironment around cells against changes in pH, salinity, and the harmful effects of toxins (e.g., heavy metals).

Because Mn oxide formation in the subsurface is dominated by biogenic processes and because this surface is an important one for metal contaminants due to its high affinity for cations, its large surface area, and its microporous structure, an understanding of its formation, surface properties, and characteristics is critical in assessing contaminant behavior. Several studies have focused on the mineralogy and molecular structure of biogenic Mn oxides using synchrotron x-ray diffraction (SR-XRD)

and x-ray absorption spectroscopy (XAS) on *Bacillus* sp strain SG-1 (Barger et al. 2000), *Pseudomonas putida* MnB1 (Villalobos et al. 2003), and *L. discophora* SP-6 (Jürgensen et al. 2004). Jürgensen et al. used PYG media and proposed a mixture of Mn(III) and Mn(IV) in a birnessite-like layer on the polysaccharide sheath; Pasten (2002) too found the biogenic oxide to be consistent with the phyllomaganate layered structure. In contrast, based on Raman spectroscopy (Kim et al. 2004), oxide produced from *L. discophora* SP-6 in MSVP resulted in a 3 × 3-tunneled todorokite. Interestingly, however, Mn oxide isolated from *P. putida* MnB1 was also observed to be consistent with acid-birnessite (Villalobos et al. 2003). A marine microorganism, *Bacillus* sp strain SG-1 produced biogenic Mn oxide similar to vernadite (δ-MnO_2) where the average oxidation state was 3.7; others have found similar results (Friedl et al. 1997, Kalhorn and Emerson, 1984). Mandernack et al. (1995) observed that once δ-MnO_2 was produced, additional Mn^{2+} greater than 0.5 mM resulted in transformation to feitknechtite (β-MnOOH, a layered structure), while at concentrations less than 0.5 mM, a 10 Å Na-buserite formed ($Na_4Mn_{14}O_{27} \cdot 9H_2O$, a layered structure).

These biogenic oxides often deposit on other surfaces including biofilms, clays, and silica. Because the oxides are metastable, understanding their formation, structure, morphology, and stability is critical to studying contaminant interactions, both short- and long- term, with these surfaces.

2.3 Mn Oxide Coatings

Oxides of manganese are important components in soils and sediments and major sinks for metals released into the environment from various sources (Carroll et al. 1998; Gadde and Laitinen, 1974; Green-Pederson et al. 1997; Jenne, 1977; Kraepiel et al. 1999; Lion et al. 1982; McKenzie, 1989; Meng and Letterman, 1993; Nelson et al. 2002; Pam and Liss, 1998; Sigg et al. 1999; Trivedi and Axe, 2000). Mn oxides present as coatings have been studied spectroscopically, crystallographically, and compositionally (Stahl and James. 1991; Manderneck et al. 1995; Tsadilas et al. 1998; Knocke et al. 1988). In rock varnish and dendrites, the mineralogy of the Mn oxide coating was characterized using X-ray absorption spectroscopy (XAS) (McKeown and Post, 2001), where its valance state was observed to be closer to four and the structure ranged from tunneled (todorokite and romanechite) to layered (birnessite-family). In the marine environment, Mn oxides observed with silica, carbonates, and clay have been attributed as manganite (γ-MnOOH), birnessite, todorokite, or vernadite when formed at the oxic-anoxic boundary (Friedl et al. 1997; Post, 1999; Chukhrov et al. 1979). Natural surface coatings found in streams and lakes reveal that both Mn-oxidizing bacteria and fungi can oxidize Mn^{2+} to a Mn oxide (Manceau et al. 2003; Dong et al. 2000; Manderneck et al. 1995; Tani et al. 2003; Nelson et al. 1995). Biogenic Mn oxide coatings on streambeds may serve as an indicator of soil acidification and metal leaching from soils of the corresponding watershed (Dong et al. 2003; Li et al. 2003). Moreover, Mn oxide coatings found on silica, clay, and anthracite filter media in treatment plants act as Mn greensand with the ability to adsorb soluble Mn and other heavy metals (Fan, 1996; Knocke et al. 1988). The oxide coating changes the substrate surface area, porosity, particle size, and surface charge characteristics which

influence sorption properties (Stahl and James, 1991; Tsadilas et al. 1998; Zachara et al. 1995; Al-degs et al. 2001; Green-Pederson and Pind, 2000). Numerous studies have demonstrated that surface area increases and the surface charge behavior are similar to the discrete oxide, depending on the degree of coating (Green-Pederson and Pind, 2000; Green-Pederson et al. 1997; Nachtegaal and Sparks, 2004). Furthermore, a number of researchers (Axe et al. 2000; Trivedi and Axe, 1999; 2000; Trivedi et al. 2001) have observed that metals may be effectively sequestered by discrete amorphous Mn oxide, therefore these oxide coatings are potentially important surfaces in controlling the distribution of metals in the subsurface environment (Jenne, 1977; Post, 1999).

2.4 Impact of Mn Oxide on Metal Distribution

2.4.1 Discrete Mn Oxide

Generally, metal ions such as Zn, Ni, and Pb have been observed to be strongly associated with Mn/Fe (oxyhydr)oxides and phyllosilicates in, for example, the fine-grained fraction of dredged sediment which controlled its behavior in the environment (Isaure et al. 2002). Consequently, a number of studies have focused on Zn, Ni, and Pb speciation and sorption complexes on discrete oxides (Bochatay and Persson, 2000; Li et al. 2004; Trivedi and Axe, 2000; Trivedi et al. 2001) and to a lesser extent in heterogeneous systems representative of soils and sediments (Roberts et al. 2002; Robinson, 1981; Scheinost et al. 2002; Manceau et al. 2005). X-ray absorption spectroscopic (XAS) techniques have been employed extensively to elucidate sorption mechanisms and obtain molecular-level information. Trivedi and coworkers (2000, 2001) observed outer-sphere complexation of Zn on HMO with octahedral coordination, while

Manceau et al. (2002) used polarized extended X-ray absorption fined structure spectroscopy (EXAFS) and found substitution of Zn in the interlayer of crystalline birnessite, resulting in a tridentate corner-sharing interlayer complex. Pan et al. (2004) reported inner-sphere complexation with edge-sharing linkages between $ZnO_{4,6}$ polyhedron and MnO_6 octahedra in manganite (γ-MnOOH). Bochatay and Persson (2000) observed the transformation of a mixture of tetrahedral and octahedral complexes on γ-MnOOH to a tetrahedral structure exclusively as pH increased. Zn sorption on Mn oxides has been reported as both outer-sphere to inner-sphere, forming either tetrahedral or octahedral complexes. On other surfaces such as montmorillonite, Lee et al. (2004) initially observed a polynuclear complex that transformed to a Zn-Si precipitate as a function of aging.

While a number of investigators have studied Pb and Ni sorption to manganese oxides, most work has focused on contact times less than 7 d. For example, Villalobos et al (2005) found for Pb sorption onto biogenic Mn oxide produced from *Pseudomonas putida* strain MnB1 resulted in two bonding mechanisms: a triple-corner sharing complex in the interlayer above and below cationic sheet vacancies and a double-corner sharing complex on particle edges at exposed singly coordinated –O(H) bonds. On the other hand, in probing birnessite surfaces, only one type of bond was observed by Manceau et al. (2002) and Matocha et al. (2001), where Pb formed tridentate edge-sharing interlayer complexes and coordinated to vacant sites in the Mn oxide structure; Matocha et al. observed concurrent release of Mn as Pb sorbed. Similarly, Ni substituted for Mn(III) in lithiophorite soil nodules (Manceau et al. 1987). Divalent ions potentially substitute for the Mn(III) ion or occupy vacancy sites in the oxide structure (Manceau et al. 2002). On

the other hand, with manganite (γ-MnOOH), Pb formed inner-sphere mononuclear corner-sharing complexes with two Mn sub-shells (Matocha et al. 2001).

In addition, Sparks and co-workers (e.g., Scheidegger et al. 1997; Roberts et al. 1999) have studied the clay fraction in soil and especially Al bearing minerals and observed a slow sorption process due to formation of a mixed Ni-Al layered double hydroxide (LDH) phase. On the other hand, for Ni concentrations less than 10^{-4} M and pH less than 8, Ni formed a mononuclear inner-sphere bidentate complex with surface aluminol groups on boehmite (γ-AlOOH) (Strathmann et al. 2005). Because this complex was observed as a function of time, the slow sorption process was attributed to potentially intraparticle diffusion. Others (Trivedi and Axe, 1999, 2000, 2001; Papelis, 1995; Strawn et al. 1998; Fan et al. 2005) also working with porous Al oxides observed intraparticle diffusion as the rate limiting step in the sorption process. Additional studies (Axe and Anderson 1997; Trivedi and Axe, 1999, 2000, 2001; Trivedi et al. 2001; Scheinost et al. 2001) with microporous Mn and Fe oxides have further demonstrated that intraparticle surface diffusion is a rate-limiting mechanism that results in substantial sorption to internal surface sites.

2.4.2 Heterogeneous Biogenic Systems

Interactions between microorganisms and trace metals have been observed to include complexation onto the microbe surface or extracellular polymers (Fein et al. 1997; Daughney et al. 1998), mineral formation and dissolution (Toner et al. 2005; Glasauer et al. 2003), and redox reactions with the metal ions acting as electron donors and acceptors (Kemner et al. 2004; Francis et al. 2000; Liu et al. 2002). Investigating sorption mechanisms requires an understanding of surface functional groups on, for example, the

cell wall which can be quantified through isolating functional groups (Beveridge and Murray, 1980) and evaluating the coordination environment (Kelly et al. 2002); subsequently, mechanisms can be modeled (Fein et al. 1997). Microbial cell walls possess functional groups, which include carboxyl (–COOH), aldehyde (–COH), hydroxyl (–CHOH), sulfhydryl (–SH), phosphoryl ($–PO_4H_3$), and amine ($–NH_2$) (Sarret et al. 1998; Madigan et al. 2000; Kelly et al. 2002). Na^+, Mg^{2+}, Mn^{2+}, Fe^{2+}, and Cu^{2+} preferentially bind to carboxyl sites (Fein et al. 1997; Ngwenya et al. 2003), while $Cd^{2+}$and Pb^{2+} most often bind to phosphate sites (Fein et al. 2001; Yee and Fein, 2001).

Sheath forming bacteria (e.g. *Leptothrix discophora* SP-6, *Psudomonas putida* MnB1) excrete extracellular polymeric substances (EPS), ranging from tightly structured capsules to a matrix of microbial biofilms. The functions of EPS include buffering the microenvironment around cells against changes in pH, salinity, and the harmful effects of toxins (e.g., heavy metals); protection against UV radiation; and, adhesion to other surfaces (Decho, 1990). For *Leptothrix discophora* SP-6, more than 90% of the EPS by mass consists of water (Emerson and Ghiorse, 1993) located in pores. The remaining portion of the biomass consists of polysaccharides (reducing sugar: uronic acid, amino sugar, and glucose), proteins, lipids, and inorganic matters (Emerson and Ghiorse, 1993). The polysaccharides possess abundant (anionic) carboxyl and hydroxyl groups that provide potential binding sites for metals. Of special importance are the carboxyl groups of uronic acids (carboxylated polysaccharides) that correlate strongly with the metal binding capacity of EPS (Kaplan et al. 1987) as observed with Pb, Zn, Cd, Co, and Ni (Toner et al. 2005; Decho 1990; Konhauser et al. 1994).

Although zinc is considered a micronutrient for microorganisms and plants, at high concentrations (i.e., > 5×10^{-4} M) toxicity effects are observed. Fein and coworker (1997-2001) proposed that Zn sorbed onto *Bacillus subtilis* was best fit as sorption to a combination of carboxyl and phosphoryl groups; Zn-carboxyl species were dominant at low pH, but the contribution from phosphoryl species increased as the pH approached circumneutral values. In addition, Ngwenya et al. (2003) studied Zn sorption to bacterial cells (*Enterobacteriaceae* family) as a function of pH and found that a two-site model (Zn-phosphoryl and Zn-carboxyl species) greatly improved the fit to their experimental data over a one-site model (Zn carboxyl). Zn sorption by the *P. putida* biofilm is attributed to approximately 23 (± 10) mol% carboxyl and 85 (± 10) mol% phosphoryl complexes using XAS (Toner et al. 2005). Toner et al. reported that at pH 6.9, the outer membrane of gram-negative cells is an important surface for sorption due to the presence of lipopolysaccharides and phosphoryl groups on phospholipidbilayer cell wall. Moreover, Guine et al. (2006) studied Zn sorption on three gram negative bacteria (*Cupriavidus metallidurans* CH34, *P. putida*, and *Escherichia coli* K12DH5α) and found Zn binding sites consisted of carboxyl, phosphomonoester, and unexpectedly sulfhydryl ligands. Moreover, extracellular polymeric substances, which consist of nucleic acids, proteins, polysaccharides, and lipids, played a dominant role in Zn retention processes because of their greater site capacity and affinity as compared to other membrane cell components (Guine et al. 2006).

Sheath forming microorganisms such as *L. discophora* reduce the potential impact of contaminants (Widmeyer et al. 2004) through Mn(II) and Fe(II) oxidation (Nelson and Lion, 2003; Villalobos et al. 2003; Tebo et al. 2005; Bromfield, 1956), precipitation

(Chen and Cutright, 2003), coating (Chan et al. 2004; Templeton et al. 2001), and sequestration of the contaminant. A number of these biogenic Mn oxides have been characterized using XAS and diffraction techniques where amorphous to poorly crystalline minerals form (Manderneck et al. 1995; Villalobos et al. 2003; Jürgensen et al. 2004) that are consistent with the abiotic layered Mn oxide (e.g. c-disorder birnessite). Furthermore, interactions between metal ions and biogenic Mn oxides have been studied for Pb and Zn sorption to oxide produced from *P. putida* MnB-1 (Villalobos et al. 2005; Toner et al. 2006). The greater site capacity and affinity of biogenic Mn oxide was observed as compared with δ-MnO_2, birnessite, and pyrolusite (Nelson et al. 1999, Villalobos et al. 2005). Zn and Pb occupied Mn vacancy sites, forming inner-sphere complexes (Villalobos et al. 2005; Toner et al. 2006). Similarly, biogenic Mn oxides in biofilms controlled the distribution of Ni, Co, and Cr in shallow seepage streams (Haack and Warren, 2003) and Pb in Cayuga Lake, NY (Wilson et al. 2001). Although Zn sorption on *P. putida* biofilm has been studied (Toner et al. 2005), other sheath forming bacteria (e.g., *L. discophora* SP-6) play an important role in freshwater environments. In this research, Zn interactions with sheathed *L. discophora* SP-6 and the impact of biogenic Mn oxide coatings are investigated.

In the next chapter, the objectives and hypotheses for this research are presented and followed by experimental methods designed to test the hypotheses.

CHAPTER 3

OBJECTIVES AND HYPOTHESES

Manganese oxides are ubiquitous in soils and sediments; they can sorb and accumulate heavy metal contaminants, potentially controlling metal mobility and distribution. Typically, Mn oxides occur as discrete particles and coatings in the subsurface environment. These oxides are present in various forms ranging from amorphous to crystalline in structure. Understanding the occurrence and forms of abiotic and biogenic Mn oxide coatings are important for assessing heavy metal interactions with these surfaces. The impact of Mn oxide coatings on heavy metal distribution needs to be evaluated to better understand metal mobility, bioavailability, and attenuation. Objectives for this research include the following:

1. Investigate the surface properties of the heterogeneous system of Mn oxide and montmorillonite using several techniques including XAS in studying the local coordination environment of Mn.

2. Better understand the potential impact of Mn oxide-coated clay on heavy metal distribution.

3. Evaluate the Mn oxidizing ability of *Leptothrix discophora* SP-6 as a function of Mn concentration as well as growth media.

4. Assess the surface properties and molecular structure of biogenic Mn oxide by comparing it with abiotic Mn oxide.

5. Elucidate the sorption mechanisms of zinc onto the cell wall of *L. discophora* SP-6 as well as the effect of biogenic Mn oxide on zinc distribution in a heterogeneous system.

Because of the importance of Mn oxides, several hypotheses have been proposed in this research. The hypotheses include

1. Mn oxide coatings may exhibit a similar mineralogy and morphology to that of discrete Mn oxides, depending on the degree of crystallinity. The presence of a substrate may inhibit transformation to a crystalline form.

2. Heavy metal distribution and its mobility in the coated system may be dominated by the Mn oxide phase of both abiotic and biogenic origin, resulting from the greater affinity and site capacity of the Mn oxide.

3. Based on the structure and stability of abiotic HMO, biogenic Mn oxide is expected to belong to the phyllomanganate family.

To test the proposed hypotheses, experimental methods are presented in the next chapter.

CHAPTER 4

EXPERIMENTAL METHODS AND ANALYSES

This chapter reviews all experimental procedures following quality assurance and quality control guidelines (Appendix A) based on standard methods (Greenberg et al. 1998). Research-grade chemicals and Millipore-Q Type I deionized water (DI) were employed in the studies. Initially, abiotic Mn oxides and clay were prepared and then characterized to better understand their surface properties. Subsequently, Mn oxide coatings were evaluated for their structure and surface properties. Moreover, biogenic Mn oxide was produced from *L. discophora* SP-6 and then characterized. Adsorption studies were then performed to investigate the impact of the coating on contaminant distribution.

4.1 Synthesis and Preparation of Mn Oxides and Clays

To prepare HMO, a molar ratio of 2:1 sodium hydroxide to sodium permanganate was used. One g L^{-1} batches of HMO were prepared by slowly adding manganese nitrate ($Mn(NO_3)_2$) to the alkaline $NaMnO_4$ with a final molar ratio of 3:2. The solution was mixed under a turbulent regime ($Re > 10^4$) for 3 hours and purged with nitrogen gas to remove carbon dioxide from the solution. The suspension was then centrifuged and rinsed with DI water, upon which the oxide was redispersed in a 1.5×10^{-2} M sodium nitrate solution for 16 hours prior to use.

Birnessite can be synthesized by a variety of oxidation and reduction methods; two methods were employed in this research. For the oxidation method (Method 1), Wadsley (1950) and Buser et al. (1954) prepared birnessite by bubbling air through

a mixture of a 5.5×10^{-1} M NaOH with 8.38×10^{-2} M of $Mn(NO_3)_2$ for 5 hours. The dark brown precipitate was washed with DI water several times by decantation, filtration, and repeated rinsing. The oxide was then dried at 30 °C and pulverized with a mortar and pestle. In the second method, Wadsely and Walkey (1947) employed the reduction of permanganate to synthesize birnessite (Method 2). An 8×10^{-1} M of concentrated hydrochloric acid was added dropwise to a boiling solution of 4×10^{-1} M of $NaMnO_4$ under a turbulent hydraulic regime. After boiling the solution for an additional 10 minutes, the precipitate was filtered, washed, and dried at 30 °C. Pyrolusite was obtained from Merck Chemical with the purity of 99.999% and was characterized as received.

Clay minerals, Na-kaolinite (KG-1) and Na-montmorillonite (SWy-2), were obtained from the Source Clay Repository of the Clay Minerals Society at the University of Missouri (Columbia, MO) and pretreated in accordance with Kunze and Dixon (1986) and O'Day et al. (1994) to remove of organic matter and other impurities prior to receipt (see Table 5.4).

4.2 Synthesis of Mn Oxides Coatings

HMO was coated on the montmorillonite surface through a redox process (Gadde and Laitinen, 1974). To investigate coating as a natural process, an ambient condition was selected (circum neutral pH). The coatings were produced as a function of Mn concentration, typical (and in the high end of the range) of those in natural systems between 6.1×10^{-5} to 2.50×10^{-1} g Mn $\cdot$ g^{-1} (Manceau et al. 2003; Tani et al. 2003; Mortimer and Rae, 2000). Prior to the precipitation, a 6.9×10^{-3} M $Mn(NO_3)_2$ solution was prepared in carbonate free deionized (DI) water (by purging with high purity

nitrogen gas [1 L · min^{-1} at 20 psi]) in the presence on montmorillonite and mixed for 24 hours. The montmorillonite (0.21-3.15 g · L^{-1}) and $Mn(NO_3)_2$ solution was slowly added to another solution of 1:2 (molar ratio) permanganate to sodium hydroxide and aged for 3 hours before centrifuging and rinsing the resulting suspension with DI water. The oxide-coated clay was then redispersed in DI water at 1.5×10^{-2} M ionic strength ($NaNO_3$) and mixed for 16 h in a Lab-Line shaker.

Birnessite-coated montmorillonite was prepared using a reduction-oxidation method as well (Stahl and James, 1991; Manderneck et al. 1995; Buser et al. 1954; Wadsley, 1950). An 8.38×10^{-3} M $Mn(NO_3)_2$ solution was prepared in carbonate free DI water again in the presence of montmorillonite (0.61-9.14 g · L^{-1}). The solution was slowly added to 5.5×10^{-2} M NaOH under a well-mixed condition that was purged with oxygen gas for 5 hours. The suspension was then centrifuged and rinsed with DI water. The birnessite-coated clay was dried in an oven at 30°C for 3 days. For the crystalline coating, pyrolusite-coated montmorillonite was prepared by wet oxidation at high temperature (Stahl and James, 1991; Tsadilas et al. 1998). The mixture of $Mn(NO_3)_2$ and montmorillonite was first dried in the oven at 30 °C and then heated at 120-125 °C for 52 hours until solidification was achieved. The sample was rinsed with DI water, filtered through a 0.45 μm membrane, stored at 110 °C for 1 day, and subsequently ground and reheated at 150 °C for 4 days further.

4.3 Preparation of Mn Oxyhydroxide with *Leptothrix Discophora* SP-6

Biogenic Mn(III/IV) (hydr)oxide was produced through enzymatic oxidation by the freshwater sheath-forming bacterium *L. discophora* SP-6, which was purchased from the

American Type Culture Collection (ATCC #51168) and cultured in modified MSVP (ATCC culture media 1917) and PY (ATCC culture media 1503) media, both of which were autoclaved at 121°C and 15 psi for 20 minutes. MSVP solution was added to achieve the following composition in the growth study: 0.240 g · L^{-1} $(NH_4)_2SO_4$; 0.06 g · L^{-1} $MgSO_4 \cdot 7H_2O$; 0.060 g · L^{-1} $CaCl_2 \cdot 2H_2O$; 0.020 g · L^{-1} KH_2PO_4; 0.030 g · L^{-1} Na_2HPO_4; 2.383 g · L^{-1} HEPES (N-2-hydroxyethylpiperazine-N′-2-ethanesulfonic acid); and, 1.00 g · L^{-1} Na-Pyruvate ($CH_3COCOONa$). Vitamin solution was filtered with a sterilized 0.2 μm polyvinylidene fluoride membrane and added to solution with a final concentration of 20 μg · L^{-1} biotin; 20 μg · L^{-1} folic acid; 50 μg · L^{-1} thiamine HCL; 50 μg · L^{-1} D-(+)-calcium pantothenate; 1 μg · L^{-1} vitamin B12; 50 μg · L^{-1} riboflavin; 50 μg · L^{-1} nicotinic acid (vitamin B3); 100 μg · L^{-1} puridoxine HCl; and, 50 μg · L^{-1} p-aminobenzoic acid. The PY medium in the growth studies consisted of 0.5 g · L^{-1} peptone; 0.5 g · L^{-1} yeast extract; 0.60 g · L^{-1} $MgSO_4 \cdot 7H_2O$; 0.07 g · L^{-1} $CaCl_2 \cdot 2H_2O$; and, 3.73 g · L^{-1} HEPES. The ratio by volume of *L. discophora* SP-6 to medium was approximately 1 to 20 for inoculation, resulting in a cell concentration of less than 4 mg cell · L^{-1}.

To assess and confirm the optimum pH for achieving the maximum growth rate, a series of experiments were conducted between pH 6.5 and 8 (6.5, 7.0, 7.3, 7.5, and 8.0) under turbulent conditions at 25°C with a saturated oxygen concentration maintained with sterilized air. The optical density of biomass in liquid cultures was measured at 600 nm (A_{600}) using a UV spectrophotometer (Emerson and Ghiorse, 1993). Two ml of the culture collected with a sterilized syringe needle were passed through the syringe

multiple times (at least five) to disrupt cell aggregates which were subsequently loaded in a polystyrene cuvette for absorbance.

4.3.1 Mn Oxidation Study

After the optimum pH was identified, a series of cultures from the stationary phase were exposed to Mn^{2+} concentrations of 0.1, 0.3, 0.5, 0.7, and 1.0 mM based on those commonly found in Mn-rich mine drainage (Doerr et al. 2005) and potentially non-toxic to the cells (Pasten, 2002). Upon addition, Mn^{2+} concentration in the aqueous was assessed up to 168 hrs where samples were collected, filtered through a 0.2 μm glass membrane, and measured with flame and graphite furnace atomic absorption (AA) spectrometry. The Mn oxidation studies were conducted with three different media: MSVP, PY, and deionized water with HEPES buffer all at pH 7.3. The biogenic Mn oxide-coated bacteria was characterized with a suite of analyses used for abiotic coatings as well as, and discussed in Section 4.4.

4.3.2 Lysozyme-EDTA Sheathed Isolation

The isolated (cell-free) sheath protocol was based on the lysis procedure described by Romano and Peloquin (1963) and further developed by Emerson and Ghiorse (1993). *L. discophora* SP-6 was harvested by centrifugation (at 8000 rpm, 8 min, 10 °C) and resuspended in DI water to a density 20 times more concentrated than the original. The suspension was homogenized by passing it repeatly through a 25-gauge needle to disrupt large clumps of filament that formed in the culture. Lysozyme and EDTA were then added to the suspension to final concentrations of 150 $\mu g \cdot L^{-1}$ and 2.5 mM, respectively. This mixture was incubated at 37 °C for 30 min for inducing lysis of the bacterial cells. A

detergent (sodium dodecyl sulfate (SDS)) was added to the suspension to achieve a final concentration of 10 g · L^{-1} to detach the cell wall. This solution was incubated at room temperature for 20 min. The resulting extracellular polymeric sheath was washed four times with DI water and for sorption studies, the extracellular polymeric sheath was resuspended in 10^{-2} M $NaNO_3$ at pH 6.6. Emerson and Ghiorse (1993) reported the chemical composition of sheath as 34% polysaccharides (reducing sugar: uronic acid and amino sugar), 24% proteins, 8% lipids, and 4 % inorganic ash when *L. discophora* SP-6 was grown in MSVP media. A similar chemical composition was also observed for the sheath of *Sphaerotilus natans* grown in complex media but with the polysaccharide primarily composed of a neutral sugar (glucose), with less glucosamine and no uronic acid. Therefore, the growth condition and organisms can affect the composition of the polysaccharide. In this study, *L. discophora* SP-6 is grown in complex media that may be dominated by the neutral sugar (Romano and Peloquin, 1963).

4.4 Material Characterization

The coatings were characterized using several techniques. Mineralogy was assessed with a Philips X'Pert X-ray diffractometer (XRD) and morphology was studied using a Philips Electron 2020 environmental scanning electron microscope (ESEM) and a LEO 1530 PV field emission scanning electron microscope (FE-SEM) with energy dispersive X-ray analysis (EDX). Additionally, extraction analysis (hydroxylamine hydrochloride-hydrochloric acid extraction) (Robinson, 1981; Ross and Wang, 1993) and X-ray fluorescence (XRF) were employed to analyze the Mn concentration in the oxide-coated clay. Characterization also included particle size analyses (PSA) and potentiometric

titrations to evaluate the pH point of zero net proton charge (pH_{znpc}). The specific surface area, porosity, and pore size distribution were measured by Brunauer-Emmett-Teller (BET) method and mercury porosimetry (GTI, 2003). Details for the analyses are provided in the following subsections.

4.4.1 X-ray Diffraction Spectroscopy (XRD)

PW3040-MPD XRD (Philips Electronic Instrument Company) was applied to study mineralogy. Sample preparation for XRD analysis was based on the standard procedure (Buhrke et al, 1998). The samples were placed in the sample holder with the backing filling technique. The instrument was operated at 45 kV and 40 mA (Cu K-α radiation). Oxide samples were scanned from a 10° to 120° (2θ). For clay samples, 2θ ranged from 5 to 120°. The standard powder diffraction file (PDF) (JCPDS-ICDD, 1998) was used as reference data.

4.4.2 Environmental Scanning Electron Microscopy (ESEM), Field Emission Scanning Electron Microscope (FE-SEM), and Energy Dispersive X-ray Analysis (EDX)

The surface morphology was evaluated by ESEM Model 2020 (ElectronScan Coorperation) and FE-SEM (model LEO 1530 VP). For sample preparation, the suspension was placed on conductive carbon substrate attached to the aluminum sample holder. For birnessite and pyrolusite, powders were fixed on conductive carbon substrate as well. The sample preparation and SEM procedure were described by Goldstien et al. (1992). Vapor pressure was adjusted to obtain high resolution. The EDX, Si(Li) detector (Oxford Instrument) was operated at high energy for elemental mapping on the surface of

the coated clay. The mapping provides Mn, Si, and Al as well as other elemental surface species.

4.4.3 X-ray Fluorescence Spectroscopy (XRF)

X-ray florescence spectroscopy (PW2400R, Philips Electronic Instrument Company) was performed to assess the composition of the sample. The PW2592/15 Rh tube and goniometer detector were used and the x-ray path was measured in Helium. The Philips SemiQ program was used to analyze the data. Sample was prepared according to the method described by Buhrke et al. (1998).

4.4.4 Particle Size Analyses (PSA)

Particle size was analyzed with a Beckman-Coulter LS 230 analyzer as a function of ionic strength ($NaNO_3$) and pH. Solutions of 10^{-3} and 10^{-2} NaOH and 10^{-1} HNO_3 were used to adjust pH. The particle size distribution (PSD) of oxides and clays was studied at pH 5 and 7 and ionic strengths 10^{-1}, 10^{-2}, and 10^{-3}. For PSD of sheath *L. discophora* SP-6 and biogenic Mn oxide coated bacteria, the analysis was performed as a function of Mn oxide concentration in PY media and pH 7.3. The well-mixed condition was maintained with a Lab-Line shaker operating at 250 rpm for 3 hours at room temperature before the analysis. The laser diffraction technique sizes particles by utilizing the diffraction pattern of scattered light over a range of 0.04 μm to 2 mm. The background of PSA analysis was illustrated by Allen (2003).

4.4.5 Potentiometric Titrations

Systems were purged with high purity N_2 (g) (grade 5 nitrogen gas with 20 psi gauge pressure and 1 L · min^{-1} flowrate) to remove carbonate species before and during the titration. Turbulence ($Re > 10^4$) was maintained with a magnetic stirrer. Solutions were titrated with 10^0 N HNO_3 and 10^{-2}, 10^{-1}, 10^0, and 10^1 N NaOH. The pH values were recorded after equilibrium was achieved (2 min after acid/base addition). The titration was conducted at three different ionic strengths using $NaNO_3$ to determine the pH at zero point of net charge (pH_{zpnc}). The pH_{zpnc} experiment was based on the method of Parks (1967).

4.4.6 Extraction Method

To evaluate the Mn concentration on the clay surface, Mn oxides were extracted with hydroxylamine hydrochloride-hydrochloric acid solution (0.25 M NH_2OH · HCL, 0.25 M HCl) (Ross and Wang, 1993). The extractant was preserved and stored following standard methods and then measured with atomic absorption (AA) analysis (Greenberg et al. 1998).

4.5 Adsorption Studies

Short-term adsorption studies were conducted with a contact time of 4 hrs. In these studies, the amount of adsorbate added is fixed, and equilibrium is achieved rapidly with the external surface of the oxide (Axe and Anderson, 1997). Adsorption edges and isotherms were used to assess the amount of metal ion sorbed to HMO, montmorillonite, HMO-coated clay, sheathed *L. discophora* SP-6, EPS, and biogenic Mn oxide-coated bacteria as a function pH (1.0 to 6.0), ionic strength (1.5×10^{-2} to 1.5×10^{-1} M $NaNO_3$),

and loading (10^{-8} to 10^{-3} mole of metal ions $\cdot$ g^{-1} solid). Initial concentrations of Zn, Ni, and Pb in this study were consistent with these observed naturally and in contaminanted ones (Robinson, 1981; Dong et al. 2003) and were below the solubility limit of smithsonite, $ZnCO_{3(s)}$, β-$Ni(OH)_2$ (Wallner and Gatterer, 2002), and hydrocerrusite ($Pb_3(OH)_2(CO_3)_2$) based on Mineql+ (Appendix B). All adsorption experiments were conducted in 250-mL polypropylene (Nalgene®) containers under turbulent hydraulic conditions. One g $\cdot$ L^{-1} and 10^{-1} g $\cdot$ L^{-1} of abiotic Mn oxide and coatings, respectively, were prepared for edge and isotherm studies, while adsorbent concentrations were 17.3 mg cell $\cdot$ L^{-1} of *L. discophora* SP-6, 1.3 mg of sheath $\cdot$ L^{-1} (represents fraction of EPS present on cells), and 8.6 mg Mn oxide $\cdot$ L^{-1} (0.5 mg Mn oxide mg^{-1} cells) for the biological systems. Solutions of 10^{-2} and 10^{-1} N of NaOH and HNO_3 were used for adjusting the pH, and stock solutions of Zn nitrate, Ni nitrate and Pb nitrate were tagged with the radioactive isotope ^{65}Zn, ^{63}Ni, and ^{210}Pb. After 4 hours, samples were collected and filtered using a 0.2 μm glass membrane. The activity of ^{65}Zn, ^{63}Ni, and ^{210}Pb in the suspension and in the filtrate were measured with a Beckman LS6500 Multipurpose scintillation counter.

Long-term adsorption studies were required for evaluating the slow sorption process of intraparticle diffusion along microporous surfaces (e.g., Trivedi and Axe, 2000, Axe and Anderson, 1997). To observe this process and evaluate experimental diffusivities in a convenient time frame, constant boundary condition (CBC) studies were conducted with HMO, HMO-coated clay, montmorillonite, and biogenic Mn oxide-coated bacteria (see e.g., Trivedi and Axe, 2000). The CBC studies were conducted in 1-L high-density polypropylene (Nalgene®) containers under turbulent conditions with an

initial volume of 1000-mL. Again, the tagged stock solutions of Zn nitrate, Ni nitrate, and Pb nitrate were added to maintain constant bulk concentrations, which were monitored by collecting 2.5-mL of solution, filtering with a 0.2 μm glass membrane, and measuring the activities of ^{65}Zn, ^{63}Ni, and ^{210}Pb in the filtrate. The $[Me]_{bulk}$ was assessed after 4 hours contact time when the sorption reached the equilibrium between the bulk aqueous solution and the external surface of the sorbent. The metal ion concentration in the bulk aqueous phase was maintained constant by monitoring and adding stock solution as needed. During these experiments, the solids concentration was constant and the loss of solution due to evaporation was negligible as the container was capped and opened only for sampling the solution and measuring pH. The CBC experiments ran from 36 to 144 days.

4.6 XAS Studies

XAS data were acquired on Beamline X11A of the National Synchrotron Light Source (NSLS) at Brookhaven National Laboratory, where the electron beam energy was 2.8 GeV with a beam current of 260 to 280 mA. The monochromator consists of a pair of Si (111) crystals which are adjusted over the range of energy. The wet paste samples were loaded into acrylic sample holders and sealed with Kapton windows. Energy calibration was conducted before measuring the spectra for each standard and sample. The data were collected in both transmission and fluorescence modes. Harmonic rejection was achieved by detuning 30% of I_o. For the studies on structure of Mn oxide, the spectra were collected at the Mn-K edge (6.539 keV) and over the energy range of 6.300 to 7.200 keV. The Mn K-edge was calibrated between samples with a Mn foil. The standards and

samples consisted of β-MnO_2, birnessite, todorokite, HMO, HMO-coated clay, birnessite-coated clay, and biogenic Mn oxide produced from *L. discophora* SP-6. The incident (I_o) and transmitted (I_t) ion chambers were filled with nitrogen gas. Fluorescence spectra where samples were placed at 45° to the incident beam were collected with a Lytle detector filled with argon gas.

For studies on Zn sorption, the spectra were collected at the Zn K-edge (9.659 keV) over the energy range of 9.509 to 10.408 keV. For Ni and Pb sorption samples, the spectra were collected at the Ni K-edge (8.333 keV) and Pb L_{III}-edge (13.055 keV) over the energy range of 8.133 to 9.802 keV for Ni and 12.855 to 13.606 keV for Pb. Energy calibration was conducted before measuring the spectra for each standard and sample. Standards and samples of Zn, Pb, and Ni were measured in transmission and fluorescence modes with nitrogen gas in the ion chamber before the sample (I_o), and Ar gas in the Lytle detector. For Ni and Pb, a mixture of 50 % N_2 and 50 % Ar gas was filled in the ion chamber after the sample (I_t) while only N_2 gas was used for Zn.

XAS spectra were analyzed using WinXAS (Version 2.3) (Ressler, 1998) following standard procedures (Bunker and Sayers, 1988). The background X-ray absorbance was subtracted by fitting a first order polynomial through the pre-edge region. The edge jump of a background-corrected spectrum was normalized with a zero order polynomial over 100 to 200 eV above the edge energy. The threshold energy (E_o) was determined from the first inflection point in the edge region and was used to convert the spectra from energy to k-space. An advanced spline function was employed to subtract the isolated atomic absorption and to convert the data to $\chi(k)$ that was then weighted by k^3 to enhance the higher k-space data. A Bessel function was used in Fourier transforms

in producing the radial structure function (RSF). The RSF of standards and samples was fit with reference models, generated using FEFF7 (Zabinsky et al. 1995). In fitting, all parameters were floated, but the amplitude reduction factor (S_0^2), which accounts for energy loss due to multiple electron excitations was held constant and the edge energy was constrained to being equivalent for all shells in the fit. First, each shell was isolated and fit, and was proceeded by multiple shell fitting.

In addition, principle component (PCA) and linear combination (LC) analyses were applied to Zn EXAFS ($\chi(k)\times k^3$) spectra of samples and standards to better understand relative contributions to zinc complexation. Target transformation analysis was conducted to evaluate the suitability of the reference spectra using the SPOIL function (Malinowski, 1978), which is the ratio of the real error in the target to the error from the data matrix; a value less than 1.5 is considered an excellent fit, 1.5 to 3 good, 3 to 4.5 fair, and 4.5 to 6.0 poor (Malinowski, 1978).

Samples from adsorption studies were used where the sorbed Zn, Ni and Pb concentrations were measured based on the activity of ^{65}Zn, ^{63}Ni, and ^{210}Pb in duplicate studies. Suspensions were centrifuged at 10,000 rpm for 20 minutes to obtain the wet paste. Samples included ones from CBC studies with time frames up to 7 months as well as short term samples addressing the effect of sorbent (HMO, HMO-coated clay, montmorillonite, sheathed *L. discophora* SP-6, EPS, and biogenic Mn oxide-coated bacteria), adsorbate loading from 10^{-4} to 10^{-2} mol of metal ions · g of sorbent^{-1}, pH 5 to 7, and ionic strength from 10^{-3} to 10^{-2} ($NaNO_3$ based). Given the volume of the wet paste (~1 mL) after centrifugation (and even if the entire volume consisted of water) the metal concentration remaining in the aqueous phase would be 5×10^{-6} M for the greatest

loading, two to four orders of magnitude less than the sorbed concentration and therefore not impacting the spectra.

In Chapters 5 through 10, results are presented on characterization of the Mn oxide-coated clay and the associated substrates, sorption to the abiotic coating, assessment and production of the biogenic Mn oxide, and sorption to its surface. The dissertation concludes with a chapter on a summary of the findings and potential work in future studies.

CHAPTER 5

INVESTIGATION OF MN OXIDES AND CLAY

This chapter presents results on characterization of discrete minerals of Mn oxides and clay reviewing morphology, mineralogy, particle size, composition, and surface charge (pH_{zpnc}). These results were used then in synthesizing and characterizing coated systems.

5.1 Characteristics of Mn Oxides: HMO, Birnessite, and Pyrolusite

The morphology of HMO reveals an irregular topography; particles appear aggregated forming spheres (Figure 5.1 (A)). The XRD diffractogram (Figure 5.2) is broad and flat indicative of an amorphous structure. Based on the ESEM, the average HMO particle size is approximately 15 μm and is in agreement with the particle size distribution (Figure 5.3). Moreover, the PSD is monomodal with a particle diameter ranging from 1 to 600 μm, and although it appears to be dependent on ionic strength when increased to 10^{-1}, the distribution is invariant of pH. Potassium and sodium from the sodium permanganate used in oxide synthesis (Table 5.1) appear to be impurities in the precipitates.

For crystalline Mn oxides, birnessite was prepared with two methods. Using the first method resulted in a morphology consistent with that of birnessite, a needle shaped crystal (Figure 5.1 (B)) that aggregates into a spheres (Wadsley, 1950; Buser et al. 1954), while surfaces of aggregated birnessite using Method 2 (Figure 5.1 (C)) are similar to a sponge. Moreover, the XRD pattern of birnessite (Method 1) represents a more crystalline oxide than that from Method 2. The four major peaks of birnessite

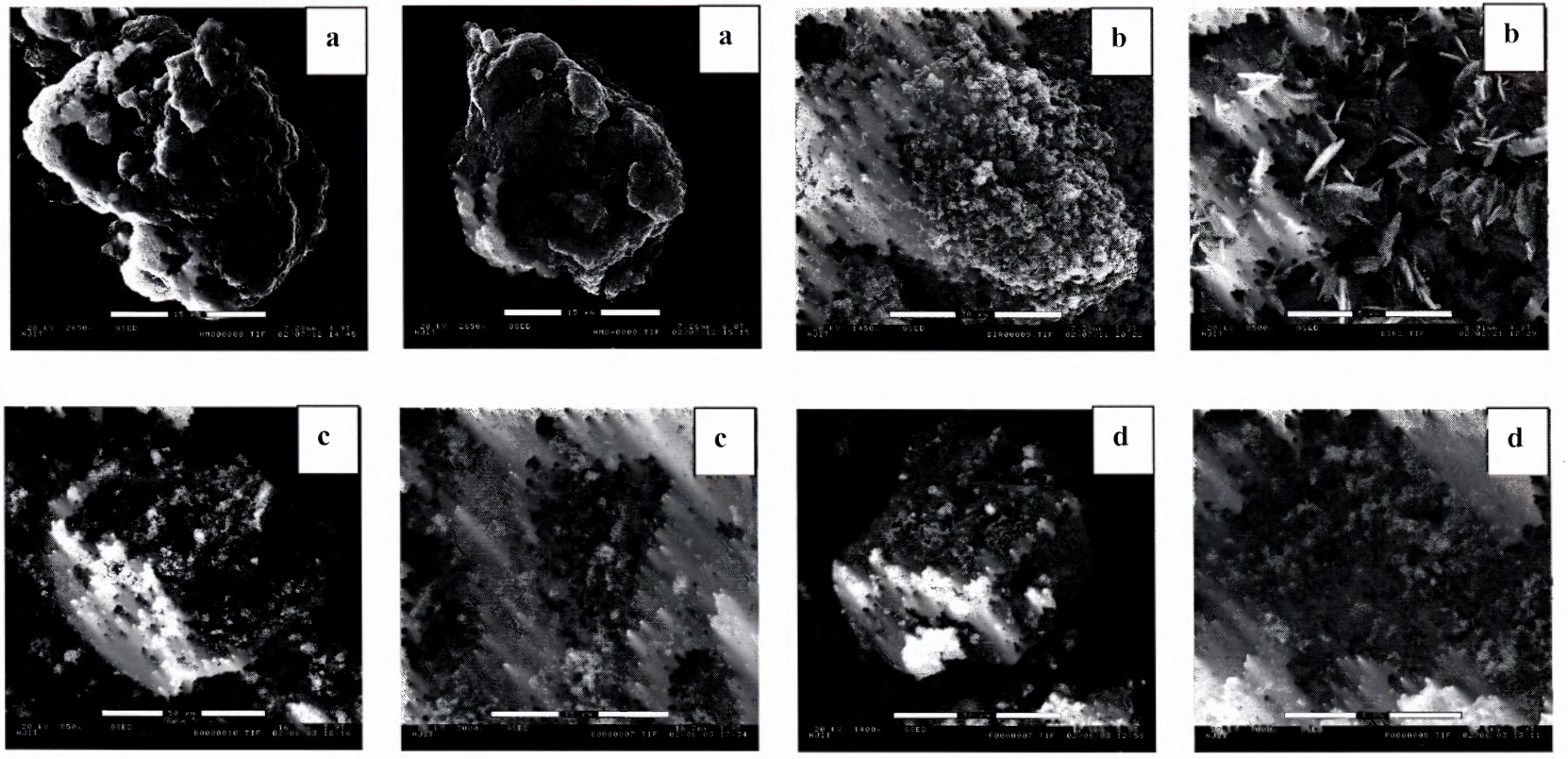

Figure 5.1 ESEM images of (a) HMO, (b) Birnessite (Method 1), (c) Birnessite (Method 2), and (d) Pyrolusite.

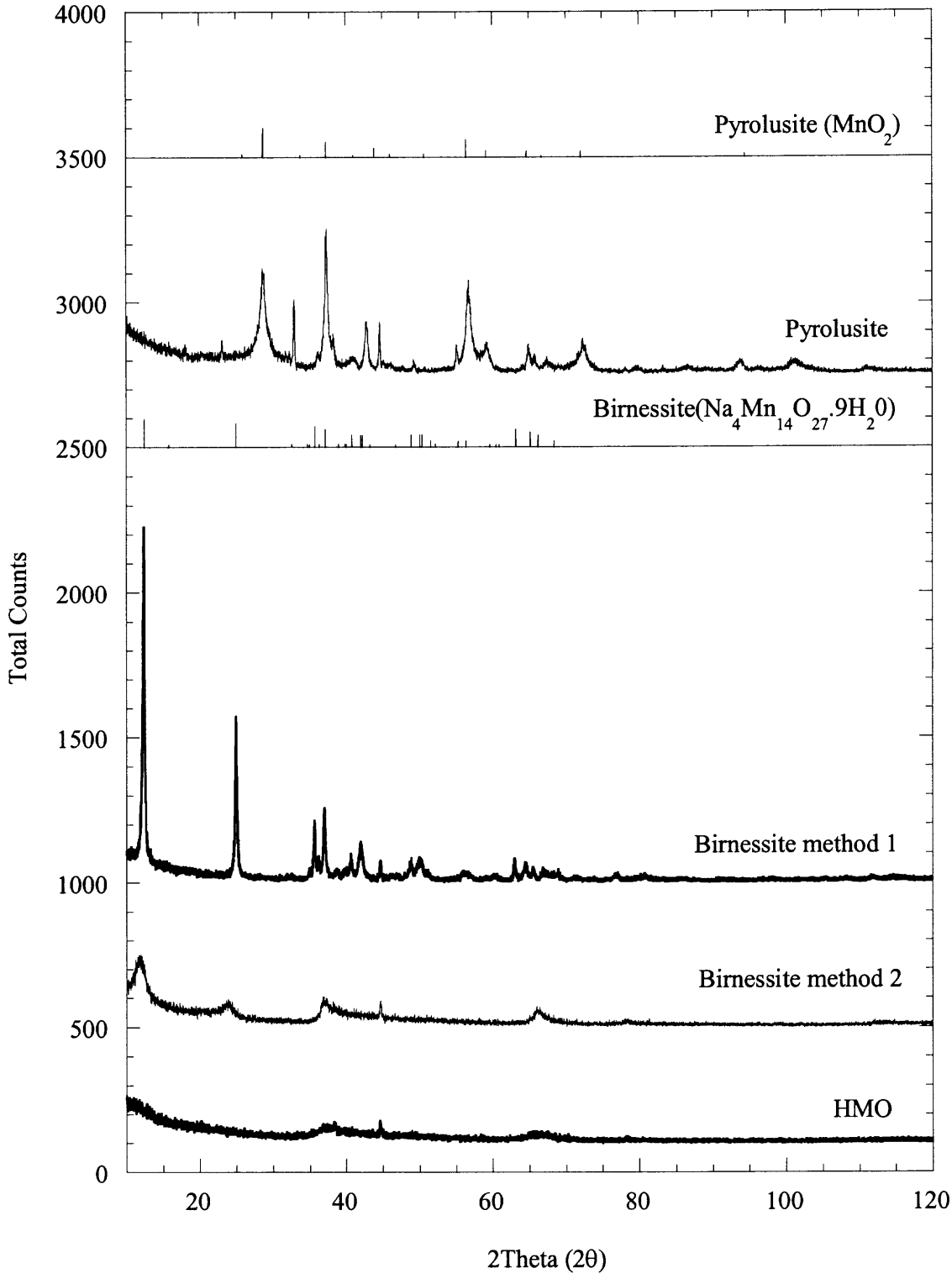

Figure 5.2 The X-ray pattern of HMO, birnessite (Method 1), birnessite (Method 2), birnessite ($Na_4Mn_{14}O_{27}\cdot 9H_20$) and pyrolusite ($MnO_2$).

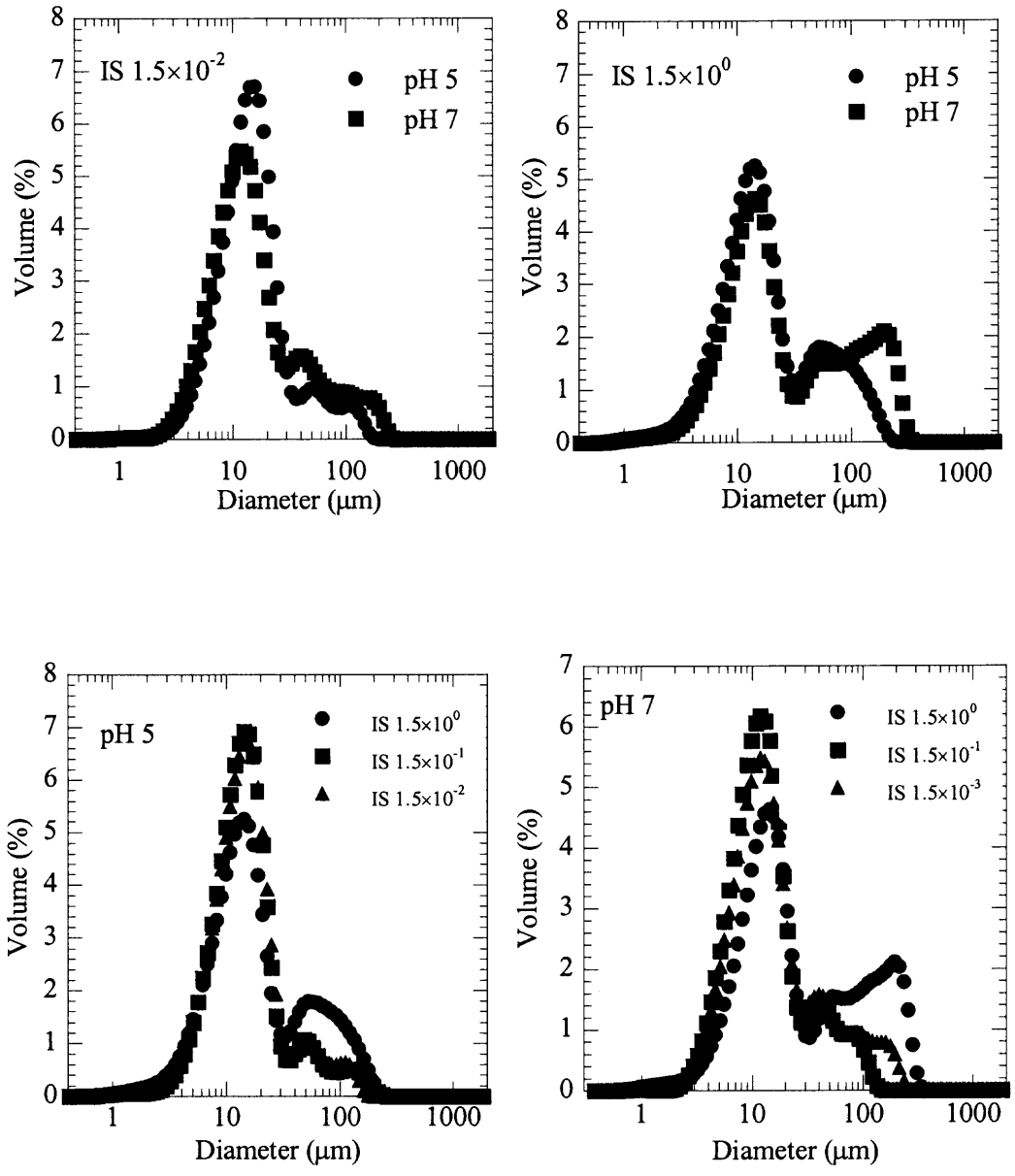

Figure 5.3 Particle size distributions of HMO (1 g·L^{-1}) at room temperature illustrate the effect of ionic strength (10^{-1}, 10^{-2}, and 10^{-3}) and pH (5 and 7).

Table 5.1 The X-ray Fluorescence Analysis on the Percent Composition of HMO, Birnessite (Method 1 and 2), and Pyrolusite

Oxide	HMO	Birnessite (Method 1)	Birnessite (Method 2)	Pyrolusite
MnO_2	96.528	96.403	97.356	100
Na_2O	3.314	3.596	1.754	-
K_2O	0.158	-	0.890	-

(Method 1) are consistent with those in the powder diffraction file (Giovanoli et al. 1970). The half height width for birnessite using Method 1 represents a well-crystallized mineral compared to that of Method 2.

From the XRD pattern of the oxide (Method 2), the structure appears to be a disordered version of the Method 1 oxide and is mostly amorphous. Overall, the XRD pattern confirms the lack of crystallinity of birnessite using Method 2 or particle size could be very small and is consistent with that observed by ESEM. The PSDs of birnessite using Method 1 (quasi-bimodal) are quite different from that of HMO; however, the particle size is independent of pH and ionic strength. Birnessite produced from Method 1 ranges from 0.1 to 500 μm (Figure 5.4). For birnessite using Method 2 (Figure 5.5), the distribution is similar to bimodal and independent of pH and ionic strength; particles range from 0.5 to 1000 μm. Because the birnessite produced by Method 2 is not consistent with others (Wadsel and Walkey, 1947), Method 1 is selected for this study due to the resulting crystallinity, morphology, and fine particle size.

Table 5.2 XRD Analysis given d-spacing (Å), 2θ, and the Width at Half Height (WHH) for Birnessite and Pyrolusite

d-spacing (Å)			2θ			Relative Intensity			hkl planes			Half height width (WHH)	
Birnessite 1	Birnessite 2	PDF	Birnessite 1	Birnessite 2	PDF	Birnessite 1	Birnessite 2	PDF	h	k	l	Birnessite 1	Birnessite 2
7.12	7.42	7.09	12.42	11.91	12.47	100	100	100	0	0	2	0.29	1.25
3.57	3.70	3.56	24.93	24.03	24.99	44.38	32.18	27	2	1	2	0.30	0.45
2.52	2.44	2.51	35.61	36.82	35.61	35.61	46.39	14	1	4	4	0.24	0.94
2.43	2.03	2.42	36.99	44.61	36.97	36.99	57.72	13	1	6	1	0.29	0.24

d-spacing (Å)		2θ		Relative Intensity		hkl planes			Half height width (WHH)
Pyrolusite	PDF	Pyrolusite	PDF	Pyrolusite	PDF	h	k	L	Pyrolusite
3.11	3.11	28.65	28.64	59.14	100	1	1	0	0.73
2.40	2.40	37.35	37.30	100	55.15	1	0	1	0.49
2.11	2.11	42.78	42.76	35.63	13.2	1	1	1	0.48
1.62	1.62	56.77	56.59	70.32	48.45	2	1	1	0.71

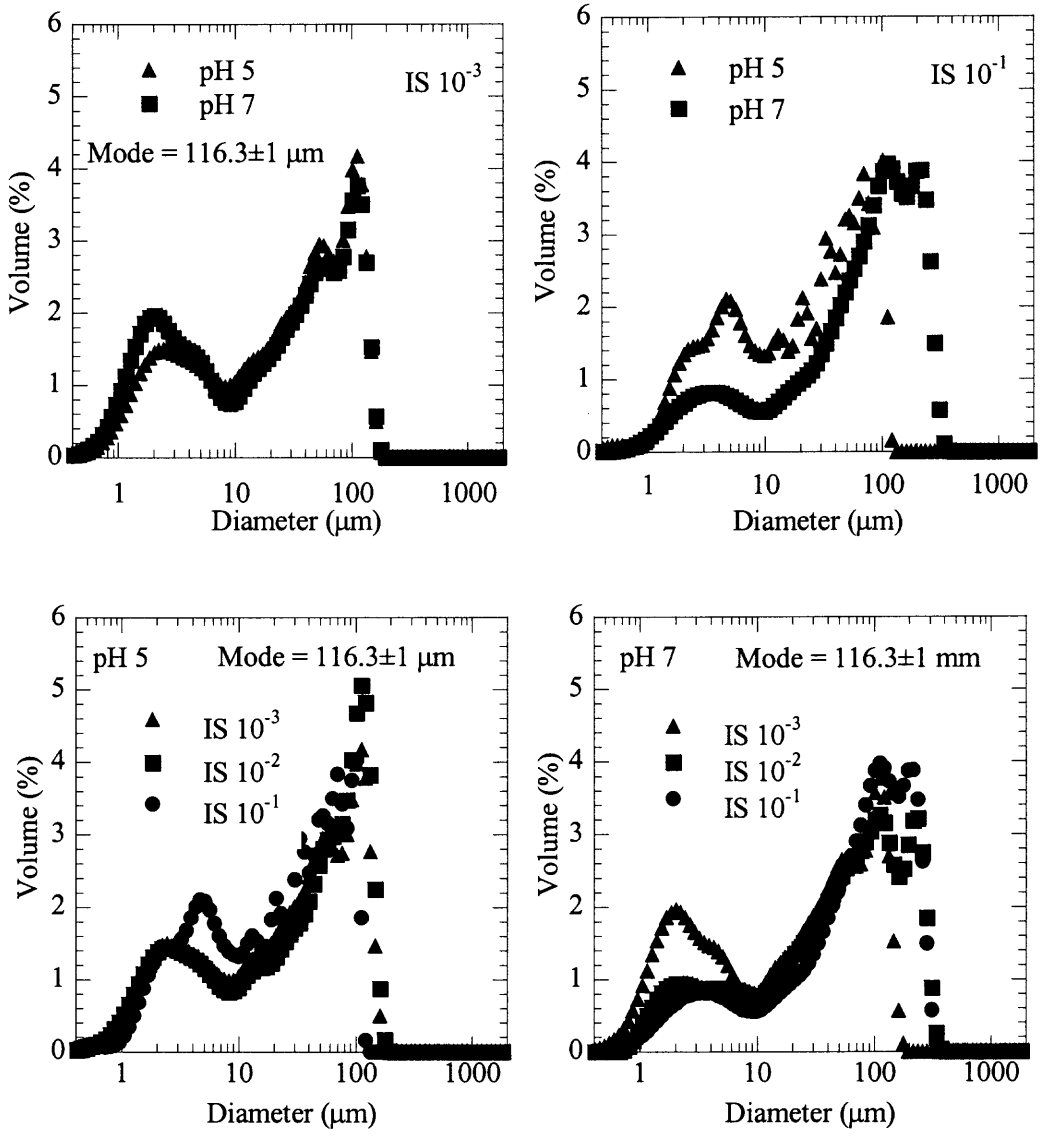

Figure 5.4 Particle size distributions of birnessite Method 1 (1 g·L^{-1}) at room temperature illustrate the effect of ionic strength (10^{-1}, 10^{-2}, and 10^{-3}) and pH (5 and 7).

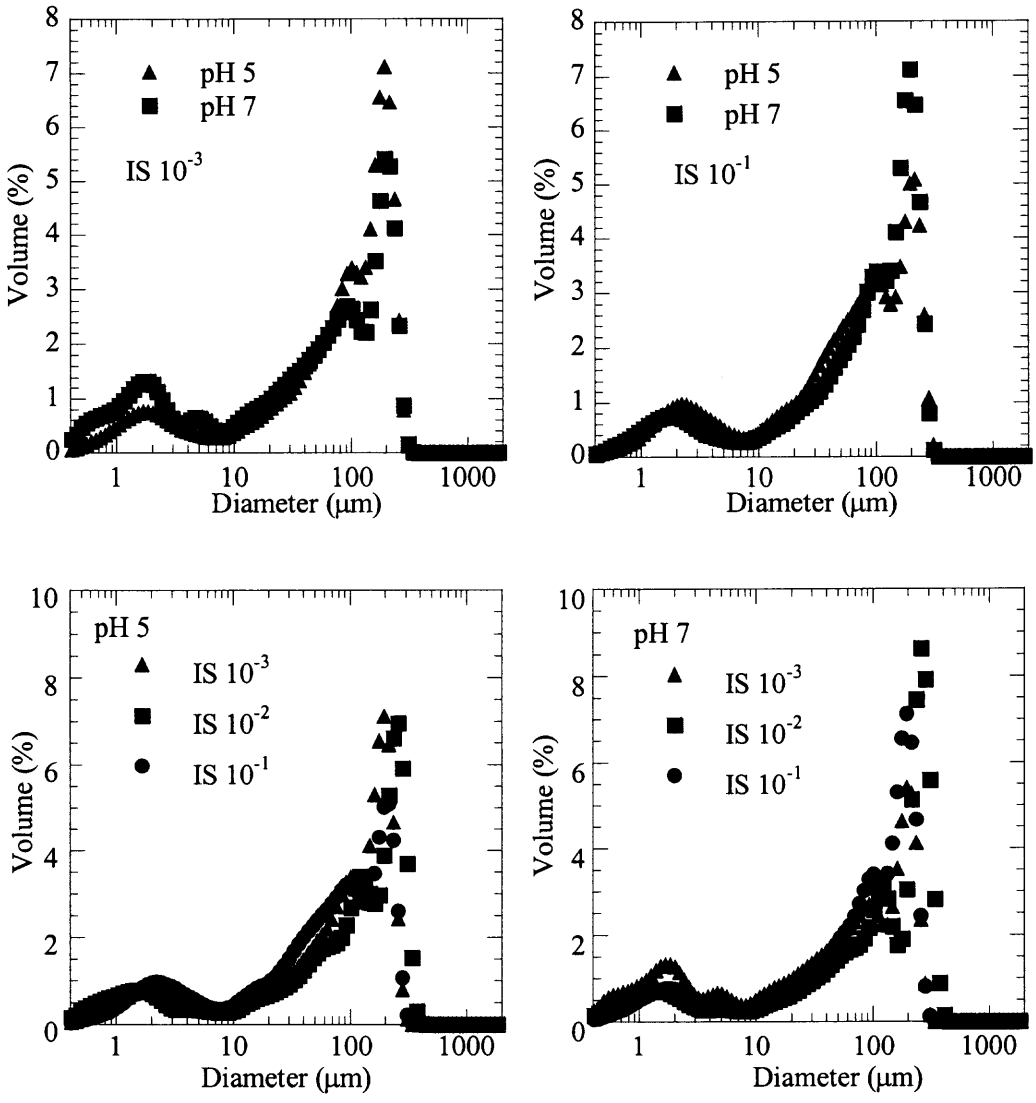

Figure 5.5 Particle size distributions of birnessite Method 2 (1 g·L^{-1}) at room temperature illustrate the effect of ionic strength (10^{-1}, 10^{-2}, and 10^{-3}) and pH (5 and 7).

For pyrolusite, the ESEM images show a cubic shape crystal with a rough surface (Figure 5.1). The cubic shape may occur under stress conditions during production (by pulverizing and heating rate). At high magnification, the surface of pyrolusite also appears sponge-like with a dimension of 30 μm. The diffraction pattern of pyrolusite is in agreement with that expected from the powder diffraction file (Hartcourt, 1942). Even though all peaks match, preferred orientation still has an effect because of the size and tensor properties of the crystalline mineral (Jenkins and Snyder, 1996). The purity of pyrolusite purchased from Merck is approximates 99.999% and was confirmed with XRF analysis. The particle size distribution of pyrolusite (Figure 5.6) is monomodal with a diameter ranging from 0.1 to 1000 μm. There is no effect of pH and ionic strength on the distribution. Most particles are approximate 85-96 μm. The particle size distribution follows order of birnessite Method 2 > birnessite Method 1 > HMO > pyrolusite.

From potentiometric titrations at ionic strengths, 1.5×10^{-1}, 1.5×10^{-2} and 1.5×10^{-3} (Figures 5.7), the pH_{zpnc} of HMO is approximately 2.4 ± 0.5, falling in the range of pH 1.5-3 reported by others (Morgan and Stumm, 1964; Stumm, 1992). Pyrolusite pH_{zpnc} was observed to be 5.5 ± 0.5; this pH values is in agreement with that observed by others (Healy et al. 1966; Kanungo and Parida, 1983; Kanungo and Mahapatra, 1988). The pH_{zpnc} of binessite was 2.6 ± 0.5 and is in the range of 2-4 reported by others as well (Morgan and Stumm, 1964; Healy et al. 1966; Kanungo and Parida, 1983; Kanungo and Mahapatra, 1988; Scott and Morgan, 1995).

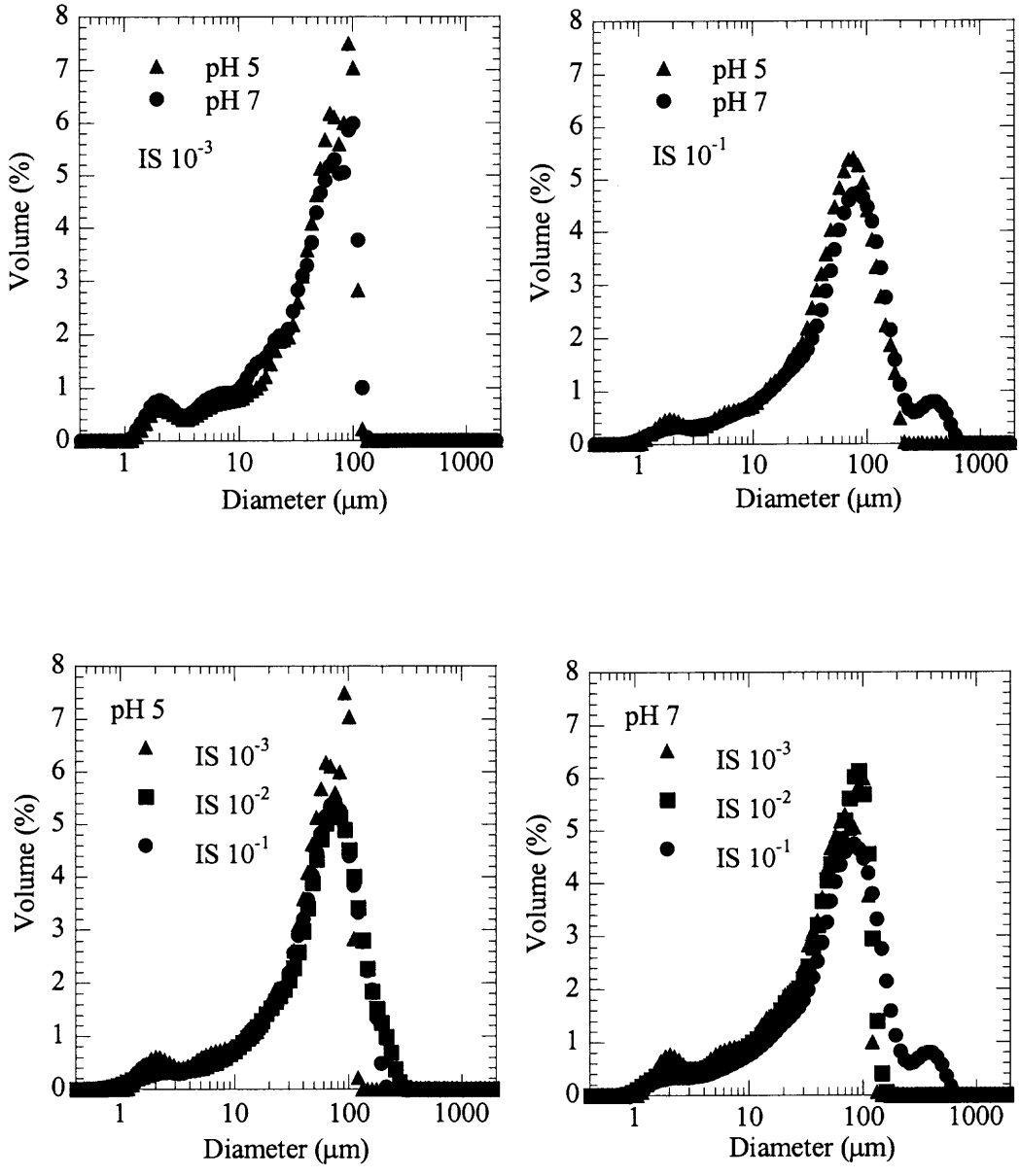

Figure 5.6 Particle size distributions of pyrolusite (1 $g \cdot L^{-1}$) at room temperature illustrate the effect of ionic strength (10^{-1}, 10^{-2}, and 10^{-3}) and pH (5 and 7).

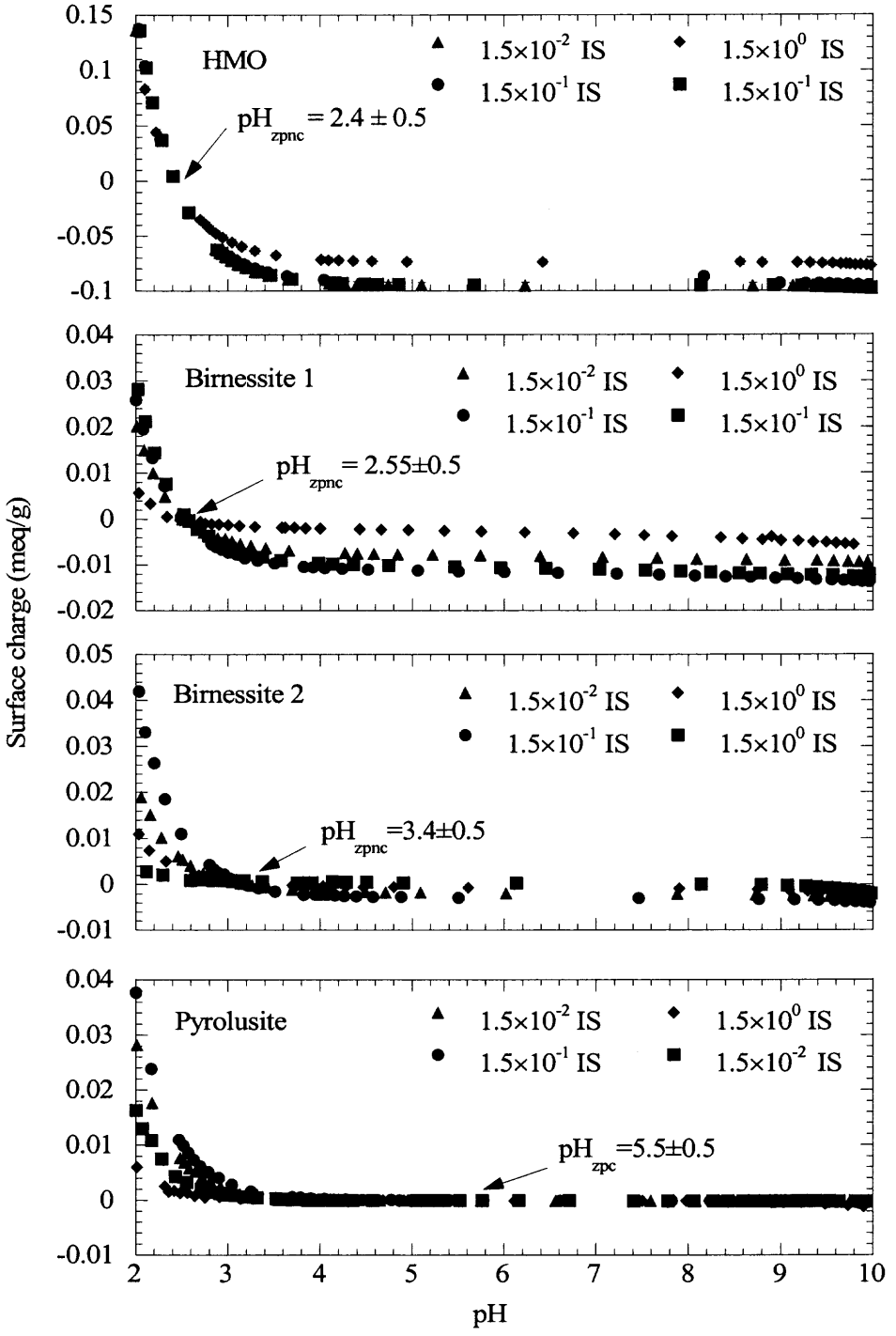

Figure 5.7 Potentiometric titration of 10^{-1} g oxide· L^{-1}, using $NaNO_3$ to adjust the ionic strength (1.5×10^{-2}, 1.5×10^{-1} and 1.5×10^{0}); all systems were purged with N_2 to remove CO_2 at 25 °C.

5.2. Characteristics of Clay: Kaolinite and Montmorillonite

Kaolinite particles are hexagonal flat plates that represent the gibbsite plane attached to a silica plane and appear to aggregate and form a stack which is approximately 5-10 μm in depth. The average size of kaolinite is less than 1 μm and approximately 0.05-0.15 μm in thickness. The morphology of montmorillonite is different from that of kaolinite where individual particles less than 1 μm aggregate into a honeycomb structure (Borchardt, 1989). The creeping structure (Figure 5.8) with irregular shape is approximately 2-5 μm. As revealed in Figure 5.8, the surface area of montmorillonite is greater than that of the flat plane structure characteristic of kaolinite. XRD analysis reveals that both kaolinite and montmorillonite are crystalline structures. However the XRD pattern of montmorillonite is different from the PDF file (Favejee, 1939) (Figure 5.9 and Table 5.3), which may be due to sample preparation including relative humidity, particle size, and temperature. In addition, peak shifts also occurred because of preferred orientation. The width at half height demonstrates the crystallinity of clay (in Table 5.3) and is smaller for kaolinite than for montmorillonite. For kaolinite, XRD pattern is consistent with the PDF file (Nedar et al. 1999) (Figure 5.9).

XRF analyses of the clays are consistent with their structure (Table 5.4 and Figure 5.10). Impurities in montmorillonite are greater than that for kaolinite. Manganese and iron are commonly found with montmorillonite. Although this analysis revealed a purity of approximately 96% for kaolinite, the data sheet reported approximately 87%. As described earlier, both clays were pretreated where surficial carbonate, iron, and organic matter were removed.

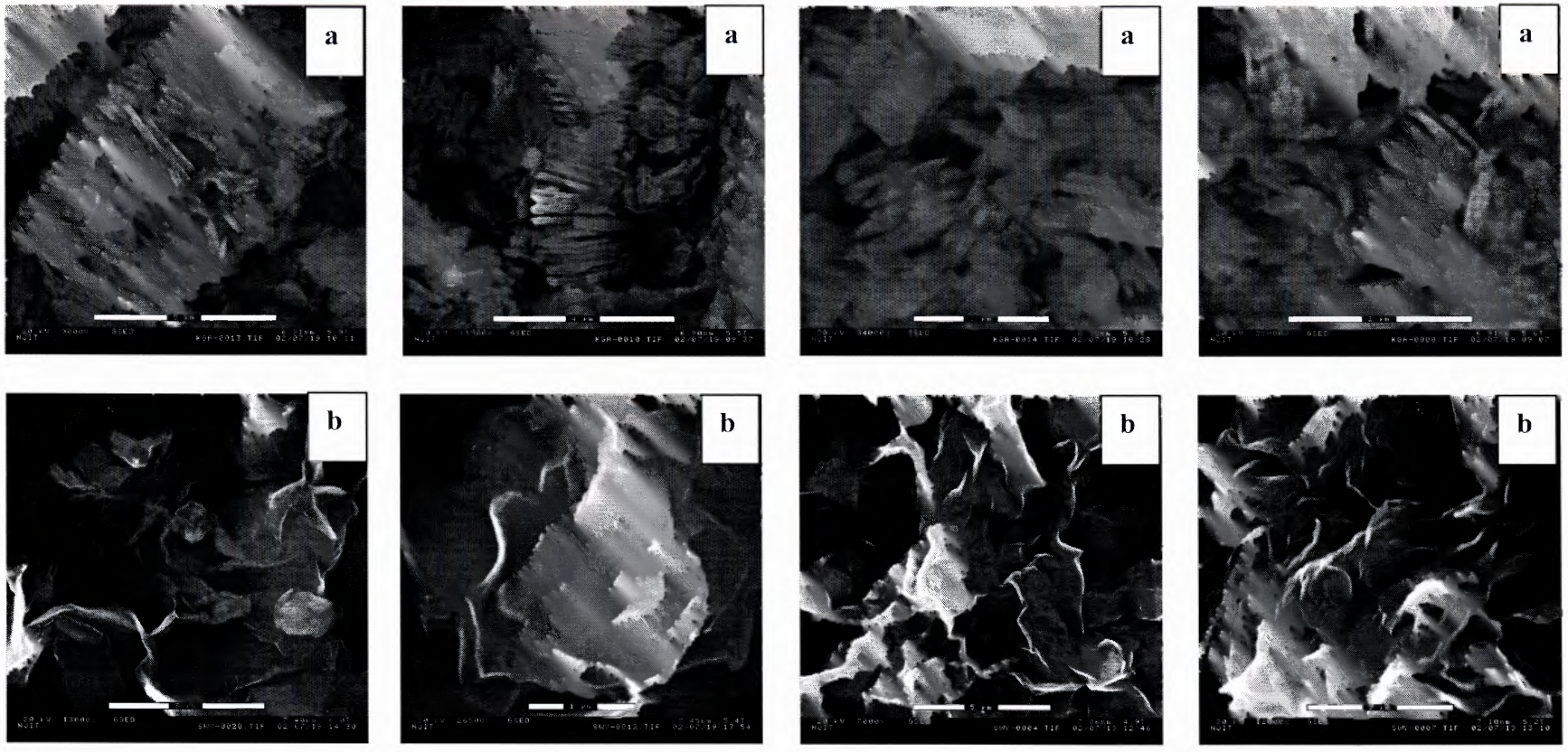

Figure 5.8 ESEM images of (a) kaolinite and (b) montmorillonite.

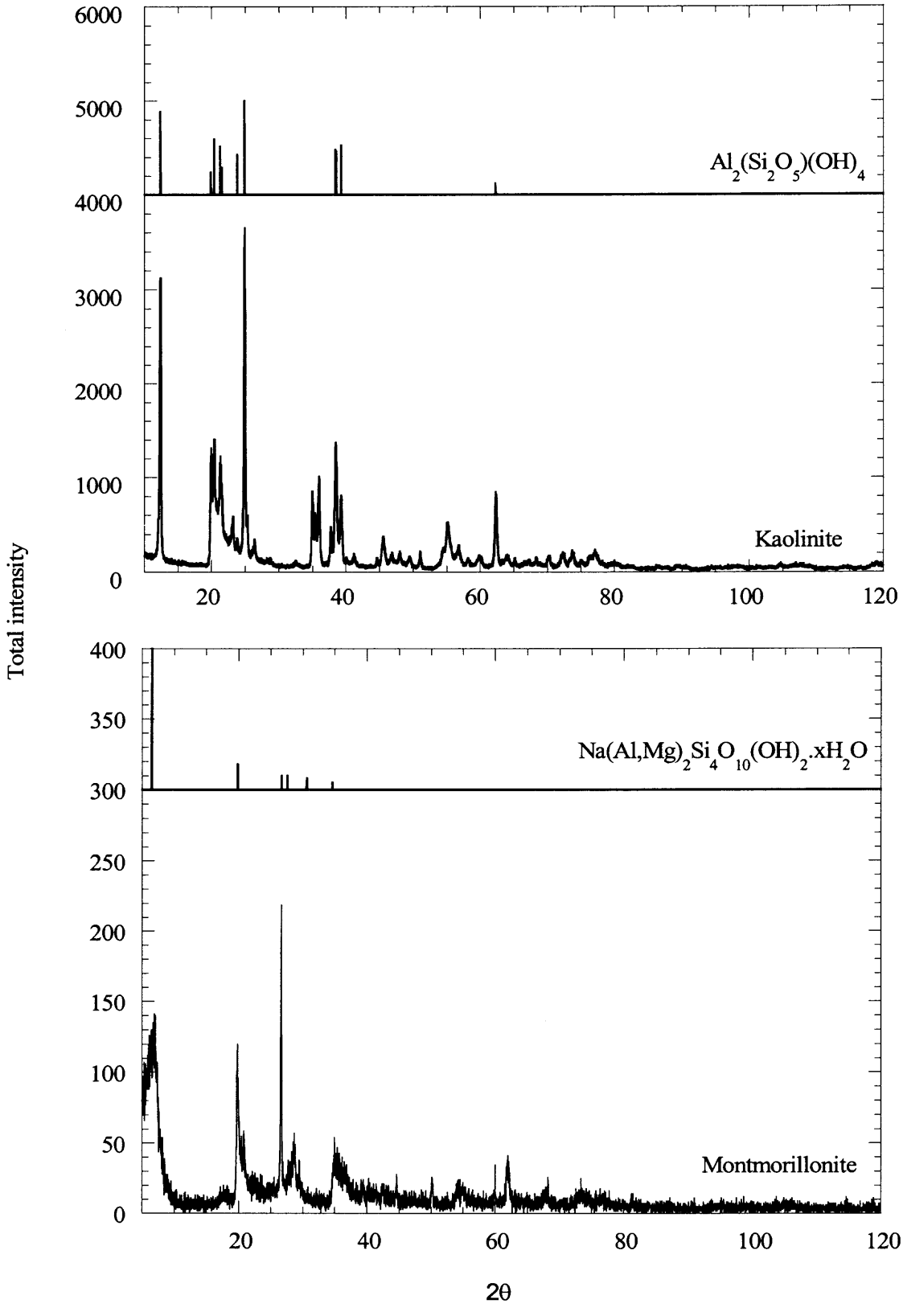

Figure 5.9 The X-ray pattern of kaolinite (KGa-1b) and montmorillonite (Swy-2).

Table 5.3 XRD Analysis given d-spacing (Å), Associated Planes, 2θ, and Width at Half Height for Kaolinite and Monmorillonite

d-spacing (Å)		2θ		Relative Intensity		hkl planes			Half height width (WHH)
Kaolinite	PDF	Kaolinite	PDF	Kaolinite	PDF	h	k	l	Kaolinite
7.13	7.15	12.39	12.36	88.51	89	0	0	1	0.1823
4.35	4.36	20.38	20.34	39.23	59	1	1	0	0.1658
4.16	4.18	21.29	21.24	33.81	52	1	1	1	0.1795
3.57	3.58	24.91	24.87	100	100	0	0	2	0.1797

d-spacing (Å)		2θ		Relative Intensity		hkl planes			Half height width (WHH)
Montmorillonite	PDF	Montmorillonite	PDF	Montmorillonite	PDF	h	k	l	Montmorillonite
13.91	13.6	6.34	6.49	32.37	100	0	0	1	0.6628
4.49	4.47	19.74	19.85	53.78	50	1	1	0	0.3068
4.25	-	20.84	-	22.41	-	-	-	-	0.3310
3.34	3.34	26.64	26.67	100	41	0	0	4	0.1633

Table 5.4 XRF Analysis of Kaolinite and Montmorillonite

Element	Percent of composition	
	Kaolinite	Montmorillonite
Sodium (Na_2O)	-	0.427
Magnesium (MgO)	-	1.061
Aluminum (Al_2O_3)	58.765	34.075
Silica (SiO_2)	37.305	48.970
Sulfur (SO_3)	-	0.281
Potassium (K_2O)	-	1.469
Calcium (CaO)	-	3.027
Titanium (TiO_2)	3.401	0.316
Manganese (MnO)	-	0.094
Iron (Fe_2O_3)	0.529	10.185
Strontium (SrO)	-	0.094
Total	100	100

The particle size of kaolinite is greater than that of montmorillonite in the dry phase; however, for these studies, the particle size in the aqueous phase is of interest. The kaolinite and montmorillonite PSDs range from 0.5 to 100 μm (Figures 5.11 and 5.12): the distributions are independent of pH and ionic strength. The average particle size of kaolinite and montmorillonite are 11 and 8 μm, respectively. However, most particles fall in the range of 4-5 μm. The PSDs observed for these clays is in agreement with others (Adeleye and Clay, 1994; Erzan and Güngör, 1995).

(a)

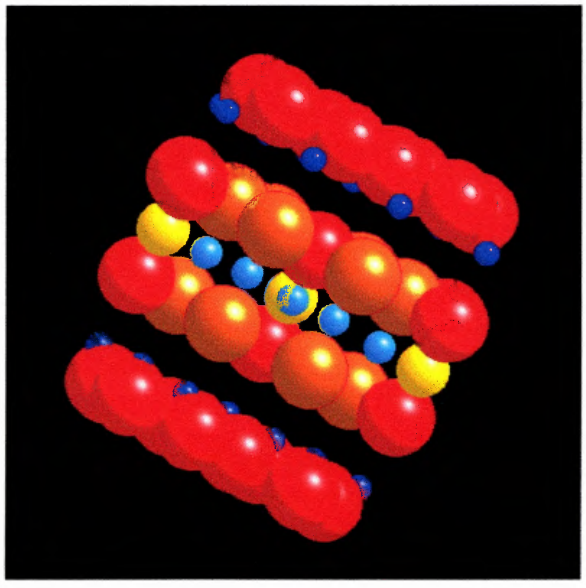

(b)

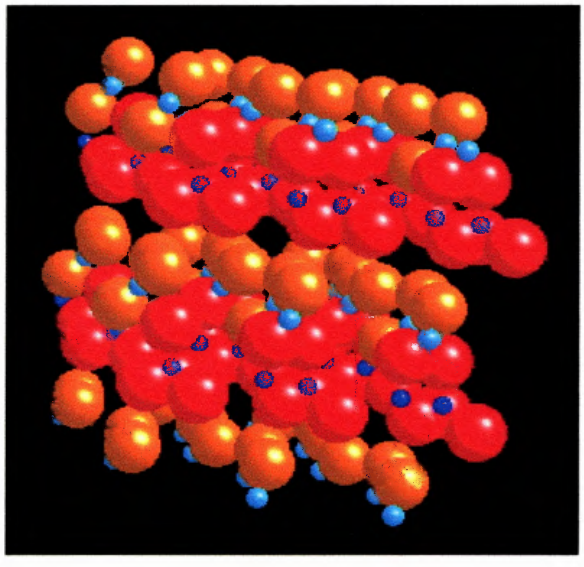

Figure 5.10 (a) Monoclinic montmorillonite structure and (b) Triclinic kaolinite structure. The small dark blue ball represent silicon atom. The large orange and red ball shows the hydroxyl and oxygen, respectively. The light blue and yellow balls are symbol of aluminum and manganese or iron.

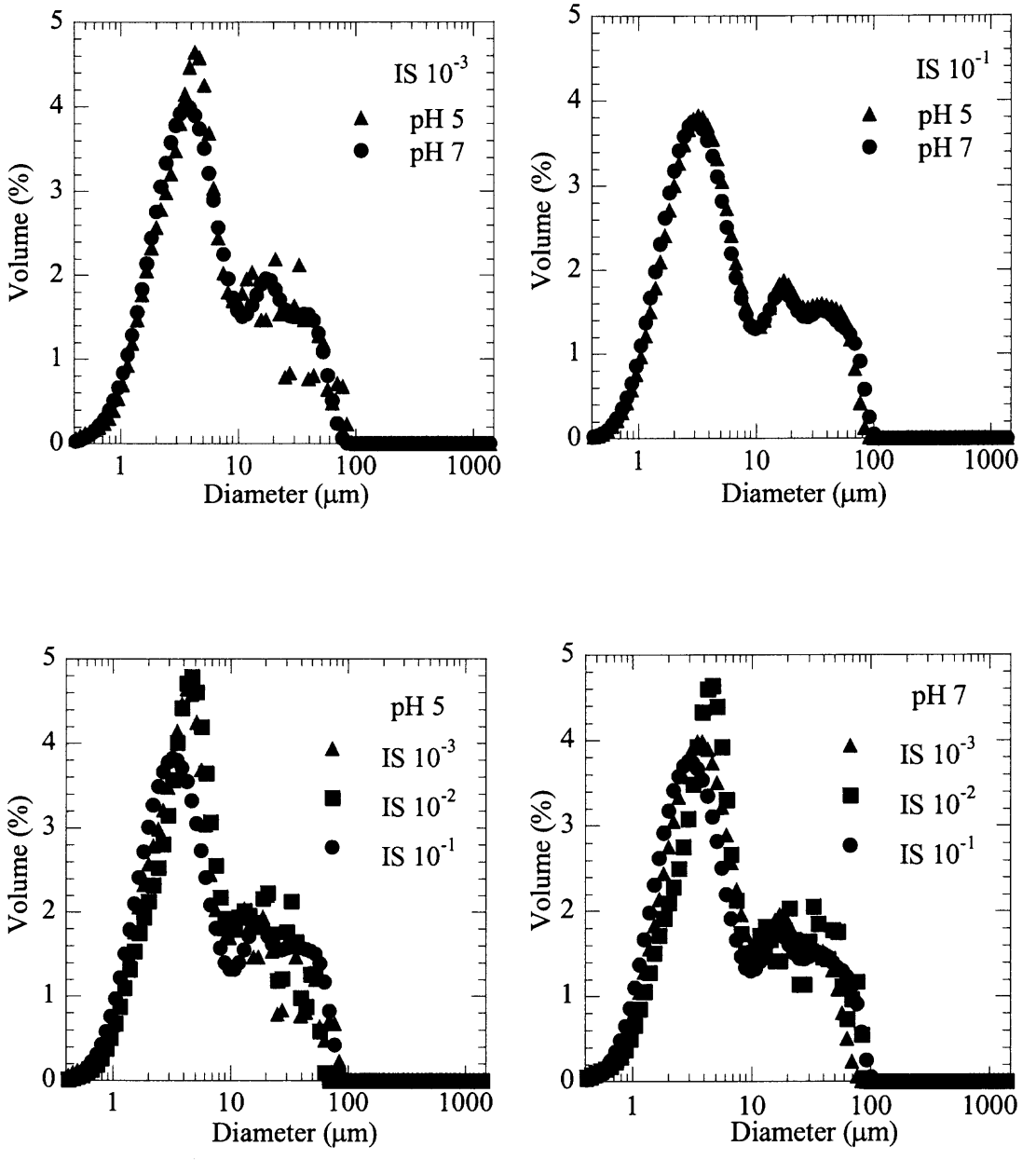

Figure 5.11 Particle size distributions of kaolinite (1 $g \cdot L^{-1}$) at room temperature illustrate the effect of ionic strength (10^{-1}, 10^{-2} and 10^{-3}) and pH (5 and 7).

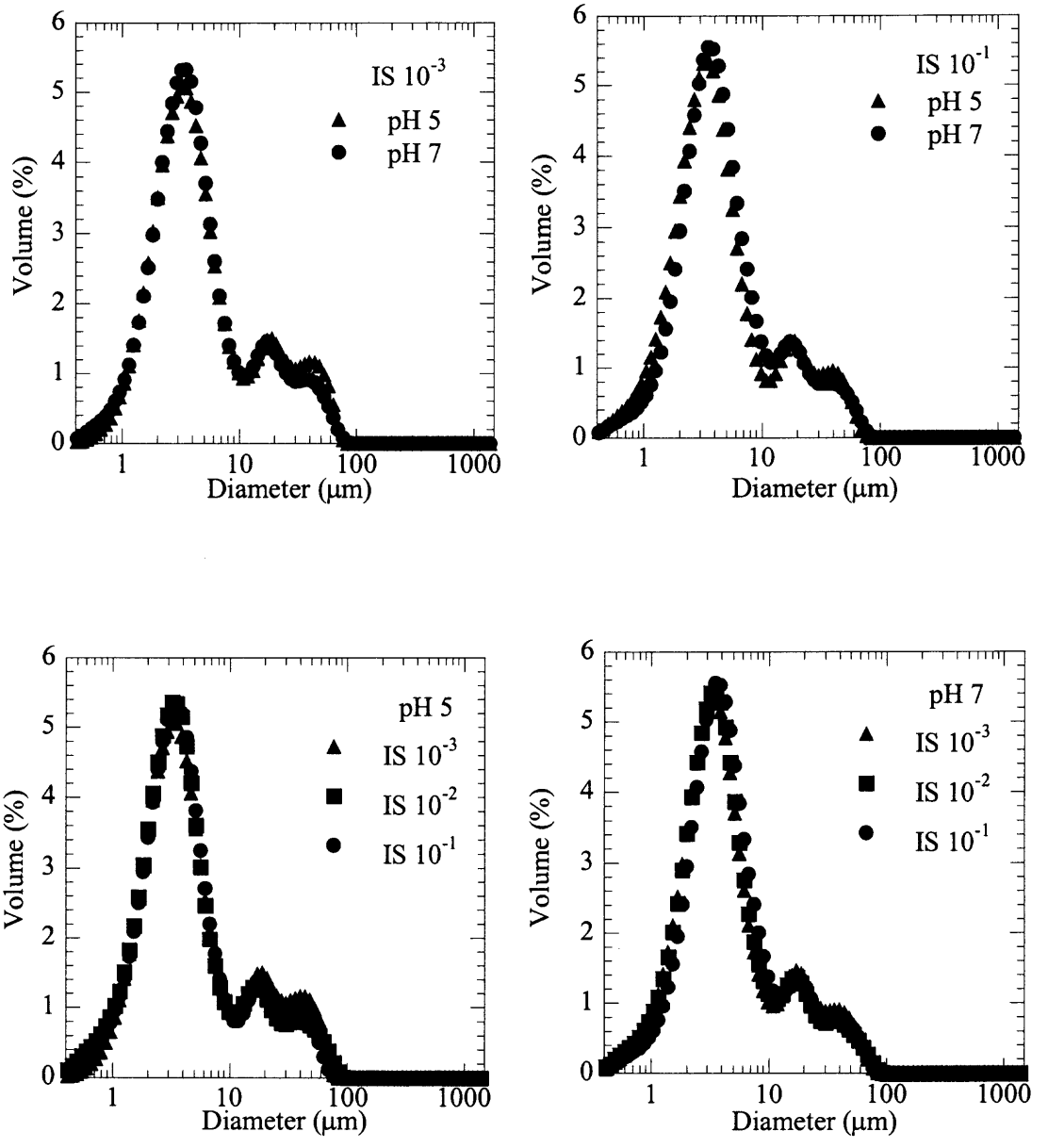

Figure 5.12 Particle size distributions of montmorillonite (1 $g \cdot L^{-1}$) at room temperature illustrate the effect of ionic strength (10^{-1}, 10^{-2} and 10^{-3}) and pH (5 and 7).

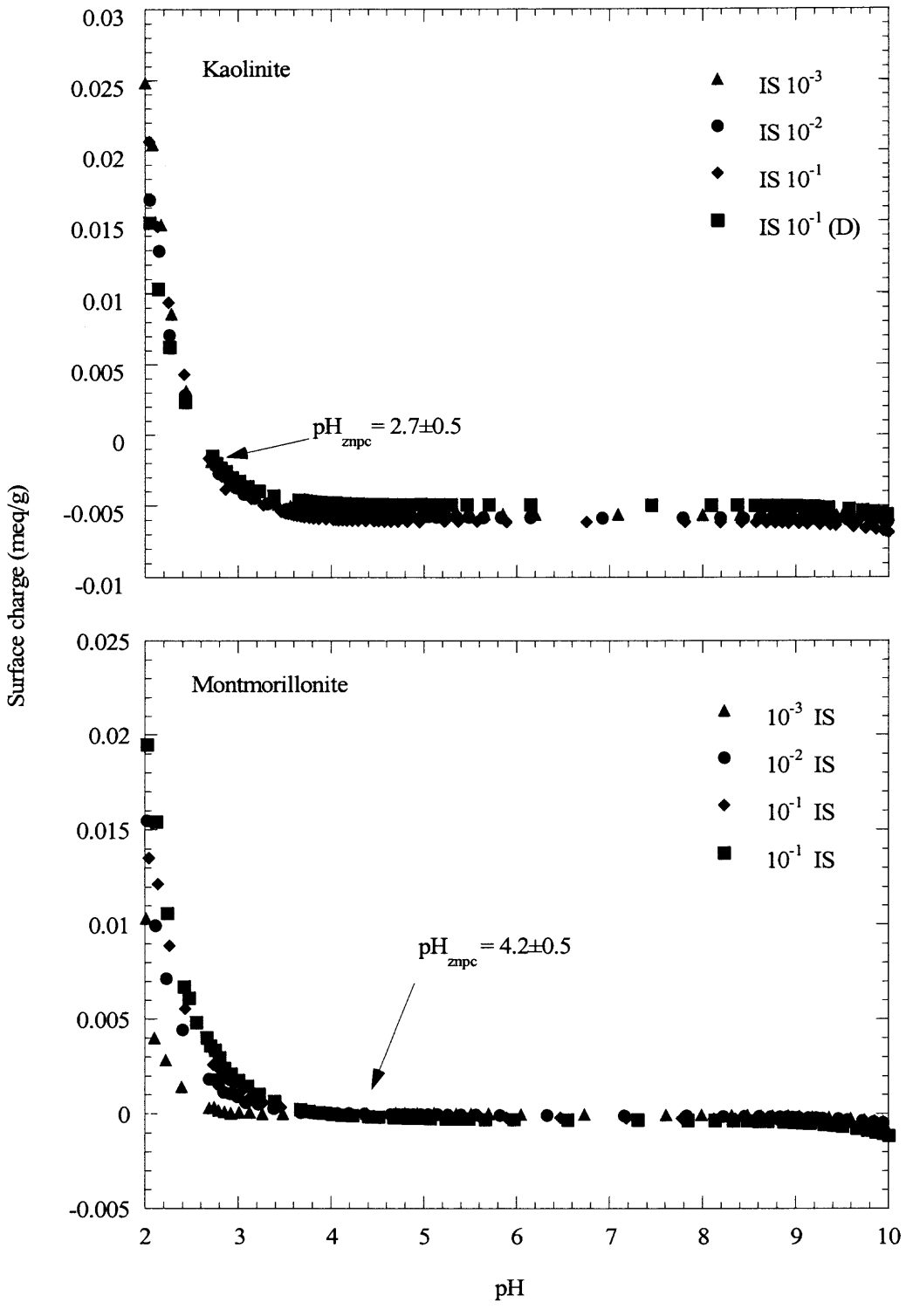

Figure 5.13 Potentiometric titration of 10^{-1} g·L^{-1} kaolinite and montmorillonite using $NaNO_3$ to adjust ionic strength (IS) purge with $N_{2(g)}$ to remove $CO_{2(g)}$ at 25°C

The pH_{zpnc} of kaolinite and montmorillonite is difficult to assess because of the potential dissolution of Al (at pH 3-4) and permanent charge that cannot be neutralized by H^+ (Green-Pederson and Pind, 2000). Generally, the charge on kaolinite and montmorillonite surfaces can be described as negative for the pH range of natural systems. In this study, the pH_{zpnc} of kaolinite is approximately 2.7 ± 0.5 (Figure 5.13) which is close to that observed by Schroth and Sposito (1997) and Arias et al. (1995). In the case of montmorillonite the pH_{zpnc} is approximately 4.2 ± 0.5 (Figure 5.12), which is greater than that reported by Stumm (1992) a value of 2.5.

Characterization of kaolinite and montmorillonite reveals differences in morphology, surface charge, and particle size distribution. Montmorillonite exhibits greater surface area (smaller particles) than kaolinite and may promote greater interaction with the Mn oxides. The smaller particle size or greater surface area is expected to promote greater loadings (Specht et al. 2000). Therefore, montmorillonite is selected for coating studies because of surface area (more irregular shape), surface charge, and particle size.

5.3 Summary

Mineralogy of the Mn oxides showed the amorphous structure of HMO, poorly to well crystalline birnessite, and well crystalline pyrolusite. Morphology of birnessite suggested aggregated needle-shaped crystals while HMO revealed an irregular structure. Overall, the particle size of these Mn oxides ranged from 1 to 600 μm with the average diameter varying from 15 to 30 μm for HMO and pyrolusite. Surface charge analysis resulted in a

pH_{znpc} of HMO, birnessite (Method 1 and 2), and pyrolusite of 2.4, 2.55, 3.4, and 5.5, respectively.

Birnessite (Method 1) appeared to be more crystalline than that of Method 2; therefore, birnessite from Method 1 is selected for the coating experiment. Both clay minerals are well crystalline as seen from XRD. Morphology showed stacking for kaolinite and a creeping structure for montmorillonite. In addition, the particle size of kaolinite is greater than that of montmorillonite, therefore the surface area of montmorillonite is greater than that of kaolinite. The pH_{znpc} of kaolinite and montmorillonite are approximately 2.7 and 4.2, respectively. Based on the surface area, particle size, and surface charge, montmorillonite is preferred for the coating study. Coating by adsorption is expected to be difficult because the surface charge and pH_{zpnc} of oxide and clay are similar. Therefore, coating through precipitation will be applied for these studies. The optimum loading and characteristics of the coatings will be investigated with the same methods used in assessing oxides and clays. Subsequent to the coating study, sorption studies follow.

CHAPTER 6

PROPERTIES AND STRUCTURE OF MANGANESE OXIDE-COATED CLAY

The enrichment of clay minerals may be an important factor in controlling manganese oxide mineralogy. Understanding the occurrence and forms of Mn oxide in the presence of montmorillonite is important for assessing heavy metal interactions with these surfaces and therefore metal mobility and bioavailability.

6.1 Characteristics of Manganese Oxide-coated Clay

The degree of coating was evaluated from the Mn concentration extracted using hydroxylamine hydrochloride-hydrochloric acid (NH_2OH-HCl) (Stahl and James, 1991; Robinson, 1980; Ross and Wang, 1993) and in situ analysis with XRF; results were consistent given the error. Because of the surface charge and large surface area of montmorillonite, Mn oxide loadings for HMO and birnessite ranged between 3.9×10^{-1} and 5.4×10^{-1} g Mn $\cdot$ g^{-1} clay and were greater than that observed for silica, which was 2.5×10^{-3} to 2.7×10^{-2} g Mn $\cdot$ g^{-1} sand based on pyrolusite coatings (Stahl and James, 1991; Guha et al. 2001). However, pyrolusite is significantly different than HMO and birnessite. The Mn oxide loadings were also in agreement with that observed for Fe and Al oxide coatings, where approximately 3.2×10^{-1} g Fe $\cdot$ g^{-1} clay was reported for ferrihydrite- and lepidocrocite-coated montmorillonite (Green-Pederson and Pind, 2000) and 1.30×10^{-3} to 1.35×10^{-1} g Al $\cdot$ g^{-1} clay for hydrous aluminum oxide (Turner et al. 1996; Arias et al. 1995; Naidja et al. 1997). Between an application of 0.50 and 1.5 g Mn $\cdot$ g^{-1} clay, the degree of coating for HMO and birnessite was relatively constant because

of potentially site saturation on the montmorillonite surface (Figure 6.1a). This effect was also observed with the birnessite-coated clay (Figure 6.1b). Interestingly, a site saturation effect can be observed using the Langmuir model (Figure 6.1), where both coated systems resulted in a maximum capacity of approximately 0.5 g Mn $\cdot$ g^{-1} clay.

The morphology of the Mn oxide coatings was also studied to observe the degree of coating. Birnessite has a needle shaped crystal, discrete HMO has an irregular topography comprised of nanoparticle aggregates, and montmorillonite usually aggregates into a honeycomb structure (Figure 6.2a, b, and c). For the HMO and birnessite coatings at 1.0×10^{-1} g Mn $\cdot$ g^{-1} clay, little to no oxide was observed using FE-SEM; however, at loadings greater than or equal to 2.5×10^{-1} g Mn $\cdot$ g^{-1} clay, coatings were observed. At 5.0×10^{-1} g Mn $\cdot$ g^{-1} clay, discrete oxide was present (Figure 6.2d and e) and both birnessite as well as HMO uniformly deposited along the clay (110) planes (Figure 6.2d, e and f). These morphological observations are in agreement with XRD analysis. For example, at the lowest loading (1.0×10^{-1} g Mn $\cdot$ g^{-1} clay), the sample was relatively similar to that of montmorillonite based on d-spacings and intensity (Figure 6.3 and Table 6.1), except for the 001 reflection. This reflection appears to have shifted to a larger d-spacing, indicating an expansion of the interlayers, which may be attributed to hydration (Brindley and Brown, 1980) as well as Mn oxide precipitation.

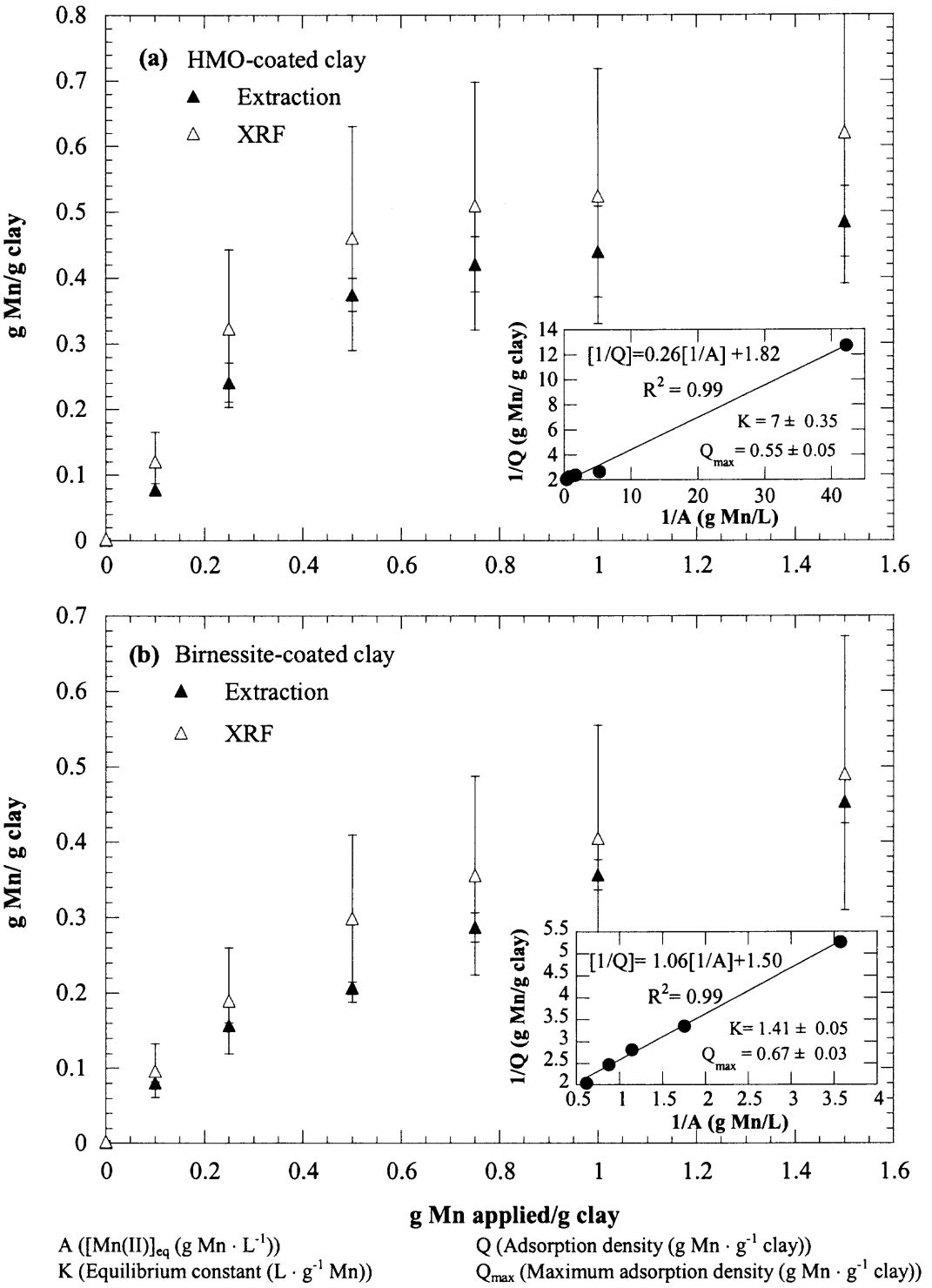

Figure 6.1 HMO (a) and birnessite (b) loadings on montmorillonite as a function of application and analyzed by extraction (empty symbols) and XRF (filled symbols).

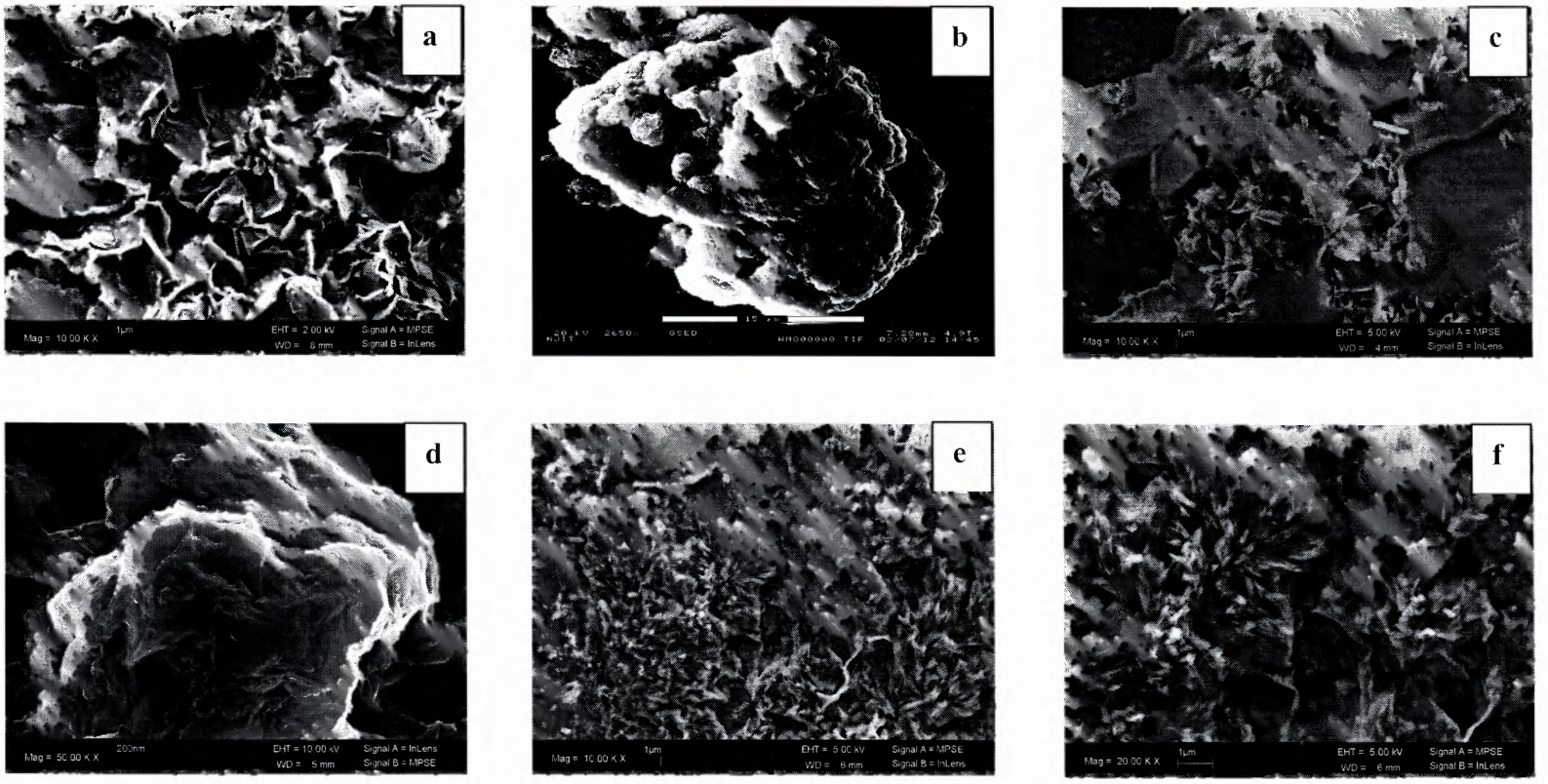

Figure 6.2 ESEM and FESEM images of (a) montmorillonite, (b) HMO, (c) birnessite, (d) HMO-coated clay at 0.50 g Mn · g^{-1} clay, (e) birnessite-coated clay at 0.50 g Mn · g^{-1} clay, and (f) birnessite–coated clay planar and intraplanar view.

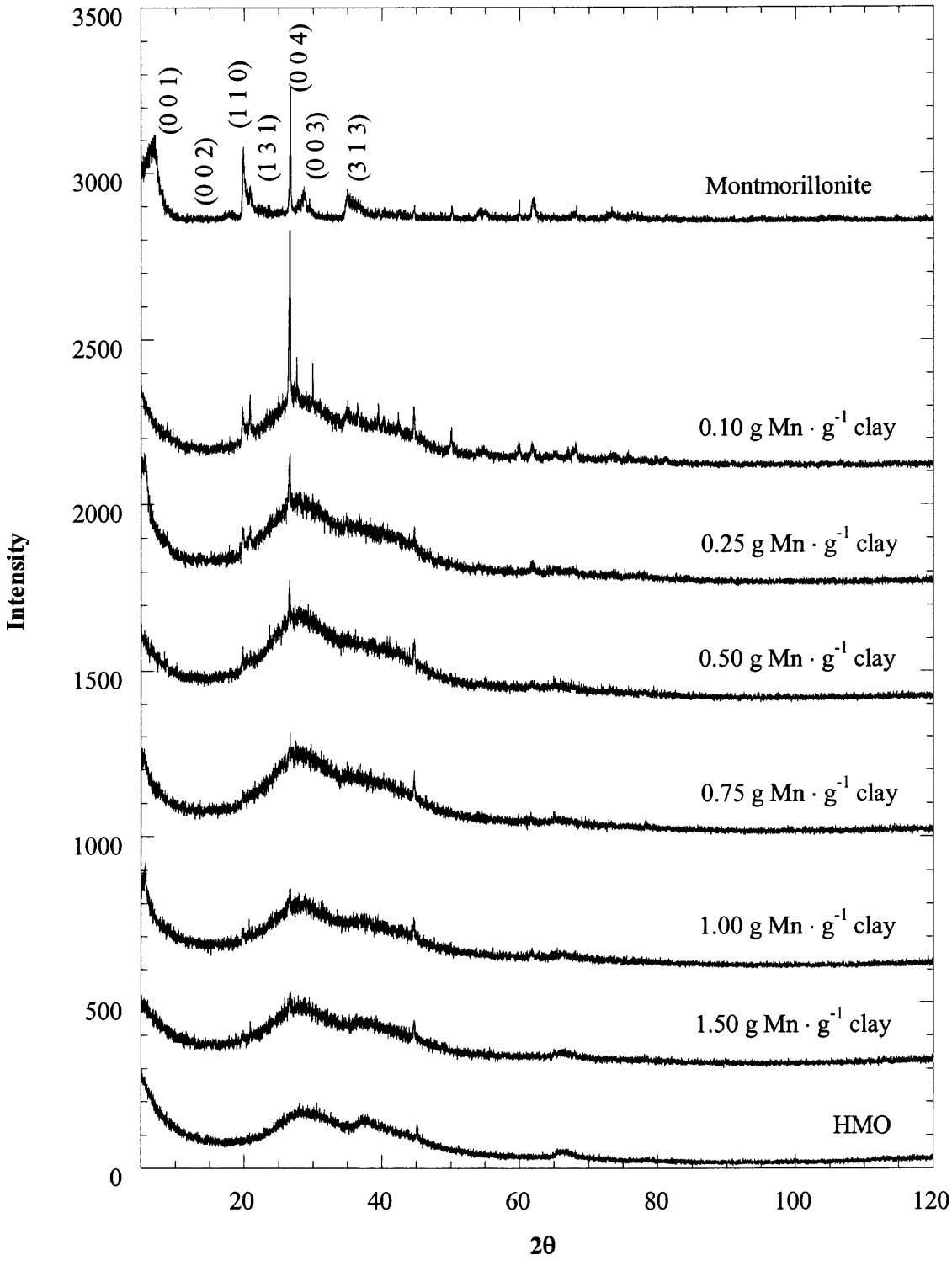

Figure 6.3 XRD patterns of HMO-coated clay as a function of loading.

However, as the loading increased to 2.5×10^{-1} g Mn $\cdot$ g^{-1} clay or greater, the pattern was consistent with discrete HMO. The diffractogram of birnessite coatings was broader and less intense as compared to birnessite produced in the lab (Wadsley, 1950), suggesting a poorly crystalline structure (Figure 6.4 and Table 6.1).

Again, at greater than 5.0×10^{-1} g Mn $\cdot$ g^{-1} clay, HMO and birnessite appear to form aggregates of discrete oxides, demonstrating a limiting capacity for the Mn oxide. With greater loading, electrostatic forces between like particles potentially prevent further coating. However, for pyrolusite-coated clay (Figure 6.4), the XRD pattern appears to be similar to that of clay, suggesting inhibition of oxide crystallization or that the oxide nucleated as nanometer particles and was not detected by XRD. This observation is also consistent with the poorly crystalline lepidocrocite-coated montmorillonite observed by Green-Pederson and Pind (2000). Inhibition of crystallization has been found not only in the presence of substrates but also when other impurities such as metal ions (Cr, Cu, Mg, Ni, and Zn) (Dalpi et al. 1993; Grases et al. 1989; Karim, 1984), organic ligands (cysteine, lysine, EDTA, and humic acid) (Dalpi et al. 1993; Koutsopoulos and Dalas, 2000), and inorganic ligands (sulfate, phosphate, and ammonium) (Couling and Mann, 1985; House, 1987; Rees et al. 2002; Storr et al. 2004) are present. Given the limiting capacity of montmorillonite for Mn oxide and the need to better understand the structure and surface properties, 5.0×10^{-1} g Mn $\cdot$ g^{-1} clay was selected for elemental mapping and the further analysis.

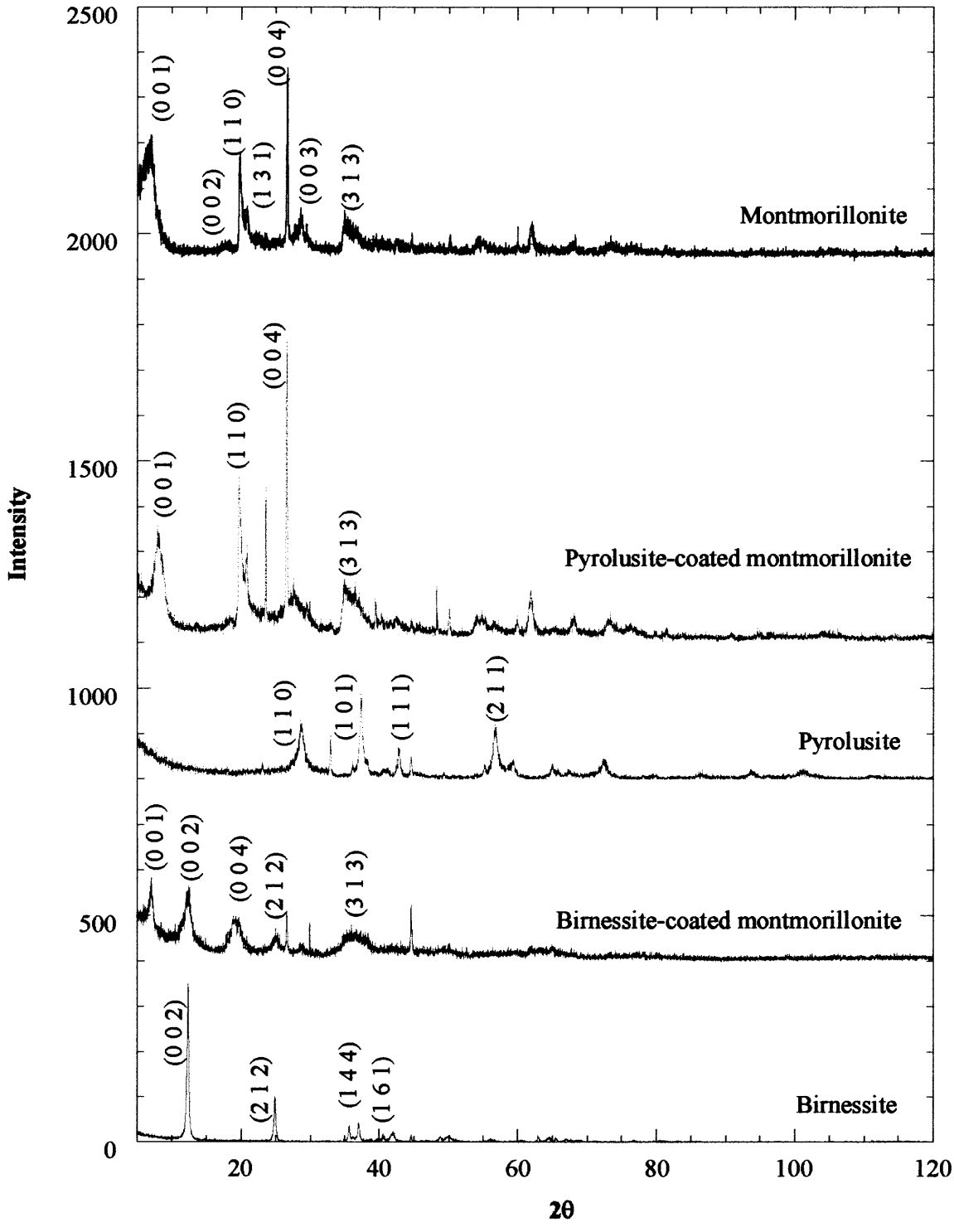

Figure 6.4 XRD patterns of birnessite- and pyrolusite-coated clay.

Table 6.1 XRD Analysis of the Mn Oxide-coated Clays with d-spacing (Å), 2θ, Relative Intensity, and Planes

	Montmorillonite	HMO-coated clay (0.5 g Mn g^{-1} clay)	Birnessite	Birnessite-coated clay (1.5 g Mn g^{-1} clay)	Pyrolusite	Pyrolusite-coated clay (1.5 g Mn g^{-1} clay)
d-spacing (Å)	12.60	3.35	7.12	12.47	3.11	11.04
	4.49		3.57	7.07	2.40	4.49
	4.25		2.52	3.34	2.11	3.76
	3.34		2.43	2.03	1.62	3.34
2θ	7.00	26.55	12.43	7.07	28.65	7.99
	19.74		24.93	12.50	37.35	19.72
	20.84		35.61	26.64	42.78	23.61
	26.63		36.99	44.57	56.77	26.62
Relative intensity	37.96	100.00	100.00	90.90	59.14	23.87
	53.78		44.38	98.53	100.00	50.57
	31.25		35.61	91.71	35.63	45.87
	100.00		36.99	100.00	70.32	100.00
h l k plane	0 0 1	0 0 4	0 0 2	0 0 1	1 1 0	0 0 1
	1 1 0		2 1 2	0 0 2	1 0 1	1 1 0
	1 3 1		1 4 4	0 0 4	1 1 1	-
	0 0 4		1 6 1	2 1 2	2 1 1	0 0 4

Montmorillonite is composed of 45% O, 19% Al, 23% Si, 7% Fe, and 2% Ca (Figure 6.5). For the lower atomic numbers, O, Si, and Al, the detection limit ranges from 0.2 to 1%. Interestingly, for both types of coatings (HMO and birnessite), Mn, O, Si, and Al concentrations were approximately equivalent (32%, 63%, 4%, and 1%, respectively). Si and Al present in the coatings were significantly smaller compared with the almost 41% total present in the original clay.

These results are consistent with the permanent charge located on silica plane, comprising ~90% of clay surface as opposed to the variable positive charge along the intraplanar area (~10%) which potentially repels the Mn oxide nucleation. The intraplanar area of montmorillonite is attributed to the edges of the octahedral sheet (gibbsite plane) where broken bonds occur (Choppin et al. 2002); Si and Al are observed along these edge areas. As seen in Figure 6.2, the intraplanar area was even observed at higher loadings suggesting as HMO increased, the affinity for oxide-oxide aggregates was greater than that for the edge area.

Moreover the effect of coatings was also observed from the particle size distribution (PSD). For the HMO-coated system at 5.0×10^{-1} g Mn $\cdot$ g^{-1} clay, the particle size distribution is consistent with that for HMO (Figure 6.6a), as montmorillonite particles range from 0.1 to 20 μm. The PSD of birnessite was bimodal (3.8 and 25 μm), while the PSD of birnessite-coated clay became a monodal distribution (Figure 6.6a). Green-Pedersen (2000) observed that the PSD of lepidocrocite-coated montmorillonite appeared much like that of pure lepidocrocite. Al, Fe, and Mn oxide-coated silica, on the other hand, have been observed to have little to no effect on the particle size distribution because generally silica is much larger (Meng and Latterman, 1993; Stenkamp and

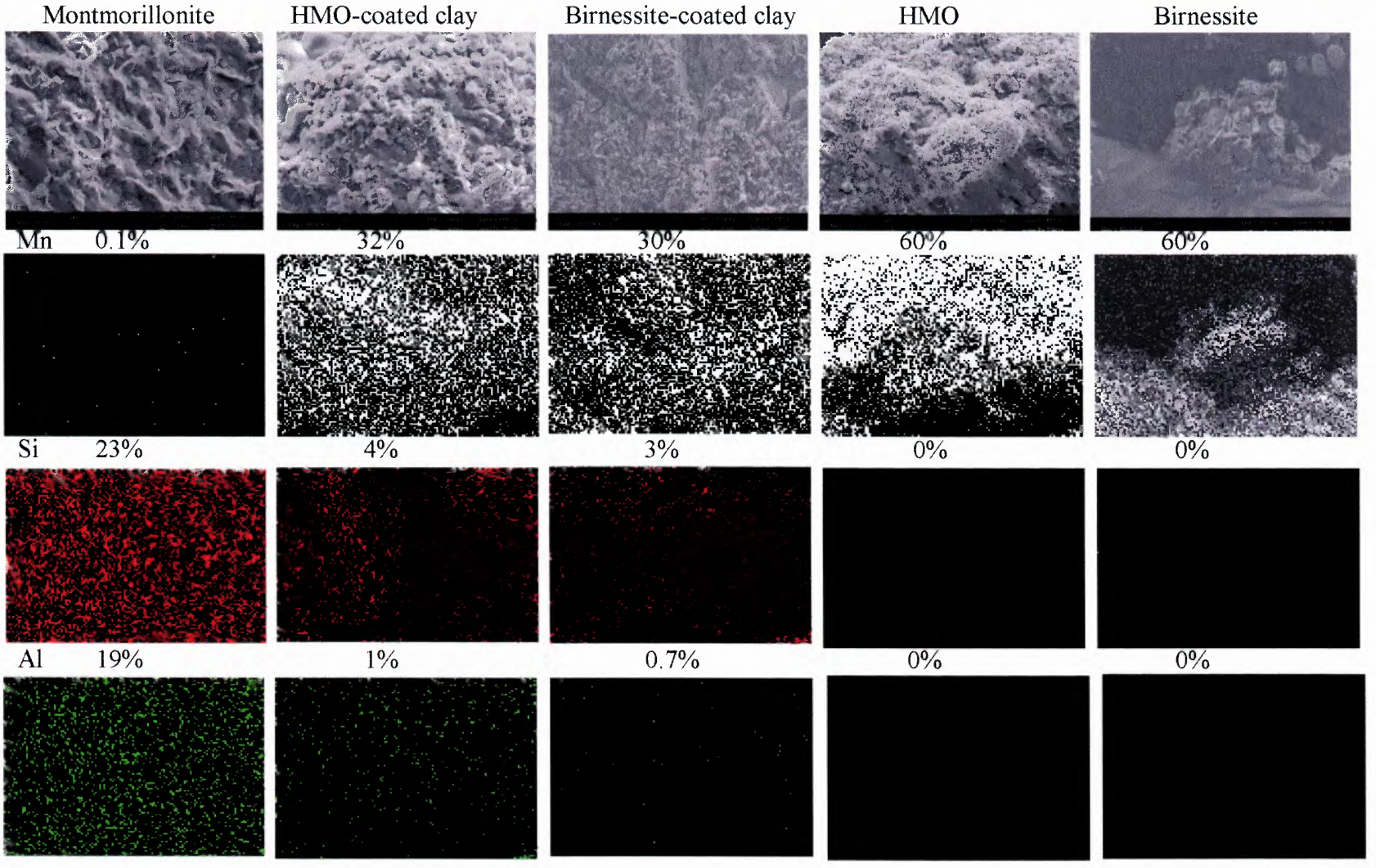

Figure 6.5 EDX mapping of manganese, silica, and aluminum on montmorillonite, HMO-coated clay (0.50 g Mn · g^{-1} clay), birnessite-coated clay (0.50 g Mn · g^{-1} clay), and discrete HMO and birnessite.

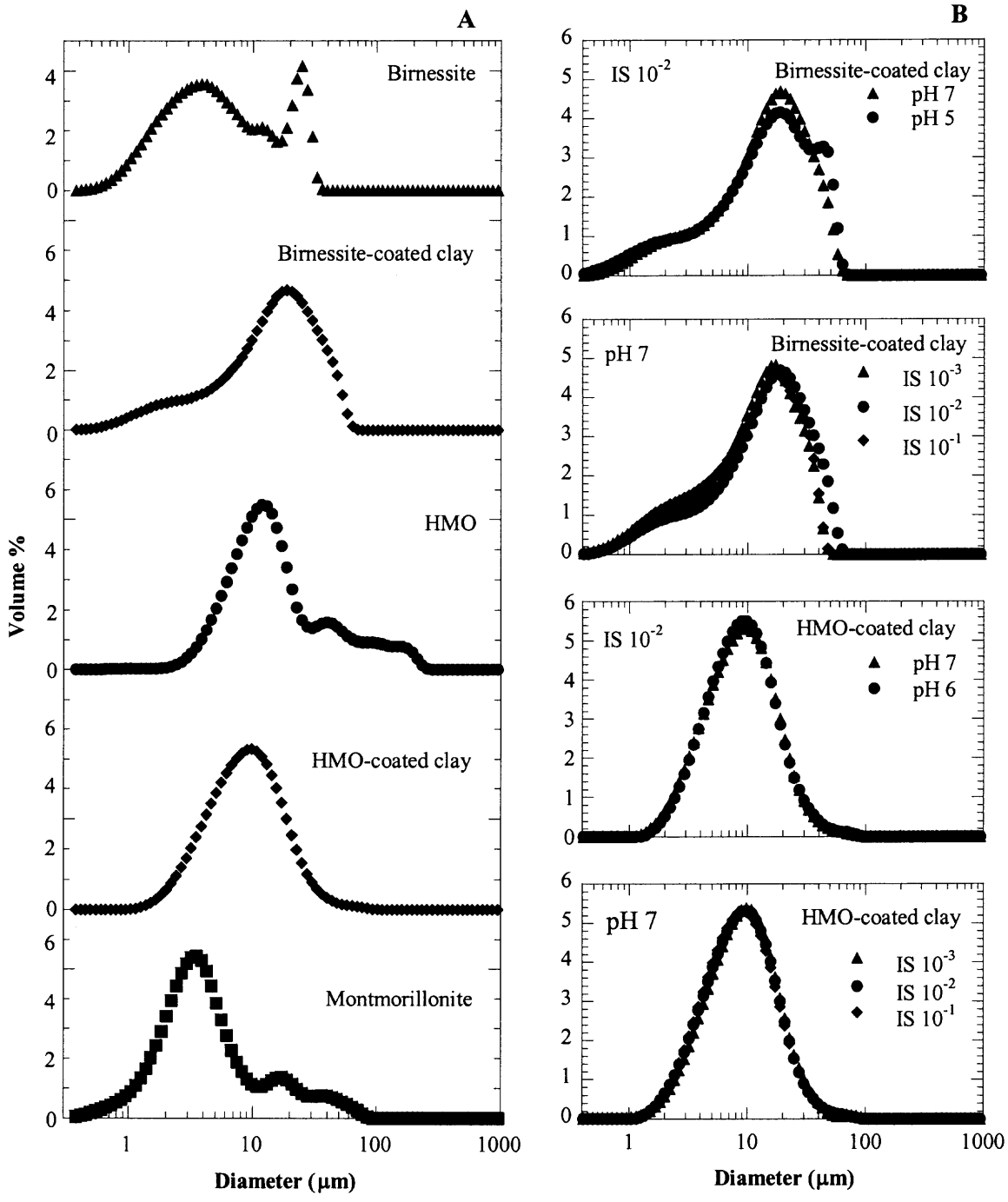

Figure 6.6 (a) Particle size distribution of HMO, birnessite, HMO-coated clay, birnessite-coated clay at pH 7 and 10^{-2} ($NaNO_3$) ionic strength; and, (b) the size distribution of birnessite- and HMO-coated clay at 0.50 g Mn · g^{-1} clay (1 g · L^{-1}) illustrating the effect of ionic strength (10^{-1}, 10^{-2}, and 10^{-3}) and pH (6 and 7).

Benjamin, 1994; Szecsody et al. 1999). Interestingly, the ionic strength and pH have no observable effect on the particle size distribution over the range of 10^{-1} to 10^{-3} ionic strength and pH 5 and 6 (Figure 6.6b)

The oxide coatings affected not only morphology, but also surface area, porosity, and pore size distribution. The surface area of the HMO coating was 95 $m^2 \cdot g^{-1}$, and is between that of HMO (359 $m^2 \cdot g^{-1}$) and montmorillonite (with an external area of 28 $m^2 \cdot g^{-1}$). HMO potentially introduces more surface area to the montmorillonite substrate, where the pore size distribution of the HMO coating resulted in an average size of approximately 8.6 nm and is close to that of discrete HMO (bimodal 2.1 and 6.1 nm). The porosity of the HMO-coated surface (81%) increased substantially as compared to HMO (35%) and montmorillonite (51%). The increase in porosity may be due to oxide aggregation. On the other hand, the surface area of the birnessite coating was 26 $m^2 \cdot g^{-1}$ which is consistent with that of montmorillonite (external surface) and is slightly less than that of discrete birnessite (32 $m^2 \cdot g^{-1}$). The porosity of the birnessite coating was similar to that of birnessite (3%), and was much less than that of montmorillonite. The pore size distribution of the birnessite coating was consistent with discrete birnessite (6 nm), suggesting a smaller pore size as compared to montmorillonite (mono-modal distribution 12.3 nm). However, in using the BET method and Hg porosimetry for Mn oxides, measurements are collected on anhydrous samples, the hydrated samples are expected to be much greater in area than the measured value because the oxide swells in the aqueous phase. In addition, when mesopores are hydrated, layers of water are sorbed along surfaces resulting in potentially smaller, micro-sized pores (Kärger and Ruthven, 1992). On the other hand, in using the BET method for montmorillonite, it accounts for

only the external surface area (~ 5%) and does not include internal surfaces (Sposito, 1984; Quirk and Murray, 1999). Theoretically, montmorillonite possesses a surface area of approximately 751 $m^2 \cdot g^{-1}$ (Sposito, 1984), which is based on crystallographic data. To better understand surface properties, potentiometric titrations were conducted. The HMO-coated clay behaved similarly to HMO where the pH_{znpc} of HMO-coated clay (2.8 ± 0.5) was approximately equivalent to that of HMO (2.4 ± 0.5) (Morgan and Stumm, 1964; Quirk and Murray, 1999) (Figure 6.7). However, the pH_{znpc} of montmorillonite has been observed to range from 2.0 to 10.0 (Hatch, 1952; Mitchill, 1963; Coppin et al. 2002), and in these studies, it was approximately 4.6 ± 0.5. In addition, the pH_{znpc} of birnessite-coated clay was approximately 3.1 ± 0.5 and falls between the two minerals. The results suggest that HMO, birnessite, and montmorillonite play important roles in surface charge behavior and metal distribution.

Further assessment of the surface properties included studying the local structure of Mn using XAS. Initially in comparing the X-ray absorption near edge structure (XANES) region of the discrete Mn oxides to that of their coated clay counterparts, each is equivalent to their discrete form. The amplitude reduction factors (S_0^2), which accounts for energy loss due to multiple electron excitations were fixed at 0.97 based on fitting the experimental β-MnO_2 spectra, with its known coordination numbers in Table 6.2. For X-ray absorption fine structure (XAFS) on HMO and HMO-coated clay, all parameters were floated and the edge energy was constrained to being equivalent for all shells in the fit. First, each shell was isolated and fit, and was proceeded by multiple shells fitting over a radial window of 0.50 to 3.08 Å.

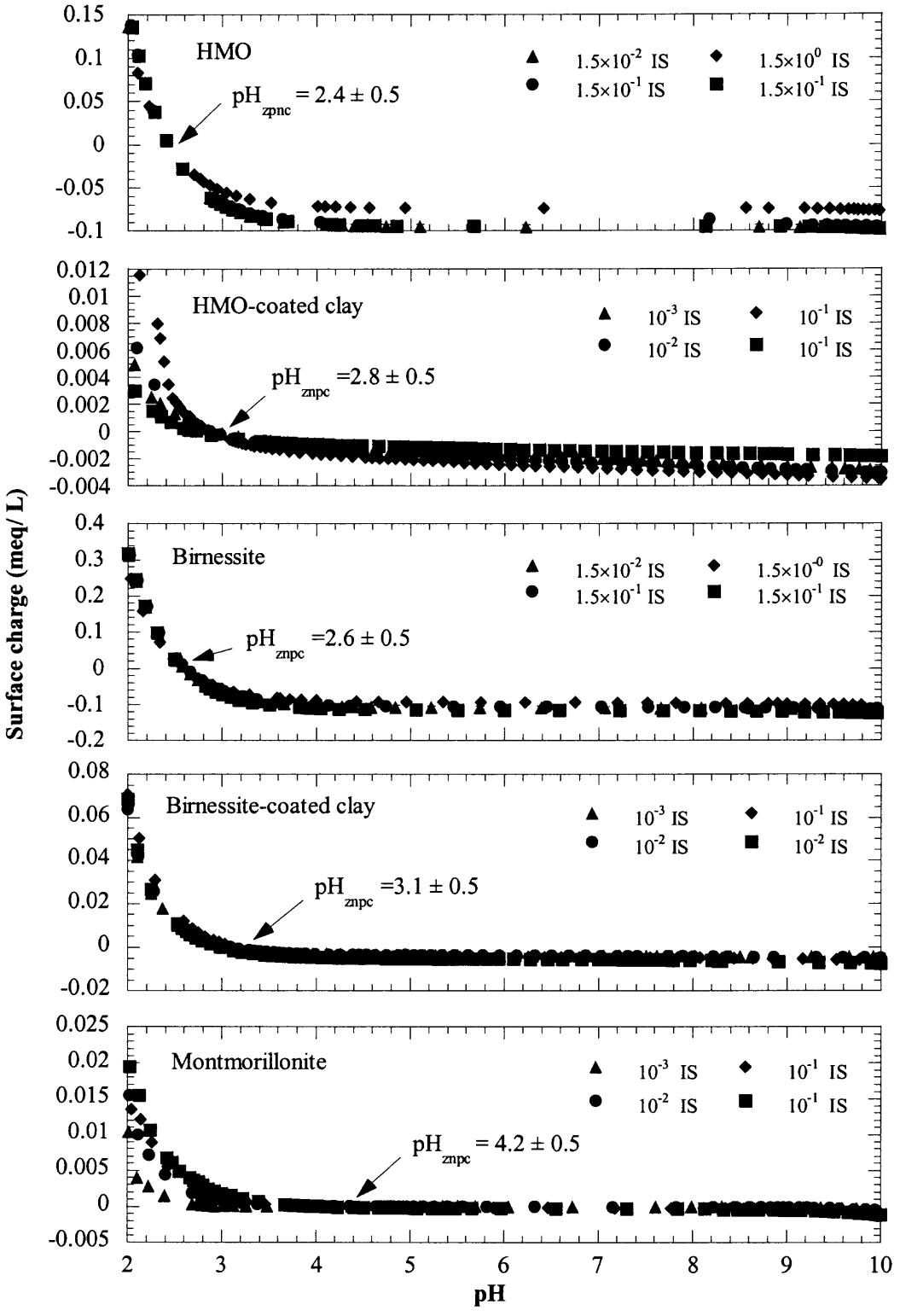

Figure 6.7 Potentiometric titrations of 10^{-1} g · L^{-1} HMO, birnessite, HMO-coated clay, birnessite-coated clay, and montmorillonite using $NaNO_3$ to adjust the ionic strength and purged with N_2 at 25 °C.

For HMO and HMO-coated clay (Figure 6.8), in the first shell, 3.1 atoms of oxygen were observed at a distance of 1.89 ± 0.02 Å, while 2.7 manganese atoms were found at an average radial distance of 2.85 ± 0.02 Å (Table 6.2). Furthermore, after aging HMO-coated clay for 1 month, the XAFS spectra showed that the local structure of HMO, HMO-coated clay, and 1-month old HMO-coated clay was equivalent.

In agreement with a number of studies (Axe et al. 2000; Manceau et al. 1987; Manceau and Combes, 1988; Pasten, 2002), the ratio of coordination numbers for these two shells is close to 1:1. Moreover, the Mn oxide structure has been reported to have a random framework of edge- and corner-sharing MnO_2 octahedra (Manceau et al. 1987; Manceau and Combes, 1988), which is similar to vernadite (Manceau et al. 1992). Interestingly, vernadite synthesis is relatively similar to HMO in considering stoichiometry; therefore HMO may potentially be equivalent to vernadite. Giovanoli et al (1980) reported that vernadite has a random stacked birnessite structure based on XRD patterns, on the other hand, Chukhrov et al. (1980) and Chukhrov and Gorshkov (1980) found that vernadite is distinct from birnessite because of disordering in the c parameter and the lack of basal plane reflections (001). Moreover, Friedl et al. (1997) characterized vernadite as a c-disordered H^+-birnessite using XAFS. In addition, Manceau and coworkers (1992, 1987) conducted XAS on several types of Mn oxides, where lithiophorite (Al, Li)$MnO_2(OH)_2$ and asbolane from New Caledonia both exhibited 3.0-3.6 atoms of oxygen in the first shell and 3.0-3.6 Mn atoms in the second shell.

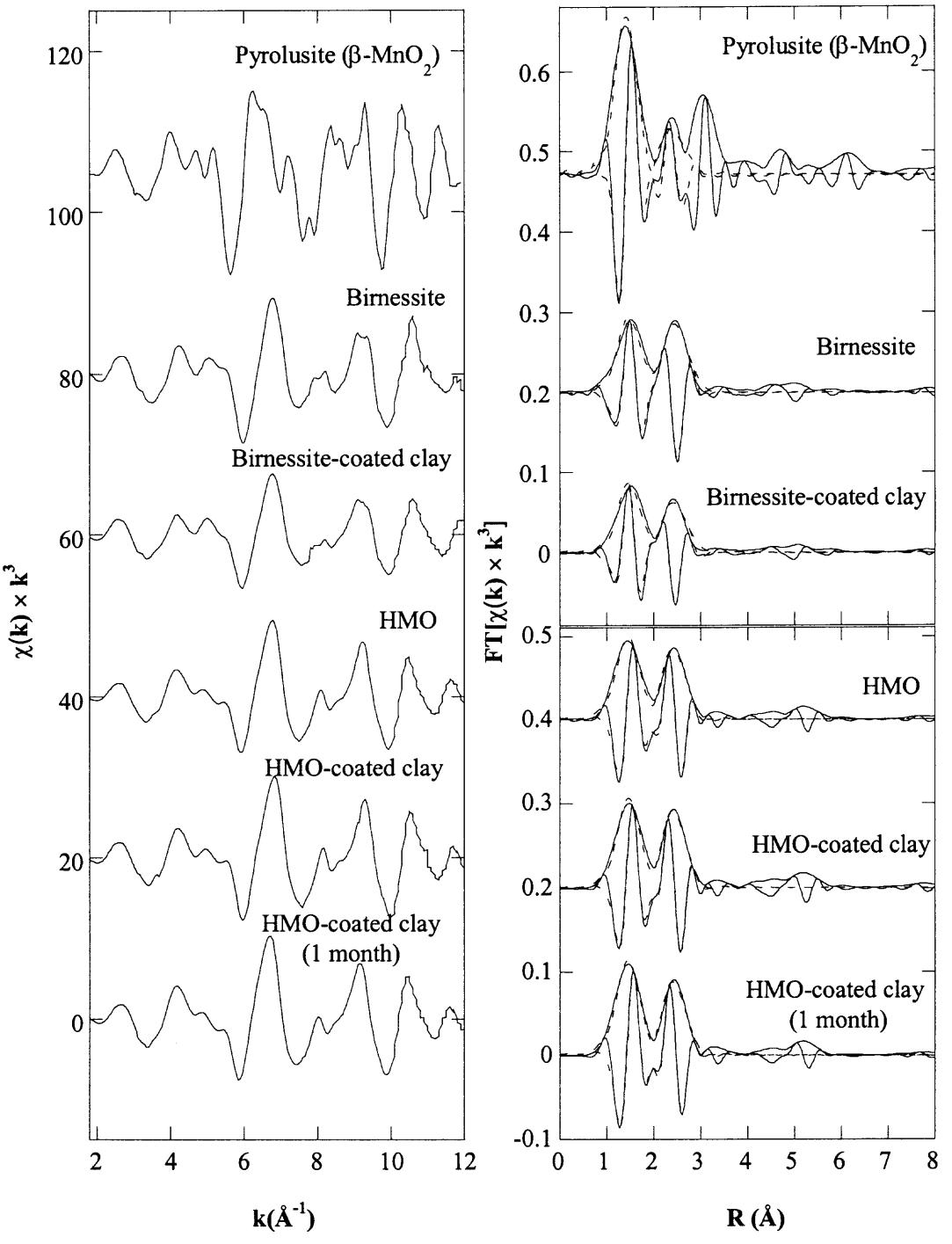

Figure 6.8 Mn K-edge $\chi(k) \cdot k^3$ spectra collected in transmission and fluorescence modes at 25 °C, and Fourier transformed $\chi(k) \cdot k^3$ spectra over 2.20 to 11.88 $Å^{-1}$ and fitted over 0.50 to 3.10 Å.

Table 6.2 XAS Fitting Results of Discrete Mn Oxides and Mn Oxide-coated Clay at Mn K-Edge

Sample	Atom	N	R (Å)	σ^2 (Å^2)	ΔE_o	% Residual
β-MnO_2	O	5.5 (6)	1.88 (1.88)	$1.49\times10^{-3} \pm 3.27\times10^{-5}$	-7.7	15.6
	Mn	2.0 (2)	2.87 (2.87)	$5.10\times10^{-2} \pm 4.32\times10^{-4}$	-7.7	
Birnessite	O	6.0(6)	1.91 (1.94)	$5.23\times10^{-3} \pm 1.92\times10^{-5}$	5.8	6.0
	Mn	6.0(6)	2.99 (2.95)	$4.90\times10^{-3} \pm 6.27\times10^{-5}$	5.8	
Birnessite-coated clay	O	6.0	1.91	$5.95\times10^{-3} \pm 8.01\times10^{-4}$	3.8	6.7
	Mn	6.0	3.00	$7.99\times10^{-3} \pm 5.18\times10^{-4}$	3.8	
HMO	O	3.5	1.89	$3.34\times10^{-3} \pm 1.90\times10^{-5}$	-4.7	8.6
	Mn	2.8	2.85	$5.13\times10^{-3} \pm 7.71\times10^{-5}$	-4.7	
HMO-coated clay	O	3.3	1.89	$2.23\times10^{-3} \pm 3.66\times10^{-5}$	-3.5	9.0
	Mn	3.1	2.85	$5.47\times10^{-3} \pm 1.02\times10^{-4}$	-3.5	
HMO-coated clay (aged 1 month)	O	3.9	1.89	$3.00\times10^{-3} \pm 3.99\times10^{-5}$	-5.2	9.4
	Mn	2.7	2.85	$4.47\times10^{-3} \pm 1.01\times10^{-4}$	-5.2	

$\chi(k) \cdot k^3$ Spectra Fourier Transformed over 2.20 to 11.88 Å^{-1} in k-space and Fitted over 0.50 to 3.10 Å. Number in parentheses corresponds to parameter determined from FEFF7 and XRD. N, R, and σ^2 represent the coordination number, distance, and variance. The quality of fits for N and R are ± 20% and ± 0.02, respectively. Errors on σ^2 are based on the statistical spread of the data.

Interestingly, the biogenic MnO_x produced from *Leptothrix discophora* SP-6 was observed to be amorphous consisting of 4.1 O atoms at 1.90 Å and 4.3 Mn atoms at 2.88 Å, consistent with HMO (Jürgensen et al. 2005). However, Kim et al. (2003) reported that its structure was similar to that of both chalcophanite and todorokite based on Raman spectra and XANES.

For birnessite and birnessite-coated clay, the coordination numbers in the first two shells were constrained given the monoclinic structure. The XAFS spectra (Figure 6.8) reveal that in the first shell 6 atoms of oxygen were observed at a distance 1.91 ± 0.02 Å, while in the second shell 6 atoms of manganese were located at 2.99 ± 0.02 Å (Table 6.2). These results are consistent with other studies (Friedl et al. 1997; McKeown and Post, 2001; Foster et al. 2003; Post and Bish, 1988) (Table 6.3). For example, Foster et al. (2003) fixed the coordination number for the first shell of 6 O atoms (resulting in an average distance of 1.91 Å) and found 5 Mn atoms at 2.87 Å. McKeown and Post (2001) constrained their fit with a Mn-Mn distance at 2.90 and 3.44 Å for second and third shells. As seen in Figure 6.8, the RSFs are potentially in agreement with edge-sharing Mn octahedral described by others (McKeown and Post, 2001; Pasten, 2002; Foster et al. 2003). On the other hand, Friedl et al. (1997) studied H^+-birnessite and observed 4.9 atoms of O in the first shell and 4.6 atoms of Mn in the second shell; parameters were neither fixed nor constrained, yet the ratio of first and second shell coordination numbers is equivalent to that for the actual structure. Furthermore, the ratio of coordination numbers of 1:1 for HMO is consistent with that for birnessite; therefore HMO may potentially be a precursor to birnessite.

Table 6.3 Structural Information of Mn Oxides: Tunneled and Layered Structures

Mineral	Crystal system	Space group	O		Mn		~ N_1: N_2	Ref
			N_1	R (Å)	N_2	R (Å)		
Layered								
HMO	-	-	3.6	1.89	3.1	2.86	1:1	Axe et al. 2000
Bacterial MnO_x	-	-	6.0	1.90	6.5	2.86	1:1	Pasten, 2002
δ-MnO_2[2]	hexagonal	-	6.0	1.90	4.9	2.88	1:1	Sung-Kim et al. 2003
Na-birnesssite[1]	monoclinic	$C2/m$	5.0	1.90	4.3	2.90	1:1	McKeow and Post 2001
H^+-birnessite	monoclinic	$C2/m$	4.9	1.91	4.6	2.87	1:1	Friedl et al. 1997
Chalcophanite[2]	trigonal-rhombohedral	$R\bar{3}$	6.0	1.91	5.2	2.81	1:1	Pasten, 2003
Lithiophorite	trigonal-hexagonal	$R\bar{3}m$	3.6	1.92	3.6	2.82	1:1	Manceau et al. 1988
Asbolane	hexagonal	-	3.0	1.92	3.6	2.81	1:1	Manceau et al. 1988
Romanechite	monoclinic	$C2/m$	4.2	1.90	4.6	2.87	1:1	Silverter et al. 1997
Tunneled								
Pyrolusite(β-MnO_2)	tetragonal	$P4/mnm$	6.0	1.88	2.0	2.87	3:1	Foster et al. 2003
Ramsdellite	orthorhombic	$Pbnm$	6.0	1.98	4.0	2.87	3:2	Wyckoff, 1963
Todorokite[2]	monoclinic	$P2/m$	6.0	1.90	4.0	2.90	3:2	Bystrom and Bystrom, 1950

[1] This fitting constrained the distance of Mn-Mn.

[2] The N in the first shell was fixed at 6 atoms.

[3] The crystallography axis (a, b, and c), crystal lattice (γ, β, and ϵ), and x, y, z coordination were shown in Appendix H.

6.2 Summary

The birnessite-coated clay resulted in a poorly crystalline oxide, where the clay substrate potentially inhibited crystallization of pyrolusite-coated clay. The short-range structure however for birnessite-coated clay was equivalent to that of the discrete birnessite. For both HMO- and birnessite-coated montmorillonite, the overall surface properties of the systems studied were consistent with their discrete oxides. Moreover, the XAS studies also suggest that the local structure of Mn in the HMO coating is similar to that in the discrete phase. Overall, results demonstrate that Mn oxides are important coatings that dominate the clay surface characteristics potentially having significant impact on metal sequestration.

CHAPTER 7

IMPACT OF MN OXIDE COATINGS ON ZN DISTRIBUTION

Macroscopic, spectroscopic, and kinetic experiments were employed to investigate the sorption behavior of Zn and the effect of montmorillonite as a substrate for the Mn oxide coating. Adsorption edges and isotherms were conducted to investigate the effect of pH, ionic strength, and surface loading. Concurrently, XAS studies were performed to evaluate the effect of these conditions along with contact time. Moreover, to better understand the slow sorption process, constant boundary condition (CBC) experiments were employed for HMO, HMO-coated clay, and montmorillonite at pH 7 to simulate the subsurface environment. Results from these studies provide a better understanding of zinc speciation and attenuation in the presence of Mn oxide and montmorillonite.

7.1 Macroscopic Adsorption Study

Adsorption edges (Figure 7.1) reveal the effect of ionic strength was clearly observed for adsorption to montmorillonite, suggesting outer-sphere complexes. Strawn and Sparks (1999) observed this type of complex when Pb sorbed to permanently charged ion exchange sites of montmorillonite. For HMO, ionic strength effects were only seen at a pH less than 4 and for a pH greater than 4, sorption may be dominated by inner-sphere complexes. Li et al. (2004) too observed similar edges at pH greater than 4. In isotherms at pH 5 and 6 (Figure 7.2), the linear relationship between the sorbed and bulk aqueous concentrations suggests that adsorption can be described with one average type of site. Given the limited solubility of Zn, the isotherm was not observed to plateau, indicating a

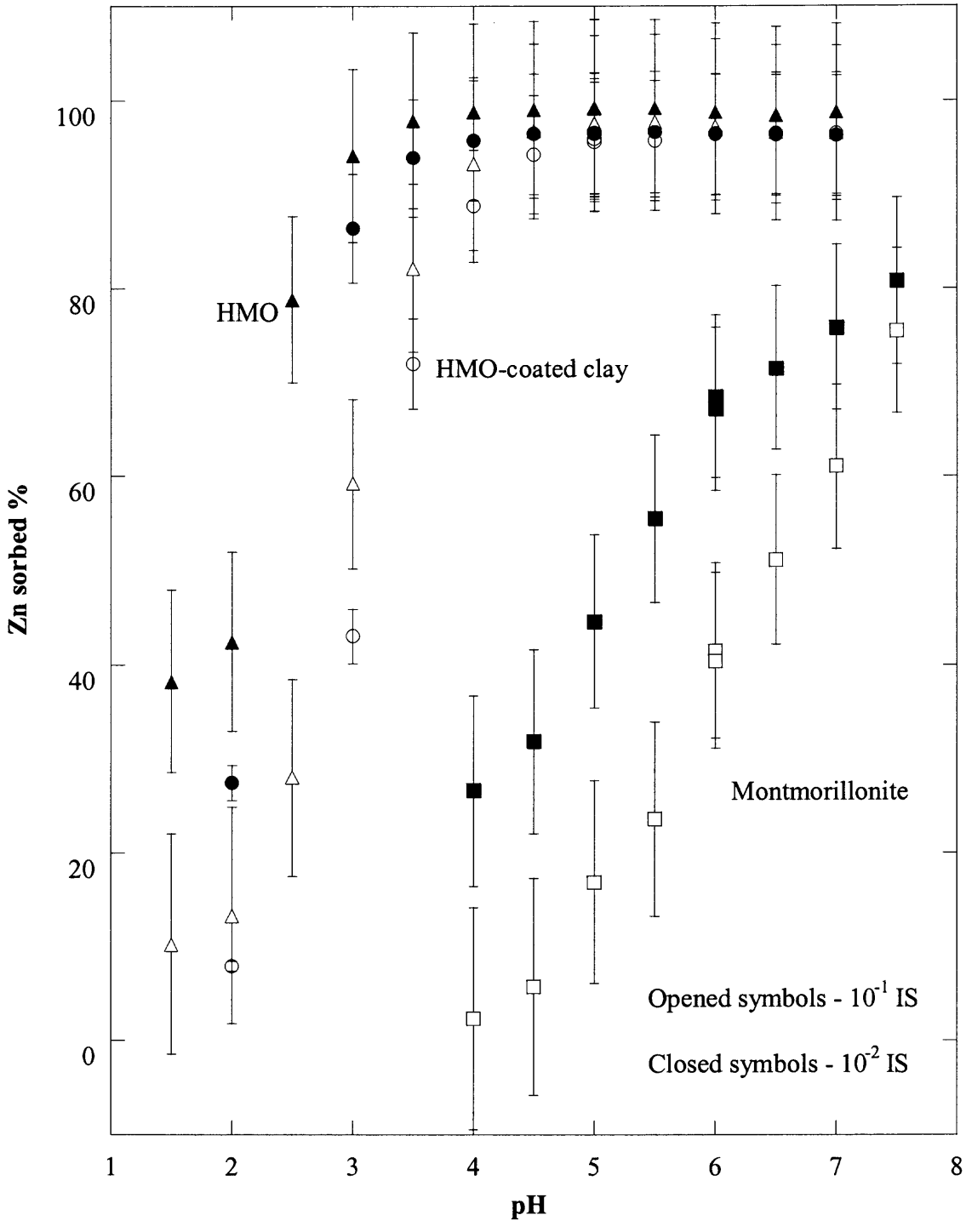

Figure 7.1 Zn adsorption edges of HMO, HMO-coated clay, and montmorillonite with 10^{-1} g sorbent L^{-1}, 10^{-9} M $[Zn]_o$, a $NaNO_3$ based electrolyte, and 25 °C.

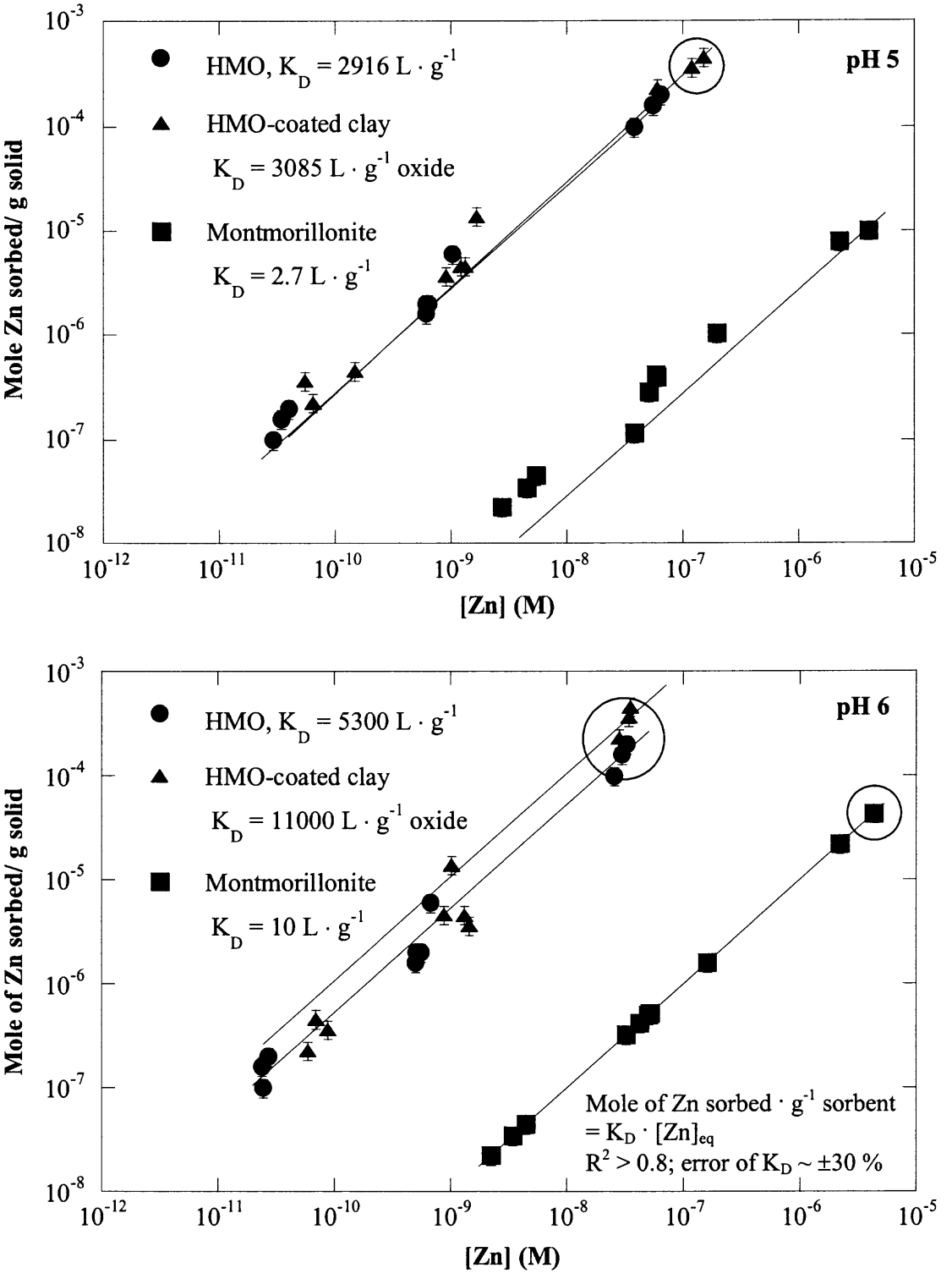

Figure 7.2 Zn adsorption isotherms for HMO, HMO-coated clay, and montmorillonite at pH 5 and 6, 1.5 × 10^{-2} ionic strength ($NaNO_3$), and 25°C. Adsorption to HMO-coated clay has been normalized to HMO present, showing the linear relationship. Circles identify XAS samples.

significant site capacity as reported by others (Kennedy et al. 2004; Tamura et al. 2003; Trivedi and Axe, 1999), ranging from 10^{-3} to 10^{-2} mole of metal ion · g^{-1}. Interestingly, normalizing the sorbed Zn on HMO-coated clay to the amount of oxide present as coating (~0.32 g Mn · g^{-1} clay (Boonfueng et al. 2005)) reveals similar sorption affinity to that of HMO. Nevertheless, the distribution coefficient (K_D) of coated systems increases as compared to discrete systems, suggesting that morphological changes may result in increased site capacity. These short-term studies suggest that Mn oxide is a dominant surface for sorption. In following section, the sorption configuration of Zn was investigated by using XAS.

7.2 XAS Analysis of Zn Sorption.

XAS data analysis followed standard procedures (Bunker and Sayers, 1988). An spline function was employed over the range 1.85 to 13.97 $Å^{-1}$ to convert the XAFS spectra to ($\chi(k)$), which were weighted by k^3 to enhance the higher k-space data. A Bessel window function was used in Fourier transforms to produce the radial structure function (RSF) over 2.21 to 10.00 $Å^{-1}$ for all standards and samples. RSFs were fit with the reference model chalcophanite, $ZnMn_3O_7 \cdot 3H_2O$ (Post and Appleman, 1988). The amplitude reduction factor (S_0^2) was fixed at 0.80 based on fitting the experimental ZnO spectra to get coordination number of Zn-O equivalent to 4. First, each shell was isolated and fit, and was proceeded by multiple shells fitting over a radial window of 0.50 to 3.70 Å.

XAS spectra of Zn sorbed onto montmorillonite were relatively similar to aqueous Zn^{2+} (Figure 7.3). The fitting revealed 4.0 to 6.0 atoms of oxygen at a distance of

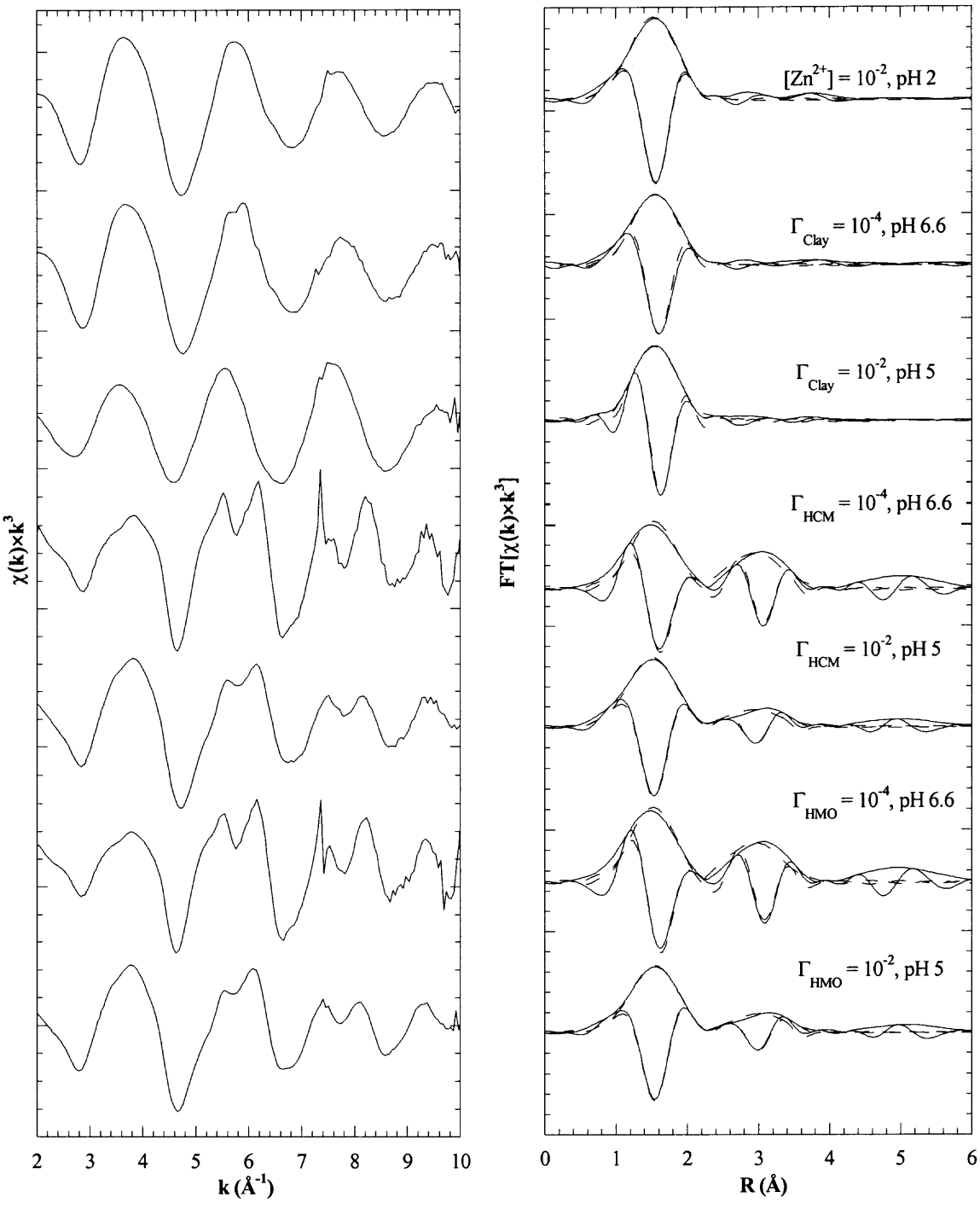

Figure 7.3 Zn K-edge $\chi(k) \cdot k^3$ spectra of Zn standard and Zn sorption samples as a function of surface loading (Γ_{solid} = mole of Zn $\cdot$ g^{-1} solid) collected at 25 °C along with Fourier transformed $\chi(k) \cdot k^3$ spectra over 2.20 to 10.00 $Å^{-1}$ and fitted over 0.50 to 3.70 Å. Solid lines represent the data and dashed lines are the fit. HCM represents HMO-coated clay.

2.06 ± 0.02 Å in the first shell (Table 7.1(A)), suggesting that upon adsorption Zn does not loose its waters of hydration. Moreover, a second shell was not observed, again consistent with outer-sphere complexation. In contrast to this work, Lee et al. (2004) observed that initially Zn formed surface precipitates on montmorillonite at pH 7, which transformed to a Zn-phyllosilicate-like phase after 20 days. Similar results were reported by Trainor et al. (2000), where Zn formed a mixed–metal Zn(II)-Al(III) coprecipitate with a hydrocalcite-type structure between pH 7 and 8.2. In this study, surface precipitation was not observed for pH less than 7.

Comparing spectra for Zn sorbed on HMO-coated clay to HMO, similar envelopes are seen (Figure 7.3). The first shell was fit well with oxygen and second shell contributions were attempted with Si, Al, Zn, and O as well as combinations of these through a principle component analysis, but fitting was only accomplished with Mn. The amplitude of the second shell in lower surface loadings (10^{-4} mol of Zn · g of sorbent^{-1}) was greater than that of higher loadings (10^{-2} mol of Zn · g of sorbent^{-1}) (Figure 7.3) and may be a result of a greater degree of disorder (σ^2) for the latter which would suppress the amplitude of the second shell. Moreover, linear combination (LC) fitting based on principle component analysis involved using back Fourier transformed data of Zn sorbed to HMO and montmorillonite at the same condition and resulted in a 95 ± 10 % contribution from sorption to HMO (Figure 7.4). The montmorillonite substrate potentially increases the site density of the system; furthermore, it may contribute to morphological changes in the HMO coating compared to the discrete mineral form. XAS spectra of Zn sorbed onto HMO-coated clay at pH 5 revealed that the sorption configuration was invariant as a function of surface loading and ionic strength, 10^{-1}

Table 7.1 XAS Fitting Results of Zn Sorption Samples at Zn K-Edge

	O			Mn			ΔE_o	%Res
	N_1	R (Å)	σ^2 (Å^2)	N_2	R (Å)	σ^2 (Å^2)	(eV)	
(A) Zn sorption as a function of sorbent and loading								
$Zn(NO_3)_{2\,(aq)}$	5.7	2.06	0.0136	-	-	-	-1.64	7.3
$\Gamma_{Clay} = 10^{-4}$ pH 6.6, IS 10^{-2}	6.0	2.05	0.0053	-	-	-	-1.12	11.5
$\Gamma_{Clay} = 10^{-2}$ pH 5, IS 10^{-2}	4.0	2.06	0.0008	-	-	-	-7.60	9.6
$\Gamma_{HMO} = 10^{-4}$ pH 6.6, IS 10^{-2}	6.9	2.05	0.0091	4.6	3.45	0.0069	-4.10	16.6
$\Gamma_{HMO} = 10^{-2}$ pH 5, IS 10^{-2}	6.6	2.06	0.0135	2.5	3.50	0.0099	0.57	8.8
$\Gamma_{HCM} = 10^{-4}$ pH 6.6, IS 10^{-2}	6.6	2.05	0.0093	3.9	3.45	0.0058	-3.48	16.6
$\Gamma_{HCM} = 10^{-2}$ pH 5, IS 10^{-2}	7.7	2.04	0.0147	2.4	3.45	0.0109	-1.83	10.9
(B) Zn sorbed on HMO-coated clay as a function of pH, loading, and ionic strength								
$\Gamma_{HCM} = 10^{-2}$ pH 6, IS 10^{-2}	7.6	2.01	0.0150	1.2	3.40	0.0079	-3.22	12.8
$\Gamma_{HCM} = 10^{-3}$ pH 5, IS 10^{-2}	6.8	2.08	0.0130	3.2	3.50	0.0111	0.17	8.8
$\Gamma_{HCM} = 10^{-2}$ pH 5, IS 10^{-1}	7.7	2.06	0.0152	2.6	3.48	0.0110	-1.19	10.9
(C) Zn sorbed on HMO-coated clay as a function of contact time								
$\Gamma_{HCM} = 10^{-3}$ pH 7, IS 10^{-2}	7.5	2.01	0.0152	1.4	3.45	0.0025	-6.24	9.5
$\Gamma_{HCM} = 10^{-3}$ pH 7, IS 10^{-2} (CBC 1 month)	5.5	2.03	0.0098	4.1	3.43	0.0134	-0.71	11.2
$\Gamma_{HCM} = 1.5\times10^{-3}$ pH 7, IS 10^{-2} (CBC 4 month)	5.0	2.04	0.0095	4.5	3.43	0.0151	0.81	10.0

Zn K-Edge $\chi(k) \cdot k^3$ spectra were Fourier transformed over 2.21 to 10.00 Å^{-1} in k-space and fitted over 0.50 to 3.70 Å in r-space. Γ is surface loading (Γ_{solid} = mole of Zn $\cdot$ g^{-1} solid). N, R, and σ^2 represent the coordination number, distance, and variance. The quality of fits for N_1, N_2, R, and σ^2 are ± 20%, ± 40%, ± 0.02, and ± 5%, respectively.

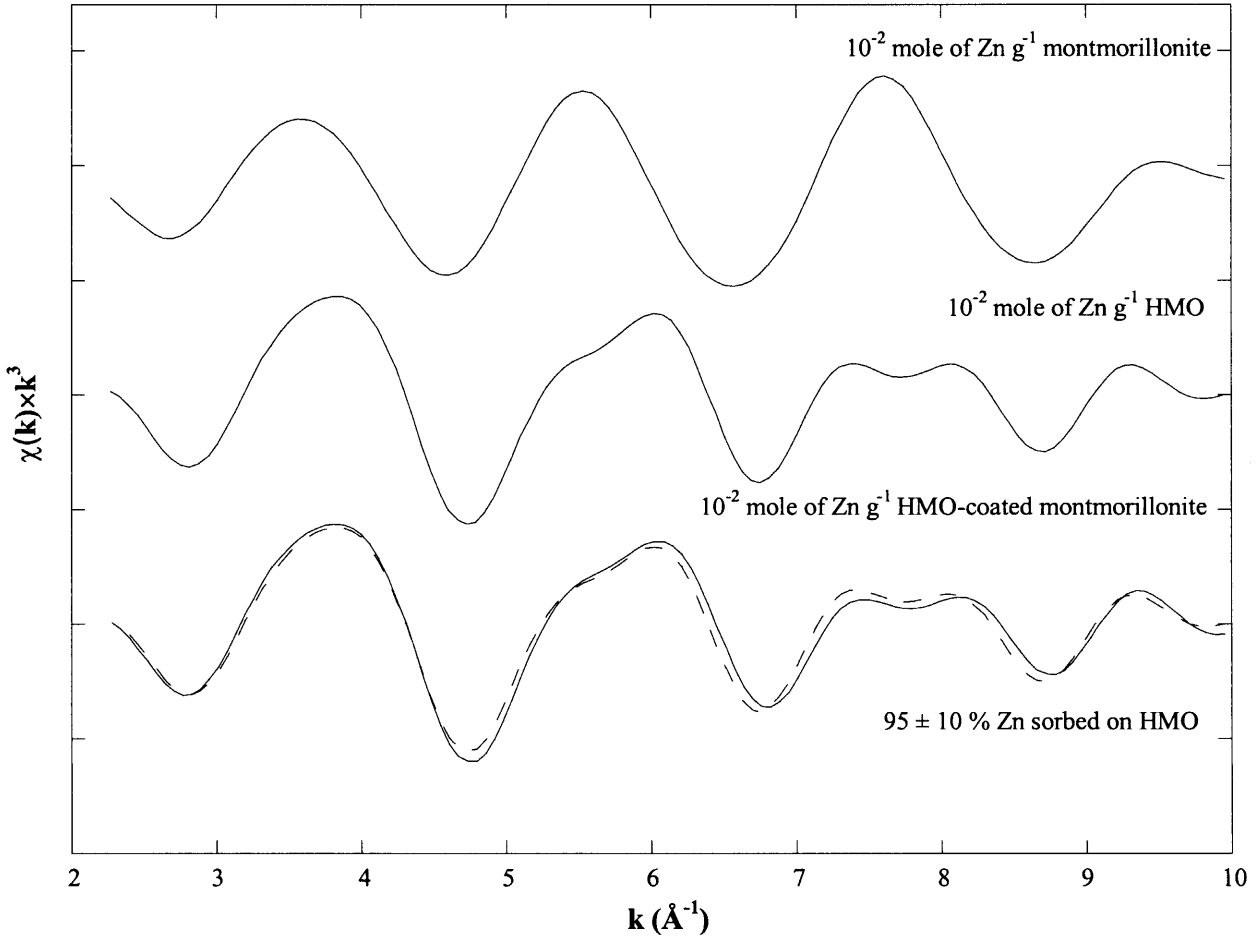

Figure 7.4 Inverse Fourier Transform of the Zn sorption samples as a function of sorbent (Γ_{solid} = 10^{-2} mole of Zn · g^{-1} solid) at pH 5 and 10^{-2} ionic strength ($NaNO_3$). Solid lines represent the data and dashed line is the LC fit of HMO-coated clay with 95 ± 10 % from Zn sorbed on HMO.

and 10^{-2} ($NaNO_3$) (Figure 7.5 and Table 7.1(B)). An average of the fitting showed a first shell of 7.3 ± 0.9 atoms of oxygen at a distance of 2.06 ± 0.02 Å, while in the second shell 3.2 ± 1.2 atoms of manganese were found at 3.47 ± 0.02 Å. Interestingly, these bond distances are relatively similar to Zn sorbed on birnessite (Manceau et al. 2002), suggesting octahedral coordination and tridentate cornering sharing complexes when sorbed on HMO and HMO-coated clay (Figure 7.5). Trivedi et al. (2001) observed approximately 7 oxygen atoms in the first shell and 8 atoms of oxygen in the second shell, concluding that the Zn ion retained its primary hydration shell. In our study, while the first shell structure was equivalent to that modeled by Trivedi et al. Fourier transforms were applied over 2.21 to 10.00 $Å^{-1}$ where Trivedi et al. used 2.4 to 9.4 $Å^{-1}$. Because of the increased k-space, second shell contributions have been refined.

For loadings greater than 10^{-4} mole of Zn · g^{-1} sorbent, as pH increased from 5 to 7, the first shell distance decreased potentially due to an increase in electrostatic interactions between Zn ions and the surface (Figures 7.6, 7.7 and Table 7.1). The effect of loading was not clearly observed in this study; however, Manceau et al. (2002) found that Zn sorbed as tridentate complexes on birnessite with tetrahedral coordination at low surface coverage (~8.0×10^{-3} mole of Zn · mole of Mn) and octahedral coordination at high surface coverage (>6.9×10^{-2} mole of Zn · mole of Mn). Nevertheless, our work is consistent with these results where we have seen octahedral coordination as was reported for the higher surface coverage. In addition to evaluating adsorption mechanisms in batch studies, CBC studies were included to evaluate the slow sorption process.

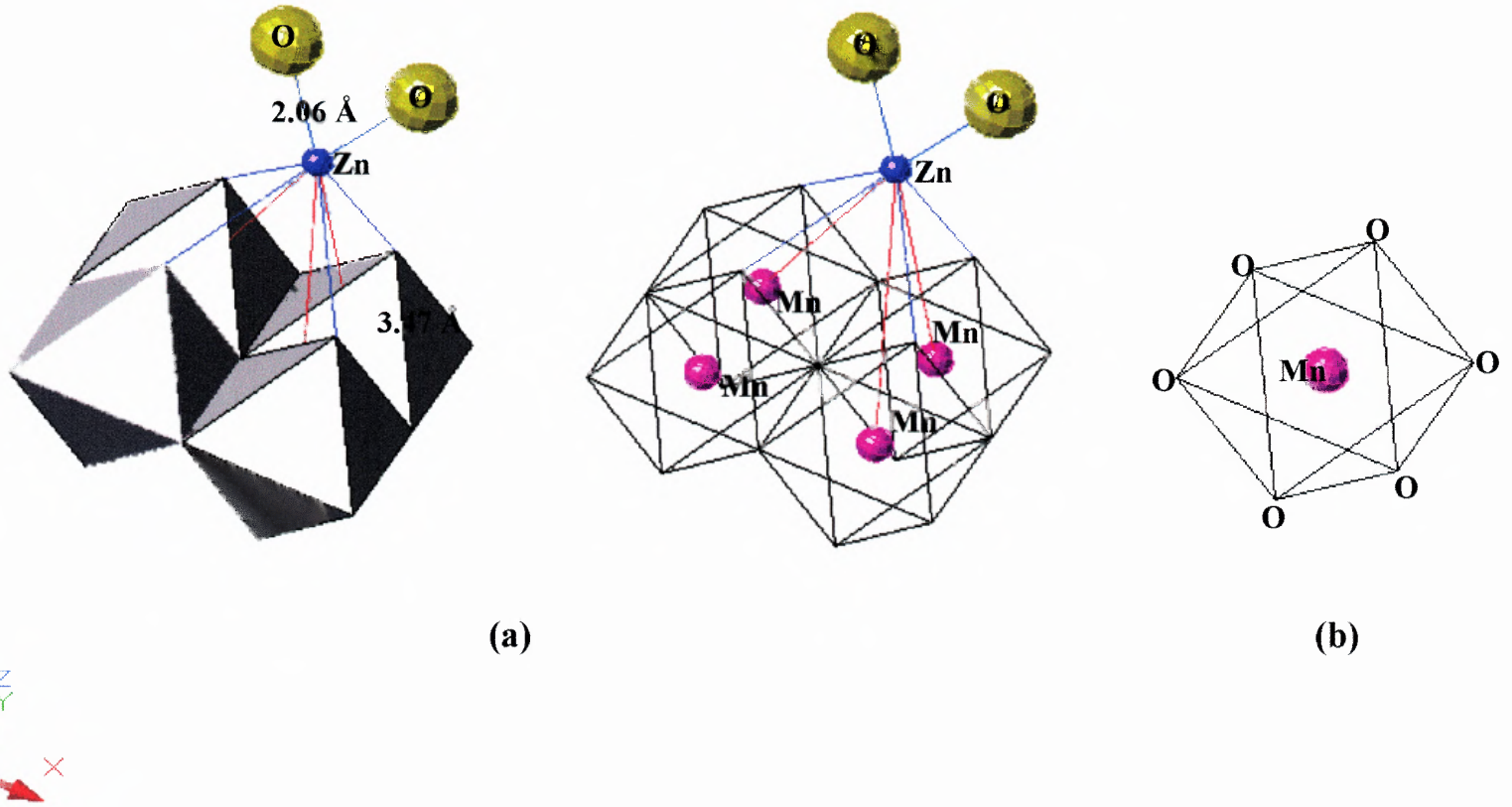

Figure 7.5 Proposed Zn sorption configuration on hydrous manganese oxide (HMO) shows (a) tridentate corner-sharing octahedral coordination, and (b) the unit cell of HMO structure.

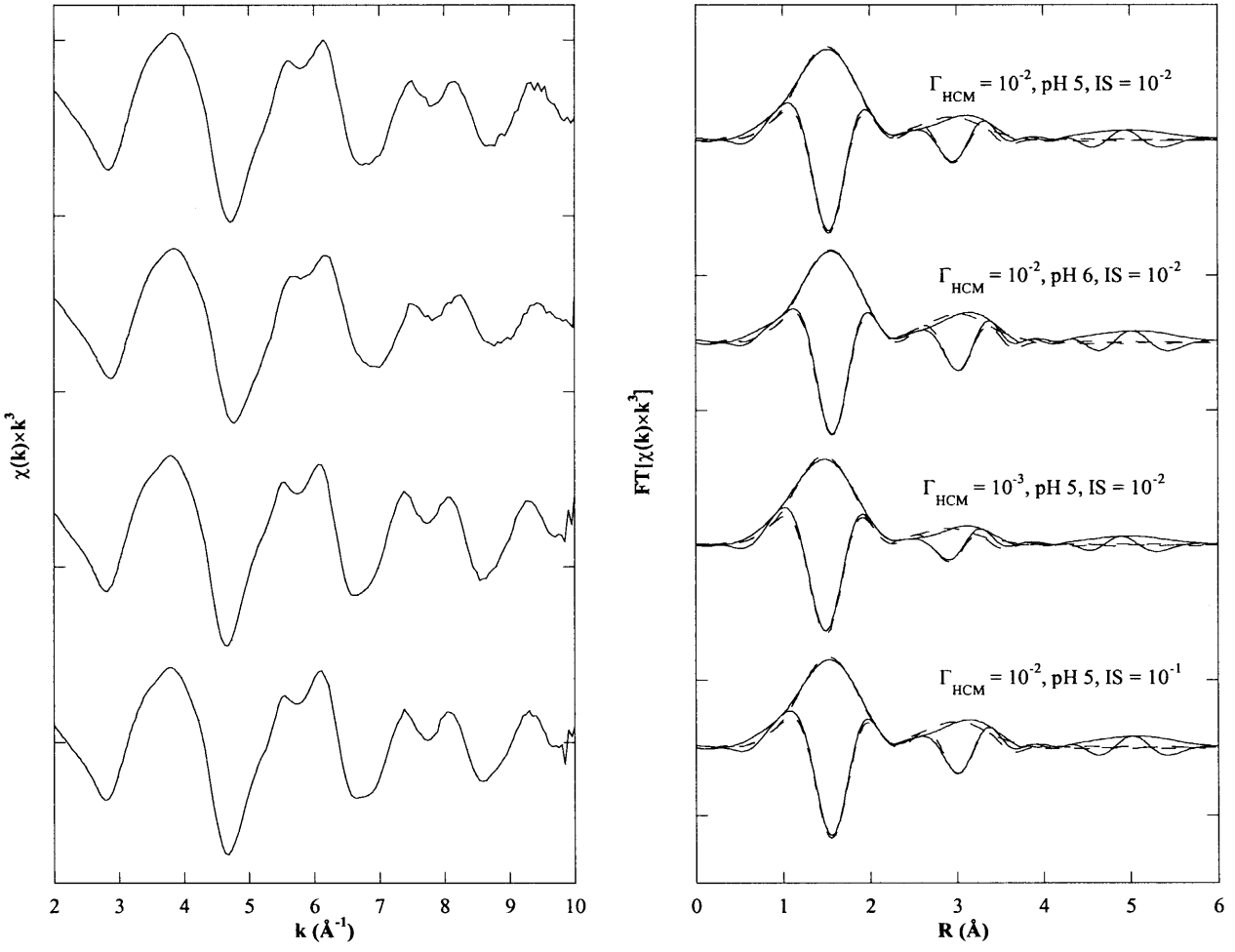

Figure 7.6 Zn K-edge $\chi(k) \cdot k^3$ spectra of Zn sorption on HMO-coated clay as a function of pH, surface loading, and ionic strength collected at 25 °C along with Fourier transformed $\chi(k) \cdot k^3$ spectra over 2.20 to 10.00 $Å^{-1}$ and fitted over 0.50 to 3.70 Å. Solid lines represent the data and dashed lines are the fit.

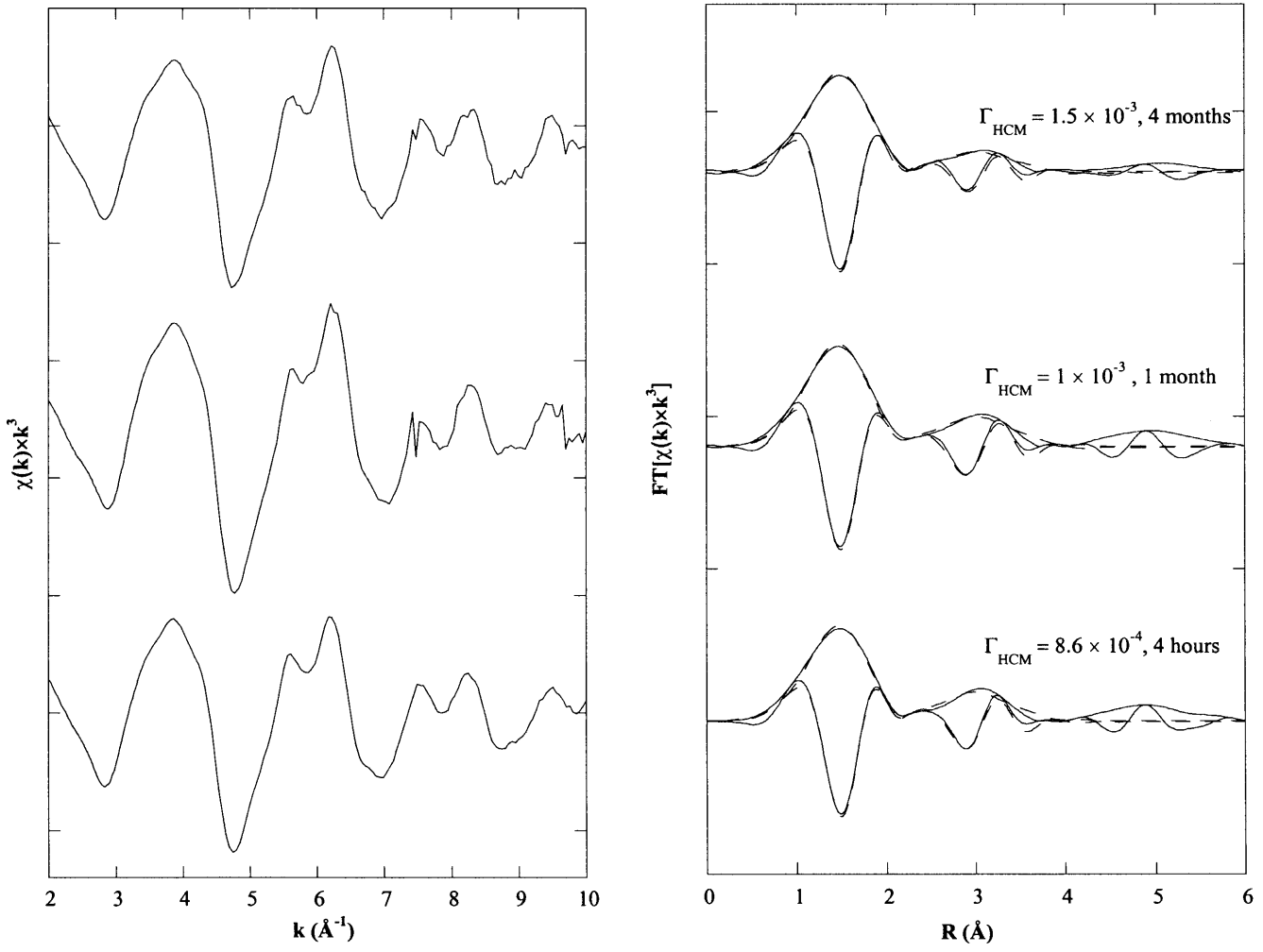

Figure 7.7 Zn K-edge $\chi(k) \cdot k^3$ spectra of HMO-coated clay as a function of contact time at pH 7, 1.5×10^{-2} ionic strength ($NaNO_3$) were collected at 25 °C and Fourier transformed over 2.21 to 10.00 $Å^{-1}$ and fitted over 0.50 to 3.70 Å.

7.3 Intraparticle Surface Diffusion of Zn

In the alternative CBC studies, slow sorption was observed for all systems (Figure 7.8). Because the oxide, oxide-coated clay, and montmorillonite exhibit microporous structures, the sorption process may be described as a slow intraparticle diffusion. Initially the amount of Zn sorbed corresponds to the isotherm results for that sorbed to the external surface. Subsequently, the amount of Zn sorbed to the oxide gradually increased due to intraparticle surface diffusion. In modeling, the assumption that internal sites are no different than external ones has been validated recently in spectroscopic results for metals ions such as Sr sorbed to hydrous iron and manganese oxide (Axe et al. 1998; 2000). In this research, the local coordination of Zn sorbed to HMO-coated clay from a 4-month CBC study (where an additional 60% of the sites became occupied as compared to 4 hr contact time) (Figure 7.7 and Table 7.1(C)) revealed that as surface loadings increased from 8.66×10^{-4} to 1.48×10^{-3} mol of Zn · g of HMO-coated clay^{-1}, the bond distances of Zn-O and Zn-Mn averaged 2.03 Å and 3.43 Å, which are consistent with octahedral tridentate corner sharing complexes (Manceau et al. 2002). Specifically, the Zn structure consisted of 7.3 ± 1.5 atoms of oxygen in the first shell and 4.0 ± 0.6 atoms of manganese in the second. Furthermore, there was no evidence of surface precipitation or solid solution formation as only Mn provided a good fit in the second shell.

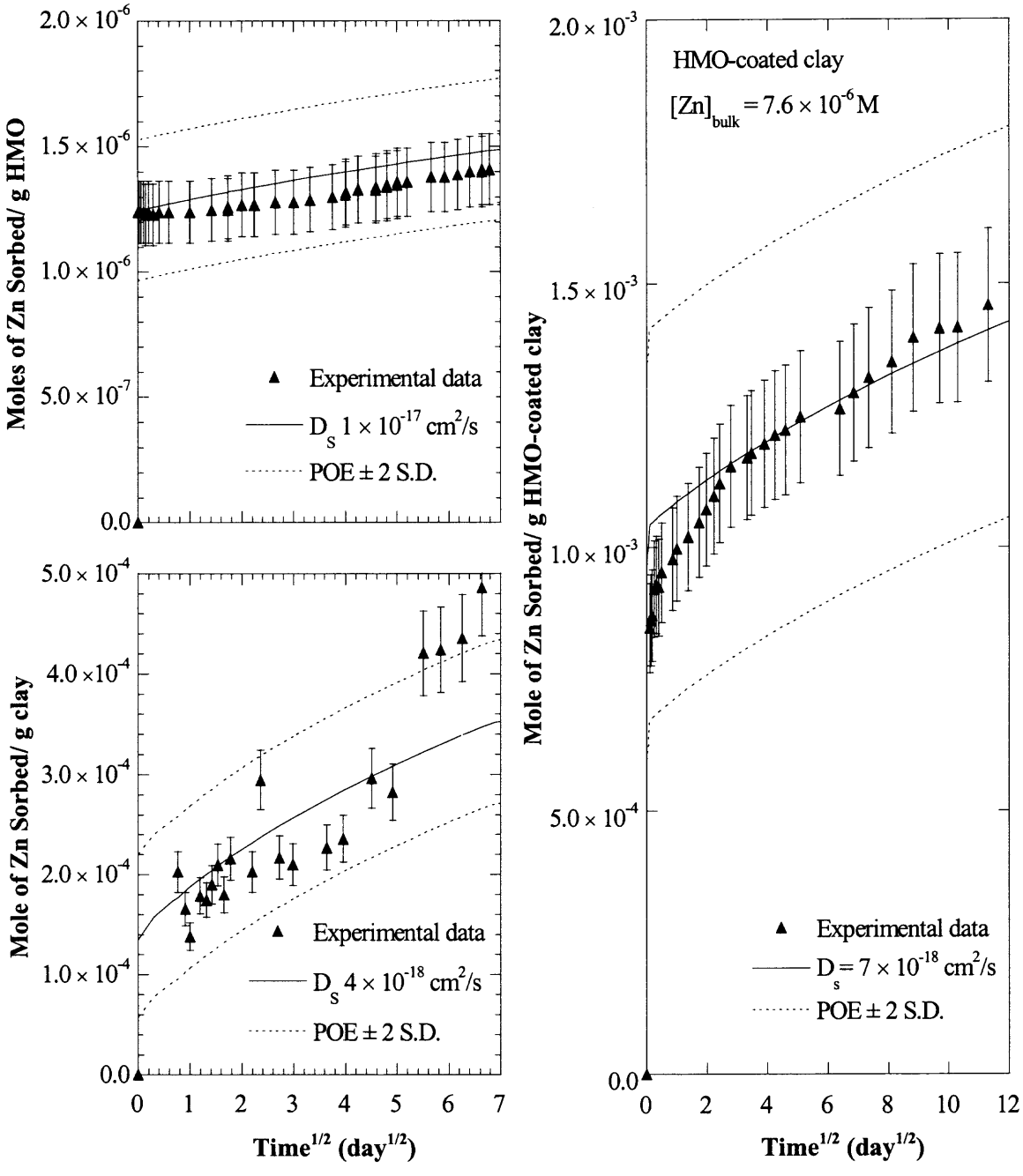

Figure 7.8 CBC studies of Zn sorption to 10^{-1} g/L HMO, HMO-coated clay, and clay at 25°C, 1.5 × 10^{-2} ionic strength with $NaNO_3$, pH 7, and a $[Zn]_{bulk}$ of 7.6 × 10^{-6} M for HMO-coated clay, 1.3 × 10^{-9} M for HMO, and 8.7 × 10^{-5} M for clay.

In modeling the slow sorption process of intraparticle surface diffusion along micropores, the analytical solution to the mass balance (see e.g., Axe and Trivedi, 2002, Axe and Anderson, 1995) given the CBC (as well as the initial condition that contaminant was not present initially [t=0]) was integrated over the volume of the particle. Minimizing the variance between experimental data and modeling results, the only fitting parameter is surface diffusivity. Errors associated with the model from the propagation of errors (POE) method (Ku et al. 1966) are also shown. The POE analysis accounts for the standard deviation in the number of particles as well as the error in the distribution coefficient describing the mass adsorbed to the surface. All data fall within two standard deviations of the model. However, from the CBC study of Zn sorption to montmorillonite (Figure 7.8), a potential change was observed after 25 days contact time. The shift in the amount sorbed may reflect analytical and modeling errors or may be indicative of a change in the sorption mechanism, as Lee et al. (2004) observed neoformation of a Zn phyllosilicate phase at the montmorillonite surface after aging 20 days.

Studies with Zn sorption to HMO, HMO-coated montmorillonite, and montmorillonite demonstrate that surface diffusivities (D_S) range from 10^{-18} to 10^{-17} cm^2/s. The D_S of HMO-coated clay was 7×10^{-18} cm^2/s, which falls between that for montmorillonite and HMO. These results indicate that the microporosity of HMO-coated clay has contributions from both the HMO and montmorillonite surfaces. Furthermore, even though much of the clay surface is coated with HMO (~90%) based on earlier characterization studies (Boonfueng et al. 2005); the oxide morphology is potentially different from discrete ones. We speculate that clay particles serve as a template for Mn

oxide when nucleation occurred; potentially changing the porosity, pore size distribution, and particle size of oxide coating. Therefore, the oxide-coated clay may exhibit unique characteristics from the discrete oxide.

7.4 Summary

Macroscopic studies showed that the affinity and capacity of the HMO coating was greater than that of montmorillonite, and when normalized to the oxide present, the coatings behaved similarly to the discrete oxide. A linear relationship was observed for the isotherms at pH 5 and 6. Moreover, XAS resulted in one type of sorption configuration as a function of loading and ionic strength at pH 5. Zn ions appear to associate with the Mn oxide phase where inner-sphere complexes dominate the sorption process, forming tridentate corner-sharing structures. After a contact time of 4 months where an additional 60% of the sites become occupied, the slower sorption process was modeled as intraparticle surface diffusion. Best fit diffusivities ranged from 10^{-18} to 10^{-17} cm^2/s, where a slower process was observed for the coated surface as compared to the discrete oxide. Interestingly, the porosity of the Mn oxide coating appears to be influenced by the substrate during its growth, as its increase and shift to a smaller pore size distribution resulted in a diffusivity between that observed for discrete HMO and montmorillonite.

CHAPTER 8

NICKEL AND LEAD SEQUESTRATION IN MANGANESE OXIDE –COATED MONTMORILLONITE

In this chapter, nickel and lead sorption mechanisms to discrete HMO and HMO-coated montmorillonite are discussed based on macroscopic and spectroscopic studies. The systematic sorption experiments were performed as a function of adsorbate concentration, pH, ionic strength, and contact time. Moreover, constant boundary condition (CBC) studies provided an approach to observe the slow sorption process of Ni and Pb to HMO, HMO-coated montmorillonite, and montmorillonite. These studies provide insight on Ni and Pb sequestration in a heterogeneous system representative of the subsurface, Mn oxide-coated montmorillonite.

8.1. Effect of Coating in Macroscopic Studies

Adsorption edges (Figure 8.1) show the affinity of HMO-coated montmorillonite for Ni and Pb was much greater than that of montmorillonite. The effect of ionic strength was clearly observed for both Ni and Pb sorbed on montmorillonite, suggesting electrostatic interactions between metal ions with the negatively charged surface. Similarly, Strawn and Sparks (1999) and Abollino et al. (2003) observed that Pb sorbed on permanently charged ion exchange sites of montmorillonite, forming an outer-sphere complex. For HMO and HMO-coated montmorillonite, the ionic strength effects were only seen at a pH less than 4 and became insignificant at pH greater than 4 over which inner-sphere complexes may dominate; we observed a similar effect in the earlier work with Zn. Matocha et al. (2001) did not observe any ionic strength effects when Pb sorbed on

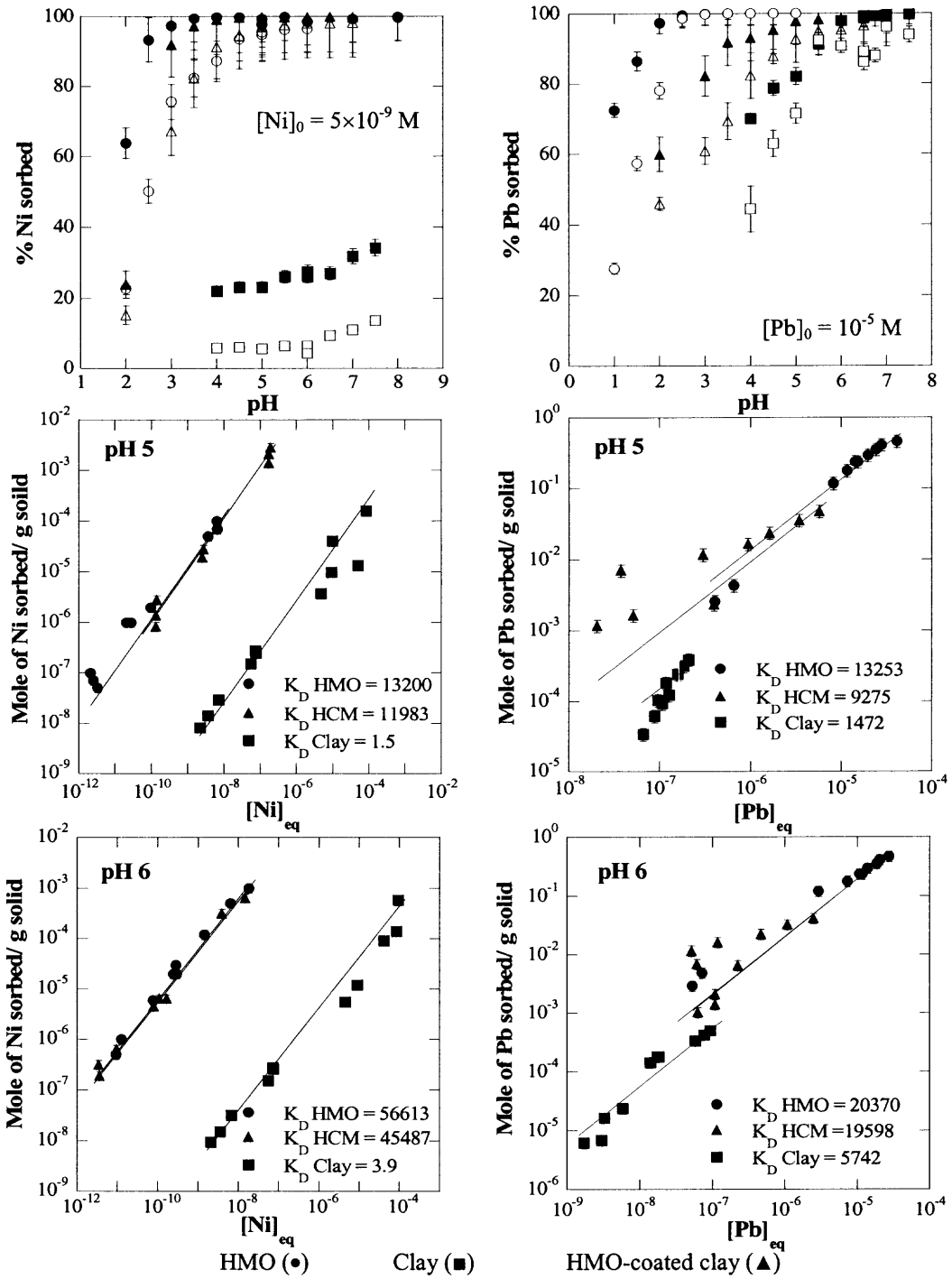

Figure 8.1 Pb and Ni adsorption edges with 10^{-1} g sorbent/L at an ionic strength (IS) 1.5 × 10^{-2} ($NaNO_3$) (open symbol) and 1.5 × 10^{-1} ($NaNO_3$) (closed symbol). Isotherms were conducted at pH 5 and 6, 1.5 × 10^{-2} IS ($NaNO_3$), and 25°C. Adsorption to HMO-coated montmorillonite (HCM) has been normalized to HMO present, showing the linear relationship.

birnessite or manganite. Adsorption isotherms were normalized to the solids concentration instead of surface area which is measured on freeze-dried oxides and may not accurately reflect the surface area in the aqueous phase. In isotherms, a linear relationship between sorbed and bulk aqueous concentrations (Figure 8.1) suggests that sorption can be potentially characterized with one average type of site. The distribution coefficient (K_D), the ratio of the contaminant sorbed to that in the bulk aqueous phase, was observed to be linear, as $n \approx 1$ in the following relationship: $q = K \cdot C^n$ for $n = 1$ $K=K_D$ (Sposito, 1984). Given the limited solubility of Ni and Pb, the isotherms do not plateau; others (Trivedi and Axe, 1999; Balistrieri and Murray, 1987; Tamura et al. 1997; Kennedy et al. 2004) have reported the site capacity to range from 10^{-3} to 10^{-2} mole of metal ion g^{-1} for HMO. Interestingly, normalizing the sorbed Ni and Pb on HMO-coated montmorillonite with the amount of oxide present in the coating (~0.32 g Mn $\cdot$ g^{-1} clay) reveals a similar affinity to that of HMO. Because isotherm studies for Ni were conducted from 10^{-12} to 10^{-8} M, the relationship may reflect the effect of higher affinity sites (Dzombak and Morel, 1990), while in Pb studies concentrations ranged from 10^{-8} to 10^{-4} M, potentially reflecting the lower affinity sites for sorption. Therefore, at pH 6, the K_D for Ni sorbed on HMO and HMO-coated montmorillonite is comparable to that for Pb studies. To elucidate the sorption mechanisms, spectroscopic studies are discussed in the following section.

8.2. Spectroscopic Studies of Pb and Ni Sorbed onto Coating

The XAS spectra were analyzed using WinXAS (Version 2.3) (Ressler, 1998) following standard procedures (Bunker and Sayers, 1988). For XANES analysis, background X-ray absorbance was subtracted by fitting a linear polynomial through the pre-edge region, and the edge jump of a background-corrected spectrum was normalized with a zero order polynomial over 100 to 200 eV above the edge, E_o, energy. The threshold energy (E_o) was determined from the first inflection point in the edge region. For X-ray absorption fine structure (XAFS) analysis, an advanced spline function was employed to subtract the isolated atomic absorption over the range 2.32 to 11.56 $Å^{-1}$ for Pb and 2.38 to 12.00 $Å^{-1}$ for Ni and convert the XAFS spectra to ($\chi(k)$), which were weighted by k^3 to enhance the higher k-space data. A Bessel window function was used in Fourier transforms to produce the radial structure function (RSF). The fitting results of Ni and Pb standards are shown in Table 8.1. The radial structure functions for sorption samples were fit with the reference model quenselite ($PbMnO_2OH$) (Wyckoff, 1988) and Ni substituted chalcophanite ($NiMn_3O_7 \cdot 3H_2O$), generated using FEFF7 (Zabinsky et al. 1995). The amplitude reduction factors (S_0^2), which accounts for energy loss due to multiple electron excitations were fixed at 0.96 and 0.72 based on fitting the experimental NiO and PbO spectra, respectively, with their known coordination numbers in Table 8.1.

8.2.1 Pb Sorption

The comparison between the XANES spectra of Pb^{2+} sorption samples with reference compounds and aqueous Pb^{2+} spectra (Figure 8.2) reveals unique coordination environments. For example, the XANES spectra for $PbO_{(S)}$ shows a small shoulder at

Table 8.1 XAS Fitting Results of Pb and Ni Standards at Pb L_{III}-Edge and Ni K-Edge

	First shell of O			Second shell of Ni			ΔE_o	%Res
	CN	R	σ^2	CN	R	σ^2	(eV)	
NiO	6.0 (6)	2.03	0.005	12 (12)	2.90	0.004	-1.0	8.9
$NiCO_3$	6.0 (6)	2.03	0.015	5.0 (6)	3.54	0.011	-2.0	7.5
	First shell of O			Second shell of Pb			ΔE_o	%Res
	CN	R	σ^2	CN	R	σ^2	(eV)	
PbO	4.0 (4)	2.23	0.006	1.5 (4)	3.53	0.005	-2.5	12.2
$PbCO_3$	11 (9)	2.61	0.013	8.0 (12)	4.15	0.009	-10.5	15.5

N, R, and σ^2 represent the coordination number, distance, and variance. The quality of fits for N_1, N_2, R, and σ^2 are ± 20%, ± 40%, ± 0.05, and ± 5%, respectively.
Number in parentheses correspond to parameters based on the power diffraction data, NiO (Wyckoff, 1988), $NiCO_3$ (Pertlik, 1986), PbO (Hill, 1985), and $PbCO_3$ (Sahl, 1974).

13.055 to 13.065 keV with one broad peak at approximately 13.120 keV, while $PbCO_{3(S)}$ exhibits one intense peak at 13.067 keV and two broad peaks from 13.080 to 13.115 keV. The spectra for Pb sorbed on HMO-coated montmorillonite were similar to that of HMO. XAS spectra of Pb sorbed onto montmorillonite were similar to that of hydrated Pb^{2+} with 7 ± 1.5 atoms of O at 2.47 ± 0.05 Å (Figure 8.3 and Table 8.2). Adsorption is dominated by outer-sphere complexation, again consistent with Strawn and Sparks (1999) where Pb sorption to montmorillonite was studied at pH 5.83.

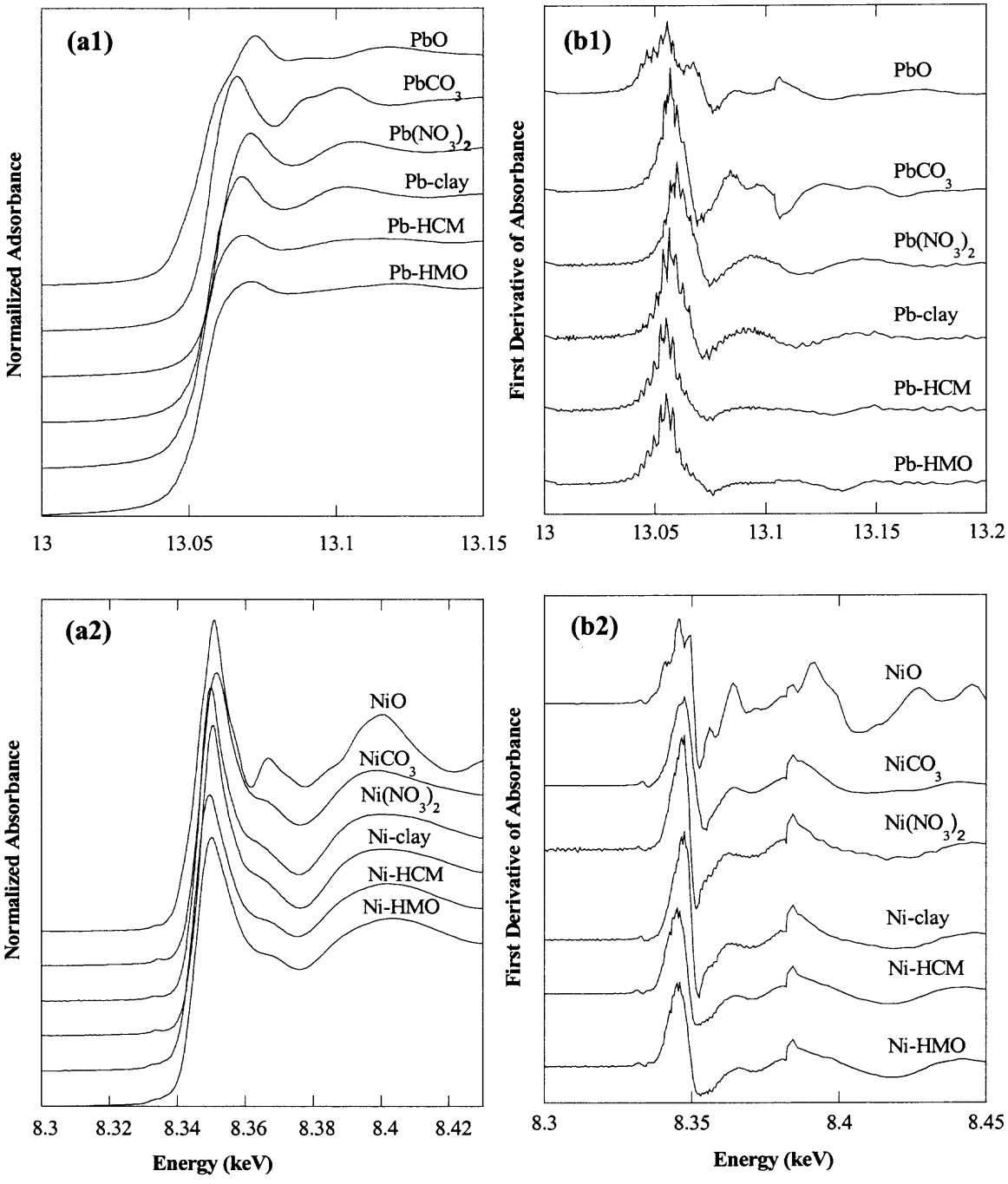

Figure 8.2 Pb L_{III}-edge and Ni K-edge XANES spectra of all standards and samples after the background removal and normalization with a zero order polynomial over 100 to 200 eV above the edge(a1-a2) averaged Pb and Ni XANES spectra and (b1-b2) the first derivative of a single Pb and Ni XANES spectrum.

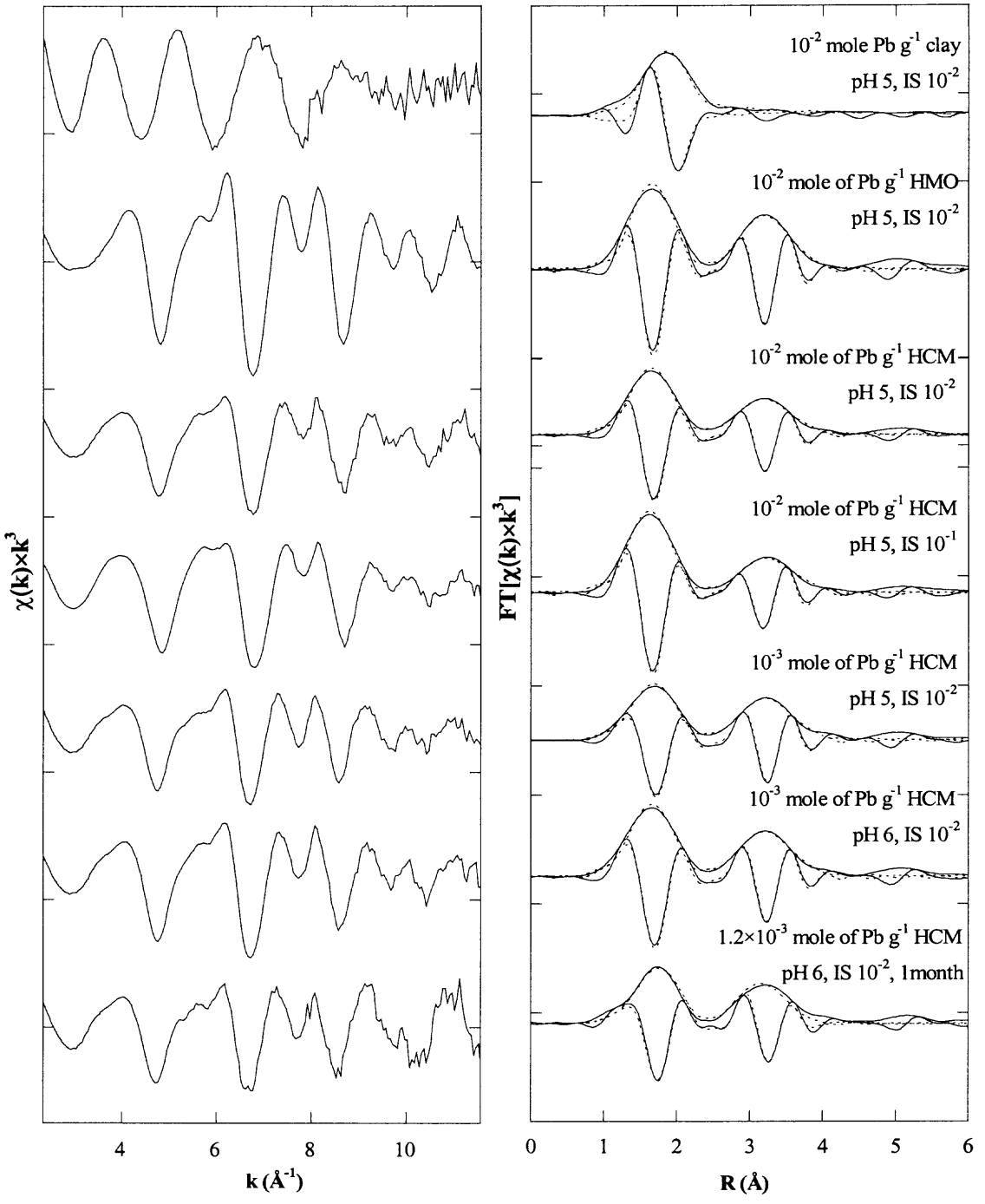

Figure 8.3 Pb L_{III}-edge $\chi(k) \cdot k^3$ spectra of standards and sorption samples collected at 25 °C along with Fourier transformed $\chi(k) \cdot k^3$ spectra over 2.32 to 11.56 $Å^{-1}$ and fitted over 0.75 to 4.60 Å. Solid lines represent the data and dashed lines are the fit. HCM represents HMO-coated montmorillonite.

Table 8.2 XAS Fitting Results of Pb Sorption Samples at Pb L_{III} Edge

	O			Mn			ΔE_o	%Res
	N	R (Å)	σ (Å^2)	N	R (Å)	σ (Å^2)	(eV)	
$Pb(NO_3)_{2(aq)} = 10^{-2}$ M pH 2	6.2	2.49	0.019	-	-	-	-7.9	5.7
$\Gamma_{Clay} = 10^{-2}$, pH 5, IS 10^{-2}	7.0	2.47	0.007	-	-	-	-6.1	8.7
$\Gamma_{HMO} = 10^{-2}$, pH 5, IS 10^{-2}	2.7	2.29	0.002	2.7	3.53	0.007	-14.3	10.4
$\Gamma_{HCM} = 10^{-2}$, pH 5, IS 10^{-2}	2.4	2.30	0.002	1.0	3.56	0.006	-17.4	10.5
$\Gamma_{HCM} = 10^{-2}$, pH 5, IS 10^{-1}	2.8	2.29	0.003	1.0	3.54	0.006	-16.7	11.7
$\Gamma_{HCM} = 10^{-3}$, pH 5, IS 10^{-2}	2.8	2.29	0.004	1.6	3.56	0.007	-16.8	10.2
$\Gamma_{HCM} = 4.9\times10^{-4}$, pH 6, IS 10^{-2}	3.0	2.30	0.003	1.7	3.56	0.007	-16.3	10.4
$\Gamma_{HCM} = 5.4\times10^{-4}$, pH 6, IS 10^{-2} (CBC 1 month)	2.2	2.29	0.004	1.6	3.55	0.005	-11.2	14.2

Pb L_{III}-edge $\chi(k) \cdot k^3$ spectra were Fourier transformed over 2.32 to 11.56 Å^{-1} in k-space and fitted over 0.75 to 4.60 Å in r-space. Γ is surface loading (Γ_{solid} = mole of Pb $\cdot$ g^{-1} solid). N, R, and σ^2 represent the coordination number, distance, and variance. The quality of fits for N_1, N_2, R, and σ^2 are ± 20%, ± 40%, ± 0.05, and ± 5%, respectively. The amplitude reduction factor (S_o^2) was fixed at 0.72.

For Mn oxide surfaces, XAS spectra of Pb sorbed on HMO-coated montmorillonite was consistent with that of discrete HMO, revealing two backscattering envelopes. For the first shell, approximately two to three atoms of O were observed at an average distance of 2.30 ± 0.05 Å and is in agreement with that reported for sorption to biogenic Mn oxide (Villalobos et al. 2005), manganite (Matocha et al. 2001), and birnessite (Manceau et al. 2002). The fitting results of the first shell suggest that Pb(II) forms highly distorted trigonal pyramid coordination by hydroxide or oxygen atoms and lone-pair electrons which occupy the pyramid, an environment first proposed by Manceau et al. (1996) and confirmed by Bargar et al. (1997). Moreover, the redox active Mn oxide surface does not affect Pb as there was no evidence of Pb^{4+} based on the XANES analysis (Figure 8.2) and the first shell distance observed as 2.30 Å, which is longer than that for Pb^{4+}-O (~2.16 Å). The second shell fitting was accomplished only with Mn; approximately one to two atoms of Mn are located at an average distance of 3.56 ± 0.08. Second shell contributions were attempted with O, C, Pb, Si, and Al as well as combinations of these, but none resulted in a feasible fit. The second shell radial distance of Pb-Mn was consistent with Pb sorbed on biogenic Mn oxide (Villalobos et al. 2005).

Furthermore, a bond valance analysis was conducted to investigate the relative stability of the bonding arrangement using Pauling's electrostatic valence principle (Pauling, 1960) and bond valance for metal-oxygen bonds (Brown and Altermatt, 1985) (see Appendix C). Accordingly, feasible surface complexes of Pb on Mn oxide include two possible configurations (e.g. Mn_2-O-Pb and Mn-O-Pb). However, constrained with the XAS analysis, Pb appears to sorb on the edges of Mn oxide and form bidentate

corner-sharing complexes, which is consistent with results of Villalobos et al. (2005). Interestingly, the sorption configuration of Pb sorbed on HMO-coated montmorillonite was invariant of pH, ionic strength, and surface loading, and supported bidentate complexation (Mn_2-O-Pb) (Figure 8.4). The Mn oxide is the dominant phase for sorption in the coated system and appears to potentially sequestrate Pb, which is further probed in the long-term studies.

8.2.2. Ni Sorption

From the standard compounds, NiO and $NiCO_{3(S)}$, the $NiO_{(S)}$ XANES spectra show a significant sharp peak at 8.350 keV and a smaller peak at 8.367 keV, while the $NiCO_3$ has a small shoulder at 8.358 keV (Figure 8.2). The XANES spectra of the HMO and HMO-coated montmorillonite are quite similar while the montmorillonite sample is consistent with that of Ni^{2+} in the aqueous phase. Spectra of $Ni(NO_3)_{2(aq)}$ (10^{-2} M Ni^{2+} at pH 2) showed one shell in octahedral coordination, 6.7 ± 1.2 O atoms at 2.02 ± 0.02 Å. Spectra of Ni sorbed on montmorillonite (Figure 8.5 and Table 8.3) revealed only a first shell of 7.3 ±1.2 atoms of O at 2.04 ± 0.02 Å, which was consistent with that of aqueous Ni^{2+} suggesting an outer-sphere complex. In contrast to this study, surface precipitation or the mixed Ni-Al LDH phase has been reported from studies on Al-bearing minerals such as kaolinite, pyrophyllite, illite, and aluminum oxides (Nachtegaal and Sparks, 2003; Scheidegger et al. 1998; Roberts et al. 1999); however, these were conducted at higher pH (~7) and longer contact times (>1 day).

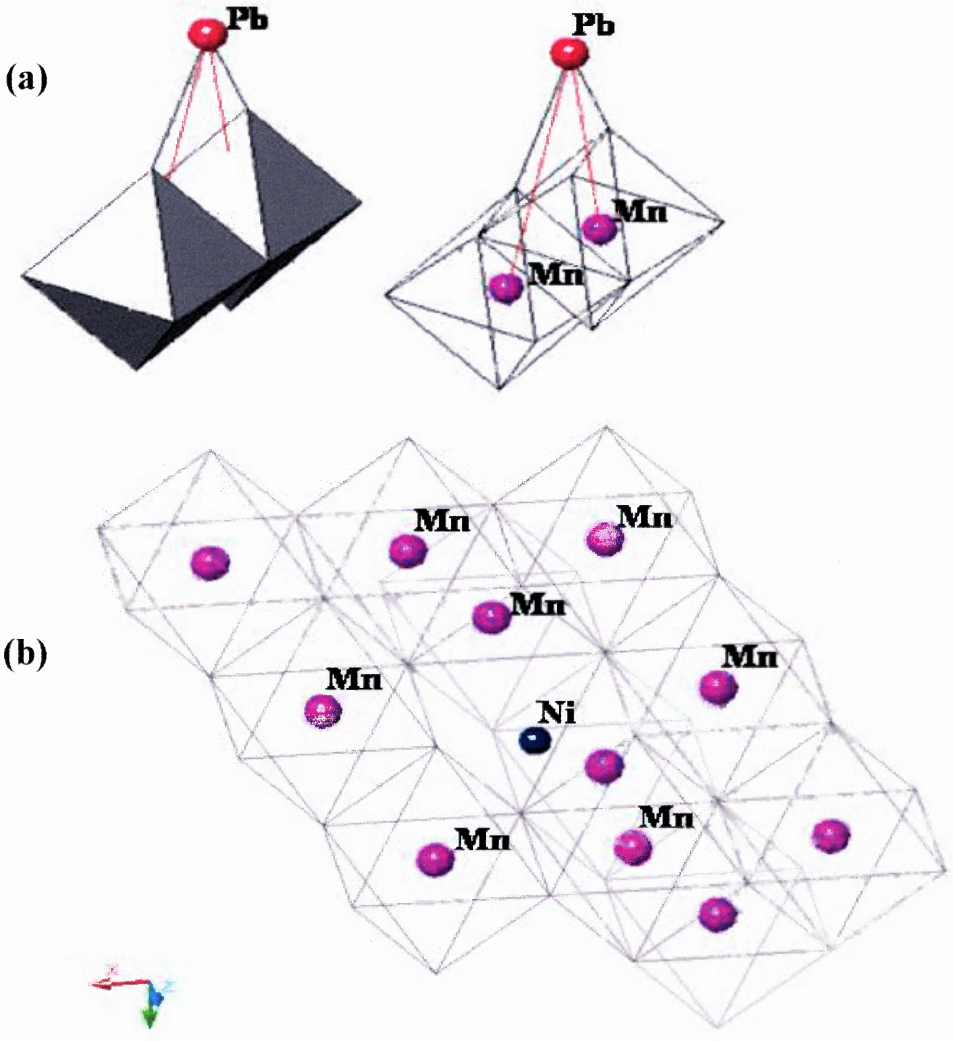

Figure 8.4 Proposed Pb and Ni sorption configurations on hydrous manganese oxide (HMO) shows (a) Pb forms bidentate corner-sharing complexes with Pb-O at 2.30 Å and Pb-Mn at 3.56 Å; (b) Ni coordinates to the vacancy site of Mn oxide with Ni-O at 2.04 Å, Ni-Mn at 3.32 Å, and Ni-Mn at 3.49 Å.

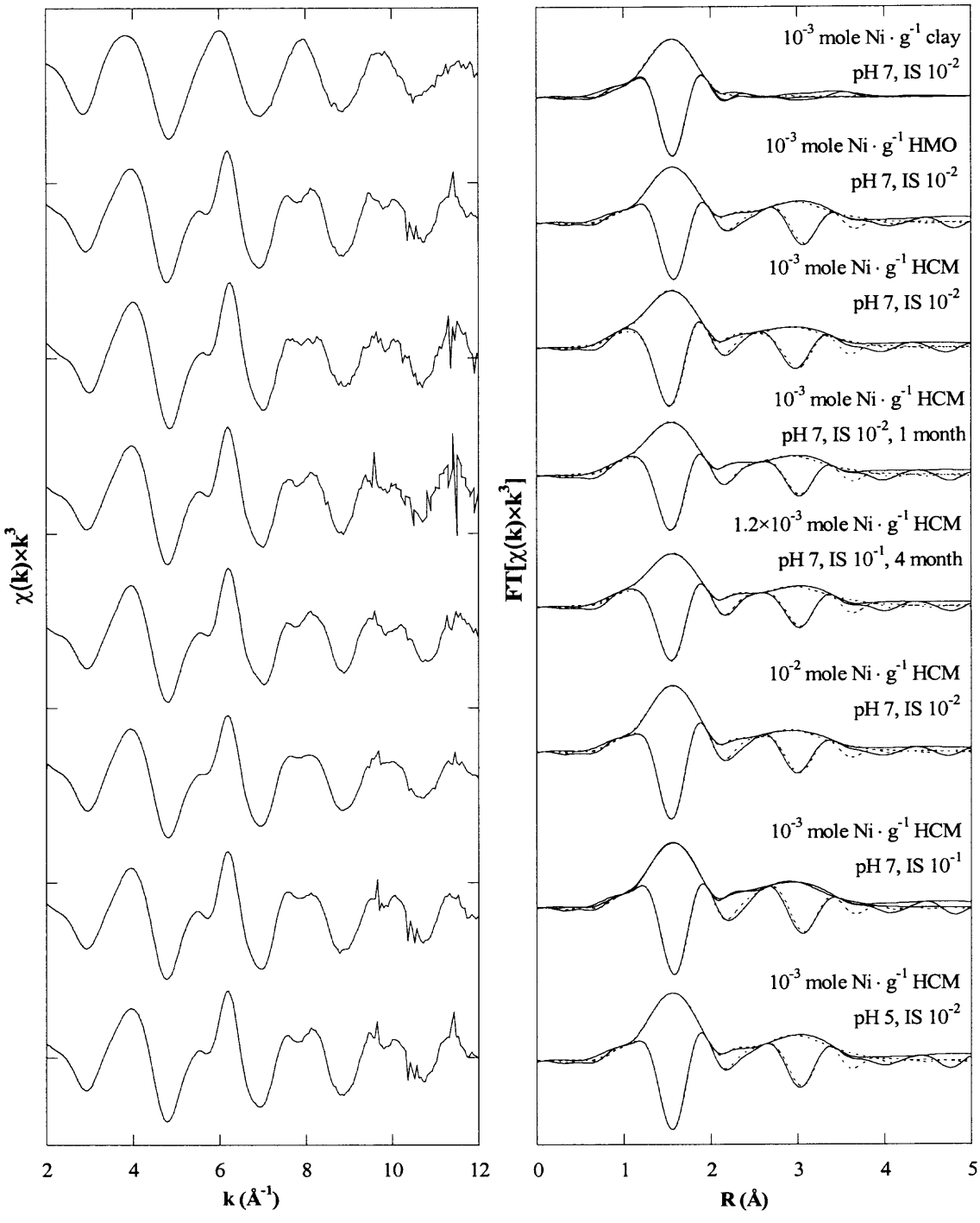

Figure 8.5 Ni K-edge $\chi(k) \cdot k^3$ spectra of standards and sorption samples collected at 25 °C along with Fourier transformed $\chi(k) \cdot k^3$ spectra over 2.50 to 12.00 $Å^{-1}$ and fitted over 0.50 to 3.75 Å. Solid lines represent the data and dashed lines are the fit.

Table 8.3 XAS Fitting Results of Ni Sorption Samples at Ni K-Edge

	O			Mn			Mn			ΔE_o	%Res
	N	R (Å)	σ (Å^2)	N	R (Å)	σ (Å^2)	N	R (Å)	σ (Å^2)	(eV)	
$Ni(NO_3)_{2(aq)} = 10^{-2}$ M pH 2	6.70	2.04	0.007	-	-	-	-	-	-	-4.07	9.16
$\Gamma_{Clay} = 10^{-2}$, pH 5, IS 10^{-2}	6.12	2.04	0.006	-	-	-	-	-	-	-4.91	7.46
$\Gamma_{HMO} = 10^{-3}$, pH 7, IS 10^{-2}	5.80	2.04	0.006	2.48	3.32	0.009	6.39	3.49	0.010	-3.40	9.15
$\Gamma_{HCM} = 10^{-3}$, pH 7, IS 10^{-2}	5.90	2.03	0.006	4.21	3.32	0.009	6.23	3.49	0.009	-3.09	14.34
$\Gamma_{HCM} = 10^{-3}$, pH 5, IS 10^{-2}	5.83	2.03	0.006	2.36	3.32	0.008	6.25	3.49	0.009	-3.67	7.67
$\Gamma_{HCM} = 10^{-3}$, pH 7, IS 10^{-1}	5.56	2.04	0.005	4.59	3.32	0.010	7.78	3.49	0.011	-4.39	9.78
$\Gamma_{HCM} = 10^{-2}$, pH 7, IS 10^{-2}	5.72	2.03	0.006	3.31	3.34	0.007	4.20	3.51	0.007	-3.91	9.08
$\Gamma_{HCM} = 10^{-3}$, pH 7, IS 10^{-2} (CBC 1 month)	6.87	2.04	0.008	3.72	3.32	0.010	7.13	3.49	0.010	-3.21	14.01
$\Gamma_{HCM} = 1.2\times10^{-3}$, pH 7, IS 10^{-2} (CBC 4 month)	5.14	2.03	0.006	4.71	3.31	0.011	7.53	3.48	0.011	-4.49	8.48

Ni K-edge $\chi(k) \cdot k^3$ spectra were Fourier transformed over 2.50 to 12.00 Å^{-1} in k-space and fitted over 0.50 to 3.75 Å in r-space. Γ is surface loading (Γ_{solid} = mole of Ni $\cdot$ g^{-1} solid). N, R, and σ^2 represent the coordination number, distance, and variance. The quality of fits for N_1, N_2, R, and σ^2 are $\pm$ 20%, $\pm$ 40%, $\pm$ 0.02, and $\pm$ 5%, respectively. The amplitude reduction factor (S_o^2) was fixed at 0.96.

For Ni sorbed on HMO and HMO-coated montmorillonite (Figure 8.5 and Table 8.3), spectra like that for Pb reveal multiple backscattering envelopes. Therefore, a matrix of configurations were considered for the second shell fitting parameters, Ni, Mn, Si, Al, C, and O as well as combinations of these; the only physically plausible fit resulted in two Mn subshells. The first shell is comprised of approximately 6 atoms of O at an average distance of 2.04 ± 0.02 Å with a second shell consisting of 3 to 5 atoms of Mn at 3.32 ± 0.05 Å and 4 to 7 atoms of Mn at 3.49 ± 0.05 Å. The sorption mechanism is invariant as a function of pH, loading, and ionic strength. Conversely, Trivedi et al. (2001) reported 5.8-6.2 (± 0.41) O atoms at an average distance of 2.07 Å in the first shell, and 5.6-8.4 (± 0.92) atoms of O at 3.32-3.35 Å in the second shell. In this study, XAS spectra were Fourier transformed over 2.2 to 12.0 $Å^{-1}$, providing a more refined analysis of the second shell as compared with Trivedi et al. where transforms were conducted over 2.45 to 9.21 Å. In our study, the fitting results of two sub-shells of Mn suggest that Ni ions potentially sorb at the vacancy sites on the Mn oxide surface (Figure 8.4), which is consistent with the observations of Manceau et al. (1987), Ni and Co substitution in lithiophorite and asbolane. Therefore as compared to Pb, Ni affinity for the surface could be greater due to complexation in vacancy sites, which is somewhat in agreement with isotherm results. In addition to the effect of pH, loading, and ionic strength, the impact of time on sorption was also investigated.

8.3 Intraparticle Surface Diffusion of Pb and Ni through Micropores.

CBC studies have been conducted to observe transient sorption. In these studies, the metal concentration (as well as pH) in the bulk aqueous phase was monitored and

maintained constant, providing a constant surface concentration at the micropore entrance. By adding stock solution as needed, the $[Ni]_{bulk}$ was maintained constant at 3.2 $\times 10^{-5}$ M for HMO-coated montmorillonite (Figure 8.6a), 3.2 $\times 10^{-9}$ M for HMO, and 3.7 $\times 10^{-5}$ M for montmorillonite. For Pb systems, the $[Pb]_{bulk}$ was maintained at 5.9 $\times 10^{-7}$ M for HMO-coated montmorillonite, 6.6 $\times 10^{-7}$ M for HMO (Figure 8.6b), and 9.5 $\times 10^{-6}$ M for montmorillonite. This slow sorption process may be described as intraparticle diffusion due to the presence of micropores. Initially, the amount of metal ion sorbed corresponded well to the isotherms, adsorption to the external surface. Subsequently, the amount sorbed gradually increased due to intraparticle surface diffusion: from 4.9 $\times 10^{-4}$ to 5.4 $\times 10^{-4}$ mol of Pb $\cdot$ g^{-1} HMO-coated montmorillonite over 3 months, and from 6.0 $\times 10^{-4}$ to 1.2 $\times 10^{-3}$ mol of Ni $\cdot$ g^{-1} HMO-coated montmorillonite over 4 months. Although the fractional increase in Pb sorbed was relatively small as compared to that for Ni, the slower diffusion of Pb along internal surface sites of micropores (Figures 8.6 and 8.7) is consistent with site activation theory where surface diffusion is a function of the affinity of the ion for the surface and the mean distance between sites. As time studies demonstrate an increase in sorption, and because the sorbent is microporous (Boonfueng, et al. 2005) with no evidence of precipitation, solid solution formation, or reconfiguration of the local structure of the adsorbate, the transient process is consistent with intraparticle surface diffusion. Specifically, the local coordination environment of Pb and Ni sorbed onto HMO-coated montmorillonite from 1 and 4-month CBC studies (where an additional 10 to 100 % of the sites became occupied) is similar to that of short-term studies (Figures 8.3 and 8.5 and Tables 8.2 and 8.3).

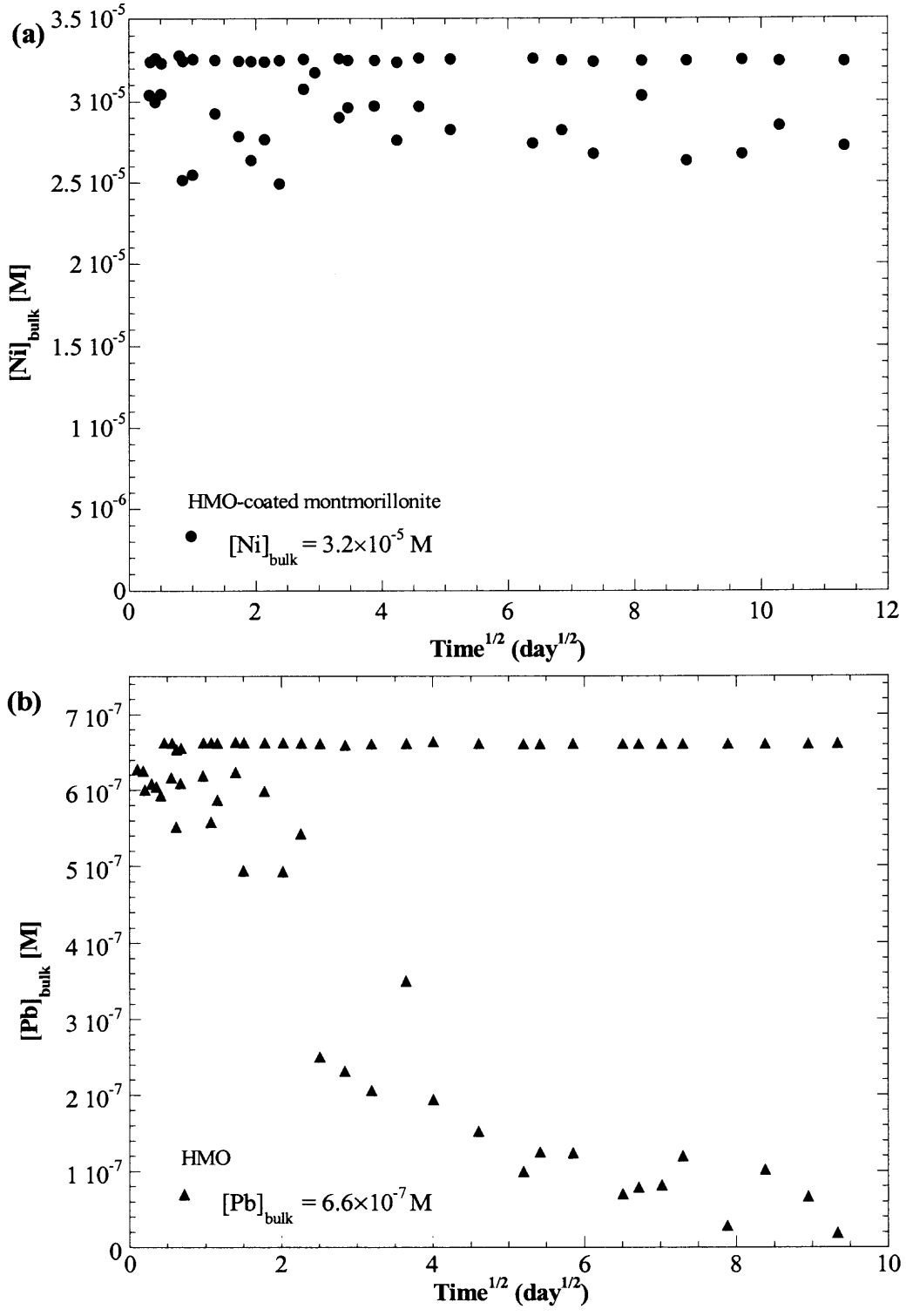

Figure 8.6 CBC studies demonstrate the monitoring and maintaining the bulk aqueous approach, showing $[Me]_{bulk}$ as a function of contact time ($day^{1/2}$) (a) Ni sorbed on HMO-coated montmorillonite and (b) Pb sorbed on HMO.

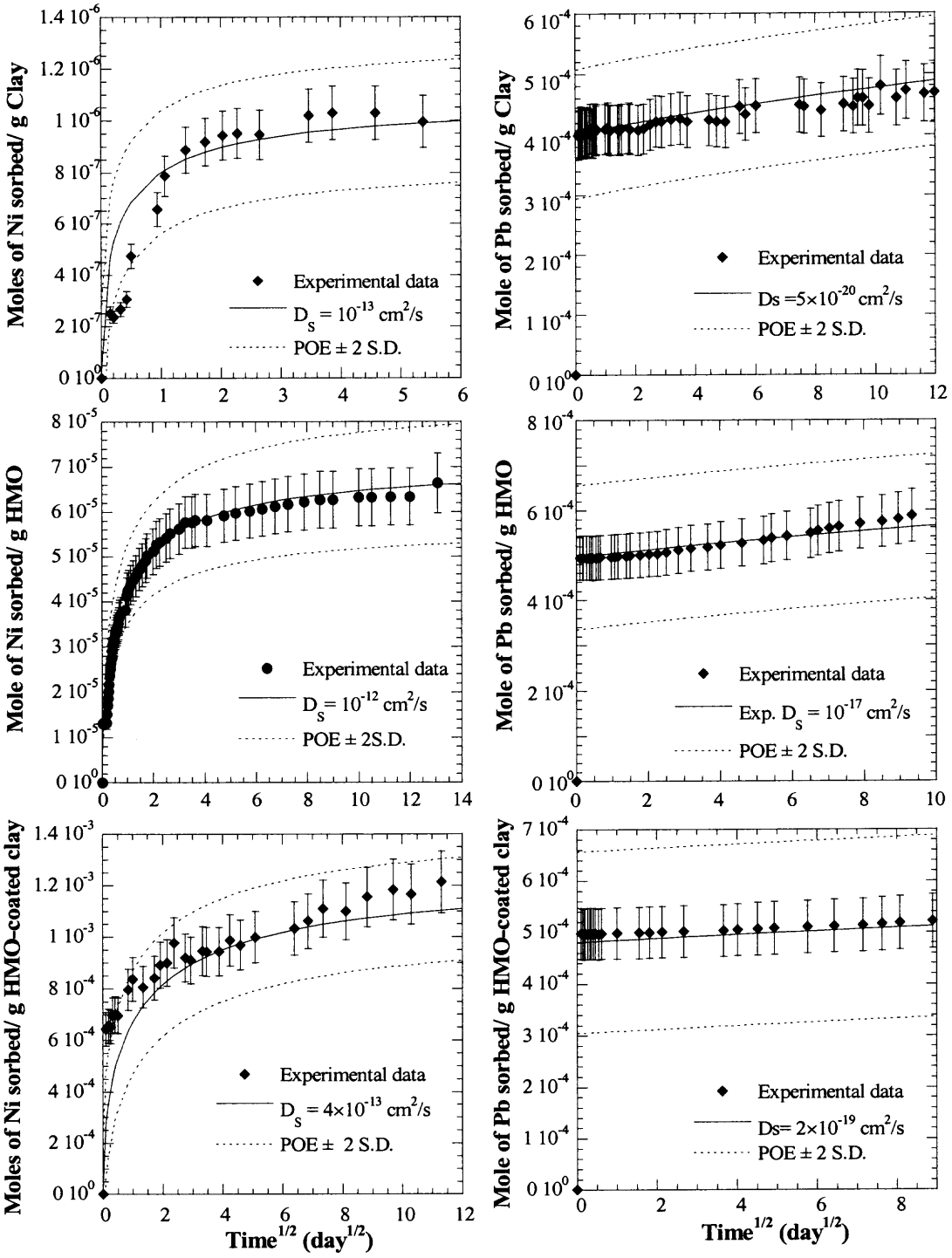

Figure 8.7 CBC studies of Ni and Pb sorption to 10^{-1} g/L HMO, HMO-coated montmorillonite, and montmorillonite at 25°C, 1.5 × 10^{-2} IS ($NaNO_3$). Ni systems were maintained at pH 7 and a $[Ni]_{bulk}$ of 3.2 × 10^{-5} M for HMO-coated montmorillonite, 3.2 × 10^{-9} M for HMO, and 3.7 × 10^{-5} M for montmorillonite. Pb were maintained at pH 6 and a $[Pb]_{bulk}$ of 5.9 × 10^{-7} M for HMO-coated montmorillonite, 6.6 × 10^{-7} M for HMO, and 9.5 × 10^{-6} M for montmorillonite.

For Pb, the fits revealed 1.8 ± 0.5 atoms of O at 2.29 ± 0.05 Å in the first shell and 0.87 ± 0.5 atoms of Mn at 3.55 ± 0.08 Å in the second, while for Ni ions, the analysis showed 7.88 ± 0.6 of O at 2.04 ± 0.02 Å in the first shell and two Mn sub-shells of 3.65 ± 0.8 atoms at 2.93 ± 0.05 Å and 4.46 ± 0.8 atoms at 3.43 ± 0.05 Å in the second shell. A slight increase in the coordination number of Mn in second shell was observed after 4 months contact time which may due to the vacancy sites in Mn oxide structure. When Ni and Pb diffuse along the micropores, complexation is similar to that on the external surface. In modeling, the assumption that internal sites are no different than external ones has been observed in other spectroscopic studies as well (Trivedi et al. 2001; Axe et al. 1998, 2000).

Minimizing the variance between experimental data and modeling results, the only fitting parameter is surface diffusivity (see e.g. Axe and Anderson, 1997, Trivedi and Axe, 1999) (Figures 8.7). Errors associated with the model from the propagation of errors (POE) method (Ku, 1966) are also shown. The POE analysis accounts for the standard deviation in the number of particles as well as the error in the distribution coefficient describing the mass adsorbed to the surface. All data fall within two standard deviations of the model. Studies with Ni and Pb sorption to HMO, HMO-coated montmorillonite, and montmorillonite demonstrate that surface diffusivities (D_S) range from 10^{-17} to 10^{-20} cm^2/s for Pb and 10^{-12} to 10^{-13} cm^2/s for Ni. The D_S in HMO-coated montmorillonite falls between that of montmorillonite and HMO. Based on earlier characterization studies (Boonfueng et al. 2005), the coated oxide surface is potentially different from the discrete oxide. We speculate that clay particles served as a template for Mn oxide when nucleation occurred, potentially impacting its growth and porosity.

The D_S for Pb is much smaller than that for Ni. Interestingly, the ratio of the primary hydration number to the hydrated radius for Pb (~1.74) is much smaller than that for Ni (~3.06), suggesting potentially a greater Coulombic energy of attraction for the amorphous oxide surface (Richen, 1997). The theoretical surface diffusivity for Ni and Pb are two orders of magnitude greater than the experimental ones (Table 8.4). Based on site activation theory and correlations developed earlier (Trivedi and Axe, 2001), the diffusivity is a function of enthalpy (standard deviation of ± 20%), resulting in a range of 10^{-12} to 10^{-9} cm^2/s for Ni and 10^{-18} to 10^{-13} cm^2/s for Pb, over which the experimental values fall. Theoretical surface diffusivities evaluated from site activation theory assuming a sinusoidal potential field along the pore surface (Axe and Anderson, 1997) are a function of the mean distance between the sites (λ) and the activation energy required for a sorbed ion to jump to the neighboring site (E_a):

$$D_S = \lambda[E_a/2m]^{1/2}\exp[-E_a/(RT)]$$

where $\exp(-E_a/RT)$ is the Boltzmann factor, and m is the molecular weight of the diffusing species. Activation energies (E_a) and mean distances (λ) were determined based on the work of Trivedi and Axe (2001a, b), where the former is proportional to the reaction enthalpy (ΔH): $E_a = \alpha\Delta H$ (Table 8.4). The polanyi relation constant (α) is approximately 0.6 for transition metals (Trivedi and Axe, 2001a) and 0.4 for Pb as estimated by Fan et al. (2005). Nevertheless, the activation energy for Pb is almost double that of Ni resulting in diffusivities that are orders of magnitude different. Based on the theoretical and experimental surface diffusivities, these small diffusivity values suggest that HMO present as coatings and discrete particles potentially acts as a sink for

metal contaminants and intraparticle surface diffusion is a rate limiting mechanism in contaminant sorption.

Table 8.4 Predicted and Experimental Sorption Parameters of Ni, Pb, and Zn Sorbed on Hydrous Mn Oxide

	Ni-HMO	Pb-HMO	Zn-HMO
λ (cm)	2.3×10^{-8}	1.5×10^{-9}	2.3×10^{-8}
m (g/mol)	58.69	207.2	65.4
K	3640	599117	155882
$\Delta H°$ (kcal/mol)*	16.5 (±3.3)	43.5 (±8.8)	24.9 (±4.9)
α (Polanyi relation constant)	0.6	0.4	0.6
E_a (kcal/mol)	10.0	17.4	15.2
Theor. D_S (cm^2/s)	10^{-10}	10^{-15}	9.6×10^{-15}
Exp. D_S (cm^2/s)	10^{-12}	10^{-17}	10^{-17}

*ΔH value are obtained from Trivedi and Axe, 2001.
α for transition metals is 0.60 for HMO (Trivedi and Axe, 2001)
α for Pb is 0.60 for HMO (Fan et al. 2005)

8.4. Summary

Sorption of Ni and Pb to HMO-coated montmorillonite demonstrates the dominance of the HMO surface in terms of affinity and site capacity as compared to montmorillonite. Moreover, XAS results revealed that Pb appears to sorb on the edges of Mn oxide and form bidentate corner-sharing complexes while Ni sorbs to vacancy sites in the structure. Interestingly, the Pb sorption configuration from the bond valence analysis is in agreement with XAS. In time studies where as much as a 100% increase in sorption occurred due to intraparticle surface diffusion, the sorption configuration was invariant, suggesting that internal surface sites appear to be no different than external ones. Best fit diffusivities ranged from 10^{-13} to 10^{-12} cm^2/s for Ni and 10^{-20} to 10^{-17} cm^2/s for Pb and based on site activation theory, theoretical surface diffusivities were predicted and given the their error were in agreement with experimental results. Mn oxides are important surfaces for sequestrating heavy metals in the environment.

CHAPTER 9

BIOGENIC MN OXIDE – NANO-PARTICLE FORMATION, CHARACTERIZATION, AND ENCRUSTATION INTO THE SHEATHED *LEPTOTHRIX DISCOPHORA* SP-6 BIOFILM

Because biogenic processes dominate in producing Mn oxide, in this chapter, the biogenic Mn oxide produced from *L. discophora* SP-6 is characterized and includes an analysis of the average oxidation state using layered- and tunneled- structure standards. Studies include the organism growth rate in two media – MSVP and PY, assessment of the optimum pH condition for growth, evaluation of the effect of Mn(II) concentration on the oxidation rate, and modeling of oxidation kinetics using the Michaelis-Menten equation. Subsequently, using 6×10^{-5} mole Mn mg^{-1} cells, several techniques are used to assess the mineralogy, morphology, surface charge, particle size distribution, surface area, and local structure. Potential transformation of the metastable amorphous phase to a more crystalline structure was evaluated based on the local structure of a 4 month aged biogenic Mn oxide.

9.1 Mn Oxidation Study

Leptothrix discophora SP-6, is a sheath forming gram negative bacteria that oxidizes Mn(II) as well as Fe(II). This oxidation is enzymatically catalyzed via non-dissimilatory pathways and usually depends on growth conditions, including pH, temperature, and substrate concentration. Because *L. discophora* is a sheath-forming organism, Mn oxide precipitates on the organism's surface. From the growth study on *L. discophora* SP-6 conducted as a function of pH (Figure 9.1a) in MSVP media with initial cell

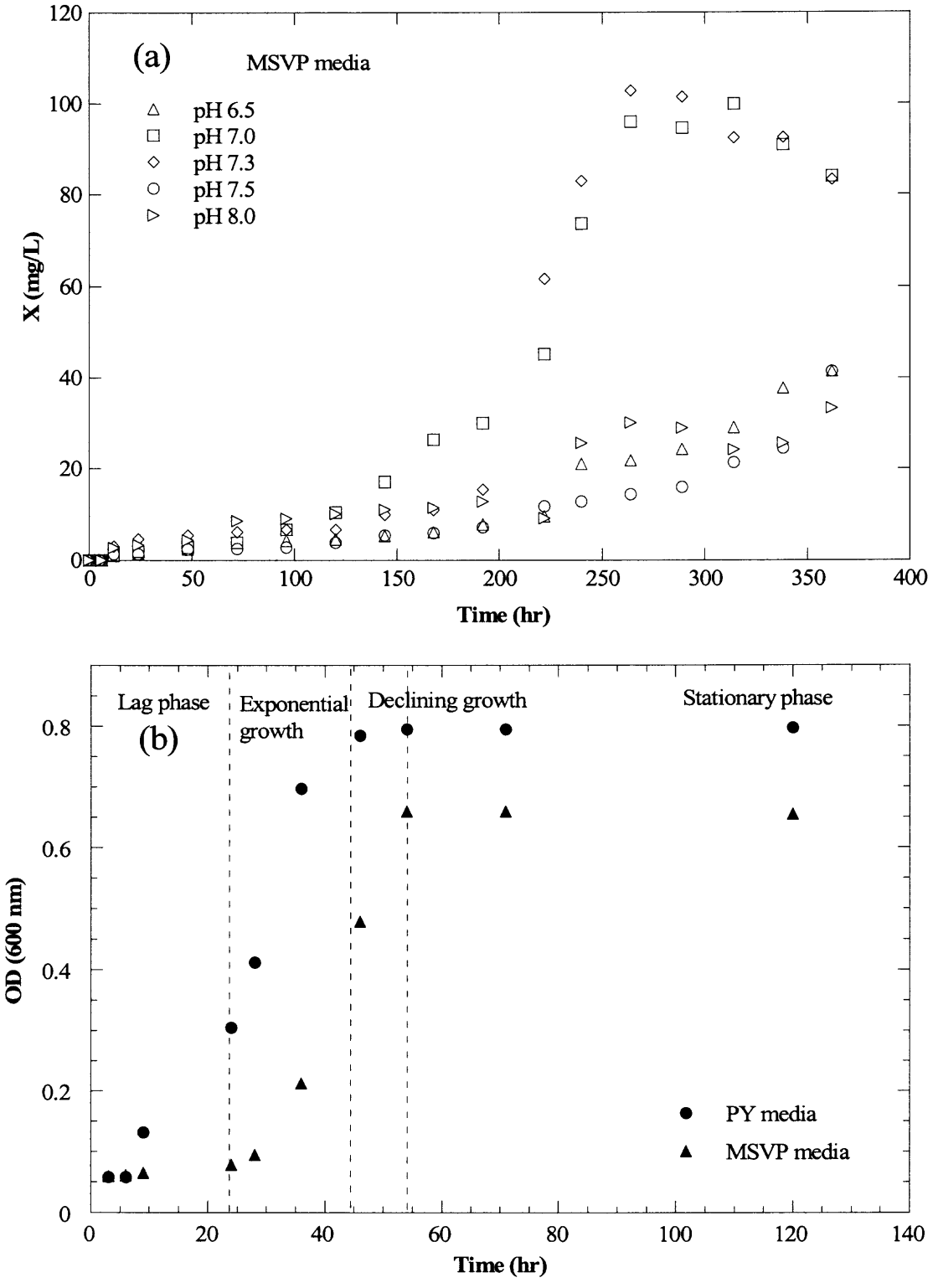

Figure 9.1 Growth curve of *L. discophora* SP-6 (a) in MSVP media as a function of pH (6.5-8) and (b) the comparison between the growth of L. discophora SP-6 in MSVP and PY media at pH 7.3 and 22 °C.

concentration of ~ 1 mg · L^{-1}, the optimum condition was observed at pH 7.0 to 7.3. The stationary phase was attained after 60 h when *L. discophora* was grown in PY and MSVP media with initial cell concentration of ~ 8.6 mg · L^{-1}. The reduced acclimation period and increased growth rate observed for the PY media over the MSVP (Figure 9.1b) are attributed to the presence of organic nutrients and amino acids such as glycine, glutamic acid, and alaine, which serve as growth factors (Madigan et al. 2000). Mn(II) oxidation experiments were conducted with systems grown at pH 7.3 and in the stationary phase. To better understand the impact of media, PY, MSVP, and HEPES solutions were employed with initial Mn(II) concentrations ranging from 0.1 to 1 mM (Figure 9.2a) at pH 7.3; at concentrations of 5 mM or greater, there was no evidence of oxidation, suggesting toxicity to the organism. In the HEPES solution, Mn oxidation was not observed, most likely due to the lack of an energy source and nutrients required in metabolism and excretion of enzymes from its extracellular filament. On the other hand, in MSVP and PY media with an initial cell concentration of 17.3 mg · L^{-1}, almost 100% of Mn(II) oxidized within the first 12 h, which is in agreement with others (Adam and Ghiorse, 1985; Zhang et al. 2002). The oxidation rate in the PY medium was much greater than that in MSVP, as the former is comprised of amino acids a simpler substrate form. In the PY media (Figure 9.2b), the maximum oxidation rate (V_{max}) and half saturation constant (K_m) were approximately 0.12 μmol · (min · mg cell)$^{-1}$ and 75 μM, respectively, while in MSVP media, the values were 0.055 μmol · (min · mg cell)$^{-1}$ and 200 μM, respectively. In contrast, for *L. discophora* SS-1, the non-sheath forming strain with MSVP media, a V_{max} of 0.0059 μmol· (min · mg cell)$^{-1}$ (Zhang et al. 2002) suggests

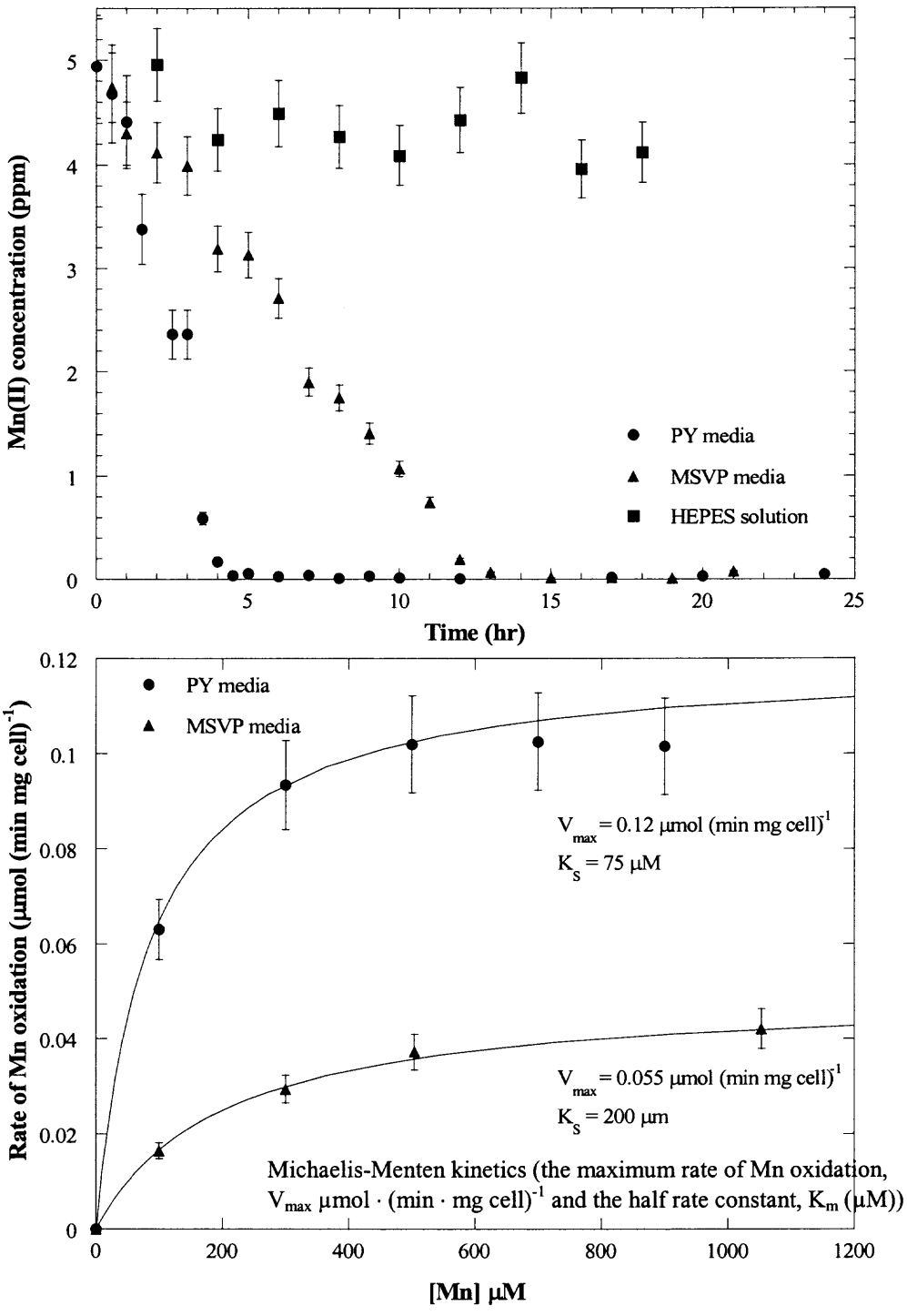

Figure 9.2 Mn oxidation by *L. discophora* SP-6 (a) comparison between three different media (MSVP, PY, and HEPES solution) at $[Mn]_0 = 10^{-4}$ M, pH 7.3, and 22 °C; and (b) Mn oxidation rate of *L. discophora* SP-6 with MSVP and PY media using Michaelis-Menten kinetics.

that the sheath forming organism produces the Mn(II) oxidizing enzyme and stores it between the sheath and outer membrane of cell, resulting in a significant increase in the maximum oxidation rate. At circumneutral pH, biogenic Mn oxidation is five orders of magnitude greater than abiotic Mn oxide (Nealson et al. 1988) and therefore may result in differing mineralogy and morphology.

9.2 Characterization of Biogenic Mn oxide

The extracellular polymeric sheath of *L. discophora* SP-6 effectively links bacteria cells through strong adhesion forces as evidenced by Tsang et al. (2006) where 0.59 μN forces were observed between N-acetylglucosamine polysaccharide sheath of *Caulobacter crescentus* and a borosilicate surface. The dendritic elongated strands of connecting cells (Figure 9.3a) exhibit an average cell length of 1-2 μm and a width of 0.5 μm that aggregate into a biofilm matrix (Decho 1990) where the nano-particulate Mn oxide can accumulate. With an initial Mn(II) concentration of 0.05 mM, oxide precipitation is not visible (Figure 9.3b) as the color of the cell suspension turns from white to yellow (Figure 9.3f). However, at slightly greater initial Mn(II) concentrations (i.e., 0.1 and 0.5 mM), a light brown cell suspension was observed and FESEM images showed aggregated nano-particles of biogenic Mn oxide deposited on the bacteria cell walls and associated extracellular polysaccharide sheath, forming the dendritic cell system (Figure 9.3c-d). Interestingly at initial Mn concentrations greater than 0.5 mM (as ~ 100% Mn^{2+} oxidized), apparently the capacity of the sheathed cell system was attained and discrete Mn oxide formed (Figure 9.3e). The particle size distribution confirmed the presence of

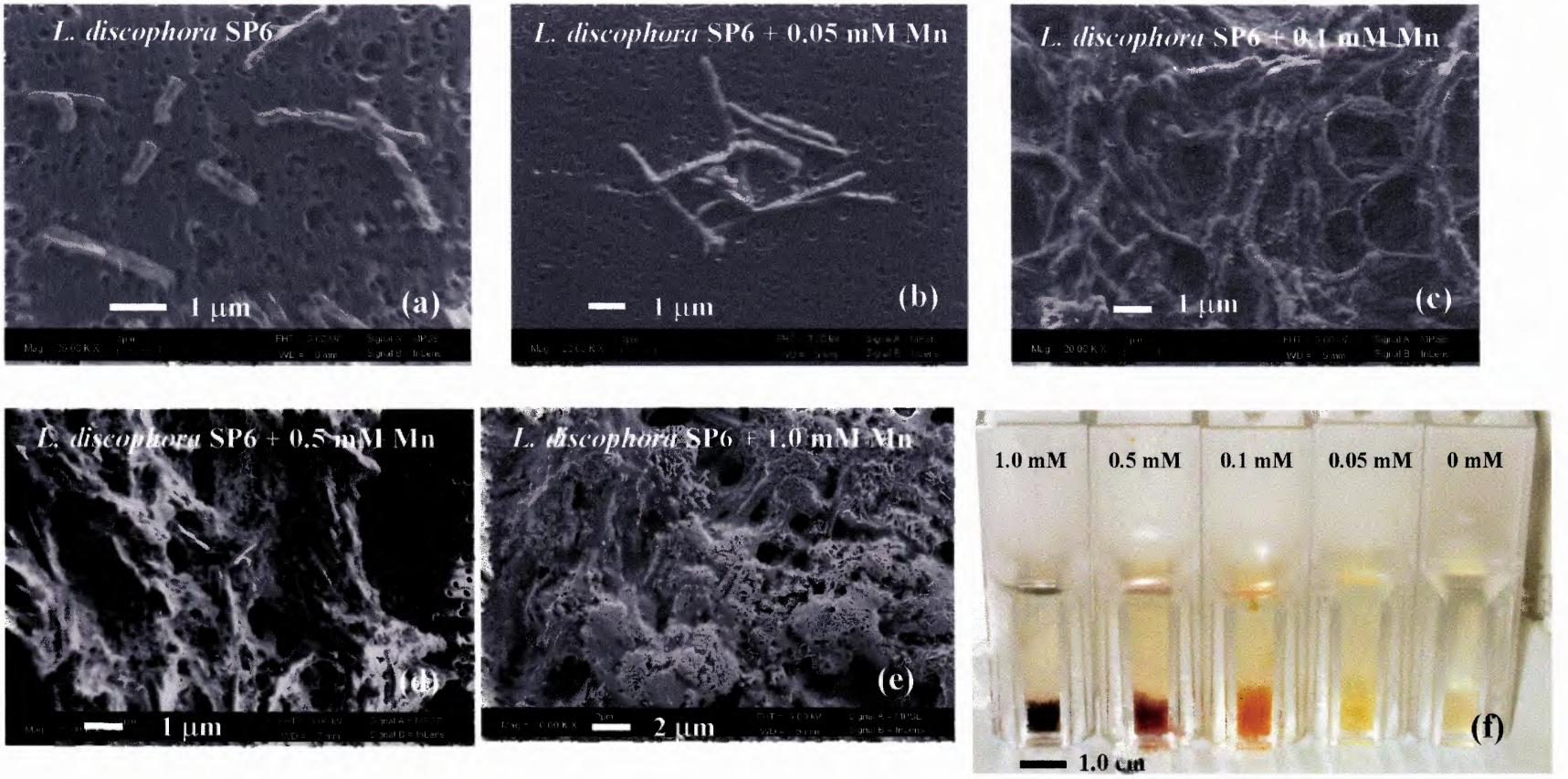

Figure 9.3 FESEM images of biogenic Mn oxide and *L. discophora* SP-6 as a function of initial Mn(II) concentration ((a) 0, (b) 0.05, (c) 0.1, (d) 0.5, and (e) 1 mM), and (f) comparison between resulting biogenic Mn oxide sheathed organisms after *L. discophora* SP-6 exposure to varying initial Mn concentrations.

discrete oxide as a bimodal particle size distribution was observed at 150 and 200 μm with an initial Mn^{2+} of 1 mM, while the particle size distributions of *L. discophora* SP-6 without Mn and at lower Mn concentrations were monomodal with an average size of 100 μm (Figure 9.4). The larger particle size observed when discrete oxide formed may be due to a bridging effect between discrete aggregated Mn oxide and the sheathed bacteria.

Based on BET analysis, the surface area of the freeze-dried biogenic Mn oxide coated *L. discophora* SP-6 was approximately 443 $m^2 \cdot g^{-1}$, yet that of the freeze dried bacteria exhibited an area of 42 $m^2 \cdot g^{-1}$. The difference between these two systems corresponds to the increase from the biogenic Mn oxide, which when isolated from the organism resulted in an area of 401 $m^2 \cdot g^{-1}$. For the biogenic Mn oxide produced from *L. discophora* SS-1, a surface are of ~224 $m^2 \cdot g^{-1}$ was reported (Nelson et al. 1999) and for abiotic hydrous Mn oxide, 359 $m^2 \cdot g^{-1}$ was measured (Boonfueng et al. 2005). Porosity for the biogenic system (0.75) more that doubled as compared to the abiotic system (0.35) (Boonfueng et al. 2005). Based on N_2 desorption, the average pore size of biogenic Mn oxide is 2.7 nm which is similar to the abiotic Mn oxide (bimodal, 2.1 and 6.1 nm). Because the nano-particulate Mn oxide was observed, we speculate that the actual pore size distribution may extend to much smaller radii than that measured here, as 2 and 6 nm are the detection limits for N_2 desorption and mercury porosimetry, respectively (Gregg and Sing, 1982). Recently, Sun et al. (2005) observed pore sizes less than 0.1 nm using positron annihilation lifetime spectroscopy, which was applied on a nanoporous Cu thin film.

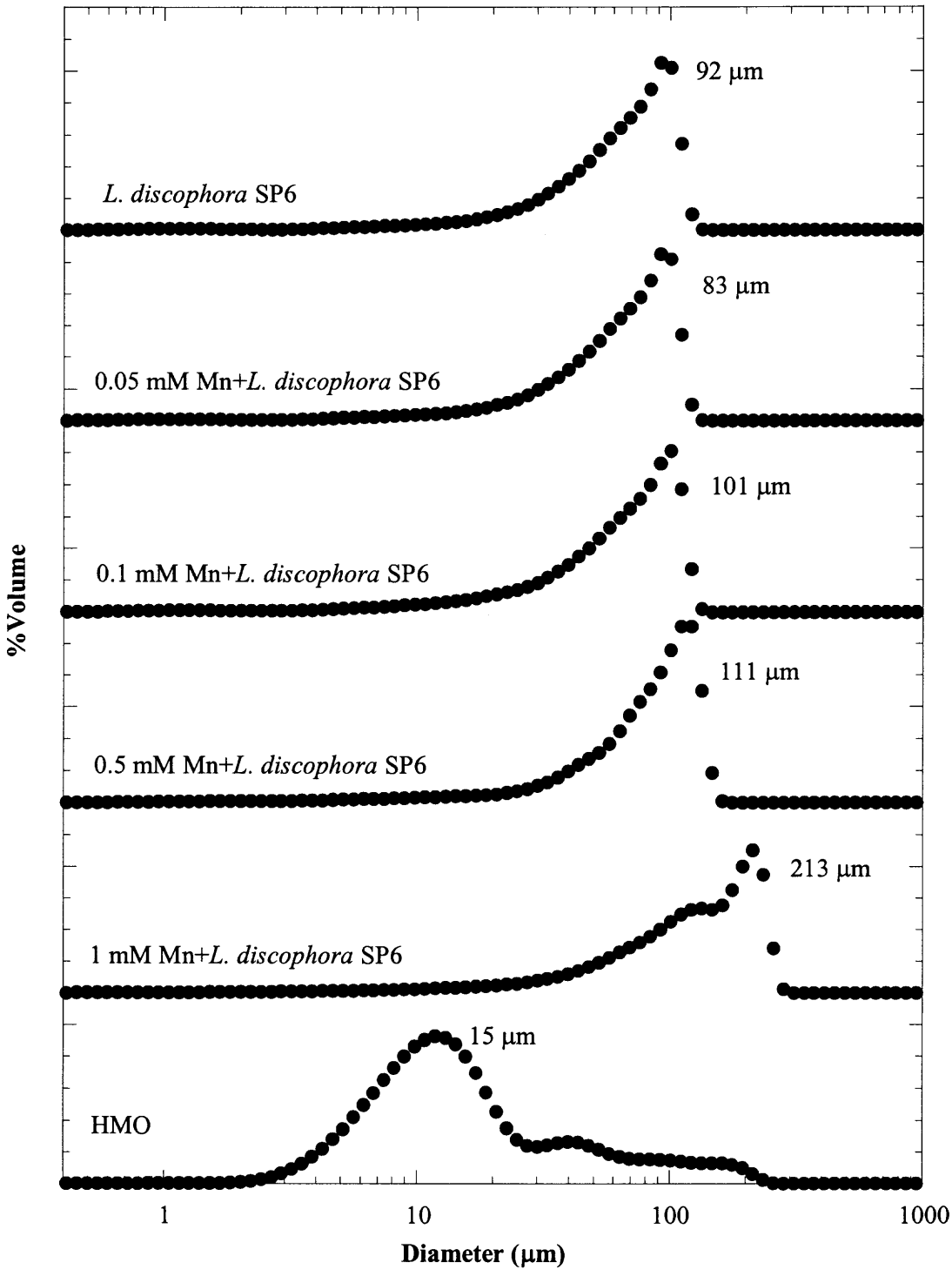

Figure 9.4 Particle size distributions of the biogenic Mn oxide and *L. discophora* SP-6 at pH 7.3 and room temperature in PY media as a function of Mn concentration (0, 0.05, 0.1, 0.5, and 1 mM) compared with abiotic Mn oxide (HMO).

Because of the large surface area with significant microporosity, the biogenic oxide surface is expected to play an important role in metal sorption and sequestration. Therefore, the surface charge density was evaluated by potentiometric titration. *L. discophora* SP-6 exhibited a negative surface charge over the entire pH range of 2 to 10 (Figure 9.5), while the pH_{znpc} of biogenic Mn oxide associated with the bacteria was 2.5 ± 0.5 consistent with abiotic hydrous Mn oxide (pH_{znpc} of HMO ~ 2.35). This observation suggests that the surface charge of the Mn oxide associated with *L. discophora* SP-6 at a Mn oxide concentration of 6×10^{-5} mole Mn · mg^{-1} cells (with an initial Mn^{2+} of 0.1 mM) behaves similar to that of discrete abiotic Mn oxide. The negative charge on *L. discophora* SP-6 surface is attributed to functional groups on the bacterial cell wall (e.g., carboxyl, phosphoryl and hydroxyl groups) and the polysaccharide sheath which possesses abundant anionic carboxyl and hydroxyl groups that are potential binding sites for the metal oxide (Kaplan et al. 1987).

The biogenic Mn oxide associated with *L. discophora* SP-6 exhibits a nanocrystalline structure (Figure 9.6), which was observed with aggregated nanoparticles of abiotic hydrous Mn oxide (HMO) as well. As compared with todorokite, birnessite, and *L. discophora* SP-6, the XRD pattern of biogenic Mn oxide was broader, less intense, and somewhat different from that of *L. discophora* SP-6. Similarly, in another study (Jürgensen et al. 2004), Mn oxide produced from *L. discophora* SP-6 consisted of two asymmetric low intensity peaks at 2θ = 36.73 and 65.59°, indicating the presence of δ-MnO_2, hexagonal birnessite. Jürgensen et al. normalized the diffractogram to the highest intensity at 19.55° (2θ) and removed the background from the biogenic Mn oxide-coated bacteria pattern using that of *L. discophora* SP-6 to strengthen the relative intensity of the

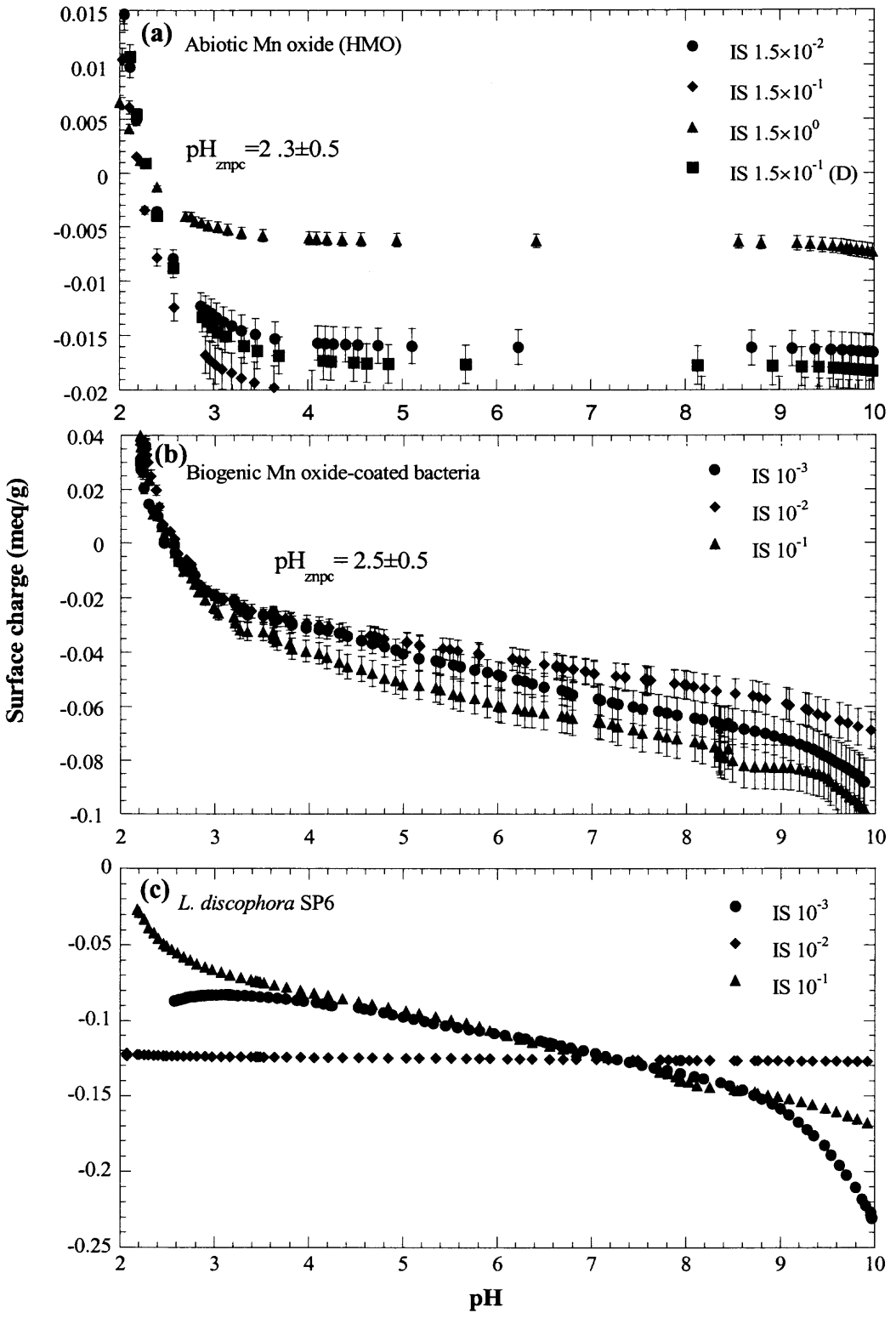

Figure 9.5 Surface charge distribution as a function of ionic strength (IS) using $NaNO_3$ for (a) abiotic Mn oxide (10^{-1} g/L), (b) biogenic Mn oxide-coated bacteria (70-90 g cells/L with 6×10^{-5} mole of Mn/mg cell), and (c) *L. discophora* SP-6 (30-60 g/L).

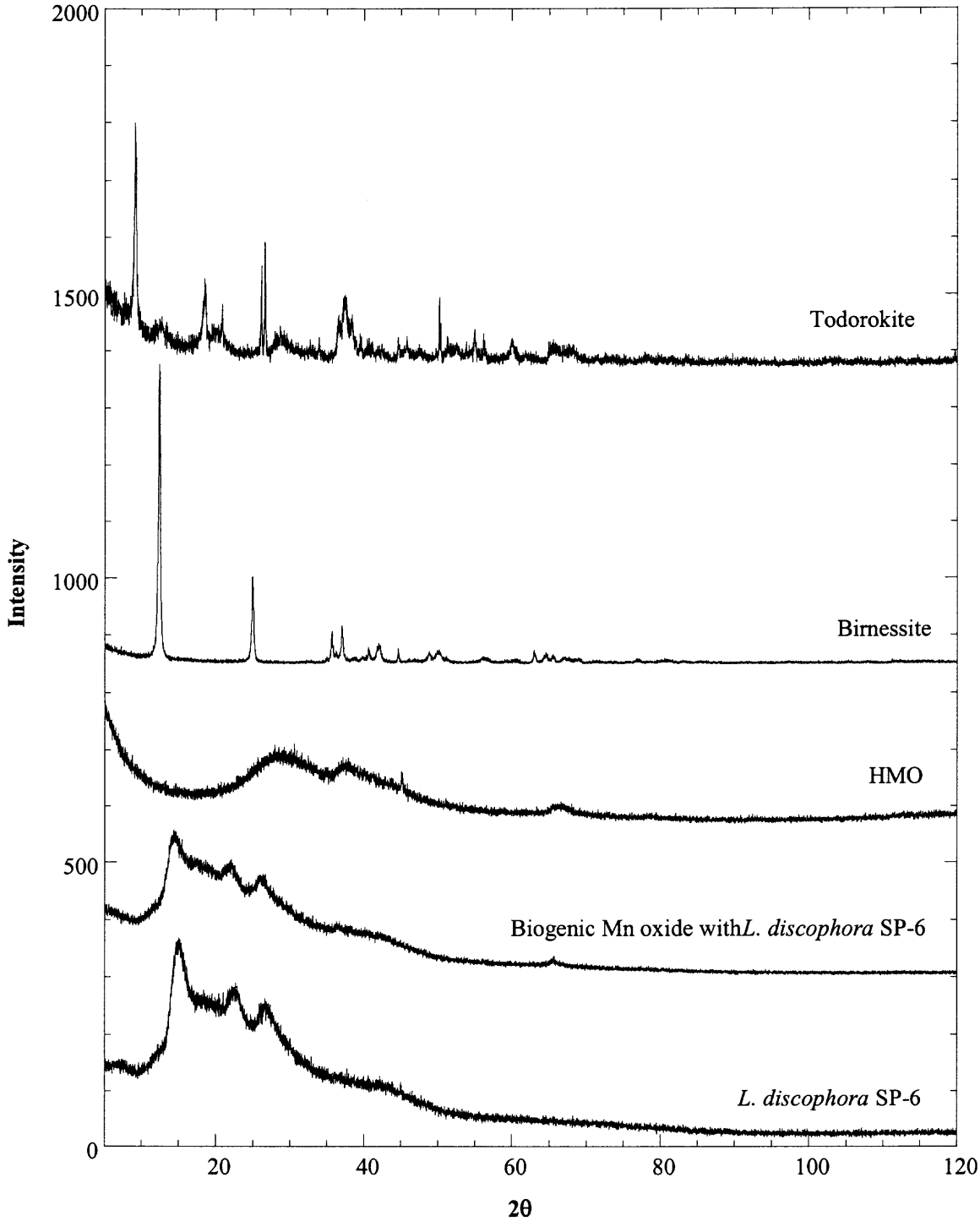

Figure 9.6 XRD patterns of biogenic Mn oxide compared with *L. discophora* SP-6, abiotic Mn oxide (HMO), and crystalline Mn oxides (birnessite and todorokite).

two peaks for the characteristic oxide. For both, the width at the half maximum was greater than 5° (2θ), indicating a poorly crystalline structure. Villalobos et al. (2003) resolved the long-range structure as acid birnessite produced via *P. putida* strain MnB1. Bargar et al. (2005) found the biogenic Mn oxide produced from marine bacteria, *Bacillus* strain SG-1, was amorphous and similar to δ-MnO_2 based on SR-XRD. Because of the lack of long-range structure, further assessment of the molecular structure and oxidation state were conducted using XAS.

The XANES spectral features of biogenic Mn oxide are similar to that of birnessite and abiotic HMO (Figure 9.7a). The oxidation state of biogenic Mn oxide was relatively close to that of birnessite (~3.7), while the oxidation state of todorokite and abiotic HMO was greater than 3.8 (Figure 9.7b). For pyrolusite (β-MnO_2), the average Mn oxidation state was 4 which is consistent with others (Pasten, 2002; Jürgensen et al. 2004). The fine structure of the biogenic Mn oxide spectra is similar to that of abiotic Mn oxide (HMO or δ-MnO_2) and birnessite (Figure 9.8), where fitting revealed 3.3 ± 1.0 atoms of O at 1.89 Å in the first shell and 2.5 ± 0.8 atoms of Mn at 2.85 Å in the second shell. As compared with poorly crystalline birnessite, todorokite, and pyrolusite (Table 9.1), the local environment of biogenic Mn oxide reveals the ratio of the coordination numbers in the first to second shells was approximately 1:1 consistent with the phyllomanganate family. Furthermore, the first and second shell distances are also in agreement with the birnessite structure. Jürgensen et al. (2004) too concluded that the *L. discophora* structure belonged in phyllomanganate family as do *Bacillus sp* SG-1 (Bargar et al., 2005) and *P. putida* MnB1 (Villalobos et al. 2003). Interestingly, the local structure of the biogenic Mn oxide-coated bacteria after aging 4 months was similar to that of

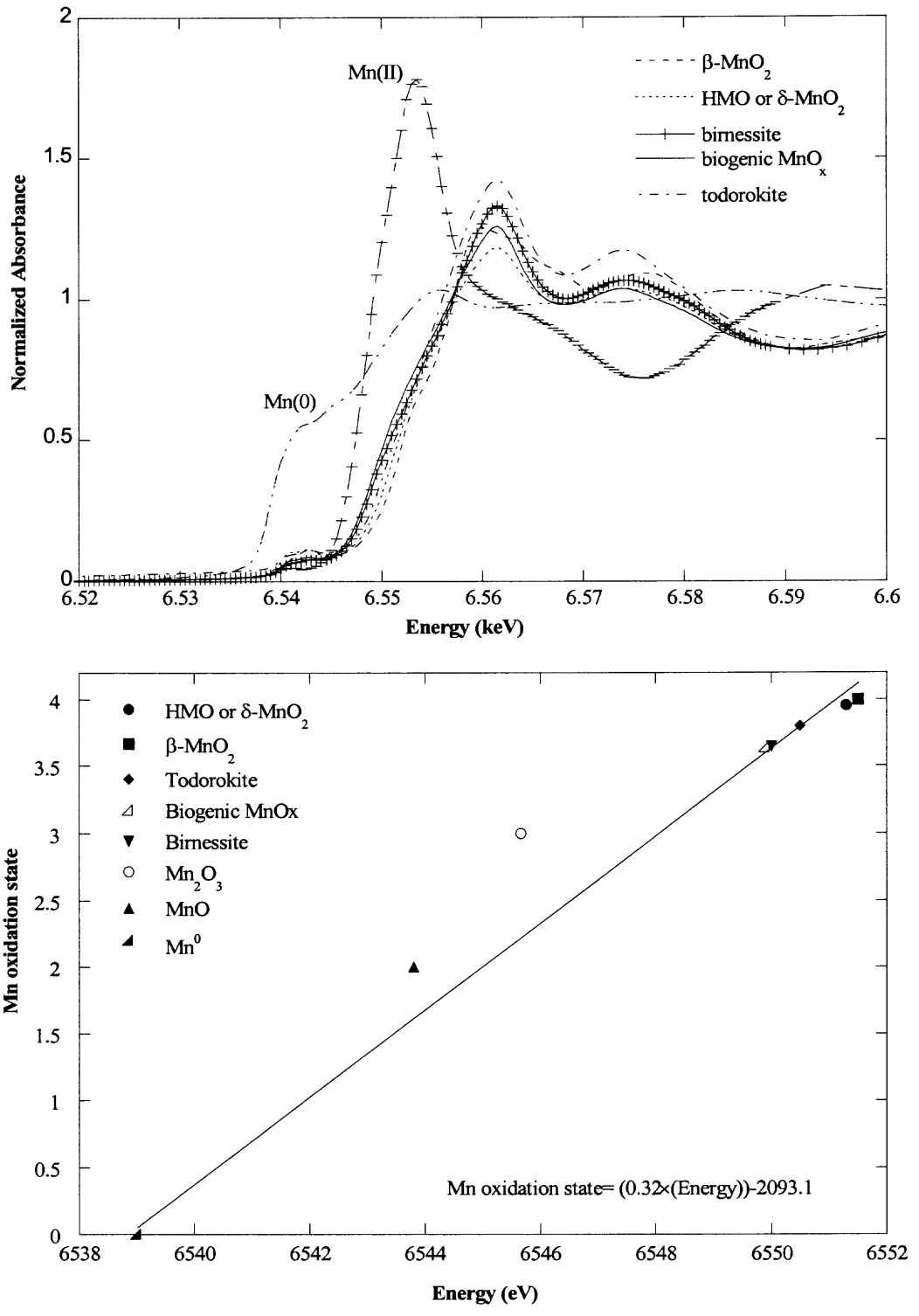

Figure 9.7 (a) Mn K-edge XANES spectra of all standards and samples after the background removal and normalization with a zero order polynomial over 6.639 to 6.739 keV above the edge. (b) Correlation between the position of edge energy (E_0) and theoretical average oxidation state of Mn standards and samples.

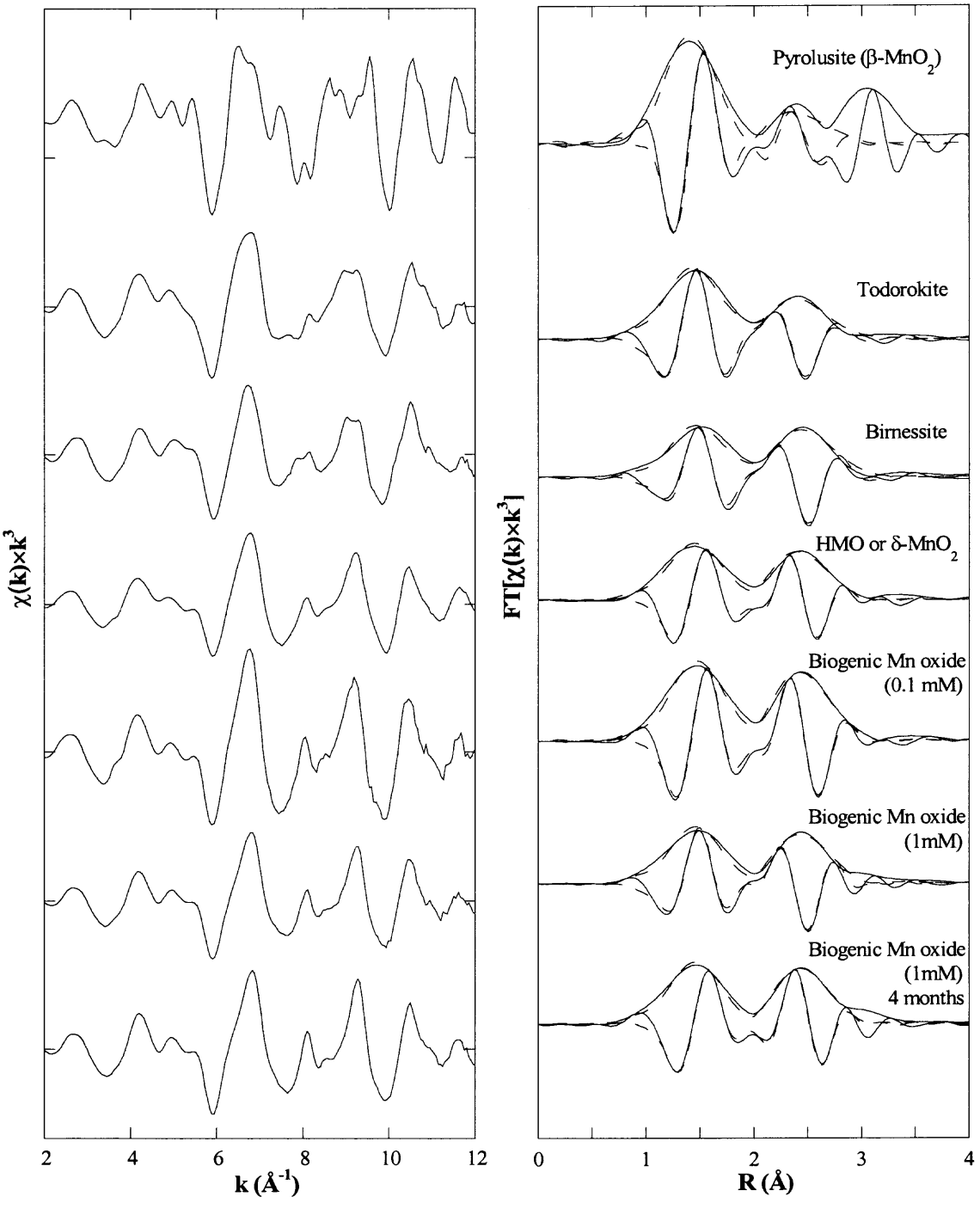

Figure 9.8 Mn K-edge $\chi(k) \cdot k^3$ spectra of Mn standards and samples collected at 25 °C along with Fourier transformed $\chi(k) \cdot k^3$ spectra over 2.20 to 11.88 $Å^{-1}$ and fitted over 0.50 to 3.10 Å. Solid lines represent the data and dashed lines are the fit.

Table 9.1 XAS Fitting Results of Biogenic and Biogenic Mn Oxides at Mn K-Edge

	O			Mn			ΔE_0	%Res
	N	R (Å)	σ (Å^2)	N	R (Å)	σ (Å^2)	(eV)	
Biogenic Mn oxide (PY) 0.1 mM	4.5	1.89	0.002	4.6	2.86	0.006	-2.5	9.2
Biogenic Mn oxide (PY) 1.0 mM	3.2	1.89	0.003	2.5	2.86	0.004	-2.1	14.4
Biogenic Mn oxide (PY), 4-m 1.0 mM	3.6	1.88	0.003	2.5	2.85	0.003	-2.5	14.1
Abiotic Mn oxide (HMO or δ-MnO_2)	3.5	1.89	0.003	2.8	2.85	0.005	-4.7	8.6
Birnessite	6.0	1.91	0.005	6.0	2.99	0.005	5.8	6.0
Todorokite	5.5 (6)	1.89 (1.90)	0.001	4.5 (4)	2.88 (2.90)	0.011	-4.5	9.1
Pyrolusite (β-MnO_2)	5.5 (6)	1.88 (1.88)	0.002	2.0 (2)	2.87 (2.87)	0.005	-7.7	15.6

Mn K-edge $\chi(k) \cdot k^3$ spectra were Fourier transformed over 2.20 to 11.88 Å^{-1} in k-space and fitted over 0.50 to 3.10 Å in r-space. N, R, and σ^2 represent the coordination number, distance, and variance. The quality of fits for N_1, N_2, R, and σ^2 are ± 20%, ± 40%, ± 0.02, and ± 5%, respectively.

freshly precipitated Mn oxide (Figure 9.8 and Table 9.1). This observation suggests that the presence of the polysaccharide sheath may inhibit transformation to a more crystalline phase even as the bacteria underwent lysis potentially creating a more reduced condition.

Overall, the biogenic Mn oxide exhibits a nano-particle, nanocrystalline structure that is associated with the polysaccharide sheathed *L. discophora* SP-6. Moreover, the surface area and surface charge were consistent with abiotic hydrous Mn oxide, while the microporosity increased. Based on its surface properties, the results suggest that this biogenic Mn oxide is an important surface in the environment.

9.3 Summary

Biogenic manganese oxides are often present as coatings on mineral substrates or associated with extracellular polymeric sheath. Because of the oxides importance in sequestering metal contaminants, its formation, characterization, and encrustation were studied. *L. discophora* is a sheath-forming organism where Mn oxide precipitates on the organism's surface. A nano-particulate Mn oxide coats the sheathed bacteria forming a dendritic biofilm structure, and at a loading of 6×10^{-5} mole Mn mg^{-1} cell, the pH point of zero net proton charge (pH_{znpc}) was 2.5 ± 0.5 consistent with abiotic Mn oxide (pH_{znpc} of hydrous Mn oxide (HMO) ~ 2.35). On the other hand, the polysaccharide sheathed organism exhibited a negative surface charge for the entire pH range. The oxidation state of biogenic Mn oxide was relatively close to that of birnessite (~3.7) and the local structure around the Mn ion consisted of 3.3 ± 1.0 atoms of O at 1.89 Å in the first shell and 2.5 ± 0.8 atoms of Mn at 2.85 Å in the second shell; this coordination environment is consistent with the phyllomanganate family. These results demonstrate that the surface properties of the coated aggregated bacteria are dominated by the nano-particulate Mn oxide.

CHAPTER 10

ZINC SORPTION MECHANISMS ONTO SHEATHED *LEPTOTHRIX DISCOPHORA* SP-6 AND THE IMPACT OF NANOPARTICULATE MN OXIDE COATINGS

In this chapter, Zn interactions with sheathed *L. discophora* SP-6 and the impact of biogenic Mn oxide coatings were investigated. Experiments were conducted by using both macroscopic and spectroscopic techniques to assess the affinity and site capacity of each component on the heterogeneous surface and to elucidate the sorption mechanisms on *L. discophora* SP-6, isolated extracellular polymeric sheath from *L. discophora* SP-6, and biogenic Mn oxide coated bacteria. Principle component (PCA) and linear combination (LC) analyses were applied to estimate the contributions from functional groups on the cell wall and sheath. Furthermore, Zn and Mn K-edge XAFS spectra were collected from the *L. discophora* SP-6 exposed to Zn and Mn as well as from long-term studies with up to 7 months aging.

10.1 Macroscopic Sorption Studies

Zn complexation with the bacterial cell wall and EPS was investigated as a function of pH, ionic strength, and metal concentration. Adsorption edges (Figure 10.1a) reveal a greater affinity for sheathed *L. discophora* SP-6 than the isolated extracellular polymeric substrate. At pH greater than 6, almost 50% of Zn sorbed to the bacteria can be attributed to the EPS sheath; Toner et al. (2005) observed similar results with EPS from the *P. putida* biofilm.

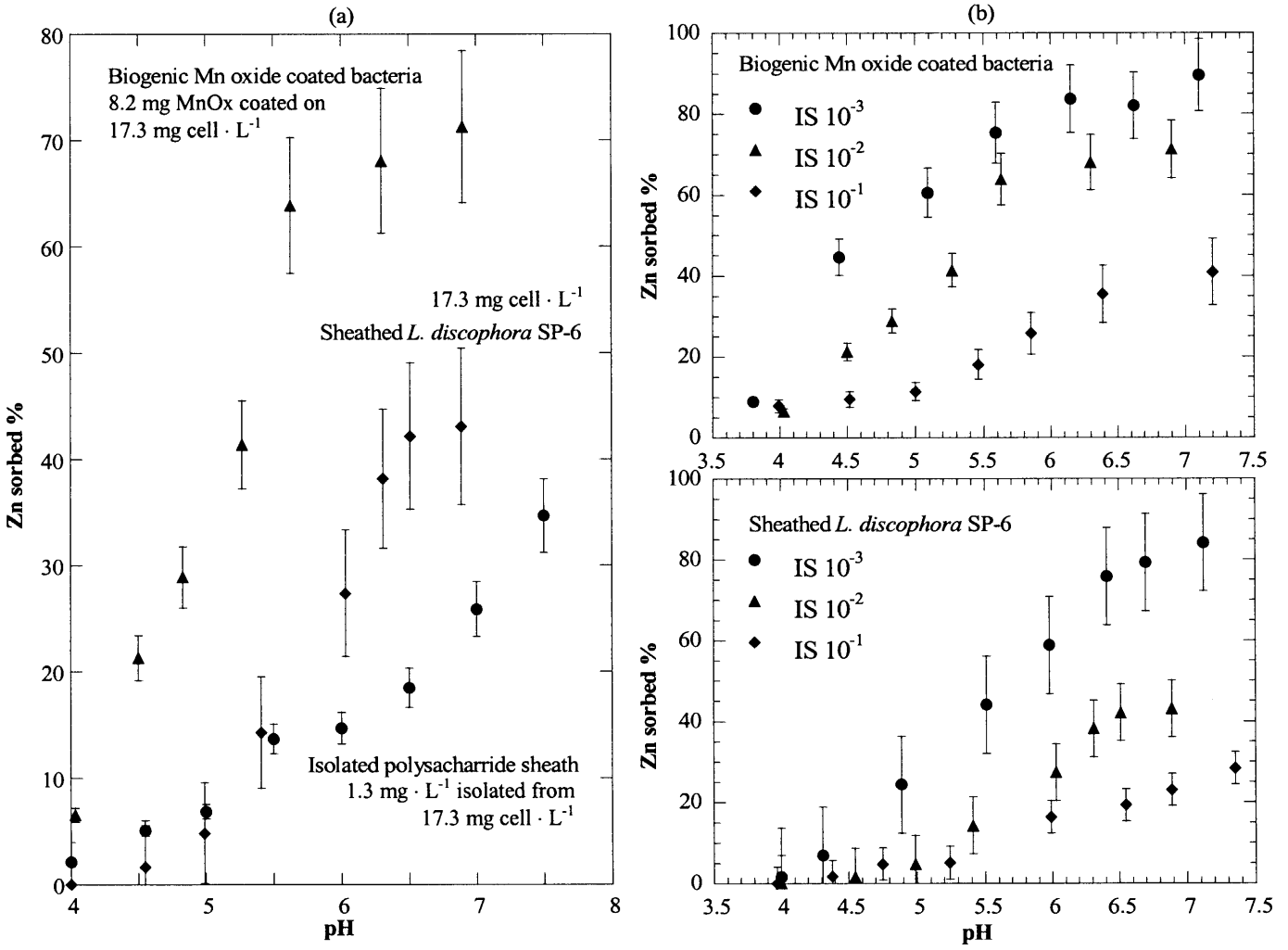

Figure 10.1 (a) Zn adsorption edges of *L. discophora* SP-6, biogenic MnO_x coated bacteria, and isolated polysaccharide sheath, 5×10^{-6} M $[Zn]_o$, ionic strength (IS)10^{-2} M $NaNO_3$, and 25 °C; (b) Zn adsorption edges of *L. discophora* SP-6 and biogenic MnO_x coated bacteria as a function of IS (10^{-3} to 10^{-1} M $NaNO_3$).

Not surprisingly, in the presence of the biogenic oxide coating (8.6 mg Mn oxide · (17.3 mg cell)$^{-1}$) sorption increased greater than approximately two times that for *L. discophora* SP-6 without the oxide. Moreover, an ionic strength effect is seen (Figure 10.1b) for adsorption to sheathed *L. discophora* SP-6 with and without the biogenic oxide coating, as adsorption decreased with increasing ionic strength. However, the biogenic Mn oxide exhibits a greater affinity for Zn potentially suppressing the electrostatic effect of the EPS sheath. Consequently, biogenic Mn oxide and the EPS sheath play important roles in Zn sorption. Isotherms were also conducted with the EPS sheath, the sheathed *L. discophora* SP-6, and the biogenic Mn oxide coated bacteria (Figure 10.2). Data from a single substrate (sheathed extracellular polymeric substrate) were modeled with the Langmuir isotherm, $q = \frac{C_t K[Zn]_{eq}}{1 + K[Zn]_{eq}}$ where C_t and K are the site capacity (mol of Zn · g^{-1}) and equilibrium constant (L · mole of Zn^{-1}), respectively. For the binary surface of the sheathed *L. discophora* SP-6, the equilibrium constant (K) or relative affinity of sheathed *L. discophora* SP-6 has contributions from both the bacterial cell wall and the extracellular polymeric substrate resulting in the following equation

$$q = \frac{C_t K[Zn]_{eq}}{1 + K_{L.\,discophora\ SP-6}[Zn]_{eq} + K_{sheath}[Zn]_{eq}} \qquad (9.1)$$

This sheathed cell wall site capacity (2.7×10^{-4} mole of Zn · g^{-1} cell) is similar to that reported for *B. subtilis* (1×10^{-4} mole of Zn · g^{-1} cell) (Fein et al. 2001), *Penicillium chrysogenum* (2×10^{-4} mole of Zn · g^{-1} cell) (Sarret et al. 1998), and the *P. putida* biofilm (greater than 6.4×10^{-4} mole of Zn · g^{-1} cell) (Toner et al. 2005).

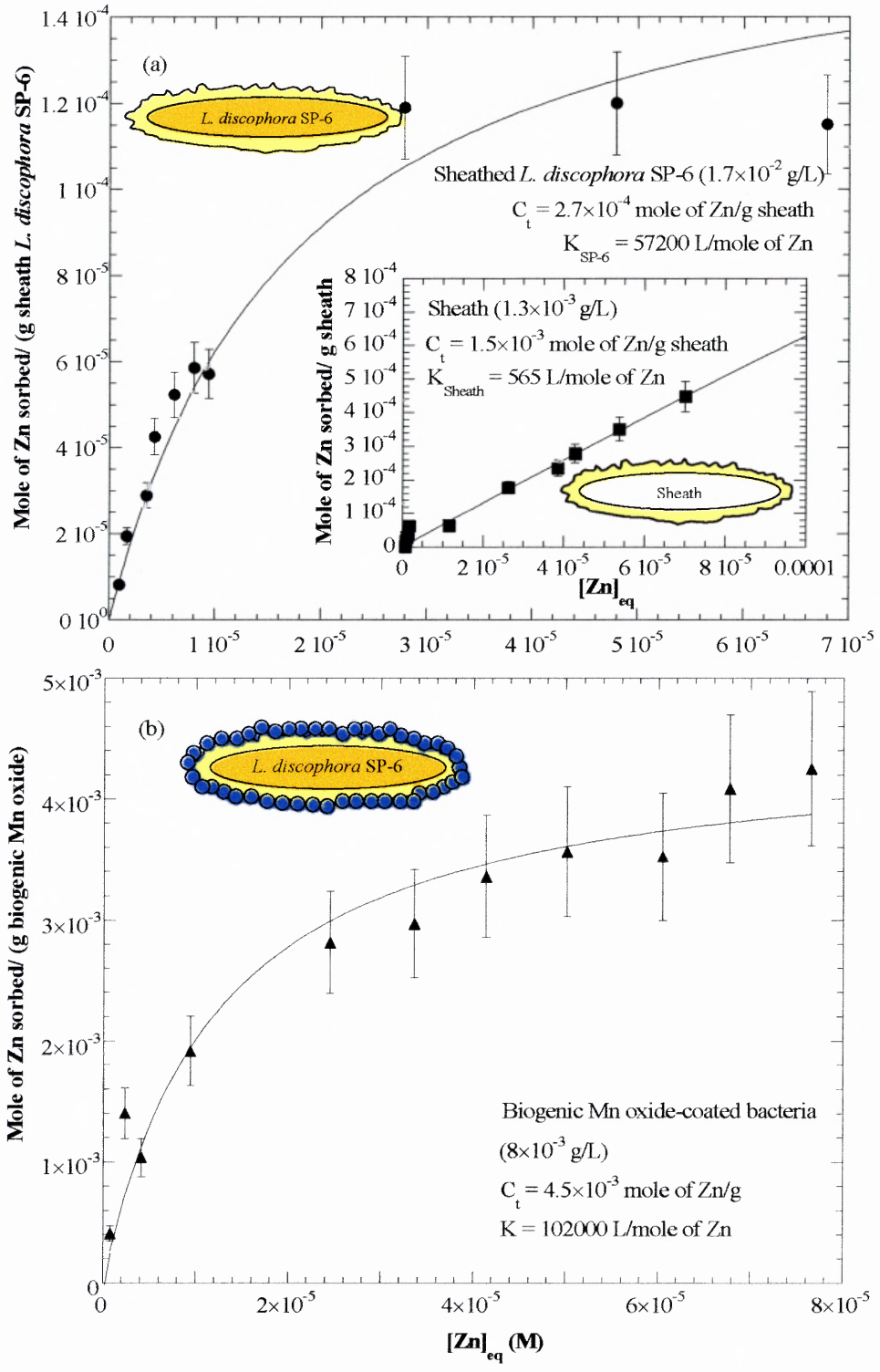

Figure 10.2 Adsorption isotherms at pH 6.6, IS 10^{-2} ($NaNO_3$), and 25°C for (a) sheathed *L. discophora* SP-6 (1.7×10^{-2} g/L) and the EPS (1.3×10^{-3} g/L), and (b) biogenic Mn oxide-coated bacteria (8×10^{-3} g/L).

Although the site capacity of bacteria was one order magnitude lower than that of the EPS sheath, the relative affinity (Figure 10.2a) of bacterial cell wall was three orders of magnitude greater; these two surfaces appear to provide low- and high- affinity sites on this bacterial biofilm. The biogenic Mn oxide-coated (sheathed) *L. discophora* SP-6 (Figure 10.2b) shows a significant increase in Zn sorption compared to the EPS and sheathed organism (Figure 10.2a); the system is well modeled with a single site Langmuir isotherm. The site capacity of biogenic Mn oxide (4.5×10^{-3} mole of Zn $\cdot$ g^{-1} Mn oxide) was approximately twenty times greater than that of the sheathed *L. discophora* SP-6 (2.7×10^{-4} mole of Zn $\cdot$ g^{-1} cell), and interestingly equivalent to that of the biogenic Mn oxide *P. putida* bioflim (4.1×10^{-3} mole of Zn $\cdot$ g^{-1} MnO_2) (Toner et al. 2006). Moreover, the relative affinity of biogenic Mn oxide coated bacteria ($K \sim 102{,}000$ L $\cdot$ mole of Zn^{-1}) was much greater than that of sheathed *L. discophora* SP-6, which is consistent with adsorption edges.

In the previous chapter on morphological properties of this biogenic oxide-coated organism, on the morphological properties of this biogenic oxide-coated organism, we observed that the nano-particulate oxide exhibits microporosity suggesting long-term sorption may be significant. Therefore, transient sorption was studied using CBC experiments (Figure 10.3), where the amount sorbed gradually increased due to intraparticle surface diffusion: from 1.5×10^{-3} to 4.1×10^{-3} mole of Zn $\cdot$ g^{-1} Mn oxide (Zn:Mn molar ratio of 0.13 to 0.34) over 7 months. In modeling, we assumed that the nano-particulate Mn oxide is spherical and that the internal sites are no different than the external ones.

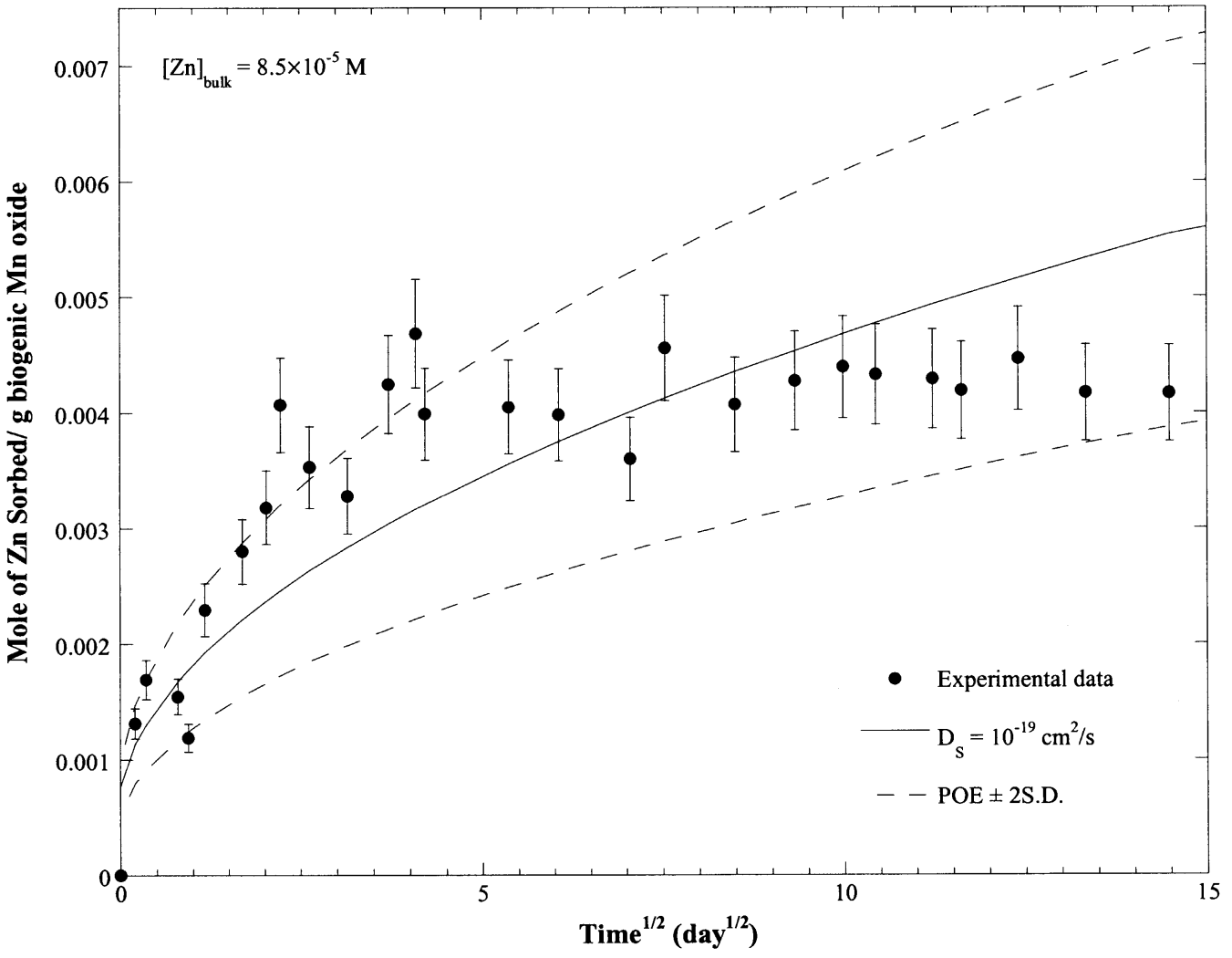

Figure 10.3 CBC studies of Zn sorption to biogenic Mn oxide-coated bacteria (8.72×10^{-3} g MnO_x/L) at 25°C, 10^{-2} ionic strength with $NaNO_3$. Zn system was maintained at pH 6.6 and a $[Zn]_{bulk}$ of 8.5×10^{-5} M.

The particle size distribution (PSD) of the biogenic Mn oxide was based on the change in volume between oxide-coated bacteria and the sheathed *L. discophora* SP-6. Assuming the oxide PSD is proportional to the initial PSD of the coated system and given that spherical oxide particles range from 100 nm to 2 μm which deposited on ellipsoid aggregated bacteria, a Gaussian distribution was invoked. At a given time, summation of Zn sorbed internally for each particle size times the number of particles over the entire particle distribution are equivalent to concentration of Zn sorbed internally. The internal sorbed plus that sorbed to external surface provides the total Zn sorbed. Minimizing the variance between experimental data and modeling results, the only fitting parameter is surface diffusivity (see e.g. Axe and Anderson, 1995, Trivedi and Axe, 1999) (Figure 10.3). Errors associated with the model from the propagation of errors (POE) method (Ku, 1966) are also shown. The POE analysis accounts for the error in the distribution coefficient describing the mass adsorbed to the surface. Data are consistent with the model. Sorption to biogenic Mn oxide-coated bacteria revealed a surface diffusivity (D_S) for Zn of approximately 10^{-19} cm^2/s, which is two orders of magnitude smaller than that for abiotic hydrous manganese oxide (HMO) (10^{-17} cm^2/s). The smaller D_S value may be due to a reduced pore size distribution in the nano-particulate oxide as compared to the abiotic system. The biogenic Mn oxide present as coatings on bacteria acts as a sink for metal contaminants in the subsurface environment.

In modeling, the assumption that internal sites are no different than external ones has been demonstrated recently in spectroscopic results for metals ions such as Zn, Ni, and Pb sorbed to abiotic HMO (Boonfueng et al. 2006; Trivedi and Axe, 2001). In this 7-month CBC study where an additional 173% of the sites became occupied as compared to

that sorbed after a 4 hr contact time, the local structure was investigated and discussed below.

10.2. X-ray Absorption Spectroscopic Studies: Zn-K Edge XAS

XAS spectra of Zn standards ($Zn(NO_3)_{2(aq)}$, $Zn_3(PO_4)_{2(S)}$, and Zn complexed with EDTA and citrate) reveal the zinc ion in the nitrate solution has only one backscattering envelope of 5.6 ± 0.5 oxygen atoms at 2.06 ± 0.02 Å (Figure 10.4 and Table 10.1), consistent with a fully hydrated ion in the aqueous phase (Richens, 1997). Surface binding sites on the bacterial cell wall (e.g., carboxyl, phosphoryl, and hydroxyl groups) can potentially be illustrated using $Zn_3(PO_4)_{2(S)}$ and Zn complexed with EDTA and citrate corresponding to the phosphoryl and carboxyl groups. Spectra for $Zn_3(PO_4)_{2(S)}$ (Table 10.1) is consistent with the powder diffraction file (Hille and Jones, 1976). In citrate complexation, approximately six carboxyl groups ($Zn[citrate]_2^{-4}$) are present based on Zn speciation at pH 7, whereas there are four carboxyl groups in the EDTA complex. In either case however, the first shell is consistent with octahedral coordination. PCA analysis (Figure 10.5) reveals SPOIL functions less than 1 (an excellent fit) for Zn citrate and $Zn_3(PO_4)_{2(S)}$ (or Zn phosphate), whereas the SPOIL function of Zn EDTA was approximately 3.4 indicating a fair fit. Therefore, Zn citrate and Zn phosphate were applied as components for the PCA LC analysis conducted on samples.

For Zn sorbed on the EPS sheath, the best fit resulted in a 95 ± 10% contribution from Zn citrate (Figure 10.6). On the other hand for sorption to the sheathed *L. discophora* SP-6, the best fit was acquired with 84 ± 10% from Zn phosphate and 16 ± 10% from Zn citrate (Figure 10.6), which again is consistent with results on *P. putida*

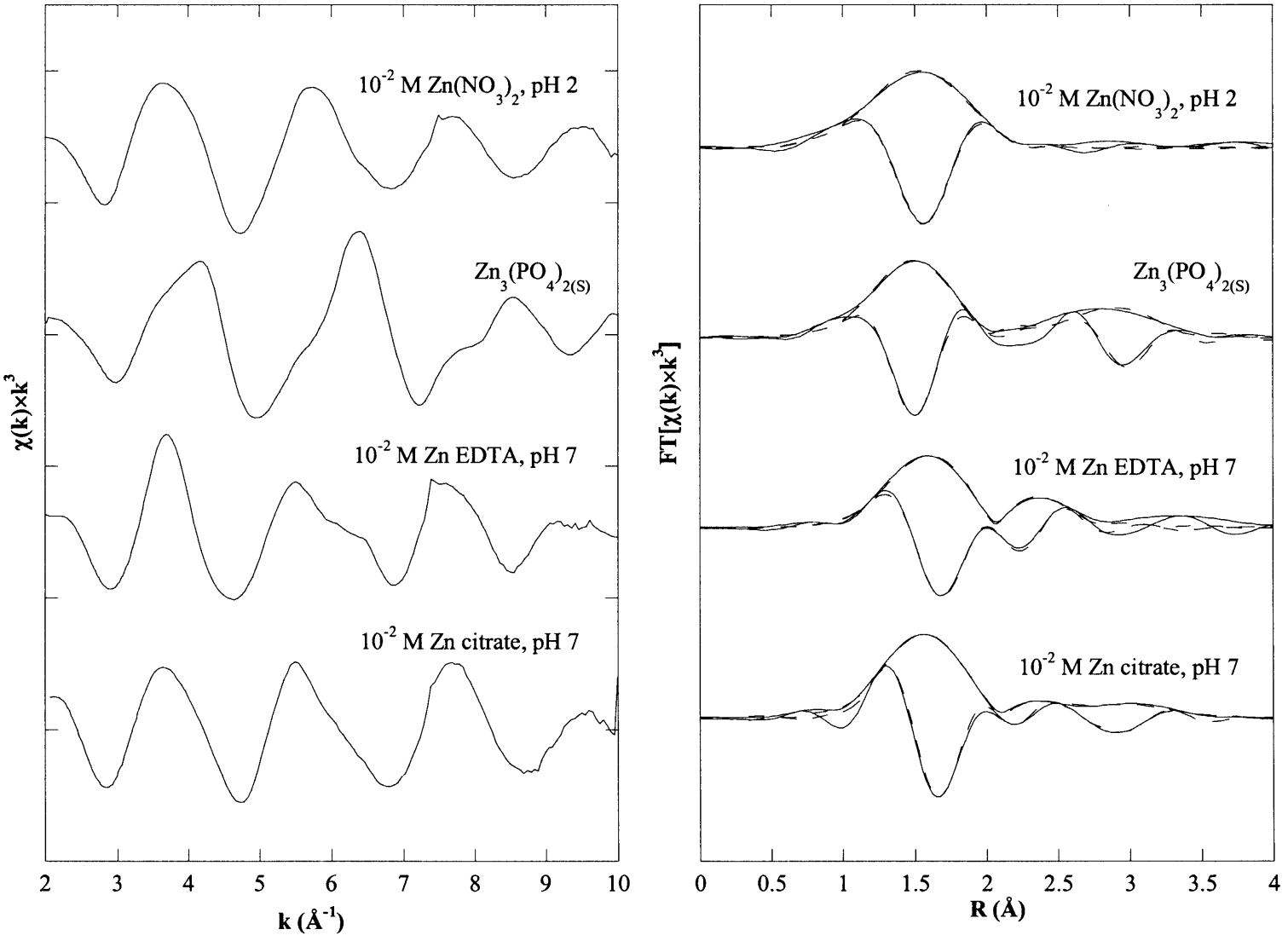

Figure 10.4 Zn K-edge $\chi(k) \cdot k^3$ spectra of standards collected at 25 °C along with Fourier transformed $\chi(k) \cdot k^3$ spectra over 2.20 to 10.00 $Å^{-1}$ and fitted over 0.50 to 3.70 Å. Solid lines represent the data and dashed lines are the fit.

Table 10.1 XAS Fitting Results for Zn Standards and Sorption on *L. discophora* SP-6, Isolated Polysaccharide Sheath, Biogenic Mn Oxide-coated Bacteria, and Abiotic Mn Oxide (HMO)

	O						ΔE_o	%Res
	N	R (Å)	σ (Å^2)	N	R (Å)	σ (Å^2)	(eV)	
$Zn(NO_3)_{2(aq)}$ 10^{-2} M, pH 2	5.7	2.06	0.013	-	-	-	-1.64	7.3
	O			C				
Zn citrate, 10^{-2} M, pH 7 72% $Zn[citrate]_2$, 28%Zn[citrate]	5.4	2.05	0.004	6.2	2.87	0.012	-1.32	16.7
Zn EDTA, 10^{-2} M, pH 7 100% $Zn[EDTA]^{2-}$	5.4	2.08	0.009	8.1	2.90	0.009	4.81	6.8
	O			P				
$Zn_3(PO_4)_{2\,(S)}$	3.8	1.94	0.008	4.4	3.50	0.013	7.21	18.4
Zn-*L. discophora* SP-6 $\Gamma = 10^{-4}$, pH 6.6, IS 10^{-2}	7.2	1.97	0.010	2.1	3.49	0.001	7.10	10.8
Zn-EPS $\Gamma = 10^{-4}$, pH 6.6, IS 10^{-2}	6.1	2.06	0.006	-	-	-	-1.19	5.2
	O			Mn				
Zn-HMO $\Gamma = 10^{-4}$, pH 6.6, IS 10^{-2}	6.6	2.05	0.009	3.9	3.45	0.006	-3.48	16.6
Zn-Mn oxide coated bacteria $\Gamma = 10^{-4}$, pH 6.6, IS 10^{-2}	6.9	1.99	0.014	6.3	3.34	0.018	-3.67	12.5

Zn K-edge $\chi(k) \cdot k^3$ spectra were Fourier transformed over 2.00 to 10.00 Å^{-1} and fitted over 0.50 to 3.70 Å. Γ is surface loading (Γ= mole of Zn $\cdot$ g^{-1} solid). EPS represent sheathed extracellular polymeric substances N, R, and σ^2 represent the coordination number, distance, and variance. The quality of fits for N_1, N_2, R, and σ^2 are ± 20%, ± 40%, ± 0.02, and ± 5%, respectively. The amplitude reduction factor (S_o^2) was fixed at 0.81.

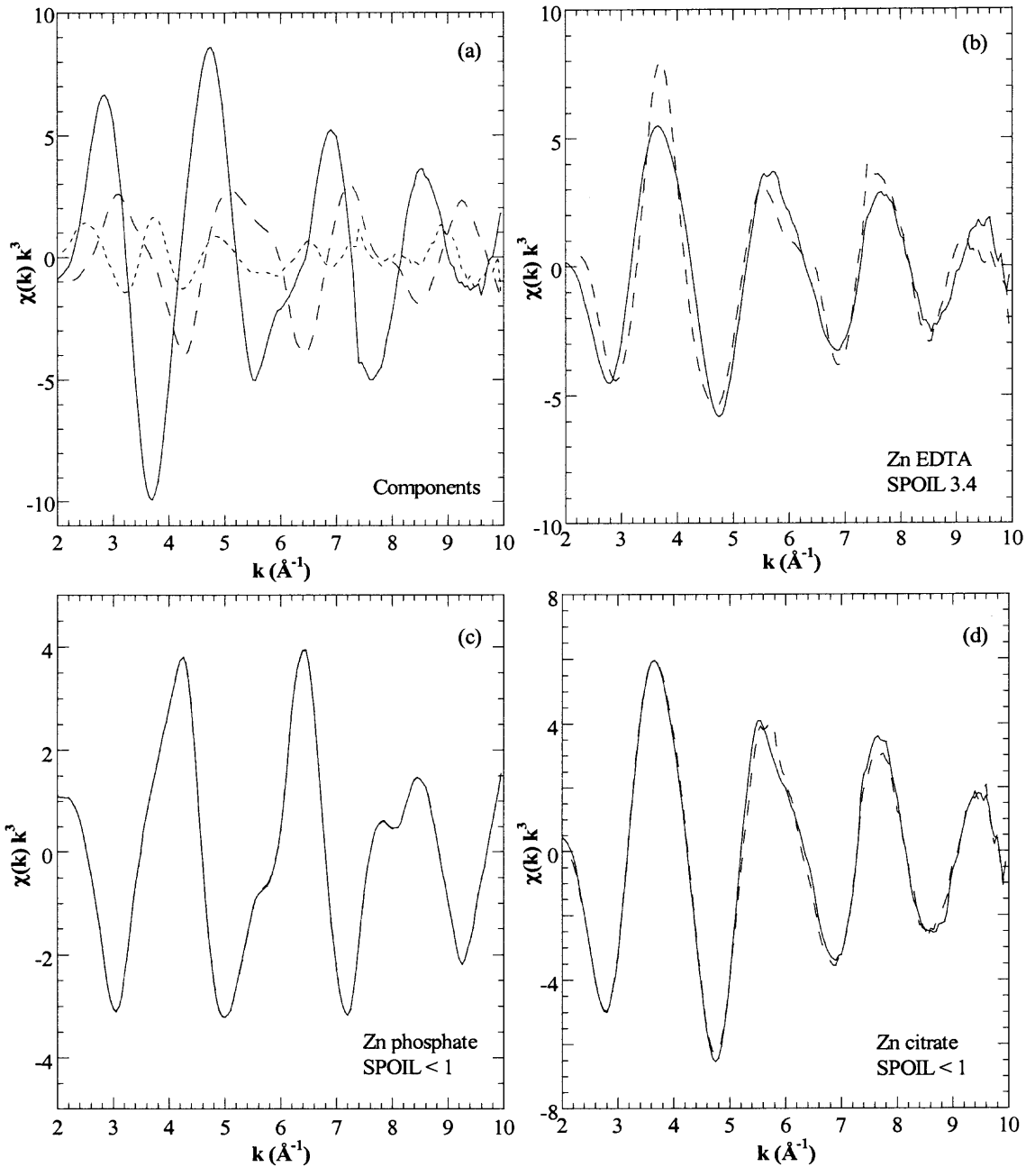

Figure 10.5 Principle component analysis (a) three components of the Zn XAS of standards, (b-d) the target transformation analysis for the standards Zn EDTA, Zn citrate, and Zn phosphate, respectively.

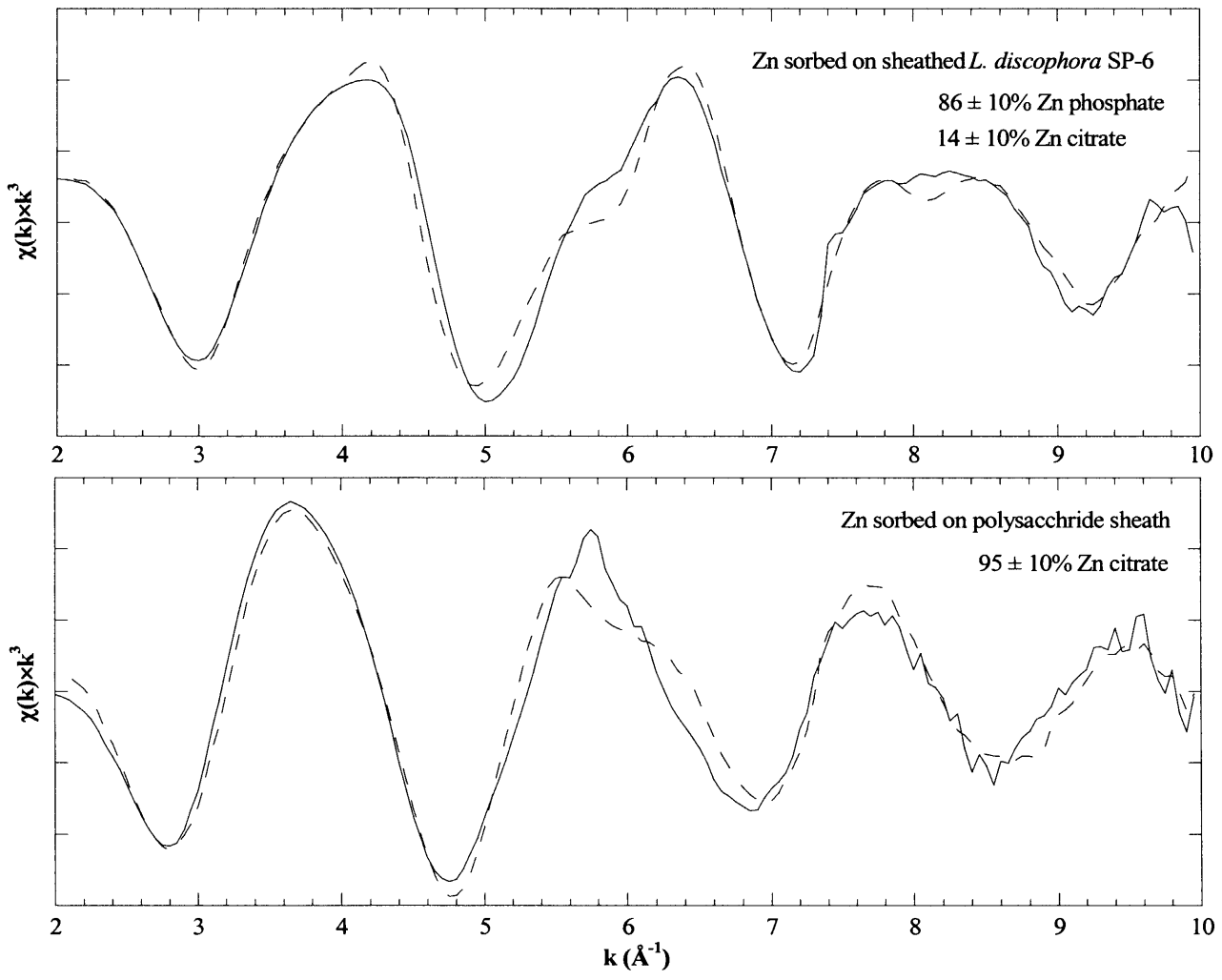

Figure 10.6 LC and PCA of Zn K-edge $\chi(k) \cdot k^3$ spectra of Zn sorbed on *L. discophora* SP-6 and isolated polysaccharide sheath using Zn citrate and $Zn_3(PO_4)_2$ as standard components. Solid lines represent the data and dashed lines are the fit.

bioflim (85% Zn phosphoryl and 23% Zn carboxyl) (Toner et al. 2005). The contribution from Zn citrate (16%) may represent the EPS sheath that surrounds the bacterial cells (~10% wt of biomass). XAS analysis for Zn sorbed on *L. discophora* SP-6 (Figure 10.7 and Table 10.1) revealed 7.2 atoms of O at 1.97 ± 0.02 Å in the first shell and 4 atoms of P at 3.50 ± 0.02 Å in the second shell; this structure suggests inner-sphere complexation with the phosphoryl group on the bacterial cell wall. Based on potentiometric titrations, Fein et al. (2001) applied a similar structure with the phosphoryl group (≡POH) for Zn sorbed on *B. subtilis*. In contrast, sorption to EPS was relatively similar to aqueous $Zn(NO_3)_2$ and Zn citrate spectra (Figures 10.4 and 10.7) revealing only one shell of 6 O atoms at 2.06 ± 0.02 Å (Table 10.1), indicative of an outer-sphere complex. This EPS sheath potentially plays an important role in the electrostatic effect observed in the adsorption edges.

For the biogenic Mn oxide-coated bacteria, the spectra are unique (e.g., feature at 6 $Å^{-1}$) as compared to that of Zn sorbed on *L. discophora* SP-6 (Figure 10.7). On the other hand, these sorption spectra for the biogenic Mn oxide-coated bacteria (10^{-4} mole of $Zn \cdot g^{-1}$ Mn oxide (Zn:Mn molar ratio of 0.0083)) were relatively similar to that of Zn sorbed on abiotic HMO (10^{-4} mole of $Zn \cdot g^{-1}$ HMO (Zn:Mn molar ratio of 0.087)); however, a slight shift in the RSF is observed for sorption to the biogenic oxide indicating a shorter average radial distance (Figure 10.7). The first shell was fit well with oxygen and second shell contributions were attempted with C, P, Zn, Mn, and O as well as combinations of these, but fitting was only accomplished with Mn. The amplitude of the second shell for Zn sorbed on HMO was greater than that for biogenic Mn oxide and may be due to a greater degree of disorder (σ^2) for the latter consistent with adsorption to

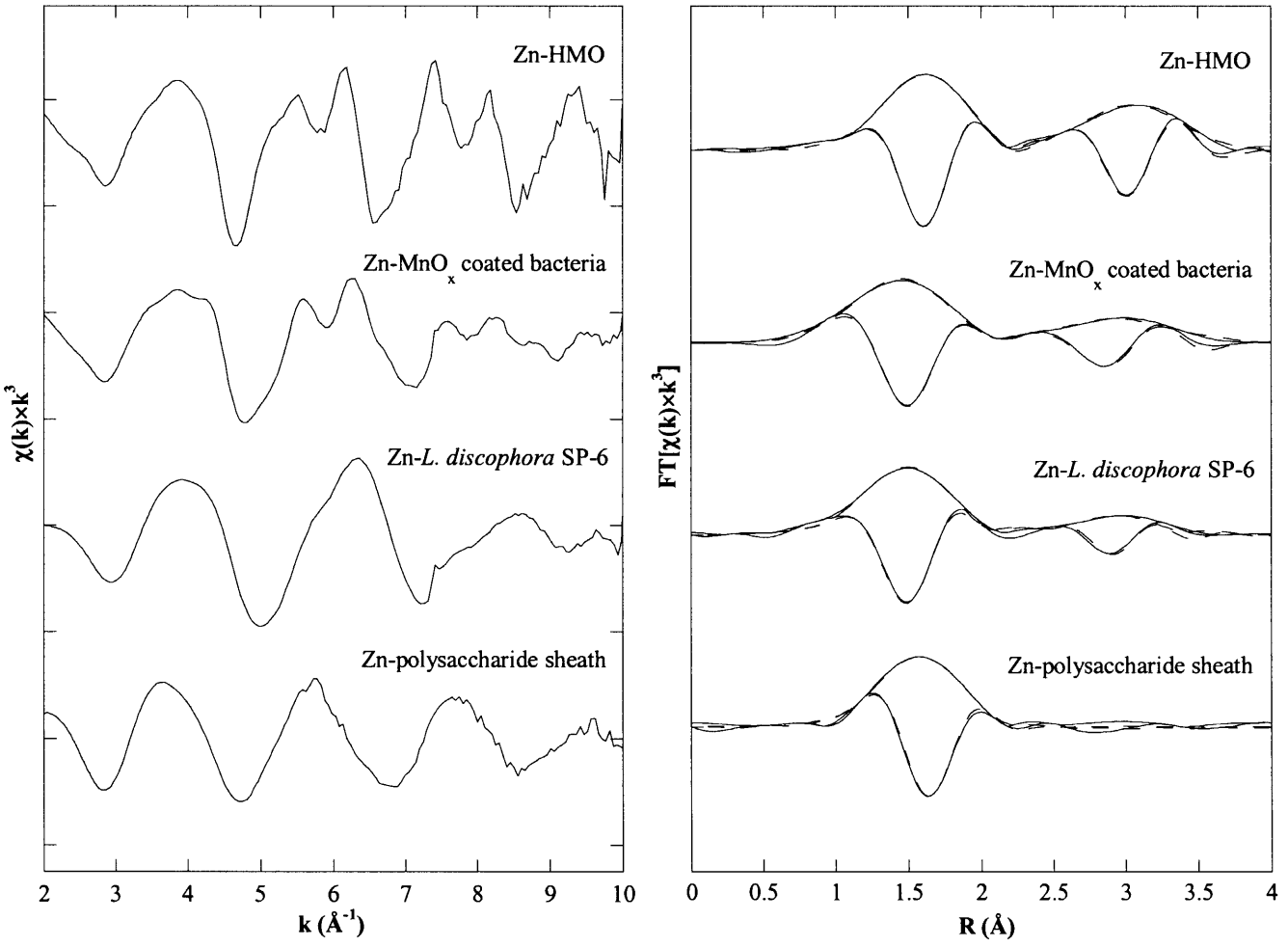

Figure 10.7 Zn K-edge $\chi(k) \cdot k^3$ spectra of sorption samples as a function of surface (*L. discophora* SP-6, isolated EPS, biogenic Mn oxide-coated bacteria, and abiotic Mn oxide (HMO)) with 10^{-4} mole of Zn $\cdot$ g^{-1} solid, pH 6.6, IS 10^{-2} M $NaNO_3$ along with Fourier transformed $\chi(k) \cdot k^3$ spectra over 2.20 to 10.00 Å^{-1} and fitted over 0.50 to 3.70 Å. Solid lines represent the data and dashed lines are the fit.

a nano-particulate amorphous phase (Toner et al. 2006; Villalobos et al. 2005). The fitting revealed a first shell of 6.9 ± 0.9 atoms of oxygen at 1.99 ± 0.02 Å, while in the second shell 6.3 ± 1.2 atoms of manganese were found at 3.34 ± 0.02 Å. Interestingly, these bond distances are relatively similar to Zn sorbed on the biogenic Mn oxide *P. putida* biofilm (Toner et al. 2006), where sorption was attributed to tetrahedral coordination and tridentate cornering sharing complexes. However, in our study the first shell appears to be in octahedral coordination which is also seen in sorption to abiotic HMO, where the local environment consisted of 6.9 ± 0.9 atoms of oxygen at 2.05 ± 0.02 Å and 4.6 ± 1.2 atoms of manganese at 3.45 ± 0.02 Å; this structure is in agreement with that observed for Zn sorbed on birnessite (Manceau et al. 2002).

For the 7-month CBC sample, the local coordination of Zn sorbed on biogenic Mn oxide-coated bacteria consisted of 6.9 ± 0.9 atoms of oxygen at 2.00 ± 0.02 Å in the first shell and 4.9 ± 1.4 atoms of manganese at 3.34 ± 0.02 Å in the second shell. The sorption configuration was invariant as a function of contact time (4 hrs to 7 months) (Figure 10.8 and Table 10.2). Furthermore, there was no evidence of surface precipitation or solid solution formation as only Mn provided a good fit in the second shell. Although surface coverage of Zn increased from a Zn:Mn molar ratio of 0.13 to 0.34 after 7 months, the effect of surface coverage on the coordination environment was not observed in this study. However, others have reported this effect for Zn sorbed on birnessite (Manceau et al. 2002) and the biogenic Mn oxide *P. putida* biofilm (Toner et al. 2006) as when the Zn:Mn molar ratio increased from 0.0008 to 0.069 for the former and 0.06 to 0.37 for the latter where the sorption configuration changed from tetrahedral to octahedral coordination.

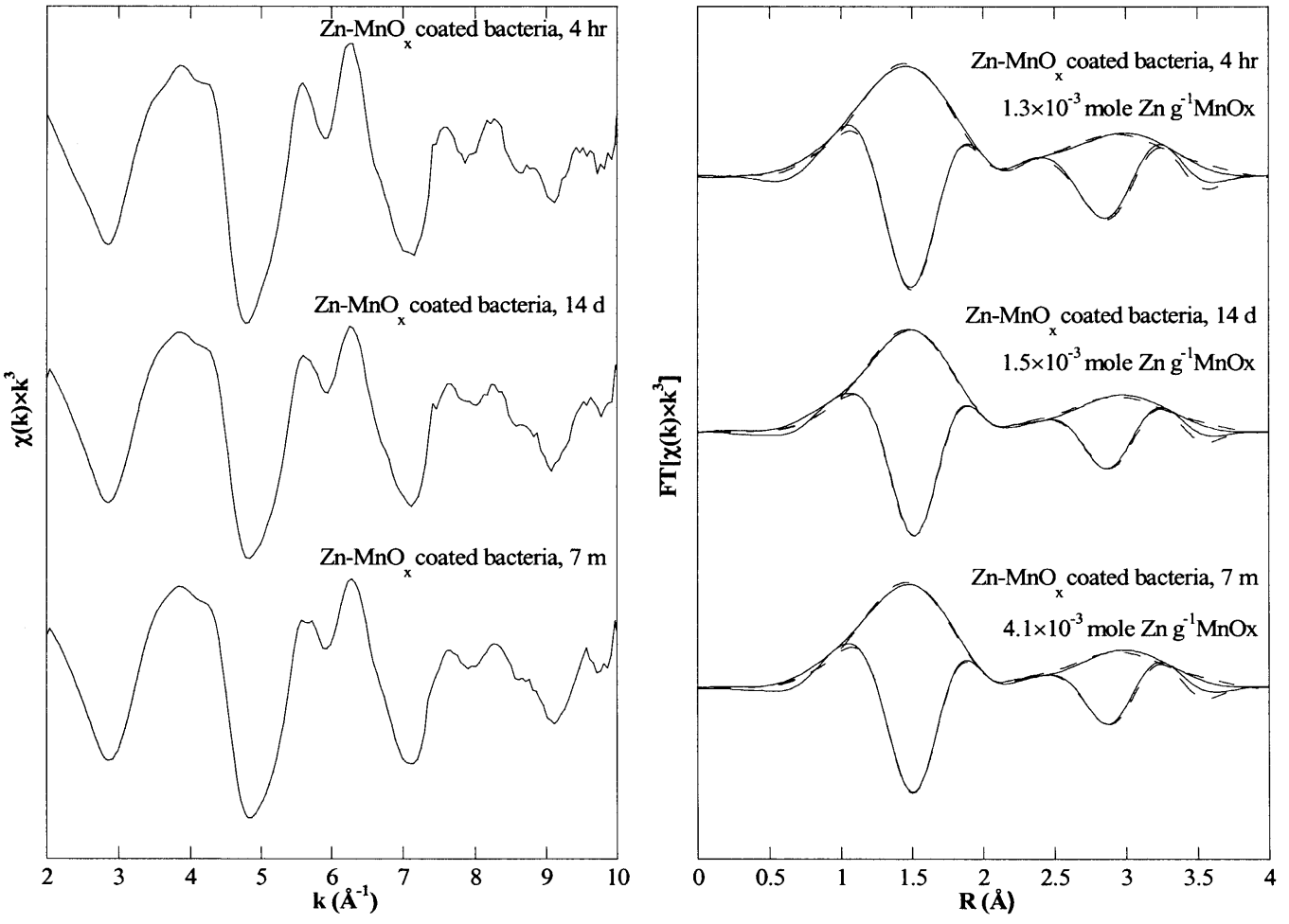

Figure 10.8 Zn K-edge $\chi(k) \cdot k^3$ spectra of Zn sorption onto biogenic Mn oxide-coated bacteria (with contact time of 4 hrs, 14 days, and 7 months) collected at 25 °C along with Fourier transformed $\chi(k) \cdot k^3$ spectra over 2.20 to 10.00 Å^{-1} and fitted over 0.50 to 3.70 Å. Solid lines represent the data and dashed lines are the fit.

Table 10.2 Fitting Results for the First (O) and Second (Mn) Shells of Zn Sorption on Biogenic Mn Oxide-coated Bacteria at pH 6.6 and IS 10^{-2} M $NaNO_3$ (as a function of contact times) and Zn Coprecipitation with Biogenic Mn Oxide-coated Bacteria

	O			Mn			ΔE_o	%Res
	N	R (Å)	σ (Å^2)	N	R (Å)	σ (Å^2)	(eV)	
Zn- Mn oxide coated bacteria, 4 hr $\Gamma=1.5\times10^{-4}$	6.9	1.99	0.014	6.3	3.34	0.018	-3.67	12.5
Zn- Mn oxide coated bacteria 14 day $\Gamma=1.5\times10^{-3}$	7.3	2.00	0.013	4.9	3.34	0.015	-2.28	10.9
Zn- Mn oxide coated bacteria 7 month $\Gamma=4.1\times10^{-3}$	7.8	1.99	0.014	4.4	3.34	0.015	-3.06	11.7
Zn-coprecipitate with MnO_x coated bacteria $\Gamma=2.9\times10^{-3}$	7.2	2.01	0.014	2.9	3.33	0.015	-1.53	12.9

Zn K-edge $\chi(k) \cdot k^3$ spectra were Fourier transformed over 2.00 to 10.00 Å^{-1} in k-space and fitted over 0.50 to 3.70 Å in r-space. Γ is surface loading (Γ= mole of Zn $\cdot$ g^{-1} MnO_x). N, R, and σ^2 represent the coordination number, distance, and variance. The quality of fits for N_1, N_2, R, and σ^2 are ± 20%, ± 40%, ± 0.02, and ± 5%, respectively. The amplitude reduction factor (S_o^2) was fixed at 0.81.

In a coprecipitation sample (2.9 $\times10^{-3}$ mole of Zn $\cdot$ g^{-1} Mn oxide (Zn:Mn molar ratio of 0.24)), the spectra (Figure 10.9) were identical to those of Zn sorbed on biogenic Mn oxide. Fitting revealed 7.0 ± 0.9 atoms of oxygen at distance of 2.01 ± 0.02 Å in the first shell and 2.9 ± 0.6 atoms of manganese at distance of 3.33 ± 0.02 Å in the second shell. Again, Zn forms inner-sphere complexes with biogenic Mn oxide.

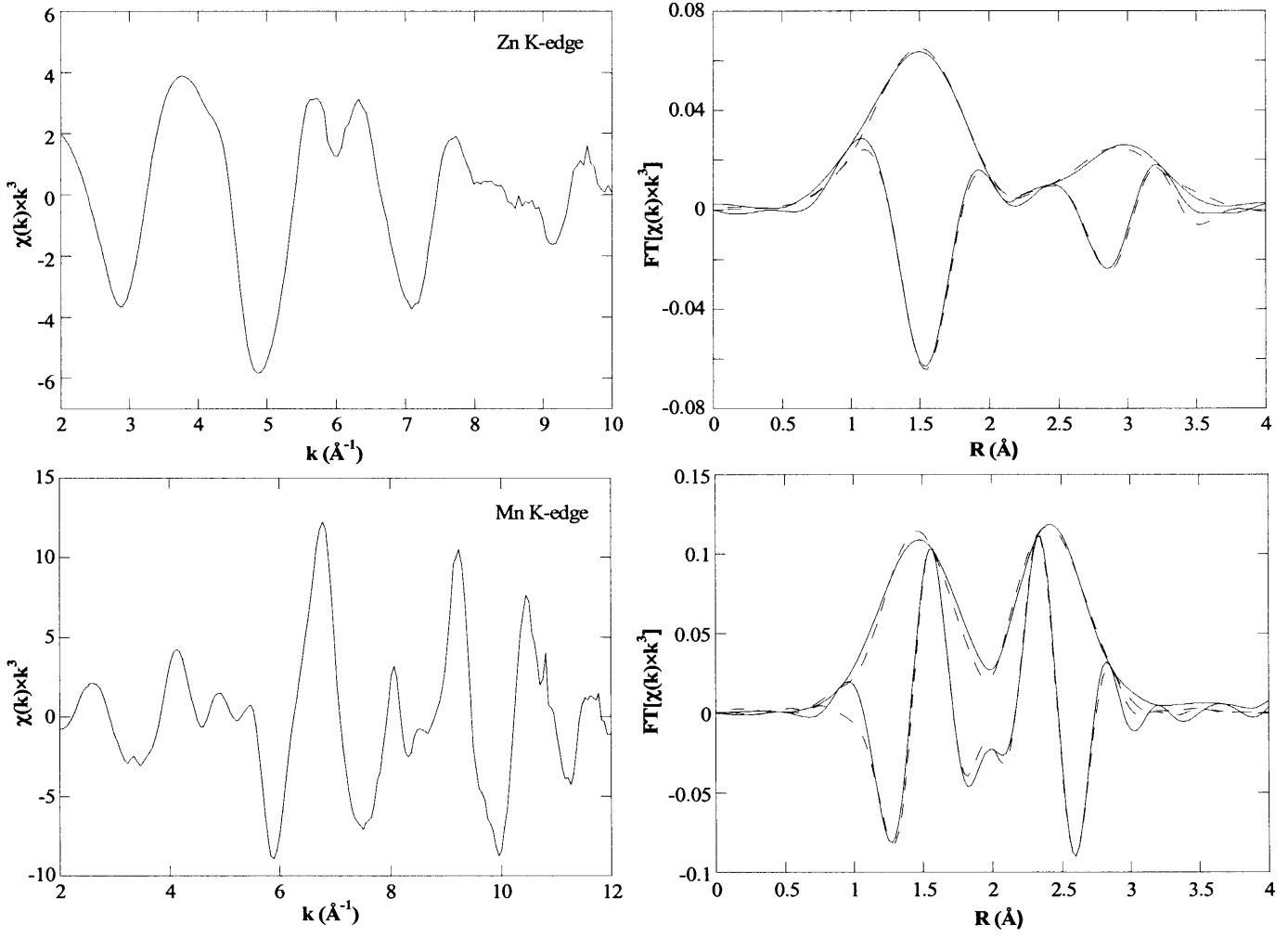

Figure 10.9 Zn K-edge and Mn K-edge $\chi(k) \cdot k^3$ spectra of Zn coprecipitation with biogenic Mn oxide-coated bacteria (Zn:Mn molar ratio of 0.29) collected at 25 °C along with Fourier transformed $\chi(k) \cdot k^3$ spectra over 2.20 to 10.00 $Å^{-1}$ for Zn and 2.20 to 11.88 $Å^{-1}$ for Mn and fitted over 0.50 to 3.70 Å for Zn and 0.50 to 3.10 Å for Mn. Solid lines represent the data and dashed lines are the fit

Furthermore, spectra collected on sorption samples at the Mn K-edge were relatively similar to that of biogenic Mn oxide with 3.4 ± 0.9 atoms of oxygen at 1.89 ± 0.02 Å and 3.6 ± 1.0 atoms of manganese at 2.85 ± 0.02 Å, equivalent to the biogenic Mn oxide (Jürgensen et al. 2004). The results suggest that Zn is not incorporated into the Mn oxide structure. Rather, through enzymatic oxidation by *L. discophora* SP-6, Mn(II) is oxidized and precipitated onto the biofilm providing a highly microporous surface for contaminant sequestration.

10.3 Summary

Zinc sorption on sheathed *Leptothrix discophora* SP-6 involves binding with phosphoryl groups of the bacterial cell wall and carboxyl groups on the EPS sheath, where however inner-sphere complexes dominate. On the other hand, Zn sorbed on the EPS sheath resulted in outer-sphere complexes consistent with the electrostatic effect observed in adsorption edges. PCA LC analysis revealed an 84% contribution from phosphoryl groups and 16% from carboxyl groups on the sheathed *L. discophora*. With nano-particulate biogenic Mn oxide coatings, a greater affinity and site capacity were observed as compared with sheathed *L. discophora* SP-6. The site capacity of biogenic Mn oxide (4.5×10^{-3} mole of Zn · g^{-1} Mn oxide) was approximately twenty times greater than that of the sheathed bacteria (2.7×10^{-4} mole of Zn · g^{-1} cell). Zn sorption was dominated by the Mn oxide phase where inner-sphere complexes resulted in octahedral structures of 6.9 ± 0.9 atoms of oxygen at 2.00 ± 0.02 Å and 4.9 ± 1.4 atoms of manganese at 3.34 ± 0.02 Å. There was no difference in the coordination environment between sorption and coprecipitation samples. Furthermore, the sorption configuration was invariant as a

function of contact time (4 hrs to 7 months) where the Zn loading increased by 173%. In this slower sorption process of intraparticle diffusion, the internal surface sites along microporous walls appear to be no different than external ones based on XAS analysis. The best fit diffusivity for Zn sorption in the nano-particulate Mn oxide coating was 10^{-19} $cm^2 \cdot s^{-1}$, which is two orders of magnitude smaller than that for the abiotic Mn oxide. This difference may be attributed to a reduced pore size distribution in the nano-particulate oxide as compared to the abiotic system. Overall, this work demonstrates that Zn sorption in this heterogeneous system was dominated by nano-particle Mn oxide because of its greater affinity and site capacity.

CHAPTER 11

CONCLUSIONS AND FUTURE RESEARCH

Mn oxides are found in a wide variety of geological environments and are nearly ubiquitous in soils and sediments, existing as discrete particles and coatings, originating via chemical and biological processes. Abiotic Mn oxide coatings are present in various forms, ranging from nanocrystalline to poorly crystalline. In this research, the HMO on the coated clay did not exhibit long-range structure, while the birnessite-coated clay resulted in a poorly crystalline oxide. The clay substrate potentially inhibited crystallization of pyrolusite-coated clay. The short-range structure however for birnessite-coated clay was equivalent to that of the discrete birnessite. For both HMO- and birnessite-coated montmorillonite, the overall surface properties of the systems studied were consistent with their discrete oxide counterparts. Moreover, XAS studies suggest that the local structure of Mn in the HMO coating is similar to that in the discrete phase.

Consistent with the characterization studies, Zn, Ni, and Pb sorption to HMO, HMO-coated montmorillonite, and montmorillonite revealed that the HMO-coated montmorillonite behaved similarly to the discrete Mn oxide, where metal ions sorbed onto the oxide coating as inner-sphere complexes. Ni potentially coordinated to the vacancy sites in the Mn oxide structure, while Zn and Pb formed tridentate and bidentate corner-sharing complexes, respectively. Even though Ni and Zn belong the group of transition metals, different sorption mechanisms were observed potentially because Ni ions exhibit a greater eletronegativity and a slightly smaller atomic radius as compared with Zn ions. Therefore, Ni ions may coordinate more easily into defect vacancy sites.

For all three metals, coordination environments were invariant not only as a function of loading, pH, and ionic strength, but also in long-term studies where sorption increased by as much as 100%. In this slower sorption process, intraparticle diffusion, the internal surface sites along microporous walls appear to be no different than external ones. Best fit diffusivities (D_S) ranged from10^{-18} to 10^{-17} cm^2/s for Zn, 10^{-13} to 10^{-12} cm^2/s for Ni and 10^{-20} to 10^{-17} cm^2/s for Pb.

Furthermore, theoretical surface diffusivities were predicted based on site activation theory and in agreement with experimental results. Interestingly, the diffusivities for metal ions in HMO-coated clay were between that for montmorillonite and HMO. These results indicate that the microporosity of HMO-coated clay has contributions from both the HMO and montmorillonite surfaces. Even though much of the clay surface is coated with HMO (~90%), the oxide morphology is potentially different from discrete ones. We speculate that clay particles serve as a template for Mn oxide when nucleation occurred, potentially changing the porosity, pore size distribution, and particle size. Therefore, the oxide-coated clay may exhibit unique characteristics from the discrete oxide.

Because biogenic processes dominate in producing Mn oxide in the oxic to suboxic environments, biogenic manganese oxides are often present as coatings on mineral substrates or associated with extracellular polymeric sheath. *L. discophora* SP-6 is a sheath forming, gram negative bacteria that oxidizes Mn(II) as well as Fe(II). This Mn oxidation is enzymatically catalyzed via non-dissimilatory pathways and usually depends on growth conditions, including pH, temperature, and substrate concentration. The excreted enzymes and proteins potentially oxidize Mn(II) are located at the

compartment between the sheath and outer membrane of the cell (Ghiorse and Ehrlich, 1992); therefore, the nano-particulate Mn oxide precipitates on the organism's surface and coats the sheathed bacteria forming a dendritic biofilm structure. The surface charge of Mn oxide coated bacteria was similar to that of abiotic Mn oxide, suppressing the contribution of the polysaccharide sheathed organism. Although no long-range order of the biogenic oxide was observed, the nano-particulate oxide forms polymer-like precursor to birnessite and is consistent with the phyllomanganate family. Overall, the surface properties of the coated bacteria are dominated by the nano-particulate Mn oxide. Interestingly, biogenic Mn oxides may be strong oxidants for complex organic compounds (e.g., humic substances) whereby smaller compounds can be assimilated by bacteria (Sunda and Kieber, 1994). In addition, the encrusted Mn oxide coating can reduce the toxicity of contaminant (Widmeyer et al. 2004). On the other hand, the Mn oxide may serve as a barrier by accumulating micronutrients such as Cu and Zn, which could result in nutrient deficiency.

Typically, Zn is considered as micronutrient to microorganisms and plants. The presence of Zn can stimulate the production of phytochelatin by eukaryotic algae in the equatorial pacific (Ahner et al. 1998) and may potentially increase Mn oxidation as a result of increasing biomass of bacteria. Interestingly, at greater concentrations, Zn sorbed on sheathed *L. discophora* SP-6, revealing a high affinity site on the bacterial cell wall characteristic of a phosphoryl group in addition to the low affinity one associated with the EPS sheath. Zn sorbed on the sheathed EPS as an outer-sphere complex with carboxylic groups. A linear combination analysis showed sorption to the sheathed *L. discophora* SP-6 was consistent with an 84% contribution from Zn binding to phosphoryl

groups and 16% contribution from carboxyl groups. With nano-particulate biogenic Mn oxide coatings, a greater affinity and site capacity were observed as compared to the sheathed organism. Zn sorption was dominated by the Mn oxide phase where inner-sphere complexes resulted in an octahedral structure. Furthermore, XAS analysis demonstrated that the coordination environment between sorption and coprecipitation samples were consistent. Long-term sorption studies conducted up to 7 months increased the Zn loading 170%. In this slower sorption process of intraparticle diffusion, the internal surface sites along microporous walls appear to be no different than external ones based on XAS analysis. The best fit diffusivity for Zn sorption in the nano-particulate Mn oxide coating was 10^{-19} cm^2/s which is two orders of magnitude smaller than that for the abiotic Mn oxide. This difference may be attributed to a reduced pore size distribution in the nano-particulate oxide as compared to the abiotic system. Biogenic Mn oxide present as nano-particles effectively sequestrates heavy metals in the environment. In conclusion, this research contributes to a better understanding of the role of abiotic and biogenic Mn oxide coatings in contaminant behavior.

In addition to this research, future work should include applying surface complexation modeling to predict the adsorption on the single and heterogeneous substrates studied in discrete abiotic and biogenic Mn oxides as well as Mn oxide coatings. Synchrotron-based studies applying for example, μXRD, μXRF, and μXAS can be used to resolve the long-range structure of biogenic Mn oxide and elemental mapping of metal ions in the heterogeneous systems. Furthermore, the nanoporosity of biogenic Mn oxide can be investigated using the positron annihilation spectroscopy which was

recently used on a Cu film (Sun et al. 2003; Racko et al. 2005). Moreover, exploiting the redox active surface of these Mn oxides may prove useful in remediation.

APPENDIX A

QA/QC PROCEDURE

General Procedures for Storage Bottles and Caps

All laboratory procedures will follow Standard Methods (Greenberg et al. 1998). All sample containers will be pre-washed with detergent and Millipore-Q water before use. The plastic containers and glass containers will be soaked in 10% nitric acid for 24 hours and 48 hours, respectively, rinse with DI water and dried and stored in a particle free environment before use. In general, containers will either be resistant boro-silicate glass and Nalgene®. The Nalgene® containers are of low-density polyethylene (LDP). This type of container was selected because it is not reactive with solution. For short term storage or when storing stock solutions, depending on their shelf life, boro-silicate bottles will be used. For long-term storage or if the sample is to be analyzed for some substance that would be affected by prolonged storages in glass bottles due to silica leaching, Nalgene® bottles will be used. Acids and alkalis will not be stored in plastics bottles.

The stoppers, caps, or plugs will be selected as to resist the attack of the material contained in the vessel. Metals are avoided due to the problem of corrosion. Glass stopper will not be used to store strong alkali due to their tendency of getting stuck. Rubber stoppers are preferable.

During transport the hard rubber and glass bottles will be packed in wooden, metal, plastic, or heavy fiberboard cases with a separate compartment for each bottle and the lining will be insulted from breakage. The samples stored in plastic bottles need no protection against breakage by impact or through freezing

General Procedures for Reagents and Chemicals

Chemicals of the American Chemical Standard (ACS) grade will be used. Some organic reagents are unstable upon exposure to the atmosphere. If the stability of a chemical or reagent is unknown, then small amounts of the chemical at frequent intervals will be purchased.

All anhydrous reagent chemicals that are required for the preparation of standard calibration solutions and titrants will be dried in an oven at 105 °C to 110 °C for at least 1 to 2 hours and preferably overnight. After cooling to room temperature in efficient desiccators, these chemicals will be promptly weighed and the proper amount dissolved. In case a different temperature is necessary, this would be specified on the chemical's label and will be adopted.

To prepare a solution of exact normality from a chemical that is not a primary standard, a relatively concentrated stock solution will be prepared and an exact dilution will be accomplished with a volumetric flask. Alternatively, a solution of slightly higher concentration can be prepared and standardized, which can be subsequently diluted. This approach is typically adopted for solutions that require frequent change in their strength and have to therefore be standardized.

Quality Control / Quality Assurance (QA/QC)

Sampling will be conducted accurately to assure that the analytical results are consistent with the actual sample composition. A sample will be handled in such a way that it does not deteriorate or become contaminated anytime prior to analysis. Representative samples will be analyzed subsequently.

Quality control will include adding known or standard samples to unknown samples, and determining the percentage recovery. Recovery tests are conducted at the same time as the sample analysis. Metal recovery indicated accuracy of the method in the case of metals recovery is practiced to verify the absence of a matrix effect, which occurs in the presence or absence of interfering substances. Percentage recovery should generally fall within the range of 85% to 115%

Control samples will be prepared. DI water or samples will know additions (DI water with one or more standard chemicals added) will be used as control samples so that a known value can be assigned to the sample. One of the most important aspects of a quality control program is the adequate supply of a stable control. Ideally, the control prepared will last for as long as 6 months which is the maximum shelf life for metals.

Method blanks will be employed with each batch of samples analyzed to monitor impurity levels. If the method blank assay indicates that the metals are present above the instrument detection limit (IDL's), the reagents and glassware will be checked for source of impurities. If impurities in the method blank exceed the method detection limit (MDL's), analyses will be suspended until the problem has been corrected.

Duplicated samples will be collected to assess precision when the concentration of the constituent to be determined is measurable. For every ten samples, one sample will be prepared for duplicate analysis. For metals, the precision of the duplicates should be between 10-25%.

All instruments will be accurately calibrated and the errors accounted for through statistical analysis.

APPENDIX B

SOLUBILITY AND SPECIATION DIAGRAM

Solubility and speciation diagrams for Zn, Ni, and Pb were calculated based on the thermodynamics data by MINEQL+.

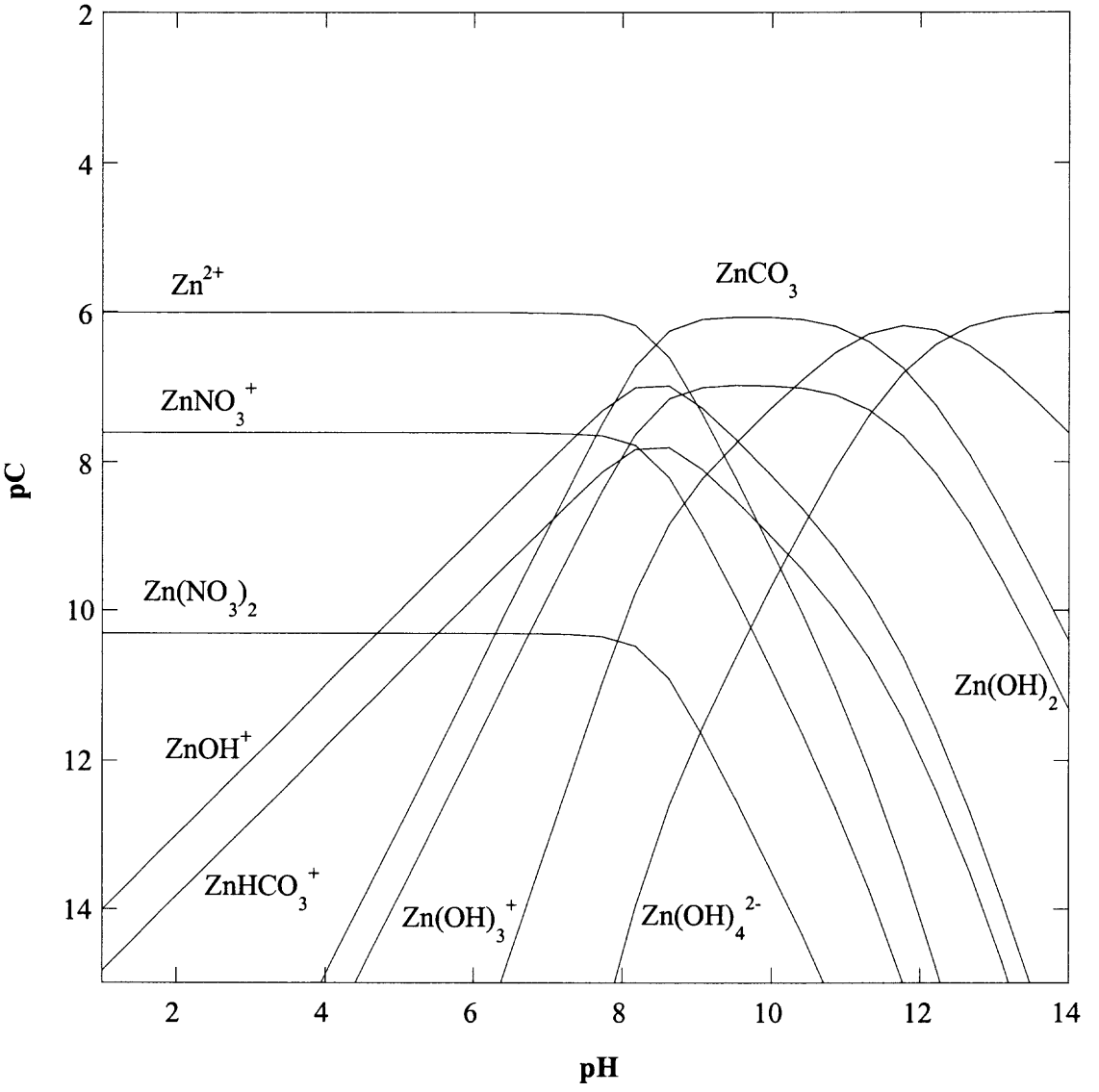

Figure B.1 Zinc speciation diagram in 10^{-6} M $Zn(NO_3)_2$ aqueous solution at 298 K.

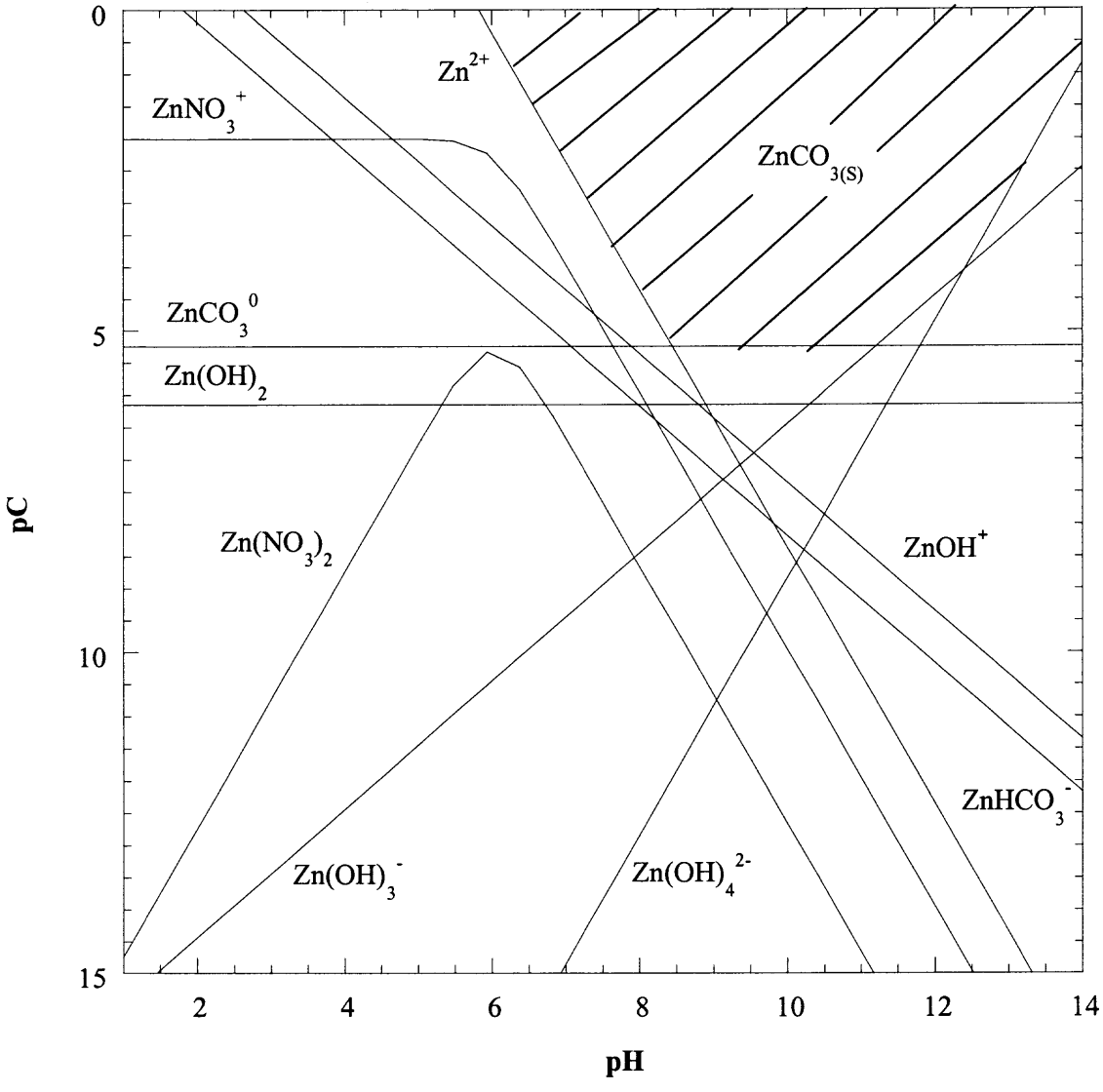

Figure B.2 Zinc solubility diagram in open system condition at 298 K.

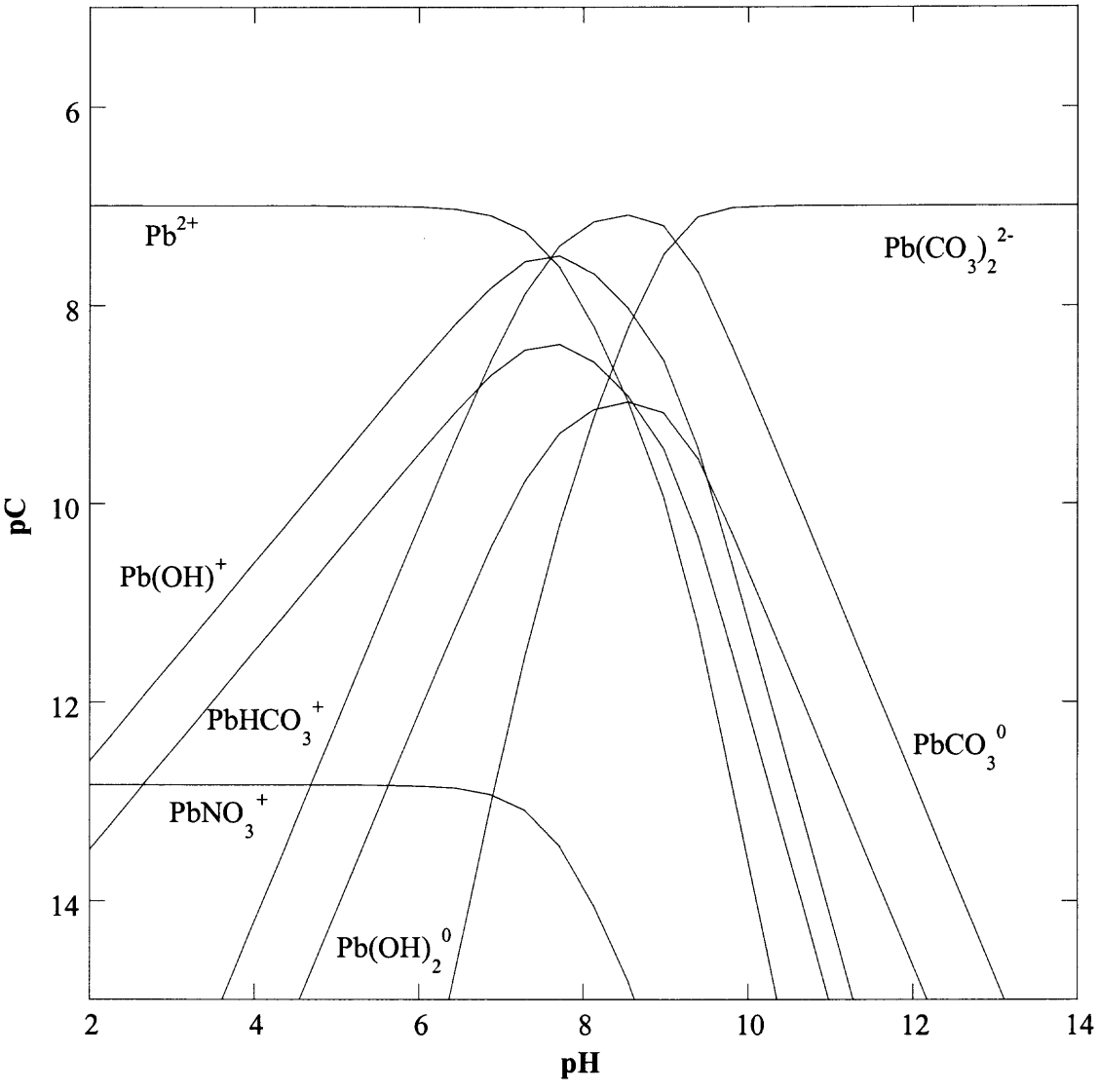

Figure B.3 Lead speciation diagram in 10^{-7} M $Pb(NO_3)_2$ aqueous solution at 298 K.

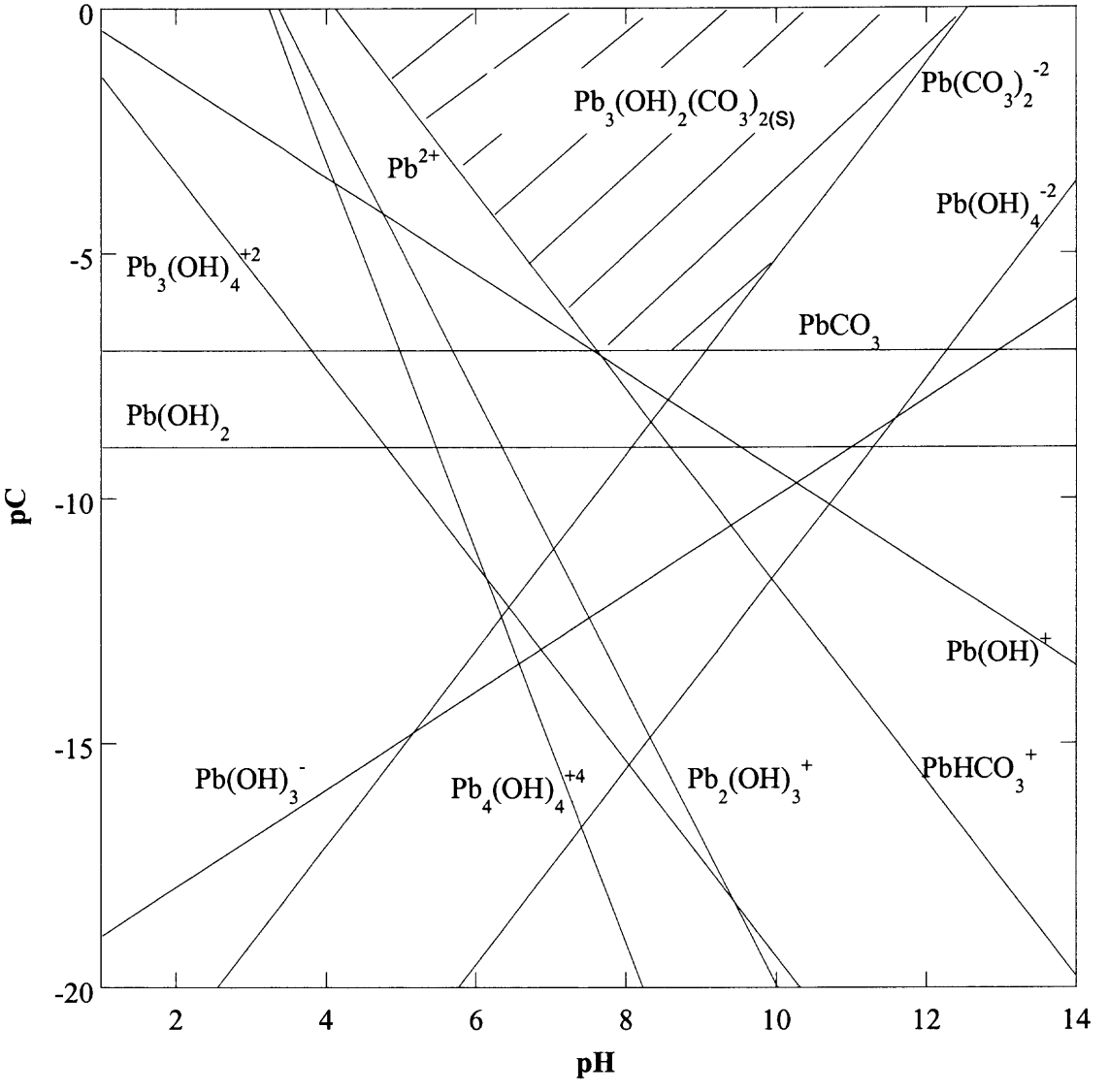

Figure B.4 Lead solubility diagram in open system condition at 298 K.

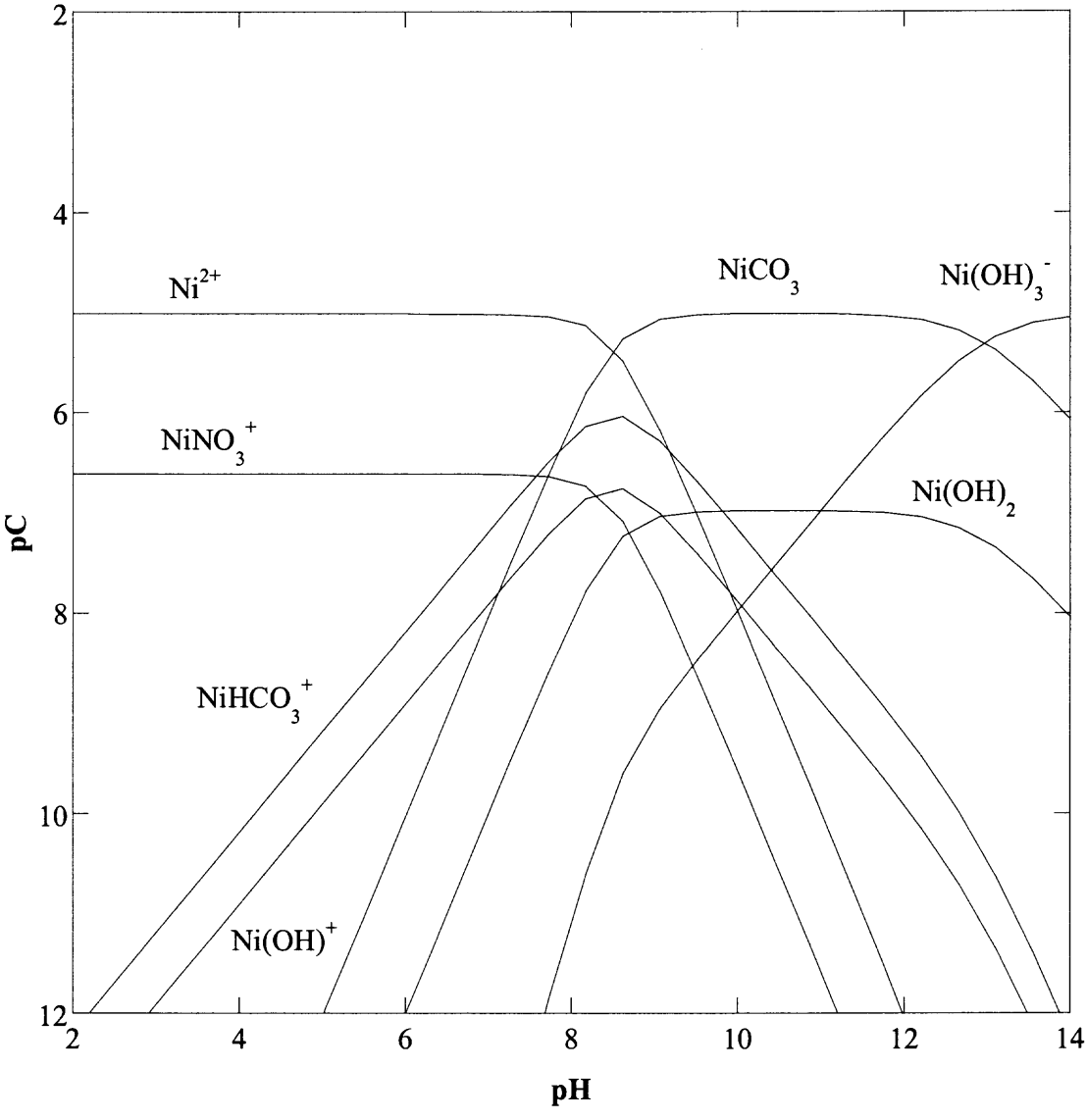

Figure B.5 Nickel speciation diagram in 10^{-5} M $Ni(NO_3)_2$ aqueous solution at 298 K.

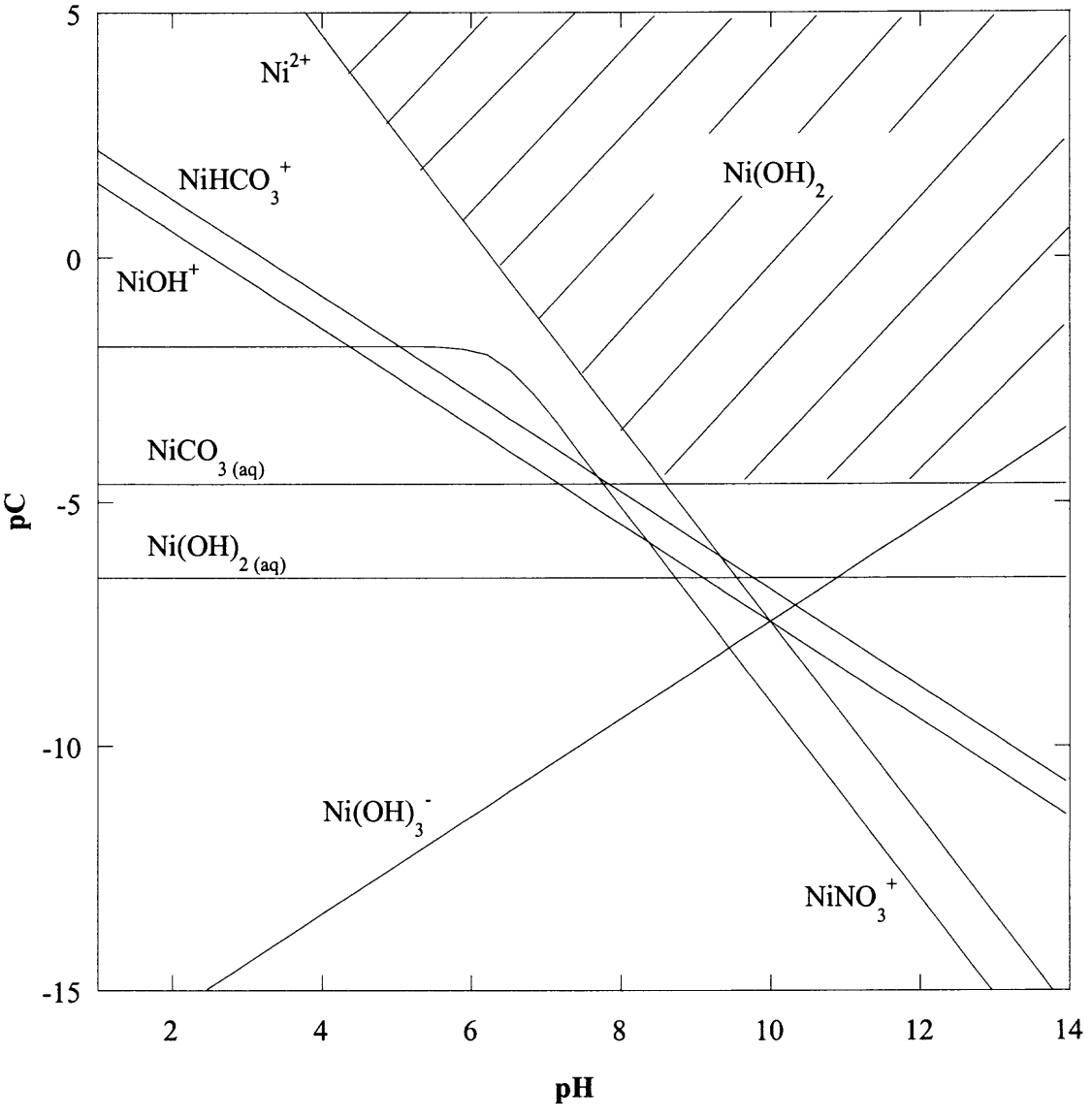

Figure B.6 Ni solubility diagram in open system condition at 298 K.

APPENDIX C

BOND VALANCE ANALYSIS

The bond valance analysis of surface functional groups and sorption complexes can contribute to our understanding of the relatively stability of the structure based on Pauling's electrostatic valance principle (Pauling, 1960) and the associated charge (Brown and Altermatt, 1985). The concept of bond valence (S_i) is a measure of the strength of individual bonds in metal oxide crystal structure. Bond valence is defined as Eq. [1]

$$S_i = \exp[(r_o - r_{m-o})/0.37] \qquad \text{valence unit (v.u.)} \qquad (C.1)$$

where r_{m-o} is the length of the metal-oxygen bond, and r_o is an effective radius that depends upon the identity and formal valence of the cation. Based on XAS analysis, the radius distance between metal and oxygen can be evaluated and the effective radius (r_o) is found in Brown and Altermatt (1985). To quantify the bond valence of the OH bond, Ziolkowski's equation for S_{OH} is calculated from least squares fitting using a number of OH bond lengths from neutron diffraction studies in which the effects of proton thermal motion were corrected, as shown

$$S_{OH} = 0.241/(R_{OH} - 0.677) \qquad (C.2)$$

the average hydroxide ion bond length in water, inorganic hydroxides, and hydrate ranges from 0.95 to 1.03 Å (Olovosson and Jonsson, 1976); therefore, S_{OH} appears to range from 0.13 to 0.26 valance unit. The sum of the bond valances between the cation and the anion (ΣS_{m-o}) are equivalent to the oxidation state (V_i) of the cation when the ion coordination is saturated. If the given ion has $\Sigma S_{m-o} < V_i$, it is theoretically more reactive and will tend

toward a saturated bonding arrangement. If in contrast, an ion in solution or on the surface is oversaturated when $\Sigma S_{m-o} > V_i$, then it should react to achieve a new local coordination of $\Sigma S_{m-o} = V_i$. The results demonstrate that the feasible surface complexes of Pb on Mn oxide include two possible configurations (j.e. Mn_2-O-Pb and Mn-O-Pb) (Table C1).

Table C.1 Bond-Valence Analysis for Reactive Functional Groups and Pb Sorption Complexes at the Surface of HMO

Surface functional	ΣS_{m-o} at Oxygen (v.u.)		Oxygen bonding state	Prediction
	No-H-bonds	With H-bonds		
Mn-$O^{4/3-}$	0.69	< 0.95	Unsaturated	Plausible
Mn-$OH^{1/3-}$	1.37-1.57	< 1.83	Unsaturated	Plausible
Mn-$OH_2^{2/3+}$	2.25-2.45		Oversaturated	Doesn't occur
Mn_2-$O^{2/3-}$	1.38	< 1.64	Unsaturated	Plausible
Mn_2-$OH^{1/3+}$	2.06-2.26		Oversaturated	Doesn't occur
Mn_3-O^0	2.07		Saturated	Stable
Pb complex bonds				
Mn-O-Pb	1.26	< 1.52	Unsaturated	Plausible
Mn-O-Pb_2	1.82	< 2.08	Unsaturated	Plausible
Mn-O-Pb_3	2.39		Oversaturated	Doesn't occur
Mn_2-O-Pb	1.95	2.08-2.20	Saturated	Stable
Mn_2-OH-Pb	2.63-2.83		Oversaturated	Doesn't occur
Mn_2-O-Pb_2	2.51		Oversaturated	Doesn't occur
Mn-OH-Pb	1.94-2.14	2.07-2.39	Saturated	Stable
Mn-OH-Pb_2	2.50-2.70		Oversaturated	Doesn't occur

APPENDIX D

ADSORPTION STUDIES ON HMO, MONTMORILLONITE, AND HMO-COATED MONTMORILLONITE

The results from Zn, Ni, and Pb sorption on HMO, montmorillonite, and HMo-coated montmorillonite are provided in this section.

Zn adsorption edge of HMO-coated clay, HMO, and montmorillonite at 25 °C, $NaNO_3$ background electrolyte

pH	% Zn sorbed on HMO		% Zn sorbed on HMO-coated clay		% Zn sorbed on montmorillonite	
	IS 0.015	IS 0.15	IS 0.015	IS 0.15	IS 0.015	IS 0.15
1.5	38.272	10.343				
2.0	42.460	13.353				
2.5	78.845	28.031				
3.0	94.148	59.235				
3.5	97.834	82.197				
4.0	98.765	93.254				
4.5	99.021	96.738				
5.0	99.139	97.590				
5.0	99.236	97.558				
5.5	99.192	97.697				
6.0	98.801	97.219				
6.5	98.397	96.577				
7.0	98.775	96.524				
2.0			27.394	8.0120		
3.0			86.384	43.110		
3.5			93.880	72.039		
4.0			95.746	88.783		
4.5			96.432	94.239		
5.0			96.473	95.931		
5.0			96.560	95.610		
5.5			96.651	95.735		
6.0			96.451	96.384		
6.5			96.311	96.517		
7.0			96.270	96.514		
4.0					26.622	2.4090
4.5					31.875	5.7900
5.0					44.644	16.926
5.5					55.556	23.601
6.0					68.540	41.513
6.0					67.226	40.462
6.5					71.585	51.176
7.0					75.929	61.099
7.5					80.844	75.591

Zn adsorption isotherm of HMO, HMO-coated clay, montmorillonite at IS 0.01, 25 °C

pH 5		pH 6	
$[Zn]_{aq}$	Mole of Zn sorbed/g HMO	$[Zn]_{aq}$	Mole of Zn sorbed/g HMO
2.9503e-11	9.9410e-8	2.4491e-11	9.9510e-8
3.4616e-11	1.5931e-7	2.4076e-11	1.5952e-7
4.0062e-11	1.9920e-7	2.7126e-10	1.9946e-7
6.1560e-10	1.5877e-6	5.0130e-10	1.5900e-6
6.3854e-10	1.9872e-6	5.1156e-10	1.9898e-6
6.1318e-10	1.9877e-6	5.5665e-10	1.9889e-6
1.0326e-9	5.9794e-6	6.7726e-10	5.9865e-6
3.8323e-9	9.9233e-5	2.5646e-8	9.9487e-5
5.5616e-8	0.00015889	2.9583e-8	0.00015941
6.4617e-8	0.00019871	3.2550e-8	0.00019935

pH 5		pH 6	
$[Zn]_{aq}$	Mole of Zn sorbed/ g HMO-coated clay	$[Zn]_{aq}$	Mole of Zn sorbed/ g HMO-coated clay
6.4500e-11	2.2800e-7	5.9143e-11	2.2822e-7
5.5300e-11	3.6800e-7	8.8197e-11	3.6544e-7
1.4800e-10	4.5600e-7	6.9430e-11	4.5869e-6
9.0700e-10	3.6600e-6	1.4450e-9	3.6284e-6
1.3300e-9	4.5700e-6	1.3144e-9	4.5582e-6
1.2200e-9	4.5700e-6	8.8040e-10	4.5783e-6
1.6700e-9	1.3800e-5	1.0208e-9	1.3810e-5
6.0300e-8	0.00022900	2.8133e-8	0.00022965
1.2000e-7	0.00036500	3.4139e-8	0.00036794
1.5200e-7	0.00045600	3.5181e-8	0.00046027

pH 5		pH 6	
$[Zn]_{aq}$	Mole of Zn sorbed/ g clay	$[Zn]_{aq}$	Mole of Zn sorbed/ g clay
2.7481e-9	2.2519e-8	2.2258e-9	2.2300e-8
4.5349e-9	3.4651e-8	3.4459e-9	3.4500e-8
5.4339e-9	4.5661e-8	4.4601e-9	4.4600e-8
3.8322e-8	1.1678e-7	3.2361e-8	3.2400e-7
5.1275e-8	2.8725e-7	4.1959e-8	4.2000e-7
6.0185e-8	3.9815e-7	5.0081e-8	5.0100e-7
5.8483e-8	4.1517e-7	5.1864e-8	5.1900e-7
1.9620e-7	1.0380e-6	1.5913e-7	1.5900e-6
2.2148e-6	7.8524e-6	2.1900e-6	2.1900e-6
4.0005e-6	9.9955e-6	4.3248e-6	4.3200e-5

Ni adsorption edge of HMO-coated clay, HMO, and montmorillonite at 25 °C, $NaNO_3$ background electrolyte

pH	% Ni sorbed on HMO		% Ni sorbed on HMO-coated clay		% Ni sorbed on montmorillonite	
	IS 0.015	IS 0.15	IS 0.015	IS 0.15	IS 0.015	IS 0.15
2.0	63.80	22.70				
2.5	93.40	50.20				
3.0	97.40	75.60				
3.5	99.50	82.50				
4.0	99.80	87.30				
4.5	99.80	93.60				
5.0	97.80	94.80				
5.0	99.40	95.50				
5.5	99.90	96.20				
6.0	98.50	96.50				
7.0	99.40	99.30				
8.0	99.70	99.90				
2.0			23.911	15.30		
3.0			92.001	67.20		
3.5			97.335	82.30		
4.0			99.155	91.40		
4.5			99.714	94.60		
5.0			99.837	97.20		
5.5			99.844	97.60		
6.0			99.812	98.10		
6.5			99.885	98.10		
7.0			99.815	98.20		
4.0					22.026	5.884
4.5					23.113	6.078
5.0					23.113	5.566
5.5					26.129	6.448
6.0					26.115	6.448
6.0					27.532	4.370
6.5					26.991	9.390
7.0					31.882	11.09
7.5					34.200	13.76

Ni adsorption isotherm of HMO, HMO-coated clay, montmorillonite at IS 0.01, 25 °C

pH 5		pH 6	
$[Ni]_{aq}$	Mole of Ni sorbed /g HMO	$[Ni]_{aq}$	Mole of Ni sorbed /g HMO
3.2086e-12	4.9968e-8	9.3560e-12	4.9900e-7
2.4845e-12	6.9975e-8	1.2758e-11	9.9900e-7
2.0302e-12	9.9980e-8	7.7869e-11	5.9900e-6
2.7673e-11	9.9972e-7	2.9272e-10	2.0000e-5
2.0549e-11	9.9980e-7	2.4178e-10	2.0000e-5
9.6169e-11	1.9990e-6	2.8394e-10	3.0000e-5
3.6337e-9	4.9964e-5	1.4305e-9	0.00012000
6.5636e-9	6.9934e-5	6.4310e-9	0.00049900
6.3508e-9	9.9937e-5	1.8516e-8	0.00099800

pH 5		pH 6	
$[Ni]_{aq}$	Mole of Ni sorbed/ g HMO-coated clay	$[Ni]_{aq}$	Mole of Ni sorbed/ g HMO-coated clay
1.3273e-10	1.3300e-7	3.6088e-12	1.3900e-7
1.3052e-10	2.2500e-7	3.4196e-12	2.3100e-7
1.3991e-10	4.5600e-7	9.5288e-12	4.6300e-7
2.4762e-9	3.1300e-6	7.9365e-11	3.2400e-6
2.7101e-9	4.5000e-6	1.0833e-10	4.6200e-6
2.6875e-9	4.5100e-6	1.6625e-10	4.6200e-6
1.7116e-7	0.00022400	3.8465e-9	0.00023100
1.7309e-7	0.00033900	1.4862e-8	0.00046200
1.9160e-7	0.00045400		

pH 5		pH 6	
$[Ni]_{aq}$	Mole of Ni sorbed / g clay	$[Ni]_{aq}$	Mole of Ni sorbed/ g clay
2.1796e-9	8.2000e-9	2.0582e-9	9.4200e-9
3.5836e-9	1.4200e-8	3.4805e-9	1.5200e-8
7.0717e-9	2.9300e-8	6.7531e-9	3.2500e-8
5.4458e-8	1.5500e-7	5.4720e-8	1.5300e-7
7.2438e-8	2.7600e-7	7.2010e-8	2.8000e-7
7.4779e-8	2.5200e-7	7.3509e-8	2.6500e-7
4.6201e-6	3.8000e-6	4.4505e-6	5.5000e-6
8.9911e-6	1.0100e-5	8.7968e-6	1.2000e-5
4.8658e-5	1.3400e-5	4.0871e-5	9.1300e-5
8.4142e-5	0.00015900	8.5948e-5	0.00014100
9.5919e-6	4.0800e-5	9.4211e-5	0.00057900

Pb adsorption edge of HMO-coated clay, HMO, and montmorillonite at 25 °C, $NaNO_3$ background electrolyte

pH	% Pb sorbed on HMO		% Pb sorbed on HMO-coated clay		% Pb sorbed on montmorillonite	
	IS 0.015	IS 0.15	IS 0.015	IS 0.15	IS 0.015	IS 0.15
1.0	72.394	27.606				
1.5	86.438	57.239				
2.0	97.376	77.992				
2.5	99.533	98.687				
3.0	99.939	-				
3.0	99.922	99.756				
3.5	99.997	99.995				
4.0	99.996	99.985				
4.5	99.998	99.995				
5.0	99.997	99.998				
2.0			59.842	45.845		
3.0			82.237	60.743		
3.5			91.786	69.257		
4.0			93.084	82.346		
4.5			95.215	87.800		
5.0			97.826	92.686		
5.5			98.304	94.872		
6.0			98.504	95.428		
6.5			98.496	96.583		
7.0			98.455	97.390		
4.0					69.957	44.300
4.5					78.704	62.900
5.0					82.083	71.400
5.5					91.337	92.400
6.0					97.901	90.800
6.5					98.926	86.100
6.5					99.348	89.100
6.7					99.361	88.000
7.0					99.542	96.200
7.5					99.674	94.000

Pb adsorption isotherm of HMO, HMO-coated clay, montmorillonite at IS 0.01, 25 °C

pH 5		pH 6	
$[Pb]_{aq}$	Mole of Pb sorbed/g HMO	$[Pb]_{aq}$	Mole of Pb sorbed/g HMO
4.0637e-7	0.0025936	5.3089e-8	0.0029469
6.5396e-7	0.0043460	7.2394e-8	0.0049276
8.2095e-6	0.11679	2.9006e-6	0.12210
1.1593e-5	0.17591	7.2321e-6	0.18027
1.4206e-5	0.23579	1.0637e-5	0.23936
1.5287e-5	0.23471	1.1595e-5	0.23840
1.9875e-5	0.29263	1.3663e-5	0.29884
2.4324e-5	0.35068	1.8395e-5	0.35660
2.7992e-5	0.40951	2.0314e-5	0.41719
4.1554e-5	0.45845	2.7244e-5	0.47276

pH 5		pH 6	
$[Pb]_{aq}$	Mole of Pb sorbed/ g HMO-coated clay	$[Pb]_{aq}$	Mole of Pb sorbed/ g HMO-coated clay
2.0415e-8	0.0011831	6.2867e-8	0.0010343
5.1313e-8	0.0016563	1.0852e-7	0.0013996
3.9802e-7	0.0023662	1.0921e-7	0.0021078
3.7152e-8	0.0070986	2.2225e-7	0.0065727
3.7399e-8	0.0070986	6.1404e-8	0.0069533
2.9855e-7	0.011831	5.1863e-8	0.011708
9.3793e-7	0.016563	1.1725e-7	0.016286
1.6164e-6	0.023662	4.6419e-7	0.022564
3.4633e-6	0.035493	1.0792e-6	0.032939
5.7712e-6	0.047324	2.4539e-6	0.041518

pH 5		pH 6	
$[Pb]_{aq}$	Mole of Pb sorbed/ g clay	$[Pb]_{aq}$	Mole of Pb sorbed/ g clay
6.5975e-8	3.4025e-5	1.7017e-9	6.3000e-6
8.8320e-8	6.1680e-5	2.9891e-9	7.0100e-6
1.0714e-7	9.2857e-5	3.2703e-9	1.6700e-5
9.6525e-8	0.00010348	5.7960e-9	2.4200e-5
1.2645e-7	0.00012355	1.4000e-8	0.00014600
1.1728e-7	0.00018272	1.8300e-8	0.00018200
1.5734e-7	0.00024266	1.7600e-8	0.00018200
1.8436e-7	0.00031564	5.8300e-8	0.00034200
2.0849e-7	0.00039151	7.6700e-8	0.00042300
		9.3400e-8	0.00050700

Microsoft Visual C++ version 6 Code for Estimating Experimental Surface Diffusivity

```
//INTRAPARTICLE DIFFUSION CODE (Particle #)

#include <stdlib.h>
#include <iostream.h>
#include <fstream.h>
#include <math.h>
#include <string>
#include <iomanip.h>
#define STRLEN 30
#define FIRSTDELIMITER ','
#define SECONDDELIMITER '\n'
void main ()
{
// define all variables and parameters
double pi=3.14159, Ds=1e-13, S=3e-8, p=0.83, E=0.81, Kd=500;
double mass[310], Ki, sum, D, a, rad[100], num[100], Cs, summ[300], t[100], data[100],
sum1, sum2, diff, diff2, percent,persum, var,aveer;
int n=100, i, j, k, nn=0, nnn=0, ii;
char string[2][STRLEN], string1[2][STRLEN];
//build files connections
ofstream f2("resultNi.txt");
ofstream f3("new15.txt");
ifstream f4("PSDoxidecoated.txt");
ifstream f5("NiCoated.txt");
ofstream f6("dsvar5.txt");

//read particle size distribution from file into code
while(!f4.getline(string[0], STRLEN, FIRSTDELIMITER).eof())
{
f4.getline(string[1], STRLEN, SECONDDELIMITER);
rad[nn]=atof(string[0]);
num[nn]=atof(string[1]);
nn=nn+1;
}

while(!f5.getline(string1[0], STRLEN, FIRSTDELIMITER).eof())
{
f5.getline(string1[1], STRLEN, SECONDDELIMITER);
t[nnn]=atof(string1[0]);
data[nnn]=atof(string1[1]);
nnn=nnn+1;
}
//check particle size distribution correct from file output
```

```
for (k=0; k<nn; k++)
{
        f3<<rad[k]<<"\t"<<num[k]<<endl;
}
//define internal distribution coefficient
Ki=E*Kd/(1-E);
//get particle external surface concentration
Cs=S*Kd;
//obtain 100 day total concentration
for (ii=1; ii<=10; ii++)
{
//defne diffusivity
D=Ds/(1+E/(p*Ki));
sum1=0.0;
sum2=0.0;
persum=0.0;
for (j=0; j<nnn; j++)
{
summ[j]=0;
for (k=0; k<nn; k++)
{
sum=0.0;
for (i=1; i<=n; i++)
}
a=1/pow(i,2)*exp(-D*pow(i,2)*pow(pi,2)*t[j]*86400/(pow(rad[k],2)*pow(10.0, -8)));
sum=sum+a;
}
mass[k]=4*Cs*p*pi*pow(rad[k],3)*pow(10, -12)/3*(1-6/pow(pi,2)*sum)*num[k];
summ[j]=summ[j]+mass[k];
}
summ[j]=summ[j]+Cs;
diff=fabs(data[j]-summ[j]);
percent=(diff/summ[j])*100.0;
diff2=pow(diff,2);
sum1=sum1+diff;
sum2=sum2+diff2;
persum=percent+persum;
f2<<t[j]<<", "<<summ[j]<<", "<<data[j]<<endl;
}
var=(sum2-(pow(sum1,2)/nnn))/(nnn-1);
aveer=persum/nnn;
f6<<Ds<<", "<<var<<", "<<aveer<<endl;
cout<<Ds<<", "<<var<<", "<<aveer<<endl;
Ds= Ds+pow(10,-13);
}
}
```

CBC studies of Zn sorbed onto 10^{-1} g/L HMO-coated clay at pH 7, IS 10^{-2}, 25 °C, Added [Zn] = 10^{-2} M

Time (hr)	CPM	%error	Amount of Zn sorbed	% Zn sorbed	Volume added (mL)	Mole of Zn sorbed/ g	Modelling Results
0	5321.26	4.85	0	0		0	0.00093474
0.333333	712.44	4.95	4608.82	86.61		0.000866	0.00093749
0.666667	641.6	4.99	4679.66	87.94		0.000879	0.00093862
1	329.9	4.98	4991.36	93.80		0.000938	0.00093948
2	208.26	4.99	5113	96.08		0.000961	0.00094142
3	176.26	4.97	5145	96.68		0.000967	0.00094289
4	117.94	4.98	5203.32	97.78		0.000978	0.00094414
5.5	110.5	4.97	5210.76	97.92	0.0137	0.000979	0.00094573
7.5	101.69	4.98	5219.57	98.08	0.0311	0.000982	0.00094753
10	87.76	4.98	5233.5	98.35	0.0554	0.000988	0.00094945
23.3	64.67	5	5256.59	98.78	0.0976	0.000998	0.00095688
30.8	106.29	4.99	5214.97	98.00	0.02125	0.001	0.00096005
54.8	148.84	4.98	5172.42	97.20	0	0.000994	0.00096801
78.8	131.6	4.96	5189.66	97.52	0	0.000997	0.00097420
174.8	88.2	4.98	5233.06	98.34	0.05389	0.001005	0.00099178
244.8	85	4.98	5236.26	98.40	0.05955	0.000995	0.00100121
411.8	67.4	4.98	5253.86	98.73	0.09114	0.001002	0.00101860
581	75.8	4.98	5245.46	98.57	0.075867	0.00101	0.00103229
913.75	79.2	5.03	5242.06	98.51	0.069485	0.001017	0.00105335
1162.25	130	4.98	5191.26	97.55	0	0.001014	0.00106611
1540.75	82.9	5	5238.36	98.44	0.062522	0.001023	0.00108261
1951.25	92.4	5	5228.86	98.26	0.04544	0.001028	0.00109781
2238.25	82.42	5	5238.84	98.45	0.06304	0.001034	0.00110725

CBC studies of Zn sorbed onto 10^{-1} g/L Montmorillonite at pH 7, IS 10^{-2}, 25 °C, Added [Zn] = 10^{-2} M

Time (hr)	CPM	%error	Amount of Zn sorbed	% Zn sorbed	Volume added (mL)	Mole of Zn sorbed/ g	Modelling Results
0	5321.26	4.85	0	0		0	0.00013477
0.333333	712.44	4.95	4608.82	86.61		0.000866	0.00020106
0.666667	641.6	4.99	4679.66	87.94		0.000879	0.00021064
1	329.9	4.98	4991.36	93.80		0.000938	0.00021679
2	208.26	4.99	5113	96.08		0.000961	0.00022832
3	176.26	4.97	5145	96.68		0.000967	0.00023570
4	117.94	4.98	5203.32	97.78		0.000978	0.00024123
5.5	110.5	4.97	5210.76	97.92	0.0137	0.000979	0.00024766
7.5	101.69	4.98	5219.57	98.08	0.0311	0.000982	0.00025424
10	87.76	4.98	5233.5	98.35	0.0554	0.000988	0.00026063
23.3	64.67	5	5256.59	98.78	0.0976	0.000998	0.00028115
30.8	106.29	4.99	5214.97	98.00	0.02125	0.001	0.00028851
54.8	148.84	4.98	5172.42	97.20	0	0.000994	0.00030471
78.8	131.6	4.96	5189.66	97.52	0	0.000997	0.00031564
174.8	88.2	4.98	5233.06	98.34	0.05389	0.001005	0.00034172
244.8	85	4.98	5236.26	98.40	0.05955	0.000995	0.00035366
411.8	67.4	4.98	5253.86	98.73	0.09114	0.001002	0.00037322
581	75.8	4.98	5245.46	98.57	0.075867	0.00101	0.00038696
913.75	79.2	5.03	5242.06	98.51	0.069485	0.001017	0.00040607
1162.25	130	4.98	5191.26	97.55	0	0.001014	0.00041668
1540.75	82.9	5	5238.36	98.44	0.062522	0.001023	0.00042910
1951.25	92.4	5	5228.86	98.26	0.04544	0.001028	0.00044033
2238.25	82.42	5	5238.84	98.45	0.06304	0.001034	0.00045000

CBC studies of Ni sorbed onto 10^{-1} g/L HMO-coated clay at pH 7, IS 10^{-2}, 25 °C, Added [Ni] = 10^{-2} M

Time (hr)	CPM	%error	Amount of Ni sorbed	% Ni sorbed	Volume added (mL)	Mole of Ni sorbed/ g	Modelling Results
0	2749.01	4.85	0	0		0	2.2300e-05
0.25	979.27	4.95	1769.74	64.37		0.000644	6.8700e-05
0.75	944.3	4.99	1804.71	65.65		0.000656	0.00010664
15	955.97	4.98	1793.04	65.22		0.000652	0.00037969
2.5	835.86	4.99	1913.15	69.59		0.000696	0.00017792
4	824.02	4.97	1924.99	70.02		0.0007	0.00021783
6	836.84	4.98	1912.17	69.55	0.4746	0.000696	0.00025915
17	691.48	4.97	2057.53	74.84	0.4436	0.000796	0.00039927
24	700.28	4.98	2048.73	74.52	0.077	0.000837	0.00045701
44	804.62	4.98	1944.39	70.73	0.2044	0.000807	0.00057069
71.5	765.77	4.982	1983.24	72.14	0.3536	0.000841	0.00066990
88.5	724.75	4.984	2024.26	73.63	0.223	0.000892	0.00071464
109.5	760.77	4.986	1988.24	72.32	0.4968	0.000901	0.00075940
135.5	685.37	4.988	2063.64	75.06	0	0.000978	0.00080382
182	845.46	4.99	1903.55	69.24	0	0.00092	0.00086385
207	872.94	4.992	1876.07	68.24	0.08728	0.00091	0.00088922
264	797.96	4.994	1951.05	70.97	0.02981	0.000946	0.00093530
286.5	813.76	4.996	1935.25	70.39	0.01915	0.000943	0.00095017
361	816.69	4.998	1932.32	70.29	0.227514	0.000944	0.00099019
430.3	759.41	5	1989.6	72.37	0.02093	0.000987	0.0010184
504.3	816.2	5.002	1932.81	70.30	0.164109	0.000969	0.0010422
620	776.84	5.004	1972.17	71.74	0.24778	0.001	0.0010705
980.5	753.84	4.996	1995.17	72.57	0.374	0.001033	0.0011222
1124.5	776.22	5.006	1972.79	71.76	0.334	0.001062	0.0011347
1294.5	736.38	5.006	2012.63	73.21	0.2493	0.00111	0.0011463
1578.5	833.86	5.006	1915.15	69.66	0.16637	0.001099	0.0011603
1866	724.33	4.988	2024.68	73.65	0.31129	0.001156	0.0011703
2256	735.51	4.98	2013.5	73.24	0	0.001183	0.0011797
2540	783.35	4.982	1965.66	71.50	0.35512	0.001165	0.0011847
3069.5	748.35	4.984	2000.66	72.77	0.31445	0.001214	0.0011914
3642.5	750	4.986	1999.01	72.71	0.1041	0.001245	0.0011963

CBC studies of Ni sorbed onto 10^{-1} g/L Montmorillonite at pH 7, IS 10^{-2}, 25 °C, Added [Ni] = 10^{-2} M

Time (hr)	CPM	%error	Amount of Ni sorbed	% Ni sorbed	Volume added (mL)	Mole of Ni sorbed/ g	Modelling Results
0	1807	4.85	0	0		0	2.0768e-08
0.5	1353.6	4.95	453.4	25.09		2.509E-07	4.6822e-07
1	1380.77	4.99	426.23	23.58		2.358E-07	5.2628e-07
2.5	1325.67	4.98	481.33	26.63		2.663E-07	6.0686e-07
4.25	1253.18	4.99	553.82	30.64		3.064E-07	6.5436e-07
6	949.86	4.97	857.14	47.43	0.2309	4.743E-07	6.8508e-07
21	1036.8	4.98	770.2	42.62	0.1606	6.571E-07	7.9160e-07
27	1090.41	4.97	716.59	39.65	0.1188	7.881E-07	8.1135e-07
47.75	1124.53	4.98	682.47	37.76	0.09012	8.879E-07	8.5334e-07
72.5	1231.34	4.98	575.66	31.85	0.0146	9.189E-07	8.8135e-07
98.5	1213.43	5	593.57	32.84	0.027	9.435E-07	9.0033e-07
123.5	1246.14	4.99	560.86	31.03	0.004	9.524E-07	9.1347e-07
167.75	1263	4.98	544	30.10	0	9.471E-07	9.3008e-07
287.75	1138.6	4.96	668.4	36.98	0.0723	1.016E-06	9.5623e-07
357.75	1239.48	4.98	567.52	31.40	0.0079	1.032E-06	9.6573e-07
502.75	1249.86	4.88	557.14	30.83	0	1.035E-06	9.7946e-07
693	1318.86	4.83	488.14	27.01	0	9.964E-07	9.9129e-07

CBC studies of Pb sorbed onto 10^{-1} g/L HMO at pH 6, IS 10^{-2}, 25 °C, Added [Pb] = 5× 10^{-3} M

Time (hr)	CPM	%error	Amount of Pb sorbed	% Pb sorbed	Volume added (mL)	Mole of Pb sorbed/ g	Modelling Results
0	3131.13	4.85	0	0		0	0.00049433
0.25	39.31	9.51	3091.82	98.74		0.000494	0.00049539
0.75	39.16	9.52	3091.97	98.75		0.000494	0.00049614
1	37.61	9.8	3093.52	98.79		0.000494	0.00049641
2	38.11	9.71	3093.02	98.78		0.000494	0.00049724
3	37.86	9.77	3093.27	98.79		0.000494	0.00049786
4	37.11	9.94	3094.02	98.81		0.000494	0.00049838
5	41.5	9.19	3089.63	98.67		0.000493	0.00049883
7.25	38.6	9.69	3092.53	98.76	0.009	0.000494	0.00049970
9	34.56	10.67	3096.57	98.89	0.0198	0.000495	0.00050028
10.75	38.16	9.86	3092.97	98.78	0.009	0.000495	0.00050080
22.5	38.76	9.65	3092.37	98.76	0.0085	0.000496	0.00050347
27.5	34.96	10.37	3096.17	98.88	0.0202	0.000497	0.00050436
32	36.76	10.09	3094.37	98.82	0.0145	0.000497	0.00050509
46.5	39.06	10	3092.07	98.75	0.0076	0.000498	0.00050712
54	30.96	11.46	3100.17	99.01	0.0323	0.000499	0.00050803
76	37.5	9.86	3093.63	98.80	0.0123	0.0005	0.00051034
98	30.91	11.34	3100.22	99.01	0.0323	0.000502	0.00051230
122.5	33.96	10	3097.17	98.91	0.0229	0.000503	0.00051420
151	15.66	19.59	3115.47	99.49	0.0782	0.000507	0.00051616
193.25	14.51	20.76	3116.62	99.53	0.081	0.000511	0.00051870
244.25	12.91	22.98	3118.22	99.58	0.086	0.000515	0.00052136
318.75	21.96	14.77	3109.17	99.29	0.0586	0.000518	0.00052472
385	12.16	21.98	3118.97	99.61	0.0883	0.000523	0.00052733
508.5	9.56	29.72	3121.57	99.69	0.0954	0.000527	0.00053156
648	6.26	43.26	3124.87	99.80	0.1049	0.000533	0.00053564
704	7.86	35.66	3123.27	99.74	0.0999	0.000538	0.00053712
822	7.79	41.04	3123.34	99.75	0.0999	0.000543	0.00054004
1015	4.39	69	3126.74	99.85	0.10963	0.000549	0.00054429
1082	4.93	62.21	3126.2	99.84	0.10774	0.000554	0.00054564
1183	5.13	59.96	3126	99.83	0.10686	0.00056	0.00054759
1278	7.53	42.2	3123.6	99.75	0.09955	0.000564	0.00054933
1492.5	1.79	163.31	3129.34	99.94	0.11604	0.000571	0.00055299
1734	6.39	48.97	3124.74	99.79	0.10232	0.000575	0.00055672
1921.5	4.19	50.74	3126.94	99.86	0.10843	0.000581	0.00055940
2090.5	1.16	337	3129.97	99.96	0.1276	0.000588	0.00056167

CBC studies of Pb sorbed onto 10^{-1} g/L Montmorillonite at pH 6, IS 10^{-2}, 25 °C, Added [Pb] = 5×10^{-3} M

Time (hr)	CPM	%error	Amount of Pb sorbed	% Pb sorbed	Volume added (mL)	Mole of Pb sorbed/ g	Modelling Results
0	3018.04	4.85	0	0		0	0.00040034
0.25	611.65	4.95	2406.39	79.73		0.000399	0.00040148
0.5	582.27	4.99	2435.77	80.70		0.000404	0.00040195
0.75	566.53	4.98	2451.51	81.22		0.000406	0.00040231
1	591.97	4.99	2426.07	80.38		0.000402	0.00040261
1.5	596.53	4.97	2421.51	80.23		0.000401	0.00040311
2.17	595.53	4.98	2422.51	80.26		0.000401	0.00040365
2.5	578.67	4.97	2439.37	80.82		0.000404	0.00040389
3	576.3	4.98	2441.74	80.90		0.000405	0.00040422
3.5	587.67	4.98	2430.37	80.52		0.000403	0.00040452
4	573.25	5	2444.79	81.00		0.000405	0.00040480
5	585.72	4.99	2432.32	80.59		0.000403	0.00040531
6	544.46	4.98	2473.58	81.95	0.093	0.00041	0.00040576
7	612	4.96	2406.04	79.72	0	0.000403	0.00040618
8	619.31	4.98	2398.73	79.47	0	0.000402	0.00040657
9	568.86	4.98	2449.18	81.15	0.014	0.00041	0.00040693
10	573.19	4.96	2444.85	81.00	0	0.00041	0.00040726
11	595.47	4.99	2422.57	80.26	0	0.000407	0.00040758
12	579.01	4.97	2439.03	80.81	0	0.000409	0.00040789
24	579.01	4.99	2439.03	80.81	0	0.000409	0.00041079
28	564.19	4.99	2453.85	81.30	0.029	0.000412	0.00041157
30.5	593.37	4.99	2424.67	80.33	0	0.000408	0.00041202
33	600.93	5	2417.11	80.08	0	0.000407	0.00041245
48.45	593.02	4.99	2425.02	80.35	0	0.000409	0.00041479
52	600.57	5	2417.47	80.10	0	0.000407	0.00041526
57	584.34	4.98	2433.7	80.63	0	0.00041	0.00041590
75.75	573.59	4.99	2444.45	80.99	0	0.000412	0.00041803
80	589.17	4.96	2428.87	80.47	0	0.000409	0.00041847
105	596.82	4.98	2421.22	80.22	0	0.000408	0.00042082
124	584	4.98	2434.04	80.64	0	0.00041	0.00042239
149.5	540.34	4.98	2477.7	82.09	0.1	0.000417	0.00042429
174	540.97	4.98	2477.07	82.07	0.098	0.000422	0.00042594
198	573.9	4.98	2444.14	80.98	0	0.000422	0.00042742
245	551.5	4.98	2466.54	81.72	0.065	0.000425	0.00043005
294.67	560.68	4.97	2457.36	81.42	0.038	0.000427	0.00043251
335	603.78	4.98	2414.26	79.99	0	0.000422	0.00043432
478.5	585.38	4.98	2432.66	80.60	0	0.000425	0.00043987
533	601.36	4.98	2416.68	80.07	0	0.000422	0.00044171
601.5	609.46	4.96	2408.58	79.80	0	0.000421	0.00044386
720	457.1	5	2560.94	84.85	0.35	0.000446	0.00044724
770.6667	637.8	4.99	2380.24	78.86	0	0.000434	0.00044858
868	554.1	5	2463.94	81.64	0.057	0.000448	0.00045100
1340.75	562.52	5	2455.52	81.36	0.032	0.000449	0.00046083
1395.25	503.39	4.98	2514.65	83.32	0.2056	0.000446	0.00046181
1610.25	601.79	4.95	2416.25	80.06	0	0.00044	0.00046545
1922.75	541.61	4.98	2476.43	82.05	0.094	0.00045	0.00047023
2060.59	592	5	2426.04	80.38	0	0.000446	0.00047218
2127.34	507.47	4.99	2510.57	83.18	0	0.00046	0.00047309
2203.49	509.86	4.98	2508.18	83.10	0	0.00046	0.00047411
2298.99	586.41	4.99	2431.63	80.56	0	0.000447	0.00047535

2489.74	386.08	4.98	2631.96	87.20	0.5395	0.000481	0.00047774
2749.24	673.46	4.98	2344.58	77.68	0	0.00046	0.00048081
2918.99	598.63	4.97	2419.41	80.16	0	0.000472	0.00048271
3251.24	629.12	4.97	2388.92	79.15	0	0.000467	0.00048624
3449.74	618.95	4.97	2399.09	79.49	0	0.000469	0.00048824

CBC studies of Pb sorbed onto 10^{-1} g/L HMO-coated clay at pH 6, IS 10^{-2}, 25 °C, Added [Pb] = 5×10^{-3} M

Time (hr)	CPM	%error	Amount of Pb sorbed	% Pb sorbed	Volume added (mL)	Mole of Pb sorbed/ g	Modelling Results
0	3131.13	4.85	0	0		0	0.00048072
0.25	13.56	9.51	3117.57	99.56		0.000498	0.00048113
0.5	23.66	9.52	3107.47	99.24		0.000496	0.00048130
0.75	21.66	9.8	3109.47	99.30		0.000497	0.00048143
1	19.06	9.71	3112.07	99.39		0.000497	0.00048154
1.75	16.76	9.77	3114.37	99.46		0.000497	0.00048181
2.5	14.66	9.94	3116.47	99.53		0.000498	0.00048201
3	16.71	9.19	3114.42	99.46		0.000497	0.00048214
4	17.41	9.69	3113.72	99.44	0.003	0.000497	0.00048236
5	16.41	10.67	3114.72	99.47	0	0.000498	0.00048255
7	24.36	9.86	3106.77	99.22	0	0.000496	0.00048288
9	14.51	9.65	3116.62	99.53	0.009	0.000498	0.00048316
24	14.31	10.37	3116.82	99.54	0.009607	0.000498	0.00048468
57.75	12.21	10.09	3118.92	99.61	0.0161	0.000499	0.00048682
79.16667	13.46	10	3117.67	99.57	0.0122	0.0005	0.00048783
108.0833	10.46	11.46	3120.67	99.66	0.02136	0.000501	0.00048899
170.25	10.53	9.86	3120.6	99.66	0.02109	0.000502	0.00049102
320	7.79	40.97	3123.34	99.75	0.02942	0.000503	0.00049466
387	6.28	49.88	3124.85	99.79	0.03394	0.000505	0.00049598
487.25	6.19	50.37	3124.94	99.80	0.03413	0.000507	0.00049774
582.75	6.33	49.4	3124.8	99.79	0.03361	0.000508	0.00049924
797.5	0.99	290.83	3130.14	99.96	0.04968	0.000511	0.00050216
990.75	5.79	53.55	3125.34	99.81	0.03452	0.000513	0.00050444
1227.25	5.86	53.09	3125.27	99.81	0.03476	0.000514	0.00050690
1396.25	3.66	82.71	3127.47	99.88	0.041276	0.000517	0.00050850
1565.25	2.69	90.61	3128.44	99.91	0.04407	0.000519	0.00050999
1898.25	0	1000	3131.13	100.00	0.053669	0.000522	0.00051268

APPENDIX E

ADSORPTION STUDIES ON L. DISCOPHORA SP-6, EXTRACELLULAR POLYMERIC SUBSTANCES, AND BIOGENIC MN OXIDE-COATED BACTERIA

The results of Zn sorption studies on L. discophora SP-6, extracellular polymeric substances, and biogenic Mn oxide-coated bacteria are presented in this section.

Zn adsorption edge of *L. discophora* SP-6, EPS, and biogenic Mn oxide coated bacteria at 25 °C, $NaNO_3$ background electrolyte

Zn adsorption edge of *L. discophora SP-6*: pH vs percent Zn sorbed with [Zn]= 5×10^{-6} M					
pH	IS 0.001	pH	IS 0.01	pH	IS 0.1
4.0000	1.6800	4.0000	0.0000	3.9700	0.078300
4.3100	6.9200	4.5500	1.6300	4.3800	1.7500
4.8900	24.400	4.9900	4.8400	4.7500	4.7600
5.5100	44.100	5.4100	14.300	5.2400	5.1200
5.9800	58.800	6.0300	27.400	5.9900	16.400
6.4100	75.800	6.3100	38.200	6.5500	19.300
6.7000	79.300	6.5100	42.200	6.8900	23.100
7.1200	84.200	6.8900	43.100	7.3500	28.400
7.8000	84.400				
Zn adsorption edge of biogenic Mn oxide coated bacteria: pH vs percent Zn sorbed with [Zn]= 5×10^{-6} M					
pH	IS 0.001	pH	IS 0.01	pH	IS 0.1
5.0900	60.600	4.8300	28.900	4.5200	9.4700
3.8000	8.9000	4.0300	6.5500	3.9900	7.8800
4.4400	44.600	4.5000	21.300	5.4600	18.100
6.1500	83.700	5.2700	41.400	6.3900	35.500
5.5900	75.400	5.6300	63.900	5.8500	25.800
6.6200	82.100	6.9000	71.300	7.2000	40.900
7.1000	89.600	6.3000	68.100	5.0000	11.400
5.0900	60.600	4.8300	28.900	4.5200	9.4700
Zn adsorption edge of sheath: pH vs percent Zn sorbed with [Zn]= 5×10^{-6} M					
pH	IS 0.01				
4.0000	2.1400				
4.5500	5.0800				
5.0000	6.8600				
5.5000	13.700				
6.0000	14.700				
6.5000	18.500				
7.0000	25.900				
7.5000	34.700				

Zn adsorption isotherm of *L. discophora* SP-6, EPS, and biogenic Mn oxide coated bacteria at 25 °C, pH 6.6, and 10^{-2} $NaNO_3$

$[Zn]_{aq}$	Mole of Zn sorbed/g cell	$[Zn]_{aq}$	Mole of Zn sorbed/g ESP	$[Zn]_{aq}$	Mole of Zn sorbed/g MnO_x
9.3678e-7	8.1777e-06	7.2036e-7	2.0221e-06	4.1148e-6	0.0010370
1.6694e-6	1.9435e-05	8.3349e-7	1.6221e-05	9.4190e-6	0.0019149
3.5053e-6	2.9013e-05	1.0168e-6	2.9931e-05	2.4498e-5	0.0028145
4.2701e-6	4.2567e-05	1.4367e-6	4.1424e-05	3.3577e-5	0.0029692
6.1065e-6	5.2335e-05	1.6167e-6	6.2911e-05	4.1372e-5	0.0033573
7.9967e-6	5.8455e-05	1.1500e-5	6.4393e-05	5.0093e-5	0.0035661
9.3893e-6	5.7081e-05	2.6200e-5	0.00017792	6.0465e-5	0.0035217
2.7926e-5	0.00011906	3.8400e-5	0.00023557	6.7743e-5	0.0040836
4.7860e-5	0.00012003	4.2700e-5	0.00027966	7.6518e-5	0.0042508
6.7882e-5	0.00011514	5.3600e-5	0.00035138	7.8048e-7	0.00040932
				2.3188e-6	0.0014024

CBC studies of Zn sorbed onto biogenic Mn oxide coated bacteria at pH 6.6, IS 10^{-2}, 25 °C, Added [Zn] = 5×10^{-2} M

Time (hr)	CPM	%error	Amount of Zn sorbed	% Zn sorbed	Volume added (mL)	Mole of Zn sorbed/ g	Modelling Results
0	110.04	4.85	0	0		0	0.0000
1	97.51	4.95	12.53	11.38677		0.001313	0.0029727
3	93.9	4.99	16.14	14.66739		0.001692	0.0030153
15	95.31	4.98	14.73	13.38604		0.001544	0.0031213
21	98.7	4.99	11.34	10.30534		0.001189	0.0031531
33	88.16	4.97	21.88	19.88368	0.03	0.002293	0.0032030
69	89.44	4.98	20.6	18.72047	0.024	0.0028	0.0033054
98.5	91.23	4.97	18.81	17.09378		0.003181	0.0033655
119.25	81.54	4.98	28.5	25.89967	0.056	0.00407	0.0034010
166.25	100.63	4.98	9.41	8.551436		0.003529	0.0034684
238.25	102.1	5	7.94	7.215558		0.003281	0.0035502
331.75	92.01	4.99	18.03	16.38495		0.004246	0.0036339
401.75	87.2	4.98	22.84	20.75609	0.024	0.004684	0.0036861
425.75	98.83	4.96	11.21	10.1872		0.003989	0.0037025
691.75	95.07	4.98	14.97	13.60414		0.004049	0.0038503
882.5	93.35	4.98	16.69	15.16721		0.003981	0.0039315
1193.75	95.48	4.98	14.56	13.23155		0.003602	0.0040384
1361.75	85.97	4.98	24.07	21.87386		0.004561	0.0040870
1730	84.94	4.98	25.1	22.80989	0.024	0.004069	0.0041781
2083	85.61	4.98	24.43	22.20102		0.004275	0.0042510
2393.75	84.73	4.98	25.31	23.00073		0.004393	0.0043067
2616	85.21	4.98	24.83	22.56452		0.004328	0.0043426
3024	79.45	4.98	30.59	27.79898		0.004292	0.0044017
3239	80.15	4.98	29.89	27.16285		0.00419	0.0044298
3690.25	74.29	4.98	35.75	32.48819		0.004465	0.0044834
4266.25	72.17	4.98	37.87	34.41476		0.004169	0.0045429
5034.25	71.17	4.98	38.87	35.32352		0.004166	0.0046104

APPENDIX F

PARTICLE SIZE DISTRIBUTION AND TITRATION

The raw data of particle size distribution of Mn oxides, clays, and Mn oxide-coated clay are provided in this section.

Particle distribution of HMO in aqueous phase with background electrolyte of $NaNO_3$

Diameter	pH 5			pH 7		
(μm)	IS 0.015	IS 0.15	IS 1.5	IS 0.015	IS 0.15	IS 1.5
0.375	0	0	0	0	0	0.00038
0.412	0	0	0	0	0	0.00071
0.452	0	0	0	0.000039	0.000044	0.0016
0.496	0.000032	0.000027	1.30E-05	0.00047	0.00053	0.0036
0.545	0.00044	0.00042	0.00029	0.0024	0.0026	0.0073
0.598	0.0024	0.0024	0.002	0.0059	0.0065	0.013
0.656	0.0066	0.0072	0.0067	0.011	0.011	0.019
0.721	0.013	0.014	0.015	0.015	0.016	0.027
0.791	0.019	0.023	0.025	0.019	0.02	0.037
0.868	0.027	0.031	0.037	0.024	0.024	0.047
0.953	0.034	0.041	0.051	0.027	0.026	0.059
1.047	0.041	0.049	0.067	0.028	0.025	0.07
1.149	0.046	0.056	0.083	0.028	0.023	0.081
1.261	0.05	0.061	0.099	0.027	0.018	0.092
1.384	0.052	0.063	0.12	0.027	0.014	0.1
1.52	0.054	0.064	0.13	0.028	0.012	0.11
1.668	0.056	0.064	0.15	0.032	0.013	0.12
1.832	0.06	0.064	0.17	0.044	0.022	0.13
2.011	0.068	0.069	0.19	0.067	0.044	0.14
2.207	0.085	0.08	0.22	0.11	0.085	0.16
2.423	0.11	0.1	0.26	0.17	0.15	0.19
2.66	0.16	0.14	0.31	0.26	0.26	0.22
2.92	0.23	0.2	0.39	0.39	0.4	0.27
3.205	0.33	0.29	0.48	0.55	0.58	0.35
3.519	0.46	0.42	0.61	0.76	0.82	0.44
3.863	0.63	0.59	0.76	1.02	1.11	0.57
4.24	0.85	0.81	0.96	1.32	1.46	0.73
4.655	1.12	1.09	1.19	1.67	1.86	0.92
5.11	1.44	1.41	1.46	2.05	2.3	1.15
5.61	1.8	1.8	1.77	2.48	2.79	1.42
6.158	2.22	2.24	2.12	2.93	3.3	1.72
6.76	2.69	2.73	2.5	3.39	3.83	2.06
7.421	3.19	3.27	2.91	3.86	4.37	2.42
8.147	3.74	3.85	3.34	4.32	4.89	2.82
8.943	4.32	4.47	3.78	4.74	5.37	3.22
9.818	4.92	5.11	4.22	5.1	5.77	3.63
10.78	5.51	5.73	4.63	5.36	6.06	4.02
11.83	6.04	6.29	4.97	5.49	6.18	4.34

Diameter	pH 5			pH 7		
(μm)	IS 0.015	IS 0.15	IS 1.5	IS 0.015	IS 0.15	IS 1.5
12.99	6.46	6.71	5.2	5.44	6.09	4.56
14.26	6.71	6.93	5.26	5.19	5.77	4.63
15.65	6.72	6.88	5.13	4.74	5.2	4.52
17.18	6.45	6.51	4.77	4.13	4.43	4.18
18.86	5.86	5.79	4.19	3.41	3.53	3.64
20.71	4.99	4.77	3.45	2.69	2.63	2.95
22.73	3.94	3.59	2.66	2.08	1.88	2.22
24.95	2.87	2.45	1.96	1.66	1.37	1.57
27.39	1.94	1.53	1.45	1.44	1.12	1.12
30.07	1.28	0.96	1.18	1.39	1.1	0.9
33.01	0.9	0.71	1.13	1.45	1.21	0.87
36.24	0.77	0.7	1.23	1.54	1.37	0.99
39.78	0.79	0.82	1.42	1.58	1.46	1.18
43.67	0.88	0.99	1.61	1.55	1.43	1.37
47.94	0.96	1.08	1.75	1.43	1.31	1.49
52.62	0.97	1.05	1.81	1.28	1.15	1.54
57.77	0.92	0.93	1.8	1.13	1.02	1.53
63.41	0.82	0.77	1.77	1.02	0.94	1.51
69.61	0.71	0.62	1.72	0.95	0.93	1.51
76.42	0.63	0.53	1.67	0.92	0.95	1.52
83.89	0.6	0.48	1.61	0.92	0.94	1.56
92.09	0.61	0.47	1.54	0.91	0.85	1.61
101.1	0.64	0.49	1.45	0.89	0.68	1.68
111	0.65	0.51	1.34	0.85	0.46	1.75
121.8	0.61	0.52	1.22	0.81	0.23	1.8
133.7	0.49	0.5	1.08	0.79	0.077	1.84
146.8	0.3	0.46	0.91	0.79	0.013	1.89
161.2	0.12	0.39	0.72	0.79	0.00083	1.96
176.9	0.024	0.29	0.5	0.73	0	2.05
194.2	0.0019	0.19	0.29	0.6	0	2.11
213.2	0	0.096	0.12	0.37	0	2.04
234	0	0.034	0.032	0.16	0	1.78
256.9	0	0.0061	0.0042	0.032	0	1.32
282.1	0	0.00044	0.00013	0.0028	0	0.75
309.6	0	0	0	0	0	0.29
339.9	0	0	0	0	0	0.055
373.1	0	0	0	0	0	0.0042

Particle distribution of Birnessite Type 1 in aqueous phase with background electrolyte of $NaNO_3$

Diameter	pH 5			pH 7		
(μm)	IS 0.001	IS 0.01	IS 0.1	IS 0.001	IS 0.01	IS 0.1
0.375	0.014	0.016	0.03	0.033	0	0.0049
0.412	0.025	0.027	0.053	0.056	0	0.0085
0.452	0.037	0.039	0.08	0.082	0	0.013
0.496	0.056	0.057	0.095	0.12	0	0.02
0.545	0.08	0.077	0.098	0.16	0	0.028
0.598	0.11	0.1	0.093	0.21	0.00043	0.04
0.656	0.15	0.14	0.082	0.28	0.0048	0.056
0.721	0.21	0.18	0.074	0.37	0.027	0.077
0.791	0.28	0.24	0.075	0.48	0.076	0.1
0.868	0.36	0.32	0.094	0.62	0.16	0.14

0.953	0.47	0.41	0.14	0.79	0.26	0.18
1.047	0.59	0.53	0.22	1	0.37	0.23
1.149	0.73	0.66	0.35	1.22	0.5	0.29
1.261	0.88	0.8	0.5	1.46	0.62	0.36
1.384	1.03	0.95	0.69	1.69	0.74	0.43
1.52	1.17	1.09	0.89	1.9	0.82	0.5
1.668	1.29	1.22	1.07	2.06	0.88	0.57
1.832	1.39	1.32	1.23	2.17	0.92	0.63
2.011	1.46	1.4	1.35	2.21	0.95	0.68
2.207	1.49	1.44	1.42	2.19	0.95	0.73
2.423	1.5	1.46	1.45	2.12	0.94	0.77
2.66	1.48	1.45	1.47	2.01	0.92	0.79
2.92	1.45	1.42	1.49	1.9	0.89	0.81
3.205	1.42	1.39	1.57	1.8	0.88	0.82
3.519	1.39	1.35	1.69	1.73	0.88	0.82
3.863	1.36	1.32	1.86	1.69	0.88	0.82
4.24	1.33	1.28	2.01	1.64	0.88	0.81
4.655	1.29	1.23	2.11	1.58	0.88	0.78
5.11	1.24	1.16	2.09	1.48	0.88	0.75
5.61	1.18	1.08	1.97	1.34	0.88	0.71
6.158	1.12	1	1.79	1.19	0.87	0.67
6.76	1.06	0.92	1.61	1.03	0.85	0.63
7.421	1.01	0.87	1.48	0.9	0.83	0.59
8.147	0.99	0.84	1.4	0.83	0.8	0.57
8.943	1	0.85	1.35	0.8	0.78	0.56
9.818	1.05	0.9	1.33	0.83	0.77	0.56
10.78	1.13	0.98	1.37	0.91	0.78	0.59
11.83	1.22	1.07	1.5	1.03	0.82	0.64
12.99	1.3	1.13	1.61	1.17	0.88	0.7
14.26	1.36	1.17	1.55	1.31	0.97	0.76
15.65	1.4	1.18	1.4	1.42	1.07	0.83
17.18	1.44	1.19	1.47	1.51	1.18	0.89
18.86	1.51	1.24	1.84	1.56	1.28	0.95
20.71	1.61	1.32	2.13	1.6	1.36	1
22.73	1.73	1.43	1.92	1.65	1.43	1.06
24.95	1.85	1.54	1.57	1.75	1.51	1.13
27.39	1.94	1.64	1.7	1.9	1.59	1.23
30.07	2.02	1.72	2.39	2.1	1.68	1.35
33.01	2.11	1.8	2.95	2.32	1.79	1.5
36.24	2.24	1.91	2.77	2.51	1.91	1.67
39.78	2.43	2.09	2.48	2.65	2.04	1.85
43.67	2.65	2.33	2.73	2.72	2.18	2.03
47.94	2.84	2.59	3.21	2.73	2.32	2.2
52.62	2.95	2.81	3.26	2.73	2.44	2.37
57.77	2.94	2.94	3.16	2.77	2.54	2.53
63.41	2.82	2.99	3.5	2.9	2.62	2.7
69.61	2.72	3.02	3.84	3.13	2.7	2.9
76.42	2.75	3.15	3.43	3.39	2.78	3.13
83.89	3.01	3.48	3.1	3.51	2.9	3.4
92.09	3.49	4.04	3.75	3.34	3.05	3.67
101.1	3.99	4.68	4.03	2.76	3.2	3.88
111	4.18	5.06	1.86	1.73	3.26	3.98
121.8	3.79	4.82	0.16	0.74	3.16	3.91
133.7	2.78	3.83	0	0.15	2.89	3.73
146.8	1.48	2.25	0	0.013	2.59	3.56
161.2	0.5	0.88	0	0	2.42	3.52

176.9	0.083	0.17	0	0	2.53	3.67
194.2	0.0047	0.012	0	0	2.86	3.88
213.2	0	0	0	0	3.19	3.89
234	0	0	0	0	3.22	3.48
256.9	0	0	0	0	2.75	2.63
282.1	0	0	0	0	1.85	1.5
309.6	0	0	0	0	0.89	0.58
339.9	0	0	0	0	0.26	0.11
373.1	0	0	0	0	0.039	0.0088
409.6	0	0	0	0	0.0016	0

Particle distribution of Birnessite Type 2 in aqueous phase with background electrolyte of $NaNO_3$

Diameter	pH 5			pH 7		
(μm)	IS 0.001	IS 0.01	IS 0.1	IS 0.001	IS 0.01	IS 0.1
0.375	0.049	0.09	0.028	0.15	0.079	0.032
0.412	0.085	0.16	0.048	0.25	0.14	0.056
0.452	0.12	0.22	0.068	0.35	0.2	0.083
0.496	0.17	0.31	0.096	0.48	0.28	0.12
0.545	0.22	0.38	0.12	0.56	0.34	0.16
0.598	0.26	0.44	0.15	0.62	0.4	0.2
0.656	0.29	0.49	0.17	0.65	0.45	0.24
0.721	0.33	0.54	0.21	0.69	0.5	0.29
0.791	0.37	0.58	0.25	0.72	0.54	0.34
0.868	0.41	0.62	0.29	0.76	0.58	0.4
0.953	0.45	0.65	0.35	0.81	0.61	0.46
1.047	0.49	0.69	0.43	0.88	0.64	0.53
1.149	0.53	0.73	0.51	0.97	0.67	0.59
1.261	0.57	0.76	0.6	1.08	0.7	0.65
1.384	0.61	0.79	0.69	1.19	0.71	0.71
1.52	0.63	0.8	0.78	1.28	0.71	0.74
1.668	0.64	0.8	0.86	1.33	0.7	0.77
1.832	0.64	0.77	0.92	1.33	0.66	0.77
2.011	0.62	0.72	0.96	1.27	0.61	0.75
2.207	0.58	0.64	0.98	1.14	0.55	0.72
2.423	0.54	0.56	0.97	0.98	0.48	0.66
2.66	0.49	0.47	0.93	0.8	0.41	0.6
2.92	0.44	0.4	0.88	0.65	0.35	0.54
3.205	0.41	0.36	0.82	0.56	0.31	0.48
3.519	0.4	0.35	0.75	0.54	0.29	0.43
3.863	0.39	0.35	0.69	0.57	0.29	0.4
4.24	0.4	0.37	0.63	0.62	0.3	0.37
4.655	0.4	0.39	0.57	0.66	0.31	0.35
5.11	0.39	0.39	0.51	0.65	0.31	0.33
5.61	0.38	0.37	0.45	0.59	0.3	0.31
6.158	0.36	0.34	0.4	0.51	0.29	0.29
6.76	0.34	0.31	0.37	0.43	0.27	0.28
7.421	0.33	0.29	0.35	0.38	0.26	0.28
8.147	0.32	0.28	0.36	0.38	0.26	0.29
8.943	0.33	0.28	0.38	0.42	0.27	0.32
9.818	0.36	0.31	0.43	0.49	0.3	0.36
10.78	0.4	0.36	0.5	0.57	0.34	0.41
11.83	0.45	0.42	0.59	0.65	0.39	0.47
12.99	0.49	0.49	0.67	0.72	0.44	0.52

14.26	0.54	0.55	0.75	0.78	0.48	0.57
15.65	0.59	0.61	0.82	0.83	0.52	0.62
17.18	0.65	0.65	0.88	0.88	0.56	0.68
18.86	0.72	0.68	0.93	0.94	0.61	0.76
20.71	0.8	0.72	1	1.02	0.67	0.84
22.73	0.87	0.76	1.09	1.1	0.73	0.92
24.95	0.93	0.81	1.21	1.18	0.81	0.98
27.39	0.99	0.87	1.36	1.27	0.88	1.05
30.07	1.05	0.94	1.52	1.36	0.95	1.12
33.01	1.12	1.03	1.69	1.45	1.03	1.22
36.24	1.24	1.13	1.86	1.53	1.11	1.34
39.78	1.4	1.25	2.01	1.62	1.21	1.49
43.67	1.59	1.39	2.15	1.72	1.31	1.65
47.94	1.8	1.53	2.27	1.82	1.43	1.79
52.62	2	1.65	2.4	1.92	1.53	1.93
57.77	2.18	1.75	2.52	2.04	1.61	2.06
63.41	2.34	1.8	2.64	2.17	1.67	2.21
69.61	2.52	1.83	2.78	2.31	1.71	2.43
76.42	2.74	1.88	2.93	2.46	1.78	2.71
83.89	3.04	2.01	3.09	2.61	1.92	3.02
92.09	3.44	2.28	3.22	2.69	2.18	3.29
101.1	3.85	2.69	3.26	2.65	2.57	3.39
111	4.15	3.13	3.15	2.45	2.96	3.31
121.8	4.24	3.41	2.93	2.24	3.12	3.23
133.7	4.12	3.35	2.79	2.23	2.84	3.41
146.8	3.98	3.01	2.93	2.64	2.2	4.12
161.2	4.03	2.79	3.48	3.53	1.77	5.31
176.9	4.4	2.98	4.31	4.64	1.91	6.56
194.2	4.95	3.89	5.02	5.42	3.05	7.13
213.2	5.31	5.3	5.09	5.28	5.14	6.47
234	5.06	6.62	4.24	4.13	7.46	4.67
256.9	4.04	6.96	2.61	2.35	8.63	2.44
282.1	2.42	5.92	1.08	0.88	7.93	0.81
309.6	0.98	3.7	0.22	0.16	5.61	0.13
339.9	0.2	1.54	0.018	0.012	2.83	0.0077
373.1	0.016	0.31	0	0	0.89	0
409.6	0	0.027	0	0	0.14	0
449.7	0	0	0	0	0.0068	0

Particle distribution of Pyrolusite in aqueous phase with background electrolyte of $NaNO_3$

Diameter	pH 5			pH 7		
(μm)	IS 0.001	IS 0.01	IS 0.1	IS 0.001	IS 0.01	IS 0.1
0.375	0	0	0	0	0	0
0.412	0	0	0	0	0	0
0.452	0	0	0	0	0	0
0.496	0	0	0	0	0	0
0.545	0	0.000039	0	0	0	0.000055
0.598	0	0.00065	0	0	0	0.00086
0.656	0	0.004	0	0	0	0.005
0.721	0	0.013	0	0	0.00037	0.015
0.791	0	0.028	0	0	0.0047	0.033
0.868	0	0.049	0	0	0.024	0.055
0.953	0	0.076	0.0017	0	0.064	0.084

1.047	0.00013	0.11	0.028	0.0045	0.12	0.12
1.149	0.012	0.14	0.11	0.065	0.18	0.16
1.261	0.088	0.18	0.21	0.2	0.25	0.2
1.384	0.21	0.22	0.31	0.34	0.31	0.23
1.52	0.34	0.25	0.39	0.49	0.37	0.26
1.668	0.48	0.28	0.46	0.65	0.41	0.29
1.832	0.58	0.31	0.48	0.74	0.45	0.31
2.011	0.62	0.33	0.47	0.77	0.48	0.33
2.207	0.61	0.34	0.44	0.74	0.5	0.34
2.423	0.56	0.35	0.38	0.67	0.5	0.34
2.66	0.5	0.35	0.33	0.59	0.5	0.34
2.92	0.45	0.35	0.3	0.51	0.5	0.34
3.205	0.41	0.36	0.29	0.48	0.5	0.35
3.519	0.41	0.36	0.31	0.49	0.5	0.36
3.863	0.44	0.37	0.36	0.54	0.51	0.37
4.24	0.49	0.38	0.42	0.62	0.53	0.39
4.655	0.55	0.4	0.49	0.7	0.56	0.42
5.11	0.6	0.42	0.55	0.77	0.59	0.45
5.61	0.65	0.45	0.6	0.83	0.63	0.49
6.158	0.69	0.49	0.63	0.86	0.68	0.53
6.76	0.72	0.52	0.65	0.89	0.72	0.57
7.421	0.74	0.57	0.66	0.91	0.78	0.62
8.147	0.76	0.61	0.67	0.91	0.83	0.66
8.943	0.77	0.67	0.69	0.92	0.88	0.71
9.818	0.78	0.73	0.73	0.96	0.94	0.76
10.78	0.82	0.8	0.8	1.05	1	0.81
11.83	0.88	0.88	0.92	1.19	1.07	0.88
12.99	0.95	0.97	1.04	1.34	1.14	0.95
14.26	1.01	1.07	1.14	1.46	1.23	1.03
15.65	1.09	1.18	1.21	1.51	1.34	1.12
17.18	1.22	1.3	1.27	1.57	1.48	1.21
18.86	1.46	1.43	1.39	1.71	1.62	1.31
20.71	1.72	1.54	1.57	1.9	1.75	1.39
22.73	1.88	1.66	1.7	1.98	1.85	1.47
24.95	1.91	1.77	1.79	1.99	1.93	1.56
27.39	1.96	1.89	1.92	2.11	2.03	1.66
30.07	2.19	2.06	2.19	2.44	2.19	1.8
33.01	2.62	2.29	2.57	2.84	2.44	1.99
36.24	3.11	2.6	2.91	3.09	2.79	2.23
39.78	3.6	2.98	3.21	3.3	3.22	2.53
43.67	4.1	3.42	3.58	3.73	3.66	2.88
47.94	4.63	3.89	4.04	4.29	4.06	3.26
52.62	5.14	4.34	4.47	4.67	4.36	3.66
57.77	5.68	4.73	4.84	4.9	4.6	4.03
63.41	6.18	5.03	5.16	5.18	4.85	4.35
69.61	6.12	5.2	5.37	5.3	5.19	4.59
76.42	5.61	5.25	5.4	5.04	5.62	4.72
83.89	6	5.15	5.27	5.06	6.03	4.74
92.09	7.5	4.91	4.94	5.86	6.14	4.65
101.1	7.05	4.53	4.41	5.99	5.69	4.47
111	2.84	4.02	3.85	3.77	4.56	4.19
121.8	0.23	3.43	3.34	1.01	2.96	3.81
133.7	0	2.82	2.78	0.059	1.41	3.32
146.8	0	2.28	2.24	0	0.42	2.76
161.2	0	1.85	1.87	0	0.064	2.15
176.9	0	1.53	1.35	0	0.003	1.59

194.2	0	1.26	0.49	0	0	1.13
213.2	0	0.99	0.038	0	0	0.83
234	0	0.69	0	0	0	0.66
256.9	0	0.38	0	0	0	0.61
282.1	0	0.14	0	0	0	0.63
309.6	0	0.027	0	0	0	0.7
339.9	0	0.0021	0	0	0	0.77
373.1	0	0	0	0	0	0.81
409.6	0	0	0	0	0	0.79
449.7	0	0	0	0	0	0.72
493.6	0	0	0	0	0	0.57
541.9	0	0	0	0	0	0.36
594.8	0	0	0	0	0	0.16
653	0	0	0	0	0	0.033
716.8	0	0	0	0	0	0.003

Particle distribution of Kaolinite in aqueous phase with background electrolyte of $NaNO_3$

Diameter	pH 5			pH 7		
(μm)	IS 0.001	IS 0.01	IS 0.1	IS 0.001	IS 0.01	IS 0.1
0.375	0.032	0.01	0.013	0.017	0.026	0.012
0.412	0.058	0.019	0.022	0.03	0.049	0.022
0.452	0.093	0.032	0.036	0.046	0.078	0.036
0.496	0.12	0.047	0.061	0.073	0.1	0.063
0.545	0.14	0.065	0.097	0.11	0.13	0.1
0.598	0.17	0.091	0.15	0.15	0.15	0.16
0.656	0.2	0.13	0.22	0.21	0.18	0.24
0.721	0.24	0.19	0.31	0.29	0.23	0.35
0.791	0.3	0.27	0.43	0.39	0.29	0.48
0.868	0.39	0.38	0.58	0.51	0.38	0.65
0.953	0.53	0.51	0.76	0.66	0.5	0.86
1.047	0.7	0.68	0.97	0.84	0.66	1.1
1.149	0.93	0.88	1.22	1.05	0.85	1.37
1.261	1.19	1.1	1.5	1.29	1.06	1.67
1.384	1.47	1.32	1.79	1.56	1.28	1.98
1.52	1.77	1.54	2.1	1.84	1.51	2.31
1.668	2.06	1.75	2.41	2.14	1.72	2.62
1.832	2.33	1.94	2.72	2.45	1.92	2.92
2.011	2.57	2.13	3.01	2.76	2.1	3.18
2.207	2.79	2.32	3.27	3.06	2.29	3.41
2.423	2.99	2.53	3.49	3.34	2.5	3.58
2.66	3.21	2.81	3.66	3.58	2.76	3.7
2.92	3.48	3.15	3.78	3.78	3.09	3.75
3.205	3.8	3.57	3.82	3.92	3.49	3.74
3.519	4.15	4.01	3.8	3.99	3.93	3.67
3.863	4.47	4.42	3.71	3.99	4.33	3.54
4.24	4.64	4.71	3.55	3.9	4.6	3.35
4.655	4.58	4.79	3.32	3.74	4.64	3.11
5.11	4.25	4.61	3.05	3.51	4.4	2.82
5.61	3.69	4.2	2.73	3.22	3.93	2.51
6.158	3.04	3.65	2.41	2.9	3.31	2.2
6.76	2.45	3.07	2.09	2.57	2.67	1.91
7.421	2.03	2.56	1.81	2.25	2.13	1.66
8.147	1.8	2.18	1.57	1.96	1.74	1.47
8.943	1.7	1.93	1.4	1.73	1.52	1.34

9.818	1.7	1.81	1.32	1.58	1.46	1.3
10.78	1.79	1.83	1.32	1.51	1.55	1.32
11.83	1.96	1.94	1.4	1.54	1.72	1.41
12.99	2.04	2.02	1.55	1.64	1.82	1.53
14.26	1.82	1.96	1.71	1.77	1.67	1.66
15.65	1.47	1.83	1.83	1.9	1.42	1.74
17.18	1.47	1.88	1.87	1.96	1.42	1.76
18.86	1.94	2.16	1.82	1.94	1.78	1.7
20.71	2.2	2.23	1.72	1.84	2.04	1.61
22.73	1.54	1.74	1.62	1.71	1.67	1.51
24.95	0.79	1.19	1.56	1.59	1.14	1.45
27.39	0.84	1.21	1.55	1.52	1.14	1.44
30.07	1.64	1.77	1.57	1.5	1.65	1.47
33.01	2.13	2.13	1.59	1.52	2.06	1.51
36.24	1.47	1.65	1.6	1.54	1.86	1.52
39.78	0.77	0.98	1.58	1.53	1.46	1.5
43.67	0.81	0.88	1.56	1.46	1.44	1.46
47.94	1.28	1.26	1.54	1.31	1.78	1.4
52.62	1.2	1.27	1.5	1.09	1.76	1.34
57.77	0.64	0.59	1.39	0.81	1.12	1.3
63.41	0.48	0.092	1.17	0.51	0.74	1.23
69.61	0.71	0.0025	0.82	0.24	0.97	1.12
76.42	0.68	0	0.42	0.069	1.18	0.91
83.89	0.23	0	0.13	0.01	0.55	0.58
92.09	0.016	0	0.02	0.00042	0.047	0.25
101.1	0	0	0.00088	0	0	0.054
111	0	0	0	0	0	0.0048

Particle distribution of Montmorillonite in aqueous phase with background electrolyte of $NaNO_3$

Diameter	pH 5			pH 7		
(μm)	IS 0.001	IS 0.01	IS 0.1	IS 0.001	IS 0.01	IS 0.1
0.375	0.016	0.063	0.052	0.041	0.053	0.044
0.412	0.028	0.11	0.092	0.073	0.095	0.078
0.452	0.041	0.17	0.14	0.11	0.14	0.11
0.496	0.063	0.24	0.2	0.16	0.2	0.16
0.545	0.095	0.31	0.25	0.21	0.26	0.2
0.598	0.14	0.38	0.32	0.26	0.31	0.24
0.656	0.2	0.45	0.38	0.32	0.37	0.28
0.721	0.27	0.53	0.46	0.39	0.44	0.32
0.791	0.36	0.63	0.55	0.48	0.52	0.36
0.868	0.5	0.74	0.66	0.6	0.62	0.43
0.953	0.66	0.87	0.79	0.74	0.74	0.51
1.047	0.86	1.03	0.96	0.91	0.89	0.61
1.149	1.11	1.24	1.16	1.13	1.09	0.76
1.261	1.42	1.51	1.42	1.41	1.35	0.96
1.384	1.77	1.83	1.74	1.74	1.66	1.23
1.52	2.16	2.18	2.1	2.11	2.02	1.56
1.668	2.59	2.59	2.5	2.52	2.43	1.95
1.832	3.04	3.05	2.95	2.99	2.9	2.41
2.011	3.51	3.56	3.44	3.49	3.42	2.95
2.207	3.97	4.06	3.94	4	3.94	3.51
2.423	4.38	4.51	4.41	4.45	4.43	4.07
2.66	4.71	4.89	4.8	4.84	4.85	4.58

2.92	4.95	5.18	5.11	5.14	5.19	5.03
3.205	5.08	5.36	5.32	5.32	5.41	5.37
3.519	5.06	5.35	5.36	5.33	5.45	5.55
3.863	4.87	5.15	5.21	5.15	5.29	5.53
4.24	4.53	4.74	4.86	4.78	4.93	5.29
4.655	4.07	4.21	4.38	4.28	4.43	4.88
5.11	3.56	3.61	3.82	3.71	3.87	4.38
5.61	3.04	3.02	3.25	3.14	3.3	3.85
6.158	2.55	2.47	2.71	2.61	2.76	3.34
6.76	2.1	1.99	2.2	2.12	2.28	2.85
7.421	1.72	1.6	1.78	1.73	1.88	2.41
8.147	1.4	1.3	1.41	1.41	1.56	2.01
8.943	1.17	1.09	1.13	1.18	1.32	1.67
9.818	1.01	0.95	0.92	1.02	1.14	1.38
10.78	0.94	0.91	0.82	0.96	1.06	1.18
11.83	0.96	0.95	0.82	0.99	1.06	1.09
12.99	1.05	1.06	0.92	1.1	1.14	1.1
14.26	1.22	1.2	1.1	1.26	1.26	1.2
15.65	1.37	1.3	1.27	1.4	1.35	1.31
17.18	1.49	1.33	1.39	1.47	1.38	1.38
18.86	1.5	1.26	1.39	1.42	1.29	1.34
20.71	1.43	1.12	1.31	1.3	1.14	1.23
22.73	1.3	0.97	1.16	1.14	0.97	1.07
24.95	1.18	0.85	1.02	1.01	0.83	0.92
27.39	1.1	0.79	0.93	0.93	0.75	0.83
30.07	1.07	0.77	0.9	0.89	0.73	0.78
33.01	1.1	0.8	0.92	0.9	0.75	0.78
36.24	1.14	0.81	0.94	0.91	0.76	0.78
39.78	1.17	0.82	0.96	0.91	0.75	0.78
43.67	1.16	0.8	0.92	0.87	0.7	0.76
47.94	1.11	0.75	0.83	0.79	0.63	0.71
52.62	0.99	0.7	0.68	0.67	0.55	0.63
57.77	0.83	0.62	0.51	0.53	0.47	0.52
63.41	0.55	0.52	0.3	0.37	0.37	0.39
69.61	0.25	0.39	0.12	0.2	0.27	0.23
76.42	0.056	0.22	0.025	0.076	0.15	0.097
83.89	0.0054	0.086	0.0022	0.014	0.055	0.02
92.09	0	0.016	0	0.0011	0.01	0.0017
101.1	0	0.0012	0	0	0.00068	0

Particle distribution of HMO-coated clay in aqueous phase with background electrolyte of $NaNO_3$

Diameter	pH 6			pH 7		
(μm)	IS 0.001	IS 0.01	IS 0.1	IS 0.001	IS 0.01	IS 0.1
0.375	0.017	0	0	0.011	0	0
0.412	0.029	0	0	0.02	0	0
0.452	0.042	0	0	0.029	0	0
0.496	0.057	0	0	0.039	0	0
0.545	0.065	0	0	0.044	0	0
0.598	0.069	0	0	0.047	0	0
0.656	0.069	0	0	0.047	0	0
0.721	0.067	0	0	0.046	0	0
0.791	0.06	0	0	0.044	0	0
0.868	0.052	0	0	0.043	0	0

0.953	0.045	0	0	0.044	0.00032	0.000039
1.047	0.043	0.000036	0.00015	0.052	0.0042	0.0013
1.149	0.048	0.0014	0.0028	0.069	0.023	0.01
1.261	0.064	0.011	0.018	0.1	0.065	0.042
1.384	0.095	0.047	0.062	0.15	0.13	0.1
1.52	0.15	0.12	0.14	0.21	0.22	0.19
1.668	0.22	0.22	0.25	0.31	0.33	0.31
1.832	0.33	0.35	0.39	0.43	0.48	0.46
2.011	0.47	0.52	0.56	0.58	0.65	0.64
2.207	0.65	0.73	0.78	0.77	0.87	0.87
2.423	0.86	0.98	1.05	0.99	1.11	1.13
2.66	1.12	1.27	1.35	1.24	1.39	1.42
2.92	1.42	1.59	1.69	1.53	1.7	1.75
3.205	1.75	1.95	2.05	1.85	2.04	2.1
3.519	2.12	2.34	2.45	2.2	2.4	2.47
3.863	2.51	2.74	2.86	2.57	2.77	2.86
4.24	2.93	3.16	3.27	2.94	3.14	3.24
4.655	3.35	3.57	3.68	3.33	3.51	3.62
5.11	3.77	3.97	4.07	3.71	3.87	3.98
5.61	4.17	4.34	4.43	4.07	4.21	4.32
6.158	4.56	4.68	4.75	4.41	4.52	4.62
6.76	4.9	4.98	5.03	4.72	4.79	4.88
7.421	5.2	5.23	5.25	4.99	5.02	5.09
8.147	5.44	5.41	5.4	5.2	5.19	5.23
8.943	5.59	5.51	5.46	5.34	5.3	5.3
9.818	5.64	5.51	5.42	5.39	5.32	5.29
10.78	5.58	5.4	5.28	5.35	5.25	5.18
11.83	5.38	5.18	5.03	5.2	5.08	4.98
12.99	5.06	4.85	4.68	4.95	4.82	4.68
14.26	4.62	4.43	4.26	4.59	4.46	4.3
15.65	4.1	3.93	3.77	4.14	4.02	3.86
17.18	3.51	3.4	3.26	3.63	3.53	3.37
18.86	2.93	2.85	2.75	3.09	3	2.86
20.71	2.38	2.34	2.28	2.56	2.47	2.37
22.73	1.9	1.88	1.86	2.06	1.98	1.92
24.95	1.51	1.49	1.5	1.64	1.54	1.53
27.39	1.21	1.18	1.19	1.29	1.18	1.2
30.07	0.97	0.92	0.94	1.02	0.9	0.93
33.01	0.78	0.72	0.72	0.79	0.68	0.72
36.24	0.61	0.55	0.54	0.6	0.52	0.54
39.78	0.46	0.41	0.4	0.44	0.39	0.4
43.67	0.32	0.3	0.29	0.29	0.29	0.29
47.94	0.21	0.22	0.21	0.18	0.22	0.21
52.62	0.14	0.18	0.17	0.11	0.17	0.16
57.77	0.1	0.15	0.14	0.078	0.14	0.13
63.41	0.084	0.13	0.12	0.076	0.12	0.12
69.61	0.073	0.12	0.1	0.089	0.095	0.11
76.42	0.06	0.09	0.074	0.099	0.067	0.094
83.89	0.038	0.053	0.042	0.089	0.036	0.066
92.09	0.016	0.02	0.016	0.056	0.012	0.034
101.1	0.0032	0.0038	0.003	0.023	0.0019	0.01
111	0.00026	0.00026	0.00023	0.0043	0.000091	0.0014
121.8	0	0	0	0.0003	0	0.000048

Particle distribution of Birnessite-coated clay in aqueous phase with background electrolyte of $NaNO_3$

Diameter (μm)	pH 5	pH 7		
	IS 0.01	IS 0.001	IS 0.01	IS 0.1
0.375	0.0053	0.019	0.0091	0.0062
0.412	0.01	0.034	0.016	0.011
0.452	0.02	0.054	0.027	0.021
0.496	0.039	0.087	0.046	0.04
0.545	0.072	0.13	0.073	0.07
0.598	0.12	0.17	0.11	0.11
0.656	0.18	0.23	0.15	0.16
0.721	0.25	0.29	0.20	0.23
0.791	0.34	0.37	0.26	0.31
0.868	0.44	0.45	0.33	0.39
0.953	0.55	0.53	0.40	0.49
1.047	0.66	0.62	0.48	0.59
1.149	0.78	0.71	0.56	0.7
1.261	0.89	0.79	0.63	0.8
1.384	1	0.86	0.70	0.9
1.52	1.1	0.93	0.77	0.99
1.668	1.18	0.99	0.83	1.07
1.832	1.25	1.04	0.87	1.15
2.011	1.31	1.08	0.91	1.21
2.207	1.36	1.12	0.95	1.27
2.423	1.4	1.15	0.98	1.33
2.66	1.44	1.19	1.01	1.38
2.92	1.49	1.24	1.04	1.44
3.205	1.54	1.30	1.08	1.50
3.519	1.61	1.38	1.14	1.57
3.863	1.69	1.47	1.20	1.65
4.24	1.79	1.58	1.29	1.74
4.655	1.91	1.71	1.39	1.84
5.11	2.04	1.86	1.52	1.96
5.61	2.19	2.04	1.66	2.09
6.158	2.36	2.23	1.83	2.23
6.76	2.56	2.44	2.02	2.39
7.421	2.78	2.68	2.23	2.57
8.147	3.02	2.94	2.47	2.77
8.943	3.28	3.22	2.73	3.00
9.818	3.56	3.52	3.02	3.25
10.78	3.86	3.83	3.33	3.51
11.83	4.17	4.13	3.65	3.78
12.99	4.46	4.41	3.97	4.06
14.26	4.66	4.65	4.25	4.31
15.65	4.74	4.81	4.48	4.50
17.18	4.69	4.83	4.63	4.59
18.86	4.55	4.70	4.69	4.54
20.71	4.38	4.44	4.64	4.38
22.73	4.19	4.10	4.49	4.17
24.95	3.93	3.77	4.26	3.95
27.39	3.51	3.47	3.98	3.73
30.07	2.87	3.15	3.67	3.44
33.01	2.06	2.77	3.35	3.03
36.24	1.15	2.24	3.03	2.43

39.78	0.45	1.44	2.69	1.54
43.67	0.088	0.65	2.29	0.68
47.94	0.0072	0.14	1.84	0.15
52.62	0	0.014	1.17	0.014
57.77	0	0	0.54	0
63.41	0	0	0.12	0
69.61	0	0	0.011	0

Potentiometric titration of HMO with 1 g/L with $NaNO_3$ background electrolyte, purged with high purity N_2 at 20 psi.

pH	IS 0.015	pH	IS 0.15	pH	IS 1.5	pH	IS 0.15
2.00	0.13624	1.98	0.13894	2.10	0.083050	1.99	0.16733
2.05	0.13536	2.03	0.13756	2.22	0.044368	2.04	0.13620
2.11	0.10360	2.10	0.10384	2.40	0.004434	2.11	0.10262
2.18	0.071781	2.18	0.070641	2.70	-0.034920	2.18	0.071069
2.28	0.037915	2.27	0.038436	2.76	-0.039437	2.28	0.037481
2.40	0.004974	2.40	0.0047122	2.80	-0.042922	2.40	0.0048107
2.57	-0.028193	2.58	-0.028629	2.87	-0.047226	2.57	-0.028085
2.86	-0.061578	2.91	-0.062460	2.94	-0.051183	2.88	-0.061817
2.91	-0.065108	2.96	-0.065781	3.04	-0.055490	2.93	-0.065251
2.97	0.068725	3.02	-0.069179	3.15	-0.059479	2.98	-0.068529
3.03	0.072136	3.09	-0.072584	3.29	-0.063380	3.04	-0.071880
3.10	0.075553	3.19	-0.076237	3.52	-0.067437	3.12	-0.075414
3.19	0.079069	3.29	-0.079549	4.01	-0.071428	3.32	-0.082214
3.29	0.082424	3.43	-0.082945	4.09	-0.071788	3.46	-0.085533
3.44	0.085951	3.64	-0.086352	4.20	-0.072165	3.69	-0.088958
3.65	0.089371	4.04	-0.089714	4.36	-0.072555	4.16	-0.092308
4.10	0.092844	8.17	-0.086656	4.56	-0.072911	4.24	-0.092625
4.18	0.093180	8.99	-0.092908	4.94	-0.073267	4.48	-0.093269
4.27	0.093507	9.27	-0.093195	6.42	-0.073575	4.62	-0.093560
4.40	0.093848	9.42	-0.093471	8.56	-0.073811	4.85	-0.093859
4.53	0.094154	9.53	-0.093745	8.80	-0.074035	5.67	-0.094179
4.74	0.094470	9.62	-0.094022	9.18	-0.074320	8.13	-0.094413
5.10	0.094775	9.73	-0.094340	9.32	-0.074574	8.92	-0.094683
6.23	0.095051	9.84	-0.094693	9.45	-0.074844	9.23	-0.094970
8.70	0.095309	9.95	-0.095091	9.56	-0.075122	9.41	-0.095372
9.13	0.095596	10.02	-0.095445	9.65	-0.075402	9.57	-0.095668
9.37	0.095898			9.71	-0.075664	9.67	-0.095950
9.54	0.096213			9.75	-0.075911	9.74	-0.096276
9.66	0.096526			9.81	-0.076190	9.83	-0.096613
9.76	0.096847			9.87	-0.076482	9.91	-0.096955
9.84	0.097166			9.93	-0.076788	9.98	-0.097272
9.91	0.097489			9.98	-0.077088	10.03	-0.097472
9.99	0.097857			10.02	-0.077377		

Potentiometric titration of Birnessite Type 1 with 1 g/L with $NaNO_3$ background electrolyte, purged with high purity N_2 at 20 psi.

pH	IS 0.015	pH	IS 0.15	pH	IS 1.5	pH	IS 0.15
2.01	0.31189	1.95	0.34702	1.92	0.33950	2.00	0.31797
2.09	0.23983	2.02	0.31386	2.03	0.24596	2.08	0.24479
2.19	0.16722	2.10	0.24226	2.16	0.15792	2.18	0.17104
2.32	0.094647	2.20	0.17012	2.34	0.071218	2.31	0.097333
2.51	0.021560	2.33	0.098007	2.48	0.026153	2.49	0.024562
2.57	0.0057650	2.52	0.025396	2.70	-0.02004	2.82	-0.049413
2.66	-0.016062	2.57	0.010935	2.75	-0.02836	2.87	-0.056658
2.74	-0.031250	2.66	-0.01098	2.82	-0.03762	2.93	-0.064092
2.89	-0.053624	2.79	-0.03413	2.90	-0.04669	3.00	-0.071542
2.97	-0.061864	2.88	-0.04809	3.00	-0.05584	3.09	-0.079236
3.04	-0.068973	2.95	-0.05596	3.12	-0.06465	3.18	-0.086234
3.13	-0.076304	3.02	-0.06325	3.29	-0.07354	3.32	-0.093827
3.25	-0.083798	3.10	-0.07041	3.58	-0.08251	3.50	-0.10103
3.41	-0.091180	3.21	-0.07791	3.62	-0.08337	3.82	-0.10828
3.66	-0.098502	3.22	-0.07858	3.72	-0.08515	3.92	-0.10969
4.27	-0.10572	3.37	-0.08605	3.84	-0.08687	4.05	-0.11111
4.40	-0.10639	3.57	-0.09314	4.00	-0.08855	4.24	-0.11253
4.58	-0.10705	3.98	-0.10038	4.43	-0.09100	4.52	-0.11387
4.84	-0.10768	4.13	-0.10178	4.66	-0.09171	5.06	-0.11509
5.22	-0.10825	4.36	-0.10318	4.96	-0.09232	5.50	-0.11560
5.74	-0.10872	4.74	-0.10448	5.35	-0.09285	6.00	-0.11604
6.39	-0.10915	5.46	-0.10556	5.75	-0.09330	6.58	-0.11645
7.07	-0.10955	5.96	-0.10601	6.22	-0.09373	7.22	-0.11685
7.66	-0.10996	6.45	-0.10642	6.75	-0.09413	7.68	-0.11726
8.09	-0.11037	7.03	-0.10682	7.20	-0.09454	8.07	-0.11767
8.63	-0.11082	7.53	-0.10723	7.52	-0.09494	8.40	-0.11809
9.04	-0.11135	7.91	-0.10763	7.82	-0.09535	8.67	-0.11853
9.39	-0.11201	8.24	-0.10805	8.90	-0.09589	8.94	-0.11901
9.57	-0.11266	8.55	-0.10848	8.35	-0.09617	9.18	-0.11954
9.73	-0.11338	8.77	-0.10893	8.58	-0.09661	9.38	-0.12011
9.85	-0.11411	9.07	-0.10944	8.80	-0.09705	9.55	-0.12074
9.94	-0.11483	9.33	-0.11003	9.00	-0.09753	9.68	-0.12138
10.03	-0.11562	9.56	-0.11072	9.19	-0.09803	9.79	-0.12205
		9.96	-0.11221	9.35	-0.09857	9.88	-0.12273
		9.79	-0.11202	9.49	-0.09914	9.96	-0.12343
		9.89	-0.11273	9.60	-0.09972	10.02	-0.12410
		9.96	-0.11340	9.70	-0.10032		
		10.01	-0.11402	9.79	-0.10095		
				10.02	-0.10702		

Potentiometric titration of Birnessite Type 2 with 1 g/L with $NaNO_3$ background electrolyte, purged with high purity N_2 at 20 psi.

pH	IS 0.015	pH	IS 0.15	pH	IS 1.5	pH	IS 1.5
1.99	0.024882	2.03	0.042023	1.92	0.011216	1.99	0.0047455
2.06	0.018975	2.10	0.033214	2.03	0.010940	2.11	0.0028714
2.16	0.015146	2.20	0.026365	2.15	0.007443	2.29	0.0021874
2.28	0.010248	2.32	0.018608	2.33	0.005042	2.59	0.0009501
2.46	0.006159	2.49	0.011057	2.62	0.001728	2.65	0.0013795
2.51	0.005499	2.80	0.004302	2.68	0.001999	2.70	0.0011655
2.59	0.004138	2.84	0.003419	2.73	0.001666	2.76	0.0010536
2.73	0.002433	2.89	0.002679	2.79	0.001423	2.83	0.0009507
2.78	0.002209	2.96	0.002217	2.86	0.001193	2.92	0.0009801
2.79	0.002327	3.02	0.001350	2.94	0.000892	3.03	0.0009523
2.84	0.001892	3.11	0.000783	3.05	0.000775	3.17	0.0008383
2.89	0.001303	3.20	-0.00005	3.18	0.000463	3.37	0.0006683
2.96	0.000991	3.33	-0.00074	3.37	0.000178	3.75	0.0004928
3.04	0.000619	3.51	-0.00147	3.70	-0.000159	3.82	0.0004869
3.14	0.000271	3.82	-0.00221	3.75	-0.000201	3.91	0.0004945
3.26	-0.00018	3.94	-0.00212	3.80	-0.000259	4.13	0.0006521
3.43	-0.00060	4.00	-0.00219	3.86	-0.000309	4.28	0.0006111
3.70	-0.00108	4.07	-0.00228	3.94	-0.000339	4.50	0.0005642
4.49	-0.00159	4.16	-0.00235	4.03	-0.000382	4.90	0.0005040
4.71	-0.00167	4.26	-0.00244	4.13	-0.000442	6.13	0.0003916
5.09	-0.00177	4.39	-0.00252	4.28	-0.000484	8.14	0.0002050
6.02	-0.00189	4.57	-0.00261	4.47	-0.000548	8.79	0.0000031
7.88	-0.00207	4.88	-0.00270	4.80	-0.000616	9.07	-0.000139
8.73	-0.00229	5.50	-0.00282	5.61	-0.000718	9.27	-0.000302
9.13	-0.00234	7.46	-0.00299	7.90	-0.000896	9.38	-0.000473
9.36	-0.00245	8.76	-0.00316	8.75	-0.001072	9.50	-0.000633
9.53	-0.00255	9.15	-0.00330	9.09	-0.001238	9.58	-0.000798
9.66	-0.00265	9.41	-0.00342	9.29	-0.001402	9.68	-0.000947
9.77	-0.00273	9.58	-0.00353	9.44	-0.001561	9.75	-0.001102
9.87	-0.00280	9.70	-0.00364	9.56	-0.001716	9.80	-0.0012656
9.95	-0.00287	9.81	-0.00375	9.65	-0.001873	9.85	-0.0014247
10.02	-0.00294	9.90	-0.00384	9.73	-0.002027	9.90	-0.0015789
		9.97	-0.00395	9.80	-0.002179	9.94	-0.0017381
		10.0	-0.00403	9.86	-0.002331	9.98	-0.0018935
				9.92	-0.002475	10.02	-0.0020447
				9.97	-0.002623		
				10.0	-0.002765		

Potentiometric titration of Pyrolusite with 1 g/L with $NaNO_3$ background electrolyte, purged with high purity N_2 at 20 psi.

pH	IS 0.015	pH	IS 0.15	pH	IS 1.5	pH	IS 0.015
2.01	0.028147	2.00	0.037691	2.01	0.0060041	2.07	0.013048
2.18	0.017683	2.17	0.023831	2.32	0.0025426	2.17	0.010878
2.48	0.007684	2.47	0.010982	2.36	0.0016242	2.28	0.007619
2.53	0.006920	2.52	0.009946	2.42	0.0017550	2.43	0.004403
2.58	0.005809	2.57	0.008586	2.48	0.0013491	2.55	0.003344
2.65	0.005310	2.63	0.007377	2.56	0.0014340	2.80	0.001747
2.72	0.004296	2.70	0.006182	2.64	0.00082706	2.91	0.001296
2.81	0.003482	2.79	0.005183	2.75	0.00058342	2.98	0.001095
2.92	0.002575	2.90	0.004098	2.91	0.00060118	3.07	0.000949
3.07	0.001702	3.04	0.002884	3.14	0.00030754	3.17	0.000712
3.32	0.001012	3.25	0.001692	3.69	0.00012035	3.31	0.000524
3.52	0.000582	3.70	0.000604	3.81	8.1442e-05	3.52	0.000342
3.94	0.000241	3.79	0.000504	3.99	6.6601e-05	3.58	0.000311
4.11	0.000171	3.90	0.000395	4.28	3.1803e-05	3.64	0.000258
4.38	0.000089	4.05	0.000290	4.38	3.0927e-05	3.71	0.000207
4.65	0.000062	4.28	0.000185	4.50	2.4664e-05	3.81	0.000182
4.95	0.000039	4.46	0.000127	4.68	2.3316e-05	3.92	0.000132
5.11	0.000029	4.77	0.000069	4.91	6.1759e-06	4.00	0.000120
5.34	0.000018	4.86	0.000055	5.11	-0.0000005	4.09	0.000102
5.75	0.000003	4.98	0.000042	5.43	-0.0000109	4.20	8.092e-05
6.56	-0.000022	5.14	0.000027	6.11	-0.0000295	4.35	6.107e-05
7.59	-0.000057	5.36	0.000017	7.50	-0.0000695	4.57	3.832e-05
8.08	-0.000089	5.77	-0.00001	7.98	-0.0000994	5.04	1.575e-05
8.34	-0.000121	6.61	-0.00003	8.23	-0.0001358	5.22	9.238e-06
8.54	-0.000149	7.82	-0.00001	8.36	-0.0001729	5.35	6.032e-06
8.70	-0.000176	8.24	-0.00010	8.43	-0.0002111	5.52	2.347e-06
9.10	-0.000229	8.47	-0.00013	8.54	-0.0002473	5.76	-2.04e-06
9.75	-0.000256	8.65	-0.00016	8.90	-0.0003446	6.16	-7.41e-06
10.0	-0.000262	8.80	-0.00019	9.48	-0.0006306	6.71	-1.50e-05
2.00		8.93	-0.00021	9.73	-0.0009099	7.41	-2.34e-05
2.17		9.03	-0.00024	9.90	-0.0011777	7.78	-3.18e-05
2.47		9.22	-0.00027	10.0	-0.0014603	8.06	-3.94e-05
2.52		9.52	-0.00036			8.27	-4.63e-05
2.57		9.85	-0.00049			8.59	-5.768e-5
2.63		10.0	-0.00062			8.71	-6.242e-5
2.70			0.006181			8.82	-6.617e-5
2.79			0.005183			8.90	-7.051e-5
2.90			0.004098			9.07	-7.445e-5
3.04			0.002884			9.18	-8.014e-5
3.25			0.001691			9.38	-9.276e-5
3.70			0.000604			9.53	-0.000101
3.79			0.000504			9.81	-0.000122

Potentiometric titration of Kaolinite with 1 g/L with $NaNO_3$ background electrolyte, purged with high purity N_2 at 20 psi.

pH	IS 0.001	pH	IS 0.01	pH	IS 0.1	pH	IS 0.1
2.00	0.18662	1.98	0.19060	1.97	0.19411	1.97	0.19415
2.08	0.14995	2.05	0.15556	2.04	0.15860	2.05	0.15621
2.17	0.11452	2.15	0.11781	2.13	0.12197	2.14	0.11961
2.28	0.079533	2.26	0.082511	2.25	0.084533	2.26	0.082202
2.44	0.043504	2.43	0.045283	2.42	0.046779	2.43	0.044484
2.71	0.0068411	2.71	0.0081994	2.68	0.010100	2.72	0.0064689
2.76	0.0027371	2.75	0.0045401	2.73	0.0058795	2.76	0.0028003
2.81	-0.001137	2.79	0.0010295	2.77	0.0022849	2.81	-0.001081
2.86	-0.004807	2.85	-0.003001	2.82	-0.001515	2.87	-0.005071
2.92	-0.008573	2.91	-0.006766	2.86	-0.004807	2.93	-0.008803
2.99	-0.012348	2.98	-0.010539	2.95	-0.009335	3.01	-0.012771
3.08	-0.016247	3.06	-0.014244	3.04	-0.013386	3.10	-0.016592
3.19	-0.020093	3.17	-0.018133	3.14	-0.017215	3.22	-0.020501
3.34	-0.023963	3.31	-0.021937	3.27	-0.021043	3.38	-0.024349
3.43	-0.025811	3.52	-0.025756	3.46	-0.024899	3.65	-0.028271
3.56	-0.027765	3.55	-0.026152	3.49	-0.025325	3.69	-0.028667
3.59	-0.028147	3.58	-0.026534	3.51	-0.025666	3.73	-0.029046
3.63	-0.028571	3.61	-0.026904	3.54	-0.026068	3.78	-0.029447
3.66	-0.028927	3.65	-0.027313	3.57	-0.026455	3.83	-0.029827
3.70	-0.029317	3.68	-0.027658	3.60	-0.026830	3.89	-0.030217
3.74	-0.029692	3.73	-0.028078	3.63	-0.027194	3.96	-0.030608
3.79	-0.030088	3.77	-0.028437	3.67	-0.027595	4.05	-0.031012
3.84	-0.030463	3.82	-0.028815	3.71	-0.027978	4.15	-0.031394
3.90	-0.030848	3.88	-0.029205	3.76	-0.028386	4.21	-0.031585
3.98	-0.031258	3.95	-0.029595	3.81	-0.028770	4.29	-0.031789
4.06	-0.031633	4.03	-0.029978	3.87	-0.029165	4.32	-0.031863
4.17	-0.032026	4.12	-0.030347	3.94	-0.029561	4.38	-0.031984
4.30	-0.032399	4.16	-0.030472	4.02	-0.029949	4.42	-0.032061
4.33	-0.032472	4.20	-0.030591	4.05	-0.030072	4.47	-0.032142
4.37	-0.032553	4.25	-0.030737	4.08	-0.030190	4.55	-0.032259
4.41	-0.032630	4.32	-0.030898	4.12	-0.030341	4.65	-0.032376
4.45	-0.032704	4.39	-0.031047	4.17	-0.030501	4.74	-0.032458
4.50	-0.032783	4.48	-0.031201	4.23	-0.030667	4.84	-0.032535
4.55	-0.032857	4.54	-0.031283	4.29	-0.030821	4.97	-0.032593
4.65	-0.032974	4.60	-0.031359	4.37	-0.030985	5.06	-0.032633
4.77	-0.033088	4.67	-0.031435	4.46	-0.031143	5.16	-0.032670
4.87	-0.033162	4.75	-0.031510	4.51	-0.031220	5.29	-0.032708
4.99	-0.033235	4.86	-0.031588	4.57	-0.031299	5.46	-0.032745
5.16	-0.033308	4.98	-0.031661	4.64	-0.031378	5.70	-0.032779
5.36	-0.033373	5.05	-0.031696	4.72	-0.031455	6.15	-0.032812
5.49	-0.033404	5.13	-0.031730	4.82	-0.031534	7.45	-0.032842
5.65	-0.033434	5.24	-0.031766	4.95	-0.031612	8.09	-0.032871
5.85	-0.033462	5.35	-0.031798	5.22	-0.031683	8.37	-0.032903
6.20	-0.033490	5.48	-0.031830	5.37	-0.031720	8.56	-0.032935
7.09	-0.033516	5.64	-0.031859	5.57	-0.031755	8.69	-0.032968
8.00	-0.033546	5.83	-0.031887	5.89	-0.031789	8.79	-0.033001
8.40	-0.033581	6.15	-0.031914	6.75	-0.031820	8.90	-0.033038
8.65	-0.033620	6.92	-0.031941	7.81	-0.031847	8.96	-0.033070
8.77	-0.033654	7.79	-0.031966	8.19	-0.031876	9.01	-0.033101
8.89	-0.033693	8.19	-0.031995	8.42	-0.031907	9.09	-0.033162
8.98	-0.033731	8.44	-0.032027	8.57	-0.031937	9.19	-0.033233

9.06	-0.033770	8.61	-0.032060	8.68	-0.031967	9.24	-0.033292
9.13	-0.033810	8.74	-0.032093	8.78	-0.032000	9.35	-0.033422
9.18	-0.033846	8.84	-0.032127	8.85	-0.032030	9.57	-0.033769
9.28	-0.033925	8.93	-0.032163	8.92	-0.032062	9.72	-0.034121
9.37	-0.034008	9.07	-0.032234	9.03	-0.032125	9.83	-0.034472
9.44	-0.034089	9.18	-0.032307	9.12	-0.032189	9.92	-0.034827
9.50	-0.034170	9.26	-0.032376	9.26	-0.032317	9.98	-0.035149
9.55	-0.034248	9.34	-0.032452	9.37	-0.032448		
9.78	-0.034694	9.44	-0.032567	9.43	-0.032542		
9.93	-0.035141	9.56	-0.032751	9.62	-0.032885		
9.96	-0.035261	9.66	-0.032943	9.75	-0.033227		
9.98	-0.035344	9.83	-0.033355	9.86	-0.033584		
10.0	-0.035428	9.95	-0.033764	9.94	-0.033927		
		9.97	-0.033865	9.97	-0.034087		
		9.99	-0.033947	10.0	-0.034252		

Potentiometric titration of Montmorillonite with 1 g/L with $NaNO_3$ background electrolyte, purged with high purity N_2 at 20 psi.

pH	IS 0.001	pH	IS 0.01	pH	IS 0.1	pH	IS 0.1
2.01	0.010323	2.02	0.015472	2.99	0.0009135	2.02	0.019491
2.10	0.003985	2.11	0.0099493	3.08	0.0006154	2.12	0.015432
2.22	0.002846	2.23	0.0071410	3.21	0.0005290	2.24	0.010604
2.39	0.001409	2.40	0.0044308	3.38	0.0003018	2.42	0.0067210
2.69	0.000317	2.69	0.0018325	3.67	0.0001033	2.47	0.0061251
2.74	0.000366	2.74	0.0018177	3.72	0.0001099	2.55	0.0048275
2.79	0.000185	2.79	0.0015831	3.77	9.3731e-5	2.66	0.0040128
2.85	0.000108	2.84	0.0011525	3.83	8.8243e-5	2.70	0.0035988
2.92	3.7053e-5	2.91	0.0010708	3.89	5.7267e-5	2.75	0.0033806
3.01	0.000102	2.99	0.0009136	3.97	4.9583e-5	2.80	0.0029732
3.12	0.000103	3.08	0.0006154	4.07	4.5171e-5	2.85	0.0023971
3.26	1.2512e-5	3.21	0.0005290	4.19	2.7326e-5	2.92	0.0021245
3.48	6.4408e-6	3.38	0.0003018	4.36	1.2758e-5	3.00	0.0017874
3.96	2.6313e-5	3.67	0.0001034	4.64	-3.363e-6	3.10	0.0014773
4.07	5.0421e-5	3.72	0.0001099	4.68	-5.504e-6	3.22	0.0010557
4.19	3.7293e-5	3.77	9.373e-5	4.73	-5.335e-6	3.39	0.00066106
4.38	4.5890e-5	3.83	8.824e-5	4.78	-7.392e-6	3.67	0.00025344
4.70	4.3781e-5	3.89	5.726e-5	4.83	-1.143e-5	3.76	0.00018228
4.80	4.1087e-5	3.97	4.958e-5	4.89	-1.453e-5	3.87	0.00010205
4.93	3.8359e-5	4.07	4.517e-5	4.97	-1.531e-5	3.94	6.7052e-05
5.11	3.4572e-5	4.19	2.732e-5	5.05	-1.937e-5	4.01	8.1211e-06
5.35	2.4340e-5	4.36	1.276e-5	5.15	-2.315e-5	4.11	-2.6742e-05
5.51	1.6697e-5	4.64	-3.364e-6	5.26	-2.918e-5	4.23	-7.2482e-5
5.70	6.4339e-6	4.68	-5.504e-6	5.40	-3.583e-5	4.40	-0.0001155
6.05	-3.705e-6	4.73	-5.335e-6	5.56	-4.507e-5	4.51	-0.0001421
6.73	-1.723e-5	4.78	-7.392e-6	5.82	-5.416e-5	4.67	-0.0001637
7.61	-3.298e-5	4.83	-1.143e-5	6.33	-6.491e-5	4.75	-0.0001741
7.99	-4.812e-5	4.89	-1.454e-5	7.16	-8.054e-5	4.83	-0.0001893
8.31	-5.881e-5	4.97	-1.531e-5	7.83	-9.570e-5	4.94	-0.0002019
8.48	-7.033e-5	5.05	-1.937e-5	8.22	-0.000073	5.07	-0.0002173
8.63	-7.939e-5	5.15	-2.315e-5	8.45	-0.000117	5.24	-0.0002344
8.75	-8.744e-5	5.26	-2.918e-5	8.61	-0.000126	5.35	-0.0002437
8.92	-0.000103	5.40	-3.583e-5	8.73	-0.000135	5.48	-0.0002540
9.04	-0.000126	5.56	-4.507e-5	8.83	-0.000143	5.66	-0.0002646
9.18	-0.000143	5.82	-5.416e-5	8.91	-0.000152	5.97	-0.0002752

9.36	-0.000174	6.33	-6.491e-5	8.97	-0.000162	6.55	-0.0002882
9.59	-0.000233	7.16	-8.054e-5	9.03	-0.000170	7.30	-0.0003048
9.74	-0.000291	7.83	-9.571e-5	9.14	-0.000183	7.84	-0.0003205
9.85	-0.000351	8.22	-0.000107	9.22	-0.000200	8.13	-0.0003353
9.94	-0.000406	8.45	-0.000117	9.29	-0.000215	8.33	-0.0003491
10.0	-0.00045	8.61	-0.0001269	9.46	-0.000255	8.48	-0.0003623
		8.73	-0.0001357	9.56	-0.000291	8.60	-0.0003749
		8.83	-0.0001438	9.72	-0.000353	8.70	-0.0003871
		8.91	-0.0001522	9.84	-0.000410	8.87	-0.0004089
		8.97	-0.0001620	9.94	-0.000456	8.98	-0.0004326
		9.03	-0.0001702	10.0	-0.000526	9.07	-0.0004559
		9.14	-0.0001838			9.15	-0.0004779
		9.22	-0.0002000			9.30	-0.0005337
		9.29	-0.0002152			9.41	-0.0005900
		9.46	-0.0002554			9.50	-0.0006452
		9.56	-0.0002916			9.65	-0.0007438
		9.72	-0.0003533			9.77	-0.0008399
		9.84	-0.0004103			9.86	-0.0009378
		9.94	-0.0004568			9.94	-0.0010278
		10.0	-0.0005268			10.0	-0.0011304

Potentiometric titration of HMO-coated clay with 1 g/L with $NaNO_3$ background electrolyte, purged with high purity N_2 at 20 psi.

pH	IS 0.001	pH	IS 0.01	pH	IS 0.1	pH	IS 0.1
2.07	0.0049682	2.09	0.0061829	2.12	0.011561	2.07	0.0030139
2.25	0.0025285	2.28	0.0034587	2.31	0.0079864	2.26	0.0014993
2.34	0.0020902	2.64	0.00076200	2.34	0.0069210	2.35	0.0011454
2.49	0.0013519	2.71	0.00056794	2.38	0.0051765	2.45	0.00069972
2.63	0.00058118	2.87	3.2644e-05	2.43	0.0035157	2.58	0.00025255
2.78	0.00022416	2.98	-0.0002337	2.47	0.0024487	2.64	0.00013093
3.00	-0.0001839	3.13	-0.0004938	2.51	0.0021376	2.72	4.7188e-05
3.17	-0.0004005	3.34	-0.0007930	2.55	0.0017829	2.88	-0.0002721
3.44	-0.0006381	3.40	-0.0008492	2.59	0.0013885	3.17	-0.0005465
3.51	-0.0007012	3.50	-0.0009451	2.65	0.0011322	3.40	-0.0007193
3.65	-0.0007886	3.63	-0.0010413	2.70	0.00073006	3.45	-0.0007641
3.77	-0.0008518	3.74	-0.0011092	2.77	0.00041616	3.55	-0.0007843
3.91	-0.0009281	3.86	-0.0011921	2.85	8.3436e-05	3.63	-0.0008256
4.00	-0.0009670	4.02	-0.0012776	2.95	-0.0002415	3.72	-0.0008699
4.09	-0.0010137	4.12	-0.0013232	3.08	-0.0005670	3.84	-0.0009124
4.20	-0.0010613	4.23	-0.0013736	3.11	-0.0006363	3.92	-0.0009326
4.33	-0.0011123	4.35	-0.0014288	3.14	-0.0007118	4.01	-0.0009542
4.47	-0.0011694	4.49	-0.0014874	3.17	-0.0007929	4.12	-0.0009764
4.63	-0.0012310	4.64	-0.0015511	3.21	-0.0008557	4.20	-0.0010062
4.80	-0.0012978	4.82	-0.0016178	3.25	-0.0009271	4.34	-0.0010321
4.89	-0.0013327	4.92	-0.0016525	3.30	-0.0009871	4.48	-0.0010619
4.99	-0.0013681	5.01	-0.0016888	3.34	-0.0010754	4.66	-0.0010929
5.09	-0.0014045	5.22	-0.0017626	3.40	-0.0011390	4.82	-0.0011275
5.21	-0.0014412	5.33	-0.0018004	3.46	-0.0012152	4.92	-0.0011451
5.33	-0.0014787	5.45	-0.0018386	3.53	-0.0012910	5.04	-0.0011628
5.44	-0.0015171	5.56	-0.0018774	3.61	-0.0013700	5.16	-0.0011811
5.55	-0.0015558	5.68	-0.0019165	3.71	-0.0014477	5.27	-0.0011999
5.68	-0.0015947	5.80	-0.0019558	3.82	-0.0015367	5.40	-0.0012189
5.81	-0.0016340	5.93	-0.0019953	3.96	-0.0016288	5.51	-0.0012383
5.94	-0.0016735	6.06	-0.0020350	4.05	-0.0016755	5.64	-0.0012577

6.07	-0.0017132	6.19	-0.0020748	4.15	-0.0017257	5.77	-0.0012773
6.20	-0.0017530	6.33	-0.0021147	4.26	-0.0017800	5.91	-0.0012971
6.33	-0.0017929	6.47	-0.0021547	4.38	-0.0018386	6.06	-0.0013169
6.48	-0.0018329	6.61	-0.0021947	4.52	-0.0019001	6.20	-0.0013368
6.61	-0.0018729	6.76	-0.0022348	4.59	-0.0019329	6.37	-0.0013567
6.76	-0.0019130	6.92	-0.0022749	4.67	-0.0019660	6.53	-0.0013767
6.89	-0.0019531	7.09	-0.0023150	4.76	-0.0019997	6.69	-0.0013968
7.04	-0.0019932	7.25	-0.0023551	4.84	-0.0020351	6.85	-0.0014168
7.18	-0.0020333	7.40	-0.0023951	4.94	-0.0020704	7.03	-0.0014368
7.32	-0.0020734	7.56	-0.0024351	5.03	-0.0021071	7.18	-0.0014569
7.46	-0.0021135	7.74	-0.0024750	5.14	-0.0021439	7.35	-0.0014769
7.61	-0.0021535	7.89	-0.0025149	5.24	-0.0021816	7.52	-0.0014970
7.73	-0.0021935	8.05	-0.0025545	5.35	-0.0022197	7.68	-0.0015170
7.87	-0.0022333	8.21	-0.0025939	5.46	-0.0022583	7.84	-0.0015369
8.00	-0.0022731	8.37	-0.0026328	5.57	-0.0022973	8.03	-0.0015567
8.32	-0.0023516	8.53	-0.0026713	5.69	-0.0023364	8.25	-0.0015763
8.42	-0.0023909	8.68	-0.0027091	5.81	-0.0023758	8.42	-0.0015958
8.72	-0.0024667	8.82	-0.0027462	5.94	-0.0024154	8.60	-0.0016149
9.00	-0.0025388	8.98	-0.0027814	6.07	-0.0024551	8.75	-0.0016338
9.25	-0.0026056	9.09	-0.0028169	6.20	-0.0024950	8.89	-0.0016523
9.47	-0.0026655	9.20	-0.0028511	6.33	-0.0025349	9.00	-0.0016707
9.61	-0.0027262	9.47	-0.0029082	6.48	-0.0025749	9.27	-0.0017045
9.76	-0.0027771	9.66	-0.0029610	6.63	-0.0026150	9.50	-0.0017351
9.88	-0.0028255	9.83	-0.0030040	6.78	-0.0026551	9.66	-0.0017648
9.99	-0.0028675	9.96	-0.0030442	6.93	-0.0026952	9.81	-0.0017910
		10.0	-0.0030694	7.09	-0.0027353	9.94	-0.0018144
				7.24	-0.0027754	10.0	-0.0018410
				7.41	-0.0028155		
				7.57	-0.0028555		
				7.74	-0.0028954		
				7.90	-0.0029353		
				8.07	-0.0029749		
				8.25	-0.0030143		
				8.41	-0.0030533		
				8.57	-0.0030918		
				8.73	-0.0031296		
				8.87	-0.0031668		
				9.00	-0.0032031		
				9.12	-0.0032386		
				9.22	-0.0032738		
				9.48	-0.0033340		
				9.68	-0.0033881		
				9.84	-0.0034368		
				9.97	-0.0034813		
				10.0	-0.0035116		

Potentiometric titration of Birnessite-coated clay with 1 g/L with $NaNO_3$ background electrolyte, purged with high purity N_2 at 20 psi.

pH	IS 0.001	pH	IS 0.01	pH	IS 0.1	pH	IS 0.01
2.00	0.065821	2.00	0.063566	2.00	0.070841	2.00	0.068505
2.10	0.041798	2.11	0.042019	2.12	0.050443	2.10	0.045020
2.25	0.024882	2.28	0.025603	2.29	0.030928	2.25	0.026698
2.37	0.017798	2.57	0.0090789	2.59	0.012160	2.53	0.011003
2.53	0.010144	2.62	0.0077244	2.69	0.0085354	2.57	0.009344
2.57	0.0085650	2.67	0.0060915	2.75	0.0067150	2.62	0.007970
2.62	0.0072706	2.74	0.0049494	2.82	0.0049042	2.66	0.005881
2.74	0.0046087	2.81	0.0033953	2.91	0.0032437	2.72	0.004409
2.81	0.0031055	2.90	0.0020012	2.97	0.0025524	2.79	0.002945
2.90	0.0017633	2.92	0.0017106	3.03	0.0016941	2.88	0.001651
3.02	0.00053847	2.95	0.0012337	3.18	-0.0020389	2.98	7.0993e-5
3.10	-4.9869e-8	3.09	4.229e-10	3.28	-0.0021237	3.12	-0.001361
3.19	-0.0006446	3.18	-0.0006393	3.36	-0.0021990	3.21	-0.002098
3.30	-0.0013272	3.29	-0.0013166	3.42	-0.0029311	3.33	-0.002776
3.42	-0.0018268	3.34	-0.0016166	3.53	-0.0030327	3.45	-0.003373
3.54	-0.0021930	3.40	-0.0018892	3.62	-0.0033770	3.53	-0.003644
3.65	-0.0024083	3.47	-0.0021595	3.73	-0.0033372	3.63	-0.003906
3.71	-0.0025455	3.56	-0.0023943	3.80	-0.0035086	3.76	-0.004168
3.84	-0.0028839	3.61	-0.0025268	3.88	-0.0036885	3.84	-0.004309
3.97	-0.0029471	3.66	-0.0026873	3.98	-0.0038648	3.93	-0.004469
4.11	-0.0030789	3.72	-0.0028347	4.11	-0.0040413	4.06	-0.004600
4.26	-0.0032704	3.80	-0.0029493	4.29	-0.0040255	4.14	-0.004670
4.39	-0.0033411	3.89	-0.0030844	4.43	-0.0039900	4.24	-0.004738
4.48	-0.0033914	3.99	-0.0032467	4.50	-0.0040640	4.36	-0.004815
4.56	-0.0034207	4.14	-0.0033800	4.63	-0.0040769	4.48	-0.004881
4.64	-0.0034582	4.25	-0.0034358	4.72	-0.0041205	4.55	-0.004917
4.74	-0.0034950	4.39	-0.0034978	4.82	-0.0041680	4.64	-0.004951
4.86	-0.0035345	4.46	-0.0035237	4.94	-0.0041780	4.74	-0.004989
4.93	-0.0035555	4.54	-0.0035516	5.00	-0.0042056	4.86	-0.005029
4.99	-0.0035812	4.63	-0.0035832	5.07	-0.0042332	4.92	-0.005053
5.07	-0.0036051	4.75	-0.0036126	5.15	-0.0042612	4.98	-0.005079
5.16	-0.0036302	4.88	-0.0036511	5.23	-0.0042912	5.04	-0.005107
5.27	-0.0035778	4.95	-0.0035564	5.32	-0.0042426	5.12	-0.005133
5.37	-0.0036071	5.04	-0.0036163	5.42	-0.0042743	5.20	-0.005162
5.50	-0.0036364	5.12	-0.0036421	5.53	-0.0043070	5.29	-0.005191
5.64	-0.0036677	5.22	-0.0036677	5.66	-0.0043405	5.41	-0.005219
5.80	-0.0037004	5.34	-0.0036942	5.79	-0.0043755	5.53	-0.005251
5.95	-0.0037353	5.47	-0.0037230	5.94	-0.0044114	5.67	-0.005283
6.12	-0.0037710	5.62	-0.0037535	6.10	-0.0044481	5.82	-0.005317
6.30	-0.0038076	5.78	-0.0037861	6.26	-0.0044858	5.94	-0.005354
6.49	-0.0038449	5.95	-0.0038204	6.43	-0.0045240	6.10	-0.005390
6.69	-0.0038826	6.14	-0.0038559	6.61	-0.0045625	6.28	-0.005427
6.89	-0.0039206	6.33	-0.0038926	6.80	-0.0046013	6.46	-0.005465
7.06	-0.0039588	6.51	-0.0039302	7.00	-0.0046403	6.62	-0.005503
7.23	-0.0039970	6.69	-0.0039681	7.17	-0.0046793	6.82	-0.005541
7.40	-0.0040351	6.87	-0.0040063	7.33	-0.0047184	7.00	-0.005580
7.51	-0.0040733	7.03	-0.0040446	7.45	-0.0047574	7.13	-0.005619
7.62	-0.0041114	7.20	-0.0040829	7.55	-0.0047965	7.26	-0.005658
7.71	-0.0041494	7.31	-0.0041214	7.84	-0.0048336	7.39	-0.005697
7.78	-0.0041875	7.42	-0.0041598	7.97	-0.0048715	7.49	-0.005736
8.02	-0.0042226	7.74	-0.0041962	8.08	-0.0049092	7.56	-0.005775

8.22	-0.0042563	7.90	-0.0042331	8.31	-0.0049823	7.63	-0.005813
8.40	-0.0043269	8.01	-0.0043091	8.44	-0.0050565	7.71	-0.005853
8.50	-0.0043992	8.22	-0.0043817	8.64	-0.0051636	7.79	-0.005891
8.62	-0.0044684	8.37	-0.0044540	8.85	-0.0052627	7.97	-0.005967
9.26	-0.0044272	8.65	-0.0045533	9.17	-0.0053647	8.20	-0.006041
9.66	-0.0043493	8.86	-0.0046472	9.34	-0.0055110	8.27	-0.006117
9.92	-0.0044205	9.31	-0.0047330	9.53	-0.0057401	8.30	-0.006195
10.0	-0.0046669	9.60	-0.0047673	9.77	-0.0058340	8.91	-0.006538
		9.83	-0.0049270	9.96	-0.0059138	9.34	-0.006818
		10.0	-0.0050487	10.1	-0.0060554	9.67	-0.007004
						9.90	-0.007126
						9.98	-0.005807
						10.0	-0.007467

APPENDIX G

BIOGENIC MN OXIDE STUDIES

The Mn oxidation studies and characteriatic results of biogenic Mn oxide coated bacteria are listed below.

Growth curve of *L. discophora* SP-6 in MSVP media as a function of pH (6.5-8)

Time (hrs)	OD_{600} in PY media	OD_{600} in MSVP media
3	0.058	0.060
6	0.058	0.061
9	0.132	0.065
24	0.305	0.079
28	0.412	0.095
36	0.697	0.213
46	0.785	0.479
54	0.795	0.660
71	0.795	0.660
120	0.797	0.655

The comparison between the growth of *L. discophora* SP-6 in MSVP and PY media at pH 7.3 and 22 °C

Time (hr)					
	pH 6.5	pH 7.0	pH 7.3	pH 7.5	pH 8.0
0	0	0	0	0	0
6	0	0	0	0	0
12	1.0288	1.2002	3.0863	1.3717	2.7434
24	1.5431	1.8861	4.6294	1.3717	3.4292
48	2.4004	2.9148	5.4867	2.4004	4.4580
72	3.9436	3.9436	6.1726	2.5719	8.573
96	4.2865	6.6869	6.6869	2.9148	9.0874
120	4.6294	10.459	6.6869	3.9436	10.116
144	5.3153	17.146	9.9447	5.4867	11.145
168	6.1726	26.405	10.973	6.0011	11.488
192	7.8872	30.006	15.431	7.2013	12.859
222	9.6018	45.265	61.726	11.831	9.2588
240	21.090	73.728	82.987	12.859	25.719
264	21.775	96.018	102.88	14.403	30.177
289	24.347	94.646	101.5	15.946	28.977
314	29.148	99.961	92.417	21.433	24.176
338	37.721	90.874	92.588	24.519	25.719
362	41.493	84.015	83.33	41.493	33.435

Mn oxidation rate of *L. discophora* SP-6 with MSVP and PY media as a function of Mn concentration at 22 °C

Mn(μmol)	Rate of Mn oxidation μmol/(min mg cell)	Mn(μmol)	Rate of Mn oxidation μmol/(min mg cell)
0	0	0	0
100	0.063078	100	0.016522
300	0.093438	300	0.037229
500	0.10199	504	0.042117
700	0.10258	1052	0.029427
900	0.10159		

Mn oxidation by *L. discophora* SP-6 (a) comparison between three different media (MSVP, PY, and HEPES solution) at $[Mn]_0 = 10^{-4}$ M, pH 7.3, and 22 °C

Time (hr)	Mn(II) ppm in MSVP	Time (hr)	Mn(II) ppm in PY	Time (hr)	Mn(II) ppm in HEPES
0.5	4.74	0.005	4.94	2	4.96
1	4.30	0.5	4.68	4	4.24
2	4.12	1	4.41	6	4.49
3	3.99	1.5	3.38	8	4.27
4	3.19	2.5	2.36	10	4.09
5	3.13	3.5	0.59	12	4.43
6	2.71	4	0.17	14	4.83
7	1.90	5	0.0564	16	3.96
8	1.75	6	0.029	18	4.12
9	1.41	7	0.042		
10	1.07	8	0.011		
11	0.745	9	0.0298		
12	0.192	10	0.0131		
13	0.0705	12	0.0075		
15	0.0137	17	0.0196		
17	0.0163	20	0.0300		
19	0.0113	24	0.0484		
21	0.0792				
36	0.0266				
38	0.0197				
41	0.0131				
45	0.0094				
49	0.0119				
53	0.0415				
61	0.0203				

Particle size distributions of the biogenic Mn oxide and *L. discophora* SP-6 at pH 7.3 and room temperature in PY media as a function of Mn concentration (0, 0.05, 0.1, 0.5, and 1 mM) compared with the pure suspension of *L. discophora* SP-6 and abiotic Mn oxide.

Diameter (μm)	*L. discophora* SP-6	0.05 M Mn^{2+}	0.1 M Mn^{2+}	0.5 M Mn^{2+}	1.0 M Mn^{2+}
0.375	0.005	0.0053	0.0037	0.0015	0.005
0.412	0.011	0.011	0.0074	0.0031	0.0094
0.452	0.019	0.019	0.013	0.0059	0.016
0.496	0.028	0.028	0.021	0.0095	0.022
0.545	0.039	0.039	0.029	0.014	0.027
0.598	0.051	0.051	0.039	0.020	0.032
0.656	0.064	0.064	0.050	0.027	0.036
0.721	0.077	0.077	0.062	0.036	0.039
0.791	0.09	0.090	0.074	0.045	0.041
0.868	0.10	0.10	0.086	0.054	0.043
0.953	0.11	0.11	0.097	0.064	0.045
1.047	0.12	0.12	0.11	0.073	0.045
1.149	0.12	0.12	0.11	0.081	0.046
1.261	0.12	0.12	0.11	0.088	0.046
1.384	0.12	0.12	0.11	0.093	0.047
1.52	0.11	0.11	0.11	0.096	0.048
1.668	0.098	0.098	0.10	0.097	0.049
1.832	0.086	0.086	0.094	0.096	0.052
2.011	0.075	0.075	0.086	0.095	0.055
2.207	0.065	0.065	0.079	0.095	0.060
2.423	0.059	0.059	0.075	0.096	0.066
2.66	0.058	0.058	0.075	0.099	0.073
2.92	0.063	0.063	0.081	0.11	0.082
3.205	0.074	0.074	0.093	0.12	0.091
3.519	0.091	0.091	0.11	0.13	0.10
3.863	0.11	0.11	0.14	0.15	0.11
4.24	0.14	0.14	0.17	0.16	0.12
4.655	0.16	0.16	0.20	0.18	0.13
5.11	0.19	0.19	0.23	0.20	0.14
5.61	0.21	0.21	0.26	0.22	0.15
6.158	0.23	0.23	0.28	0.24	0.16
6.76	0.25	0.25	0.31	0.25	0.17
7.421	0.28	0.28	0.34	0.26	0.19
8.147	0.30	0.30	0.38	0.28	0.21
8.943	0.33	0.33	0.42	0.29	0.23
9.818	0.37	0.37	0.46	0.31	0.25
10.78	0.40	0.40	0.51	0.34	0.27
11.83	0.44	0.44	0.57	0.36	0.30
12.99	0.49	0.49	0.63	0.39	0.33
14.26	0.54	0.54	0.70	0.41	0.35
15.65	0.61	0.61	0.79	0.43	0.38
17.18	0.71	0.71	0.89	0.45	0.40
18.86	0.84	0.84	1.01	0.48	0.43
20.71	0.98	0.98	1.13	0.53	0.47
22.73	1.15	1.15	1.26	0.62	0.53
24.95	1.34	1.34	1.40	0.73	0.59
27.39	1.60	1.60	1.60	0.88	0.68
30.07	1.94	1.94	1.85	1.07	0.78
33.01	2.33	2.33	2.18	1.29	0.90

36.24	2.75	2.75	2.56	1.58	1.04
39.78	3.23	3.23	2.99	1.95	1.20
43.67	3.76	3.76	3.48	2.36	1.39
47.94	4.35	4.35	4.01	2.75	1.63
52.62	5.06	5.06	4.62	3.14	1.91
57.77	5.79	5.79	5.30	3.67	2.23
63.41	6.44	6.44	5.94	4.48	2.56
69.61	7.07	7.07	6.51	5.46	2.88
76.42	7.78	7.78	7.11	6.32	3.20
83.89	8.86	8.86	7.97	7.12	3.56
92.09	10.5	10.5	9.31	8.19	4.00
101.1	10.2	10.2	10.1	9.6	4.51
111	5.42	5.42	7.72	11.1	4.97
121.8	1.00	1.0	2.7	11.1	5.28
133.7	0.032	0.032	0.2	7.0	5.34
146.8	0	0	0	1.87	5.27
161.2	0	0	0	0.11	5.55
176.9	0	0	0	0	6.53
194.2	0	0	0	0	7.98
213.2	0	0	0	0	9.02
234	0	0	0	0	7.47
256.9	0	0	0	0	2.81
282.1	0	0	0	0	0.22
309.6	0	0	0	0	0
339.9	0	0	0	0	0
373.1	0	0	0	0	0
409.6	0	0	0	0	0
449.7	0	0	0	0	0
493.6	0	0	0	0	0
541.9	0	0	0	0	0
594.8	0	0	0	0	0
653	0	0	0	0	0
716.8	0	0	0	0	0

Potentiometric titration of biogenic Mn oxide-coated bacteria with ~ 70-90 g/L with $NaNO_3$ background electrolyte, purged with high purity N_2 at 20 psi.

pH	IS 0.001	pH	IS 0.01	pH	IS 0.1
2.2099	0.031222	2.2651	0.036832	2.2268	0.040801
2.2099	0.030686	2.2651	0.036143	2.2268	0.040092
2.2099	0.030153	2.2651	0.035457	2.2285	0.039725
2.2099	0.029092	2.2703	0.035011	2.2285	0.038323
2.2117	0.027246	2.272	0.032622	2.2303	0.035892
2.2345	0.026306	2.2877	0.030051	2.2513	0.034434
2.2432	0.020432	2.3173	0.024873	2.2828	0.030288
2.2957	0.014512	2.3747	0.019619	2.3283	0.023832
2.343	0.012174	2.4077	0.013443	2.3265	0.01078
2.3955	0.0099319	2.4512	0.006890	2.4280	0.010051
2.4374	0.0061093	2.5243	0.004268	2.4420	0.006069
2.4585	5.81e-5	2.5678	0.001471	2.5120	0.003074
2.5652	-0.000491	2.6044	-0.003959	2.5488	0.000208
2.5757	-0.003376	2.6948	-0.006146	2.6048	-0.00348
2.6124	-0.006826	2.7453	-0.007827	2.6398	-0.00658
2.6649	-0.009132	2.7697	-0.012894	2.6958	-0.01036
2.7507	-0.009761	2.8636	-0.015981	2.7658	-0.01268
2.7805	-0.011745	2.9228	-0.017398	2.8183	-0.01507
2.8224	-0.015292	3.008	-0.018924	2.8865	-0.01784
2.8942	-0.017954	3.0916	-0.020522	2.9460	-0.02072
2.9869	-0.01886	3.1977	-0.022115	3.0213	-0.02347
3.0307	-0.020196	3.3056	-0.023381	3.1005	-0.02555
3.1969	-0.020862	3.3839	-0.024964	3.2015	-0.02695
3.2127	-0.022141	3.5092	-0.026896	3.2295	-0.02916
3.2652	-0.024362	3.7475	-0.027706	3.3660	-0.03175
3.344	-0.026224	3.805	-0.028282	3.4273	-0.03234
3.5085	-0.026276	3.9703	-0.029333	3.4308	-0.03229
3.6135	-0.025607	4.1008	-0.030072	3.4325	-0.03248
3.6135	-0.025765	4.2069	-0.030947	3.4325	-0.03268
3.6135	-0.025921	4.3513	-0.032316	3.4325	-0.03308
3.6135	-0.026234	4.6454	-0.033681	3.4780	-0.03336
3.617	-0.026835	4.6941	-0.033859	3.4798	-0.03438
3.6572	-0.027845	4.6889	-0.033863	3.5638	-0.03558
3.7902	-0.028825	4.6889	-0.034059	3.58305	-0.03674
3.8147	-0.029628	4.6889	-0.034254	3.6793	-0.03861
3.9634	-0.030932	4.7376	-0.034613	3.8385	-0.03944
4.1034	-0.031477	4.7915	-0.035107	3.8595	-0.04023
4.1857	-0.031913	5.0334	-0.036049	3.9208	-0.04172
4.3152	-0.032829	5.0369	-0.03646	4.0135	-0.04353
4.4009	-0.033968	5.1656	-0.037245	4.1833	-0.04516
4.5532	-0.035553	5.1726	-0.037683	4.2638	-0.04606
4.6687	-0.036654	5.4145	-0.038513	4.36705	-0.04765
4.7982	-0.037836	5.4893	-0.03877	4.58755	-0.04942
4.9172	-0.039043	5.5745	-0.039291	4.5858	-0.05026
4.9925	-0.040391	5.7938	-0.040324	4.84305	-0.05174
5.1622	-0.042187	5.8077	-0.040947	4.84305	-0.05215
5.3425	-0.04309	6.1557	-0.042169	4.90255	-0.05296
5.3897	-0.043554	6.1557	-0.042433	4.95855	-0.05375
5.5262	-0.044469	6.2323	-0.042958	5.14055	-0.05529
5.6014	-0.045166	6.2966	-0.04341	5.2543	-0.0561

5.7554	-0.046384	6.4898	-0.044305	5.36805	-0.05703
5.8902	-0.047315	6.6272	-0.044839	5.4818	-0.05824
6.004	-0.048182	6.6255	-0.045408	5.66905	-0.05967
6.0372	-0.048772	6.6742	-0.045407	5.66905	-0.06003
6.2105	-0.049934	6.6916	-0.045576	5.72505	-0.06074
6.2892	-0.050459	6.6934	-0.045745	5.94905	-0.06146
6.3644	-0.051416	6.8012	-0.046081	5.9473	-0.06173
6.4887	-0.052089	6.7978	-0.046309	5.9473	-0.06227
6.6795	-0.053967	6.9265	-0.046764	6.1853	-0.06332
6.7354	-0.054514	6.9283	-0.047023	6.1853	-0.06362
6.7932	-0.055592	7.0205	-0.047537	6.1853	-0.06421
7.0627	-0.057186	7.017	-0.047919	6.4338	-0.06538
7.089	-0.057629	7.2519	-0.048678	6.4828	-0.06569
7.2115	-0.058503	7.3493	-0.048912	6.5265	-0.06631
7.2744	-0.059057	7.3459	-0.049242	6.6508	-0.06754
7.4355	-0.060125	7.5599	-0.049894	6.7488	-0.06849
7.5317	-0.060813	7.619	-0.050117	7.0043	-0.06978
7.7049	-0.061743	7.5877	-0.050117	7.0761	-0.07205
7.7924	-0.062327	7.5842	-0.050276	7.2423	-0.07119
7.8974	-0.063208	7.579	-0.050435	7.3403	-0.07193
8.0864	-0.064207	7.5842	-0.050752	7.5048	-0.073
8.1687	-0.064713	7.8696	-0.051376	7.6063	-0.07383
8.2982	-0.065535	7.8713	-0.051543	7.7883	-0.07494
8.4382	-0.066286	7.9757	-0.051874	7.9108	-0.07563
8.3472	-0.066291	8.0001	-0.052104	8.0805	-0.07642
8.342	-0.066365	8.0732	-0.052563	8.2328	-0.07701
8.3525	-0.066438	8.188	-0.053244	8.2555	-0.07754
8.363	-0.066585	8.1368	-0.054157	8.4095	-0.07859
8.4032	-0.066876	8.5151	-0.055264	8.4725	-0.07909
8.4854	-0.067449	8.6996	-0.05596	8.4673	-0.08008
8.608	-0.068287	8.7622	-0.056415	8.7403	-0.08199
8.7199	-0.069133	8.837	-0.057323	8.8173	-0.08241
8.8337	-0.070018	9.0545	-0.058856	8.7018	-0.08243
8.9282	-0.070911	9.0876	-0.059574	8.7018	-0.08252
9.0227	-0.071886	9.2599	-0.06091	8.7018	-0.08262
9.1014	-0.072893	9.2894	-0.061548	8.7018	-0.08281
9.1994	-0.073974	9.3869	-0.06277	8.7053	-0.08243
9.273	-0.074891	9.4739	-0.063806	8.77005	-0.08252
9.3429	-0.075934	9.6218	-0.065181	8.9048	-0.08262
9.4024	-0.077034	9.7088	-0.066191	8.9258	-0.08281
9.4515	-0.078196	9.8167	-0.067561	8.99405	-0.08318
9.4987	-0.078778	9.9559	-0.06886	9.0623	-0.08391
9.5267	-0.07952	10.017	-0.069881	9.1358	-0.08454
9.5844	-0.080722			9.2233	-0.08948
9.6404	-0.081722			9.3178	-0.09086
9.6895	-0.0827			9.3755	-0.09206
9.7262	-0.083758			9.4578	-0.09354
9.7787	-0.084852			9.5610	-0.09476
9.8224	-0.085749			9.6540	-0.09565
9.8364	-0.086771			9.70805	-0.09682
9.875	-0.087918			9.7868	-0.09796
9.882	-0.088053			9.78505	-0.09797

Potentiometric titration of *L. discophora* SP-6 with ~30-60 g/L with $NaNO_3$ background electrolyte, purged with high purity N_2 at 20 psi.

pH	IS 0.001	pH	IS 0.01	pH	IS 0.1
9.9712	-0.2307	2.3861	-0.12191	2.1821	-0.0266
9.973	-0.23014	2.3861	-0.12196	2.2066	-0.02862
9.9626	-0.22961	2.3861	-0.12201	2.2556	-0.03286
9.9609	-0.22852	2.3921	-0.12212	2.3011	-0.03869
9.9575	-0.22636	2.4068	-0.12232	2.3554	-0.04184
9.9042	-0.22228	2.4431	-0.12276	2.4026	-0.04563
9.868	-0.21814	2.507	-0.12353	2.4569	-0.04921
9.7958	-0.21027	2.5986	-0.12268	2.4901	-0.05061
9.6995	-0.20215	2.685	-0.12274	2.5478	-0.05281
9.6255	-0.19595	2.761	-0.12288	2.6091	-0.05518
9.5361	-0.18913	2.8993	-0.12308	2.6721	-0.05784
9.4707	-0.18296	2.9891	-0.12318	2.7438	-0.05989
9.3538	-0.17638	3.1187	-0.12331	2.8086	-0.06257
9.2832	-0.1725	3.2518	-0.12342	2.8979	-0.06432
9.1904	-0.16748	3.3658	-0.12347	2.9731	-0.06617
9.0906	-0.16266	3.5628	-0.12354	3.0694	-0.06797
8.9994	-0.15842	3.7062	-0.12362	3.1621	-0.06982
8.9117	-0.15531	3.7909	-0.12371	3.2776	-0.07138
8.8034	-0.15224	4.0639	-0.12378	3.3844	-0.0729
8.7156	-0.14953	4.254	-0.12386	3.4369	-0.07359
8.5987	-0.1462	4.5391	-0.12392	3.4369	-0.07359
8.4611	-0.14321	4.5944	-0.12398	3.4386	-0.07399
8.3648	-0.14109	4.6083	-0.12404	3.4578	-0.07392
8.1859	-0.13844	5.353	-0.1241	3.4806	-0.07423
8.0861	-0.137	5.3617	-0.12416	3.5261	-0.07492
7.9399	-0.13499	5.3651	-0.12421	3.6346	-0.07626
7.8023	-0.13317	5.3686	-0.12423	3.7641	-0.07796
7.6647	-0.13132	6.4278	-0.12423	3.9146	-0.07982
7.5306	-0.12947	6.4693	-0.12424	4.0581	-0.08158
7.3998	-0.1276	6.4814	-0.12424	4.2069	-0.08339
7.2691	-0.12571	6.7855	-0.12425	4.3591	-0.08528
7.147	-0.12381	6.7976	-0.12427	4.5289	-0.08724
7.0438	-0.12186	6.8927	-0.12432	4.6741	-0.08901
6.9148	-0.11969	7.0067	-0.12437	4.8439	-0.09114
6.7789	-0.11787	7.0102	-0.12443	5.0328	-0.09332
6.6774	-0.11646	7.3627	-0.12449	5.1746	-0.09508
6.5932	-0.11535	7.361	-0.12455	5.3461	-0.09723
6.576	-0.11535	7.5061	-0.12461	5.5106	-0.09939
6.5725	-0.1152	7.5009	-0.12468	5.6716	-0.10161
6.5742	-0.11504	7.4992	-0.12474	5.8099	-0.10392
6.5605	-0.11474	7.7498	-0.12481	5.9201	-0.10657
6.4986	-0.11414	7.8638	-0.12488	6.1073	-0.10997
6.459	-0.11335	7.9347	-0.12494	6.2403	-0.11207
6.3025	-0.1118	7.9364	-0.12501	6.3734	-0.11419
6.2302	-0.11097	8.2008	-0.12508	6.5588	-0.11671
6.0789	-0.10946	8.2613	-0.12515	6.7006	-0.11856
5.9671	-0.10827	8.2422	-0.12523	6.8406	-0.12061
5.8123	-0.10686	8.3114	-0.12532	7.0506	-0.12295
5.6988	-0.10577	8.3096	-0.12543	7.1783	-0.12435
5.5732	-0.10447	8.4099	-0.1255	7.4356	-0.12619

5.4528	-0.10312	8.4513	-0.12557	7.4916	-0.12704
5.3204	-0.10171	8.5377	-0.12565	7.7313	-0.13353
5.2258	-0.1004	8.6742	-0.12571	7.7243	-0.13391
5.1105	-0.09885	8.8246	-0.12578	7.8136	-0.13465
4.9987	-0.09735	8.9317	-0.12586	7.8119	-0.13494
4.8835	-0.09587	9.0579	-0.1259	7.8924	-0.13718
4.7923	-0.09446	9.1702	-0.12597	7.9466	-0.13979
4.6582	-0.09294	9.2739	-0.12599	7.9309	-0.14008
4.5842	-0.09192	9.3551	-0.12621	7.9571	-0.14036
4.524	-0.09108	9.457	-0.12622	8.0323	-0.14093
4.2454	-0.08993	9.5192	-0.12624	8.1164	-0.14325
4.223	-0.08954	9.5884	-0.12625	8.2511	-0.1443
4.1542	-0.08884	9.6454	-0.12633	8.5101	-0.14567
4.0785	-0.08805	9.6938	-0.12641	8.5451	-0.14634
3.9461	-0.0871	9.7318	-0.12642	8.7306	-0.14762
3.8721	-0.08641	9.7594	-0.12643	8.7586	-0.14826
3.7552	-0.08563	9.7871	-0.12645	8.8653	-0.14949
3.6674	-0.08505	9.8095	-0.12653	8.9739	-0.15056
3.5711	-0.08448	9.8303	-0.12656	9.0928	-0.15193
3.4817	-0.08401	9.851	-0.12661	9.2241	-0.15374
3.394	-0.08366	9.8666	-0.12663	9.3378	-0.15581
3.3183	-0.08334	9.8787	-0.12667	9.4761	-0.15823
3.2426	-0.08316	9.8925	-0.12669	9.5934	-0.16055
3.1824	-0.08289	9.9011	-0.12673	9.7123	-0.16302
3.1532	-0.083	9.908	-0.12677	9.8174	-0.16552
3.1635	-0.08279	9.9184	-0.12682	9.9223	-0.16814
3.1635	-0.08272			10.027	-0.1707
3.16	-0.08272			10.117	-0.17322
3.1566	-0.08265			10.132	-0.174
3.1411	-0.0827				
3.117	-0.08268				
3.074	-0.08262				
3.0173	-0.08282				
2.9743	-0.08283				
2.9296	-0.08307				
2.8917	-0.08325				
2.859	-0.08337				
2.8264	-0.08363				
2.7971	-0.08387				
2.7713	-0.08405				
2.761	-0.08416				
2.7438	-0.08423				
2.7197	-0.08455				
2.6974	-0.08486				
2.6767	-0.08517				
2.6578	-0.08544				
2.6389	-0.0858				
2.6234	-0.08599				
2.6062	-0.08637				
2.5907	-0.08668				
2.577	-0.08693				
2.5752	-0.0869				
2.5305	-0.13499				

APPENDIX H

CRYSTALLOGRAPHY DATA

The crystallography information of all minerals provides the space group, unit cell, and XYX coordination.

Mineral name: Todorokite (Post and Bish, 1988)
Space group P 2/M
a = 9.764
b = 2.8416
c = 9.551
$\beta = 94.06$; $\gamma = 90.00$; $\alpha = 90.00$

Atom	X	Y	Z
Mn	0.500	0.500	0.000
Mn	0.764	0.000	0.001
Mn	0.000	0.000	0.500
Mn	0.974	0.500	0.765
O	0.178	0.500	0.119
O	0.418	0.000	0.079
O	0.665	0.500	0.090
O	0.917	0.000	0.150
O	0.913	0.500	0.407
O	0.880	0.000	0.649
O	0.363	0.000	0.353
O	0.696	0.500	0.380
O	0.500	0.500	0.500

Mineral name: Ramsdellite MnO_2 (Bystrom, 1949)
Space group P b n m
a = 4.533
b = 9.270
c = 2.866
$\beta = 90.00$; $\gamma = 90.00$; $\alpha = 90.00$

Atom	X	Y	Z
Mn	0.022	0.136	0.250
O	0.333	0.275	0.250
O	0.211	-0.033	0.250

Mineral name: Birnessite (Post and Veblen, 1990)
Space group C 2/m
a = 5.174
b = 2.850
c = 7.336
$\beta = 103.18$; $\gamma = 90.00$; $\alpha = 90.00$

Atom	X	Y	Z
Mn	0.000	0.000	0.000
O	0.376	0.000	0.133
Na	0.595	0.000	0.500
O	0.595	0.000	0.500
O	0.000	0.000	0.500

Mineral name: Pyrolusite (β-MnO_2) (Wyckoff, 1963)
Space group P 42/m n m
a = 4.396
c = 2.871
$\beta = 90.00$; $\gamma = 90.00$; $\alpha = 90.00$

Atom	X	Y	Z
Mn	0.000	0.000	0.000
O	0.302	0.302	0.000

Mineral name: Chalcophanite (Post and Appleman, 1988)
Space group R-3
a = 7.533
b = 7.533
c = 20.794
$\beta = 90.00$; $\gamma = 120.00$; $\alpha = 90.00$

Atom	X	Y	Z
Zn	0.000	0.000	0.099
Mn	0.718	0.578	0.999
O	0.528	0.623	0.047
O	0.261	0.206	0.050
O	0.000	0.000	0.712
O	0.179	0.931	0.164

Mineral name: Romanechite (Ba, $H_2O)_2Mn_5O_{10}$ (Turner and Post, 1988)
Space group C2/m
a = 13.939
b = 2.8359
c = 9.678
$\beta = 92.39$; $\gamma = 90.00$; $\alpha = 90.00$

Atom	X	Y	Z
Mn	0.000	0.500	0.000
Mn	0.999	0.000	0.269
Mn	0.340	0.000	0.484
Mn	0.000	0.167	0.000
Mn	0.500	0.167	0.267
Mn	0.839	0.166	0.484
O	0.567	0.000	0.177
O	0.098	0.000	0.462
O	0.766	0.000	0.392
O	0.426	0.000	0.337
O	0.925	0.000	0.068
O	0.067	0.166	0.177
O	0.597	0.167	0.423
O	0.266	0.166	0.398
O	0.924	0.166	0.334
O	0.427	0.168	0.075
Ba	0.245	0.000	0.123
Ba	0.747	0.166	0.124
O	0.249	0.000	0.143
O	0.753	0.173	0.129

Mineral name: Lithiophorite (Post and Appleman, 1994)
Space group R-3m
a = 2.925
c = 28.169
$\beta = 90.00$; $\gamma = 90.00$; $\alpha = 90.00$

Atom	X	Y	Z
Mn	0.000	0.000	0.000
Al	0.333	0.667	0.016
Li	0.333	0.667	0.016
O	0.667	0.333	0.034
O	0.667	0.333	0.132
H	0.667	0.333	0.099

REFERENCES

Abollino O., Aceto M., Malandrino M., Sarzanini C., and Mentasti E. (2003) Adsorption of heavy metals on Na-montmorillonite. Effect of pH and organic substances. *Water Research* 37, 1619-1627.

Adam L. F. and Ghiorse W. C. (1985) Influence of Mn on growth of a shealthless strain of *Leptothrix discophora. Appl. Environ. Microbiol.* 49, 556-562.

Adeleye S. A., Clay P. G., and Oladipo M. O. A. (1994) Sorption of cesium, strontium and europium ions on clay minerals. *J. Mat. Sci.* 29, 954-958.

Al-Degs Y., Khraisheh M. A. M., and Tutunji M. F. (2001). Sorption of Lead ion on diatomite and manganese modified diatomite. *Wat. Res.* 35, 3724-3728.

Allen T. (2003) Powder Sampling and Particle Size Determination, Elsevier, San Diego, CA.

Ahner B. A., Lee J. G., Price N. M., and Morel F. M. M. (1998) Phytochelatin concentration in the equatorial Pacific. *Deep-Sea Research.* I45, 1779-1796.

Arias M., Barral M. T., and Diaz-Fierros F. (1995) Effects of iron and aluminum oxides on the colloidal and surface properties of kaolin. *Clays Clay Miner.* 43, 406-416.

Axe L., Bunker G. B., Anderson P. R., and Tyson T. (1998) An XAFS analysis of strontium at the hydrous ferric oxide surfaces. *J. Colloid Interface Sci.* 199, 44-52.

Axe L., Trivedi P., and Morrison T. (2000). Local Structure Analysis of Stromtium Sorption to Hydrous Manganese Oxide. *J. Colloid Interface Sci.* 224, 408-416.

Axe L. and Trivedi P. (2002). Intraparticle surface diffusion of metal contaminants and their attenuation in microporous amorphous Al, Fe, and Mn oxides. *J. Colloid Interface Sci.* 247, 259-265.

Axe L. and Anderson P. R. (1995). Sr diffusion and reaction with Fe oxides: Evaluation of the rate-limiting mechanism for sorption. *J. Colloid Interface Sci.* 175, 157-165.

Axe L. and Anderson P. (1997) Experimental and theoretical diffusivities of Cd and Sr in hydrous ferric oxide. *J. Colloid Interface Sci.* 185, 436-448.

Axe L., Bunker G. B., Anderson P. R., and Tyson T. (1998) An XAFS analysis of strontium at the hydrous ferric oxide surfaces. *J. Colloid Interface Sci.* 199, 44-52.

Axe L., Tyson T., Trivedi P., and Morrison T. (2002). Local Structure Analysis of Strontium at the Hydrous Ferric Oxide Surface. *J. Colloid Interface Sci.* 224, 408-416.

Balistrieri L. S. and Murray J. W. (1982). The Surface Chemistry of δMnO_2 in Major Ion Sea Water. *Geochim. Cosmochim. Acta* 46, 1041-1052.

Banerjee D. and Nesbit H. W. (1999) Oxidation of Aqueous Cr(III) at Birnessite Surfaces: Constraints on Reaction Mechanism. *Geochim. Cosmochim. Acta* 63, 1671-1678.

Bargar J. R., Brown Jr. G. E., and Parks G. A. (1997) Surface complexation of Pb(II) at oxide-water interfaces: I. XAFS and bond-valance determination of mononuclear Pb(II) sorption products on aluminum oxides. *Geochim. Cosmochim. Acta* 61, 2617-2637.

Bargar J. R., Tebo B. M., and Villinski J. E. (2000) In situ charactristic of Mn(II) oxidation by spores of the marine *Bacillus sp.* Strain SG-1. *Geochimi Cosmochim Acta* 64, 2775-2778.

Bargar J. R., Tebo B. M., Bergmann U., Webb S. M., Glatzel P., Chiu V. Q., and Villalobos M. (2005) Biotic and abiotic products of Mn(II) oxidation by spores of the marine Bacillus sp. Strain SG-1, *Am. Mineral.* 90, 143-154.

Beveridge T. J. and Murray R. (1980) Sites of Metal deposition in the cell wall of *Bacillus subtillis. J. Bacteriol.* 141, 876-887.

Bochatay L. and Persson P. (2000). Metal Ion Coordination at the Water–Manganite (γ-MnOOH) Interface: II. An EXAFS Study of Zinc(II). *J. Colloid Interface Sci.* 229, 593-599.

Boonfueng T., Axe L., and Xu Y. (2005) Properties and structure of manganese oxide-coated clay. *J. Colloid Interface Sci.* 281, 80-92.

Boonfueng T., Axe L., Xu Y. and Tyson T. A. (2006) The impact of Mn oxide coatings on Zn distribution. *J. Colloid Interface Sci.* 298, 615-623.

Brindley G. W. and Brown G. (1980) Crystal structures of Clay Minerals and their X-ray Identification, Mineralogical Society, London.

Bromfield S. M. (1956) Oxidation of manganese by soil micro.ovrddot.organisms. *Austr. J Biol. Sci.* 9, 238-252.

Bromfield S. M. (1979) Manganous ion oxidation at pH values below 5.0 by cell-free substances from Streptomyces sp. cultures. *Soil Biol. Biochem.* 11,115-118.

Brouwers G. J., de Vrind J. P. M., Corstjens P. L. A. M., Cornelis P., Baysse C., and de Vrind-de Jong E. W. (1999) cumA, a gene encoding a multicopper oxidase, is involved in Mn^{2+}-oxidation in *Pseudomonas putida* GB-1. *Appl. Environ. Microbiol.* 65, 1762-1768.

Brouwers G. J., Corstjens P. L. A. M., de Vrind J. P. M., Verkamman A., de Kuyper M., and de Vrind-de Jong E. W. (2000) Stimulation of Mn^{2+}-oxidation in *Leptothrix discophora* SS-1 by Cu(II) and sequence analysis of the region flanking the gene encoding putative multicopper oxidase MofA. *Geomicrobiol. J.* 17, 25-33.

Brown I. D. and Altermatt D. (1985) Bond-valance parameters obtained from a systematic analysis of the inorganic crystal structure database. *Acta Cryst.* B41, 244-247.

Buhrke V. E., Jenkins R., Smith D. K. (1998) A Practical Guide for the Preparation of Specimens for X-ray Fluorescence and X-ray Diffraction Analysis, Wiley-VCH, New York.

Bunker B., Sayers D. In X-ray Absorption: Principles, Applications, Techniques of EXAFS, SEXAFS, and XAFS, Koningsberger, D.C., Prins, R., Eds., Wiley: New York, 1988.

Buser W., Graf P., and Feitknecht W. (1954) Manganese(II) manganite and δ-manganese dioxide. *Helv. Chim. Acta* 269, 2322-2333.

Bystrom A. M. (1949) Crystal Structure of ramsdellite, an orthorhombic modification of manganese dioxide. *Acta Chemica Scandinavica.* 3, 163-173.

Bystrom A. and Bystrom A. M. (1950) The crystal structure of hollandite, the related manganese oxide minerals, and α-MnO_2. *Acta Cryst.* 3, 146-154.

Carroll S. A., O'Day P. A., and Piechowski M. (1998). Rock-Water Interactions Controlling Zinc, Cadmium, and Lead Concentrations in Surface Waters and Sediments, U.S. Tri-State Maining District. 2. Geochemical Interpretation. *Environ. Sci. Technol.* 32, 956-965.

Celis R., Cox L., Hermosin M. C., and Cornejo J. (1997) Sorption of Thiazafluron by Iron- and Humic Acid-Coated Montmorillonite. *Environ. Qual.* 26, 472-479.

Chan C. S., De Stasio G., Welch S. A., Girasole M., Frazer B. H., Nesterova M. V., Farka S., and Banfield J. F. (2004) Microbial polysaccharides template assembly of nanocrystal fibers. *Science* 303, 1656-1658.

Chen H. and Cutright T. J. (2003) Preliminary Evaluation of Microbially Mediated Precipitation of Cadmium, Chromium, and Nickel by Rhizosphere Consortium. *J. Environ. Eng.* 129(1), 4-9.

Chisholm-Brause C. J., Hayes K. F., Roe A. L., Brown Jr. G. E., Parks G. A., and Leckie J. O. (1990) Spectroscopic investigation of Pb(II) complexes at the γ-Al_2O_3/water interface. *Geochim. Cosmochim. Acta* 54, 1897-1909.

Chukhrov F. V., Gorshkov A. I., Beresovskaya V. V., and Sivtsov A. V. (1979) Contributions to the mineralogy of authigenic manganese phases from marine manganese deposits. *Min. Deposita.* 14, 249-261.

Chukhrov F. V. and Gorshkov A. I. (1981) Iron and Manganese Oxide Minerals in Soil. *Trans R. Soc. Edinburgh Earth Sci.* 2, 195-200.

Chukhrov F. V., Drits V. A., and Gorshkov A. I. (1987) Structural transformations of manganese oxides of the oceanic iron-manganese nodules. *Izvestiya Akademii Nauk SSSR, Seriya Geologicheskaya.* 1, 3-14.

Chukhrov F. V. and Gorshkov A. I. (1980) Contributions to the mineralogy of authigenic manganese phases from marine manganese deposts A reply. *Min. Deposita.* 15, 255-257.

Chung J. and Zasoski R. J. (2002) Oxidation of Cr(III) to Cr(VI) by pyrolusite. *Agri. Chem. Biotechnol.* 45, 125-130.

Coppin F., Berger G., Bauer A., Castet S., and Loubet M. (2002) Sorption of lanthanides on smectite and kaolinite. *Chemical Geology.* 183, 57-68.

Costanzo P. M. and Guggenheim S. (2001). Baseline studies of The Clay Minerals Society source clays: preface. *Clays Clay Miner.* 49, 433-443.

Couling S. B. and Mann S. (1985) The influence of inorganic phosphate on the crystallization of magnetite (Fe_3O_4), from aqueous solution. *J. Chem. Soc., Chem. Commun.* 23, 1713-1715.

Dalpi M., Karayianni E., and Koutsoukos P. G. (1993) Inhibition of hydroxyapatite formation in aqueous solutions by zinc and 1,2-dihydroxy-1,2-bis(dihydroxyphosphonyl)ethane. *J. Chem. Soc., Faraday Transactions.* 89, 965-969.

Daughney C. J., Fein J. B., and Yee N. (1998) A comparison of the thermodynamics of metal adsorption onto two common bacteria. *Chem. Geol.* 144, 161-176.

Decho A. W. (1990) Microbial exopolymer secretions in ocean environments: Their role(s) in food webs and marine processes. *Oceanography and Marine Biology Annual Reviews* 28, 73-153.

Dong D., Nelson Y. M., Lion L. W., Shuler L., and Ghiorse W. C. (2000). Adsorption of Pb and Cd onto metal oxides and organic material in natural surface coatings as determined by selective extractions: new evidence for the importance of Mn and Fe oxides. *Wat. Res.* 34, 427-436.

Dong D., Derry L. A., and Lion L. W. (2003). Lead scavenging from a freshwater lake by Mn oxides in heterogeneous surface coating materials. *Wat. Res.* 37, 1662-1666.

Emerson D. and Ghiorse W. C. (1993) Ultrastructure and chemical composition of the sheath of *Leptothrix discophora* SP-6. *J. of Bacteriol.* 175, 7808-7818.

Emerson D. and Ghiorse W. C. (1992) Isolation, Culture Maintenance, and Taxonomy of a shealth-forming strain of *Leptothrix discophora* and characterization of Manganese-Oxidizing activity associated with the Shealth. *Appl Environ Microbiol.* 58, 4001-4010.

Environmental Research Company, Mineql+ A chemical equilibrium modeling system, Version 4.5., 1996.

Egozy Y. (1980) Adsorption of cadmium and cobalt on montmorillonite as a function of solution composition. *Clays Clay Miner.* 28, 311-318.

Erzan A. and Gungor N. (1995) Fractal geometry and size distribution of clay particles. *J. Colloid Interface Sci.* 176, 301-307.

Exon N. F., Raven M. D., and De Carlo E. H. (2002) Ferromanganese nodules and crusts from the Christmas Island Region, Indian Ocean. *Marine Georesources & Geotechnology* 20(4), 275-297.

Fan H. J. (1996) Removal and Recovery of Cu(II) and Cd(II) by Mn Oxide-Coated Composite Adsorbent, Ph.D. Thesis, Illinois Institute of Technology, Chicago, Illinois.

Fan M., Boonfueng T., Xu Y., Axe L., and Tyson T. A. (2005) Modeling Pb Sorption to Microporous Amorphous Oxides as Discrete Particles and Coatings *J. Colloid Interface Sci.* 281, 39-48.

Favejee J. C. L. (1939) X-ray investigation of soils. *Zeitschrift fuer Kristallographie, Kristallgeometrie, Kristallphysik, Kristallchemie* 100, 425-36.

Fein J. B., Daughney C., Yee N., and Davis T. A. (1997) A Chemical equilibrium model for metal adsorption onto bacterial surface. *Geochim. Cosmochim. Acta* 61, 3319-3328.

Fein J. B., Martin A. M., and Wightman P. G. (2001) Metal adsorption onto bacterial surfaces: development of a predictive approach. *Geochim. Cosmochim. Acta* 65, 4267-4273.

Foster A. L., Brown G. E., and Parks G. A. (2003). X-ray absorption fine structure study of As(V) and Se(IV) sorption complexes on hydrous Mn oxides. *Geochim. Cosmochim. Acta* 67, 1937-1953.

Francis C. A., Obraztsova A. M., and Tebo B. M. (2000) Dissimilatory Metal Reduction by the Facultative Anaerobe *Pantoea agglomerans* SP1. *Appl Environ Microbiol.* 66, 543-548.

Friedl A., Wehrli B., and Manceau A. (1997). Solid Phases in the Cycling of Manganese in Eutrophic Lakes. *Geochim. Cosmochim. Acta* 61, 275-290.

Gadde R. R. and Laitinen H. A. (1974). Studies of Heavy Metal Adsorption by Hydrous Iron and Manganese Oxides. *Anal. Chem.* 46, 2022-2026.

Ghirose W. C. (1984) Biology of iron-and manganese-depositing bacteria. *Annu. Rev. Microbiol.* 38, 515-550.

Ghiorse W. C. and Ehrlich H. L. (1992) Microbial Biomineralization of Iron and Manganese. In: Fitzpatrick and Skinner (Eds.) Iron and manganese biomineralization processes in modern and ancient environments. Catena Cremlingen-Destedt, Germanyvol. Catena Supplement 21, p. 75-99.

Giovanoli R. (1980) Vernadite is random-stacked birnessite. A discussion of "Contributions to the mineralogy of authigenic manganese phases from marine manganese deposits. *Min. Deposita.* 15, 251-253.

Glasauer S., Weidler P. G., Langley S., and Beveridge T. J. (2003) Controls of Fe Reduction and mineral formation by a subsurface bacterium. *Geochim. Cosmochim. Acta* 67, 1277-1288.

Goldstien J. I., Newbury D. E., Echlin P., Joy D. C., Romig A. D., Lyman C. E., Fiori C., and Lifshin E. (1992) Scanning Electron Microscopy and X-ray Microanalysis, 2nd edition, Plenum Press, New York and London.

Grases F., Genestar C., and Millan A. J. (1989) The influence of some metallic ions and their complexes on the kinetics of crystal growth of calcium oxalate. *J. Crystal Growth.* 94, 507-512.

Greenberg A. E., Trussell R. T., Clesceri L. S., and Franson M. H. (1998) "Standard Methods for the examination of water wand wastewater. 20th edition, APHA, AWWA, WPCF, Washington D.C.

Green-Pederson H., Jensen B. T., and Pind N. (1997). Nickel Adsorption on MnO_2, $Fe(OH)_3$, Montmorillonite, Humic Acid and Calcite: A Comparative Study. *Environ. Technol.*, 18, 807-815.

Green-Pederson H. and Pind N. (2000) Preparation, characterization, and sorption properties for Ni(II) of iron oxyhydroxide-montmorillonite. *Colloids Surf. A.* 168, 133-145.

Grim R. W. (1950).Clay mineralogy, McGraw-Hill, New York.

GTI Gas technology Institute, Sample Analyses Report, Illinois, 2003.

Guha H., Saiers J. E., Brooks S., Jardine P., and Jayachandran K. (2001) Chromium transport, oxidation, and adsorption in manganese-coated sand. *J. Contaminant Hydrology*. 49, 311-334.

Guine V., Spadini L., Sarret G., Muris M., Delolme J., Gaudet P., and Martins J. M. F. (2006) Zinc Sorption to Three Gram-Negative Bacteria: Combined Titration, Modeling, and EXAFS Study. *Environ Sci Technol*. 40, 1806-1813.

Haack E. A. and Warren L. A. (2003) Biofilm hydrous manganese oxyhydroxides and metal dynamics in acid rock drainage. *Environ. Sci. Technol*. 37, 4138-4147.

Hatch L. P. (1952) US Atomic Energy Commission Technical Information Service, Oak Ridge, TN WASH-129, p. 119.

Healy T. W., Herring A. P., and Fuerstenau D. W. (1966). The effect of crystal structure on the surface properties of a series of manganese dioxides. *J. Colloid Interface Sci*. 21, 435-444.

Helmy A. K., Ferreiro E. A., and De Bussetti S. G. (1994) Cation Exchange Capacity and Condition of Zero Charge of Hydroxy-Al Montmorillonite. *Clays Clay Miner*. 43, 444-450.

Hill R. J. and Jones J. B. (1976) The crystal structure of hopeite. *Am. Mineral*. 61, 987-995

Hill R. J. (1985) Refinement of the structure of orthorhombic lead oxide (massicot) by Rietveld analysis of neutron powder diffraction data. *Acta Crystallogr*. C41, 1281-1284.

Hochella M. F. Jr., Kasama T., Putnis A., Putnis C. V., and Moore J. N. (2005) Environmentally important, poorly crystalline Fe/Mn hydrous oxides: ferrihydrite and a possibly new vernadite -like mineral from the Clark Fork River Superfund Complex. *Am. Mineral*. 90(4), 718-724.

House W. A. (1987) Inhibition of calcite crystal growth by inorganic phosphate. *J. Colloid Interface Sci*. 119, 505-511.

Isaure M. P., Laboudigue A., Manceau A., Sarret G., Tiffreau C., Trocellier P., Lamble G., Hazemann J. L., and Chateigner D. (2002) Quantitative Zn speciation in a contaminated dredged sediment by μ-PIXE, μ-SXRF, EXAFS spectroscopy and principal component analysis. *Geochim. Cosmochim. Acta* 66, 1549-1567.

JCPDS (1998) Handbook for diffraction data (PCPDFWIN ver. 2.00).

Jenne E. A. (1977) Controls on s on Mn, Co, Ni, Cu and Zn. Concentrations in soil and water: the significant role of hydrous Mn and Fe oxides. in: W. Chappel, Pereson (Eds.), Symposium on Molydenum in the Environment, 2. Marcel Dekker, New York, 19, 337-387.

Jürgensen A., Widmeyer J. R. M., Gordon R. A., Bendell-Yonug L. I., Moore M. M., and CrozierD. E. (2004) The structure of the manganese oxide on the sheath of the bacterium *Leptothrix discophora*: An XAFS study. *Am. Mineral.* 89, 1110-1118.

Kalhorn S. and Emerson S. (1984) The oxidation state of manganese in surface sediments of the deep sea. *Geochimi Cosmochim Acta* 48, 897-902.

Kaplan D., Christiaen D., and Arad S. (1987) Chelating properties of extracellular polysaccharide from Chlorella spp. *Appl. Environ. Microbiol.* 53, 2953-2956.

Karim Z. (1984) Influence of transition metals on the formation of iron oxides during the oxidation of an iron(II) chloride solution. *Clays Clay Miner.* 32, 334-336.

Kärger J. and Ruthven D. M. (1992).Diffusion in Zeolites and other Microporous Solids, John Wiley: New York.

Kelly S. D., Kemner K. M., Fein J. B., Fowle D. A., Boyanov M. I., Bunker B. C., and Yee N. (2002) X-ray absorption fine structure determination of pH-dependent U-bacterial cell wall interactions. *Geochim. Cosmochim. Acta* 66, 3855-3871.

Kemner K. M., Kelly S. D., Lai B., Maser J., O'Lounghlin E. J., Sholto-Douglas D., Cai Z., Schneegurt M. A., Kulpa C. F. Jr., and Nealson K. H. (2004) Elemental and redox analysis of single bacteria cells by X-ray microbeam analysis. *Science.* 306, 686-687.

Kennedy C., Smith S. D., and Warren L. A. (2004). Surface chemistry and relative Ni sorption capacities of synthetic hydrous Mn oxyhydroxides under variable wetting and drying regimes. *Geochim. Cosmochim. Acta* 68, 443-454.

Kim J. G., Dixon J. B., Chusuei C. C., and Deng Y. (2002). Oxidation of Chromium(III) to (VI) by Manganese Oxides. *Soil Sci. Soc. Am. J.* 66, 306-315.

Knocke W. R., Hamon J. R., and Thompson C. P. (1988) Soluble manganese removal on oxide-coated filter media. *J. AWWA.* 80, 65-70.

Kim H. S. and Stair P. C. (2004) Bacterially Produced Manganese Mn oxide and Todorokite: UV Raman Spectroscopic comparison. *J. Phys. Chem B.* 108, 17019-17026.

Konhauser K. O., Schultze-Lam S., Ferris F. G., Fyfe W. S., Longstaffe F. J., and Beveridge T. J. (1994) Mineral precipitation by epilithic biofims in the Speed River, Ontario, Canada. *Appl. Environ. Microbiol.* 60, 549-553.

Koutsopoulos S. and Dalas E. (2000). The Crystallization of Hydroxyapatite in the Presence of Lysine. *J. Colloid Interface Sci.* 231, 207-212.

Kraepiel A. M. L., Keller K., and Morel F. M. M. (1999) A Model for Metal Adsorption on Montmorillonite. *J. Colloid Interface Sci.* 210, 43-54.

Ku H. H. (1966). Notes on the propagation of error formulas. *J. Res. Natl. Bur. Standards - C. Eng. Instrum.* 70, 263-273.

Kunze G. W. and Dixon J. B (1982) Pretreatment for mineralogical analysis. *In* "Method of Soil Analysis, Part 1 Physical and Mineralogical Methods. In: A. Kulte (Eds.), American Society of Agronomy/Soil Science Society of America, Madison, WI, 1982, 91-100.

Lee S., Anderson P. R., Bunker G. B., and Karafil C. (2004) EXAFS Study of Zn sorption Mechanisms on Montmorillonite, *Environ. Sci. Technol.* 38, 5426-5432.

Li X., Pan G., Qin Y., Hu T., Wu Z., and Xie Y. (2004). EXAFS studies on adsorption–desorption reversibility at manganese oxide–water interfaces: II. Reversible adsorption of zinc on δ-MnO_2. *J. Colloid Interface Sci.* 271, 35-40.

Li Y., Zhang B. Y., Huang G. H., Dong D., and Hau X. (2003) Relationship between Pb/Cd adsorption and metal oxides on surface coatings at different depths in Lake Jingyuetan. *Hydrobiologia.* 494, 31-35.

Lion L. W., Altmann R. S., and Leckie J. O. (1982). Trace-metal adsorption characteristics of estuarine particulate matter: evaluation of contributions of iron/manganese oxide and organic surface coatings. *Environ. Sci. Technol.* 16, 660-666.

Liu C., Gorby Y. A., Zachara J. M., Fredrickson J. K., and Brown C. F. (2002) Reduction Kinetics of Fe(III), Co(III), U(VI), Cr(VI), and Tc(VII) in Cultures of Dissimilatory Metal-Reducing bacteria. *Biotechnology and bioengineering.* 80(6), 637-649.

Manceau A., Llorca S., and Calas G. (1987). Crystal Chemistry of Cobalt and Nickel in Lithiophorite and Asbolane from New Caledonia. *Geochim. Cosmochim. Acta* 51, 105-113.

Manceau A. and Combes J. M. (1988). Structure of Mn and Fe Oxides and Oxyhydroxides: A Topological Approach by EXAFS. Phys. *Chem. Mineral. 15*, 283-295.

Manceau A., Gorshkov A. I., and Drits V. A. (1992). Structure Chemistry of Mn, Fe, Co, and Ni in Manganese Hydrous Oxides, Part II. Information from EXAFS Spectroscopy and Electron and X-ray Diffraction. *Am. Mineral.* 77, 1133-1143.

Manceau A. and Charlet L. (1992). X-ray Absorption Spectroscopic Study of the Sorption of Cr(III) at the Oxide/Water Interface. I. Molecular Mechanism of Cr(III) Oxidation on Mn Oxides. *J. Colloid Interface Sci.*148, 425-442.

Manceau A, Boisset M. C., Sarret G., Hazemann J. L., Mench M., Cambier P., Prost R. (1996) Direct determination of lead speciation in contaminated soils by EXAFS spectroscopy. *Environ. Sci. Technol.* 30, 1540-1552.

Manceau A., Lanson B., and Drits V. A. (2002) Structure of heavy metal sorbed birnessite. Part III: Results from powder and polarized extended X-ray absorption fine structure spectroscopy. *Geochim. Coscochim. Acta* 66, 2639-2663.

Manceau A., Tamura N., Celestre R. S., Macdowell A. A., Geoffroy N., and Padmore H. A. (2003). Molecular-Scale Speciation of Zn and Ni in Soil Ferromanganese Nodules from Loess Soil of the Mississippi Basin. *Environ. Sci. Technol.* 37, 75-80.

Manceau A., Tommaseo C., Rihs S., Geoffroy N., Chateigner D., Schlegel M., Tisserand D., Marcus M. A., Tamura N, and Chen Z. (2005) Natural speciation of Mn, Ni, and Zn at the micrometer scale in a clayey paddy soil using X-ray fluorescence, absorption, and diffraction. *Geochim. Cosmochim. Acta* 69(16), 4007-4034.

Manderneck K. W., Post J., and Tebo B. M. (1995) Manganese mineral formation by bacterial spores of the marine Bacillus, strain SG-1: evidence for the direct oxidation of Mn(II) to Mn(IV). *Geochim. Cosmochim. Acta* 21, 4393-4408.

Manning B. A., Fendorf S. E., Bostick B., and Suarez D. L. (2002). Arsenic(III) Oxidation and Arsenic(V) Adsorption Reactions on Synthetic Birnessite. *Environ. Sci. Technol.* 36, 976-981.

Malinowski E. R. (1978) Theory of error for target factor analysis with applications to mass spectrometry and nuclear magnetic resonance spectrometry. *Analytica Chimica Acta* 103, 339-354.

Matocha C. J., Elzinga E. J., and Sparks D. L. (2001) Reactivity of Pb(II) at the Mn(III,IV) (oxyhyd)oxide-water interface. *Environ. Sci. Technol.* 35, 2967-2972.

McKenzie R. M. (1989). Manganese Oxides and Hydroxides in Minerals in Soil Environment (J.B. Dixon, S.B. Weeds, Eds.), Soil Science Society of America Book Series No. 1, SSSA, Madison, Wisconsin.

McKeown D. A. and Post J. E. (2001) Characterization of Manganese Oxide Mineralogy in Rock Varnish and Dendrites using X-ray Absorption Spectroscopy. *Am. Mineral.* 86, 701-713.

Medigan M., Martinko J., and Parker J. (2000) *Brock Biology of Microoganisms*. Ninth ed. Prentice-Hall, Upper Saddle River, NJ.

Meng X. and Letterman R. D. (1993). Effect of Component Oxide Interaction on the Adsorption Properties of Mixes Oxides. *Environ. Sci. Technol.* 27, 970-975.

Mitchill L. Ceramics-Stone age and Space Age, McGraw-Hill, New York, 1963.

Mortimer R. J. G. and Rae J. E. (2000) Metal speciation (Cu, Zn, Pb, Cd) and organic matter in oxic to suboxic salt marsh sediments, Severn Estuary, southwest Britain. *Mar. Poll. Bull.* 40, 377-386.

Morgan J. and Stumm W. J. (1964). Colloid Chemical Properties of Manganese Dioxide. *Journal of Colloid Science.* 19, 347-353.

Naidja A., Huang P. M., and Bollag J. M. (1997) Activity of tyrosinase immobilized on hydroxyaluminum-montmorillonite complexes. *J. Molecular Catalysis A: Chemical.* 115, 305-316.

Nachtegaal M. and Sparks D. L. (2003) Ni sequestration in a kaolinite-humic acid complexes. *Environ. Sci. Technol.* 37, 529-534.

Nachtegaal M. and Sparks D. L. (2004) Effect of iron oxide coatings on zinc sorption mechanisms at the clay-mineral/water interface. *J. Colloid Interface Sci.* 276, 13-23.

Nealson K. H., Tebo B. M., and Rosson R. A. (1988) Occurrence and mechanisms of microbial oxidation of manganese. *Adv. Environ. Microbiol.* 33. 279-318.

Neder R. B., Burghammer M., Grasl Th., Schuzl H., Bram A., and Fiedler S. (1999) Refinement of the kaolinite structure from single-crystal synchrotron data. *Clays Clay Miner.* 47, 487-494.

Nelson Y. M., Lo W., Lion L. W., Shuler L., and Ghiorse W. C. (1995). Lead Distribution in a simulated aquatic environment: Effects of bacterial biofilms and iron oxide. *Wat. Res.* 29, 1934-1944.

Nelson Y. W., Lion L. W., Shuler M. L., and Ghiorse W. C. (2002). Effect of Oxide Formation Mechanisms on Lead Adsorption by Biogenic Manganese (Hydr)oxides, Iron (Hydr)oxides, and Their Mixtures. *Environ. Sci. Technol.* 36, 421-425.

Nelson Y. M. and Lion L. W. (2003) Formation of biogenic manganese oxides and their influence on the scavenging of toxic trace elements. In: Selim, H.M., Kingery, W.L. (Eds.), *Geochemical and Hydrological Reactivity of Heavy Metals in Soils.* CRC Press, LLC, pp 169-186.

Ngwenya B. T., Sutherland I. W., and Kennedy L. (2003) Comparison of the acid-base behavior and metal adsorption characteristics of a gram-negative bacterium with other strains. *Appl. Geochem.* 18, 527-538.

Norton F. H. (1952). Elements of Ceramics, Addison-Wesley Press, Inc., Massachusetts, p. 10.

O'Day P. A., Brown G. E., and Parks G. A. (1994) X-ray Absorption Spectroscopy of Co(II) Multinuclear Surface Complexes and Surface Precipitates on Kaolinite. *J. Colloid Interface Sci.* 165, 269-289.

Olovosson I. and Jonsson P. In The hydrogen bond II Structure and Spectroscopy, Schuster, P., Zundel, G., and Sandorfy, C., Eds, North-Holland, 1976.

Pan G. and Liss P. S. J. (1998). Metastable-Equilibrium Adsorption Theory: II Experimental. *J. Colloid Interface Sci.* 201, 77-85.

Pan G., Qin Y., Li X., Hu T., Wu Z., and Xie Y. (2004) EXAFS studies on adsorption–desorption reversibility at manganese oxides–water interfaces: I. Irreversible adsorption of zinc onto manganite (γ-MnOOH). *J. Colloid Interface Sci.* 271, 28-34.

Papelis C., Roberts P. V., and Leckie J. O. (1995) Modeling the Rate of Cadmium and Selinite Adsorption on Micro- and Mesoporous Transition Aluminas. *Environ. Sci. Technol.* 29, 1099-1108.

Parks G. A. (1967) Aqueous surface Chemistry of oxides and complex oxide minerals-isoelectric point and zero point of charge. Equilibrium Concepts in Natural Water Systems. Edited by Werner Stumm, Advance in Chemistry Series 67, ACS, Washington, D.C.

Pasten P. A. (2002) Structure and formation kinetics of manganese oxides by *Leptothrix discophora* SP-6. Ph.D. Thesis, Northwestern University, Evanston, Illinois.

Pauling L. (1960) The Nature of the chemical bond, Cornell University Press, New York.

Pertlik F. (1986) Structures of hydrothermally synthesized cobolt(II) and nickel(II) carbonate. *Acta Crystallogr.* C42, 4-5.

Post J. (1999) Manganese oxide minerals: crystal structures and economic and environmental significance. *Proc. Natl. Acad. Sci. USA.* 96, 3447-3454.

Potter R. M. and Rossman G. R. (1979). Mineralogy of manganese dendrites and coatings *Am. Mineral.* 64, 1219-1226.

Post J. E. and Bish D. L. (1988) Rietveld refinement of the Todorokite Structure. *Am. Mineral.* 73, 861-869.

Post J. E. and Appleman D. E. (1988) Chalcophanite, $ZnMn_3O_7 \cdot 3H_2O$: New crystal-structure determinations. *Am. Mineral.* 73, 1401-1404.

Post J. E. and Appleman D. E. (1994) Crystal Structure refinement of Lithiphorite. *Am. Mineral.* 79, 370-374.

Post J. E. and Veblen D. R. (1990) Crystal structure determinations of synthetic sodium, magnesium, and potassium birnessite using TEM and the Rietveld method. *Am. Mineral.* 75, 477-89.

Quirk J. P. and Murray R. S. (1999). Appraisal of the Ethylene Glycol Monoethyl Ether Method for Measuring Hydratable Surface area of Clays and Soils. *Soil Sci. Soc. Am. J.* 63, 839.

Racko D., Chelli R., Cardini G., Bartos J., and Califano S. (2005) Insights into positron annihilation lifetime spectroscopy by molecular dynamics simulations Free-volume calculations for liquid and glassy glycerol. *Eur. Phys. J. D* 32, 289-297.

Rees S. G., Shellis R. P., and Embery G. (2002) Inhibition of Hydroxyapatite Crystal Growth by Bone Proteoglycans and Proteoglycan Components. *Biochem. Biophy. Res. Commun.* 292, 727-733.

Ressler T. (1998). WinXAS: a program for x-ray absorption spectroscopy data analysis under MS-Windows. *J. Synchrotron Radiation* 5, 118-122.

Richen D. T. The Chemistry of Aqua Ions, John Wiley: New York, 1997

Roberts D. R., Scheidegger A. M., and Sparks D. L. (1999) Kinetics of mixed Ni-Al precipitate formation on a soil clay fraction. *Environ. Sci. Technol.* 33, 3749-3754.

Roberts D. R., Scheinost A. C., and Sparks D. L. (2002) Zinc speciation in a smelter-contaminated soil profile using bulk and microspectroscopic techniques. *Environ. Sci. Technol.* 36, 1742-1750.

Robinson G. D. (1981) Adsorption of Copper, Zinc, and Lead near Sulfide Deposits by Hydrous Manganese-Iron Oxide Coatings on Stream Alluvium. *Chemical Geology.* 33, 65-79.

Romano A. H. and Peloquin J. P. (1963) Composition of the sheath of *Sphaerotilus natans. J. Bacteriol.* 86, 252-258.

Ross G. J. and Wang C. (1993) Extrable Al, Fe, Mn, and Si in Soil Sampling and methods of Analysis (M.R. Carter, Eds.), Canadian Society of Soil Science Lewis Publishers, p. 239.

Sahl K. (1974) Refinement of the crystal structure of cerussite ($PbCO_3$). *Z. Kristallogr., Kristallgeom., Kristallphys., Kristallchem.*139, 215-222.

Sarret G., Manceau A., Spadini L., Roux J. C., Hazemann J. L., Soldo Y., Eybert-Berard L., and Menthonnex J. J., (1998) EXAFS determination of Pb, Zn complexing sites of *Penicillium chrysogenum* cell walls. *Environ Sci Technol.* 32, 1648-1655.

Sarret G., Vangronsveld J., Manceau A., Musso M., Haen J. D., Menthoxnnex J. J., and Hazemann J. L. (2001) Accumlation forms of Zn and Pb in Phaseolus vulgaris in the Presence and Absence of EDTA. *Environ Sci Technol.* 35, 2854-2859.

Scheidegger A. M., Lamble G. M., Sparks D. L. (1997) Spectroscopic evidence for the formation of mixed-cation hydroxide phases upon metal sorption on clays and aluminum oxides. *J. Colloid Interface Sci.* 186, 118-128.

Scheinost A. C., Abend S., Pandya K. I., and Sparks D. L. (2001) Kinetic Controls on Cu and Pb Sorption by Ferrihydrite. *Environ. Sci. Technol.* 35, 1090-1096.

Scheinost A. C., Kretzschmar R., Pfister S., and Roberts D. R. (2002) Combining selective sequential extractions, X-ray absorption spectroscopy, and principal component analysis for quantitative zinc speciation in soil. *Environ. Sci. Technol.* 36, 5021-5028.

Schlegel M. L., Manceau A., Chateigner D., and Charlet L. (1999). Sorption of Metal Ions on Clay Minerals: I. Polarized EXAFS Evidence for the Adsorption of Co on the Edges of Hectorite Particles. *J. Colloid Interface Sci.* 215, 140-158.

Scott M. J. and Morgan J. J. (1995). Reaction at Oxide surfaces. 1. Oxidation As(III) by Synthetic Birnessite. *Environ. Sci. Technol.* 29, 1898-1905.

Scott M. J. and Morgan J. J. (1996). Reactions at Oxide Surfaces. 2. Oxidation of Se(IV) by Synthetic Birnessite. *Environ. Sci. Technol.* 30, 1990-1996.

Sigg L., Mason Y., Ammann A. A., and Ulrich A. (1999). Behavior of Heavy Metals, Nutrients, and Major Components during Roof Runoff Filtration. *Environ. Sci. Technol.* 33, 1588-1597.

Silvester E., Manceau A., and Drits V. A. (1997) Structure of Synthesis Monoclinic Na-rich Birnessite and Hexagonal Birnessite: II Result from Chemical Studies and EXAFS spectroscopy. *Am. Mineral.* 82, 962-978.

Sparks D. L. (1995) Environmental soil chemistry, Academic Press, California.

Sposito G. (1984).The Surface Chemistry of Soils, Oxford University Press, New York.

Stahl R. S. and James B. R. (1991). Zinc sorption by Manganese-Oxide-Coated Sand as a Function of pH. *Soil Sci. Soc. Am. J.* 55, 1291-1294.

Stahl R. S. and James B. R. (1991) Zinc sorption by iron-oxide-coated sand as a function of pH. *Soil Sci. Soc. Am. J.* 55, 1287-1290.

Stenkamp S. V. and Benjamin M. M. (1994) Effect of iron oxide coating on sand filtration. *J. AWWA*. 86, 37-50.

Strathmann T. J. and Myneni S. C. B. (2005) Effect of Soil Fulvic acid on Nickel (II) Sorption and bonding at the Aqueous-Boehmite (γ-AlOOH) Interface. *Environ. Sci. Technol.* 39, 4027-4034.

Strawn D. G., Scheidegger A. M., and Sparks D. L. (1998) Kinetics and Mechanisms of Pb(II) Sorption and Desorption at the Aluminum Oxide-Water Interface. *Environ. Sci. Technol.* 32, 2596-2601

Strawn D. G. and Sparks D. L. (1999) The Use of XAFS to Distinguish between Inner- and Outer-Sphere Lead Adsorption Complexes on Montmorillonite. *J. Colloid Interface Sci.* 216, 257-269.

Stumm W. (1992). Chemistry of the solid-Water Interface, John Wiley, New York.

Storr M. T., Taylor P. C., Monfort J. P., and Rodger M. P. (2004) Kinetic Inhibitor of Hydrate Crystallization. *J. Am. Chem. Soc.* 126, 1569-1576.

Sun J. N., Hu Y. F., Frieze D. W., and Gidley D. W. (2003) Characterizing porosity in nanoporous thin films using positronium annihilation liftetime spectroscopy. *Radiation Physics and Chemistry* 68, 345-349.

Sunda W. G. and Kieber D. J. (1994) Oxidation of humic substances by manganese oxides yield low-molecular-weight organic substates. *Nature* 367, 66-64.

Sung-Kim H., Pasten P. A., Gaillard J. F., and Stair P. C. (2003) Nanocrystalline todorokite-like manganese oxide produced by bacterial catalysis. *J. Am. Chem. Soc.* 125, 14284-14285.

Szecsody J. E., Zachara J. M., and Bruchhart P. L. (1994). Adsorption-Dissolution Reaction s Affecting the Distribution and Stability of Co(II)EDTA in Iron Oxide-Coated Sand. *Environ. Sci. Technol.* 28, 1706-1716.

Tamura H., Katayoma N., and Furuichi R. (1997). The Co^{2+} adsorption properties of Al_2O_3, Fe_2O_3, Fe_3O_4, TiO_2, and MnO_2 evaluated by modeling with the Frumkin isotherm. *J. Colloid Interface Sci.* 195, 192-202.

Tani Y., Miyata N., Iwahori K., Soma M., Tokada S., Seyama H., and Theng B. K. G. (2003) Biogeochemistry of manganese oxide coatings on pebble surfaces in the Kikukawa river system, Shizuoka, Japan. *Appl. Geochem.* 18, 1541-1554.

Tipping E., Thompson D. W., and Davison W. (1984) Oxidation products of manganese(II) in lake waters. *Chem. Geol.* 44, 359.

Templeton A. S., Trainor T. P., Traina S. J., Spormann A. M., and Brown Jr. G. E. (2001) Pb(II) distributions at biofilm-metal oxide interfaces. *Proc. Nat. Acad. Sci.* 98, 11897-11902.

Toner B., Manceau A., Marcus M. A., Millet D. B., and Sposito G. (2005) Zinc Sorption by a Bacterial Bioflim. *Environ Sci Technol.* 39, 8288-8294.

Toner B., Manceau A., Webb S. M., Sposito G. (2006) Zn sorption to biogenic hexagonal-birnessite particles with hydrated bacterial bioflim. *Geochim. Cosmochim. Acta* 70, 27-43.

Tournassat C., Charlet L., Bosbach D., and Manceau A. (2002). Arsenic(III) Oxidation by Birnessite and Precipitation of Manganese(II) Arsenate. *Environ. Sci. Technol.* 36, 493-500.

Trivedi P. and Axe L. (2000). Modeling Cd and Zn Sorption to Hydrous Metal Oxides. *Environ. Sci. Technol.* 34, 2215-2223.

Trivedi P. and Axe L. (1999). A Comparison of Strontium Sorption to Hydrous Aluminum, Iron, and Manganese oxides. *J. Colloid Interface Sci.* 218, 554-563.

Trivedi P., Axe L., and Tyson T. (2001a) Predicting Divalent Metal sorption to Hydrous Al, Fe, and Mn Oxides. *Environ. Sci. Technol.* 35, 1779-1784.

Trivedi P., Axe L., and Tyson T. (2001b) XAS Studies of Ni and Zn Sorbed to Hydrous Manganese Oxide. *Environ. Sci. Technol.* 35, 4515-4521.

Tsadilas C. D., Dimoyiannis D., and Samaras V. (1998) Boron sorption by manganese oxide coated sand. *Commun. Soil Sci. Plant Anal.* 29, 2347-2353.

Tsang P. H., Li G., Brun Y. V., Freund L. B., and Tang J. X. (2006) Adhesion of single bacterial cells in the micronewton range. *Proc. Natl. Acad. Sci. USA.* 103, 5764-5768.

Turner S. and Post J. E. (1988) Refinement of the substructure and superstructure of romanechite.*Am.Mineral.* 73, 1155-1161.

Turner G. D., Zachara Z. M., Kinley J. P., and Smith S. C. (1996). Surface-charge properties and UO_2^{2+} adsorption of a subsurface smectite. *Geochim. Cosmochim. Acta* 60, 3399-3414.

Van Veen W. L., Mulder E. G., and Deinema M. H. (1978) The *Sphaerotilus-Leptothrix* group of bacteria. *Microbiol. Rev.* 42, 329-356.

Villalobos, M.; Toner, B.; Bargar, J.R.; Sposito, G. (2003) Characterization of the manganese oxide produced by *Pseudomonas putida* Strain MnB1. *Geochimi Cosmochim Acta*, 67, 2649-2662.

Villalobos M, Bargar J, and Sposito G (2005) Mechanisms of Pb(II) sorption on a biogenic manganese oxide *Environ. Sci. Technol.* 39, 569-576.

Wadsley A. D. (1950) A hydrous manganese oxide with exchange properties. *J. Am. Chem. Soc.* 72, 1781-1784.

Wallner H. and Gatterer K. (2002) Growth of pure $Ni(OH)_2$ single crystals from solution – control of the crystal size. *Z. Anorg. Allg. Chem.* 628, 2818-2820.

Wenfeng T., Fan L., Yonghua L., Jizheng H., and Xueyuan L. (2000) Mineralogy of manganese oxide minerals in iron-manganese nodules of several main soils in China. *Pedosphere.* 10(3), 265-274.

Widmeyer J. R., Crozier E. D., Moore M. M., Jurgensen A., and Bendell-Young L. I. (2004) Role of Leptothrix discophora in mediating metal uptake in the filter-feeding bivalve Mytilus trossulus (edulis). *Environ. Sci. Technol.* 38, 769-774.

Wilson A. R., Lion L. W., Nelson Y. M., Shuler M. L., and Ghiorse W. C. (2001) The effects of pH and surface composition on Pb adsorption to natural freshwater bioflims. *Environ Sci Technol.* 35, 3182-3189.

Wu Z., Gu Z., Wang X., Evans L., and Guo H. (2003) Effects of organic acids on adsorption of lead onto montmorillonite, goethite and humic acid. *Environ. Poll.* 121, 469-475.

Wyckoff R. W. G. (1963) Crystal structure Vol. 1, John Wiley and Sons: New York, London.

Wyckoff R. W. G. (1988) Crystal Structure 1, III, Interscience Publishers.

Yee N. and Fein J. B. (2001) Cd adsorption onto bacterial surfaces: A universal adsorption edges? *Geochim. Cosmochim. Acta* 65, 2037-2042.

Zachara J. M., Gassman P. L., Smith S. C., and Taylor D. (1995). Oxidation and Adsorption of $Co(II)EDTA_2^{2-}$ complexes in subsurface materials with iron and manganese oxide grain coatings. *Geochim. Cosmochim. Acta* 59, 4449-4463.

Zabinsky S. I., Rehr J. J., Aukudinov A., Albers R. C., and Eller M. J. (1995) Multiple scattering calculations of X-ray absorption spectra. *Phys. Rev. B.* 52, 2995-3009.

Zaki M. I., Nohman A. K. H., Hussein G. A. M., and Nashed Y. E. (1995) MnOx-influenced bulk and surface behaviors of catalytic Al_2O_3. *Colloids Surf A.* 99, 247.

Zhang J., Lion L. W., Nelson Y. M., Shuler M. L., and Ghiorse W. C. (2002) Kinetics of Mn(II) oxidation by *Leptothrix discophora* SS-1. *Geochimi Cosmochim Acta* 65, 773-781.